Understanding the Dissolution Behaviour of Flax Yarn in Ionic Liquids

Fatimah Ahmed Albarakati

School of Physics and Astronomy

University of Leeds

Submitted in accordance with the requirements for the degree of
Doctor of Philosophy

March, 2025

The candidate confirms that the work submitted is her own, except where work which has formed part of jointly-authored publications has been included. The contribution of the candidate and the other authors to this work has been explicitly indicated below. The candidate confirms that appropriate credit has been given within the thesis where reference has been made to the work of others.

Acknowledgements

I would like to express my heartfelt gratitude and deepest appreciation to my supervisors, Prof. Michael E. Ries and Dr. Peter J. Hine, for their invaluable advice, guidance, and support throughout my research journey. Their wealth of knowledge, creativity, and constant encouragement have been an endless source of inspiration, and I am profoundly grateful for the countless engaging and thought-provoking discussions we shared.

A special thanks to Dr. Daniel L. Baker for his dedication to my training and for generously offering his time to solve challenges related to the lab equipment. His expertise and patience have been instrumental in overcoming many obstacles along the way.

I extend my sincere appreciation to everyone in our Biopolymer Dream Team (Nora, Amjad, Mear, Samiah, Alex, Xin Zhang, James, Ashely, Ashwaq, Sophie, Lubna, Guanyi) for their collaborative spirit, insightful discussions, and unwavering support that made this research possible. I am also grateful to the Soft Matter Physics group for their kindness, friendliness, and for fostering such a positive and stimulating research environment.

I am deeply thankful to my sponsor, the Ministry of Higher Education (Saudi Arabia), and to the University of Umm Al-Qura for their generous financial support throughout the years of my PhD. This journey would not have been possible without their contribution.

Above all, I am eternally grateful to my parents, family, my husband (Mohammed), and my children (Qusai and Qais) for their unconditional love, understanding, and unwavering belief in me. Their presence has given me the strength to pursue and complete this endeavour. I love you all more than words can express.

I would like to dedicate this thesis to my beloved grandmother, who now rests in peace but remains forever in my heart. My mother honoured you by giving me your name, and I carry it with pride.

Author's Publications

Effect of Water on the Dissolution of Flax Fiber Bundles in the Ionic Liquid 1-ethyl-3-methylimidazolium acetate

Albarakati, F.A., Hine, P.J. & Ries, M.E.

Cellulose **30**, 7619–7632 (2023).

https://doi.org/10.1007/s10570-023-05394-3

Submitted (Under Review)

The Role of Cation and Anion on The Dissolution Rate of Flax yarns in Ionic Liquids (under review)

Albarakati, F.A., Hine, P.J. & Ries, M.E.

Cellulose

Abstract

The purpose of this thesis is to study the dissolution of flax fibres in imidazolium based ionic liquids and anti-solvent mixtures. This is an important area of study, helping to understand the mechanism of cellulose solvation and the ways in which the properties of ILs (in particular different anion and cation combinations) can influence their ability to dissolve cellulose at the micro- and macro level, and how different IL features affect the dissolution process.

This study investigates the dissolution behaviour of flax yarns in three distinct imidazolium based ILs:1-ethyl-3-methylimidazolium acetate ($[C2mim]^+[OAc]^-$),1-butyl-3-methylimidazolium acetate ($[C4mim]^+[OAc]^-$), and 1-ethyl-3-methylimidazolium octanoate ($[C2mim]^+[Oct]^-$). The first two of these had the same anion ($[OAc]^-$) but a different cation, while the third had the same cation ($[C2mim]^+$), as the first but a different anion. This work was able to reveal the role of the cation and the anion on the dynamics of cellulosic yarn dissolution. The dissolution process involved submerging the yarns in the pure ILs for a range of temperatures and times, followed by coagulation in water. The coagulated material called coagulated fraction (CF) produced an outer ring that surrounded the centre yarn fibre. Optical microscopy was used to follow the growth of this 'dissolved' region and it showed an Arrhenius behaviour, enabling the determination of the dissolution activation energy from this simple measurement. The dissolution activation energies of the ILs [C2mim][OAc], [C4mim][OAc] and [C2mim] [Oct] were found to be 64 ± 5 kJ/mol, 67 ± 1 kJ/mol and 79 ± 1 kJ/mol, respectively. In addition, the growth of the outer coagulated ring's thickness of the coagulated material was investigated, enabling the IL's diffusion coefficients to be determined. NMR study (pulsed- field gradient self- diffusion measurements), viscosity, density, and Stokes-Einstein analysis provided further understanding of the properties of the pure ILs. The calculated diffusion activation energies of the ILs [C2mim][OAc], [C4mim][OAc] and [C2mim][Oct], were found to be 64 ± 5 kJ/mol, 69 ± 5 kJ/mol and, 77 ± 3 kJ/mol, respectively. The resultant data shows that the dissolution rate goes from fastest to slowest in the order [C2mim][OAc] >[C4mim][OAc] >[C2mim][Oct]. Our key result is that the dissolution of the flax yarns (in all three ILs) is controlled by the diffusion of the IL, through a region of swollen cellulose/IL solution around each fibre as the thickness of the dissolved and coagulated layer increases with the square root of time and so is diffusion controlled.

The effect of adding small amount of water on the activation energy and dissolution speed of ionic liquids ILs [C2mim][OAc] and [C4mim][OAc] was investigated

separately. For the IL [C2mim][OAc], three different water contents have been used 1%, 2% and 4% by weight and for the IL [C4mim][OAc], four different water concentration have been used 1%, 2%, 4%, and 8% by weight. The resultant data has also been compared to the results from chapter 3 (the pure IL [C2mim][OAc] was found to consist of 0.2% water), and chapter 4 (the pure IL [C4mim][OAc] was found to consist of 0% water). As expected, the coagulated outer layer was seen to form around the undissolved core fibre for the water systems of 1%, 2%, and 4%. However, there was no sign of dissolution showed by the IL [C4mim][OAc]-water system of 8%. For the IL[C2mim][OAc], the activation energies were found to be 77 ± 5 kJ/mol, 97 ± 3 kJ/mol and 116 ± 6 kJ/mol for the system containing 1%, 2% and 4% water respectively. For the IL [C4mim][OAc], the activation energies were found to be 78 ± 7 kJ/mol, 83 ± 7 kJ/mol and 110 ± 6 kJ/mol for the system containing 1%, 2% and 4% water respectively. The dissolution rate was found to exponentially decrease as a function of water content for [C2mim][OAc]; however, the dissolution rate at 1% water was found to be higher than that of 0% water for [C4mim][OAc]. This shows a level of effectiveness at 1% water could make it a viable option for both research and industrial use.

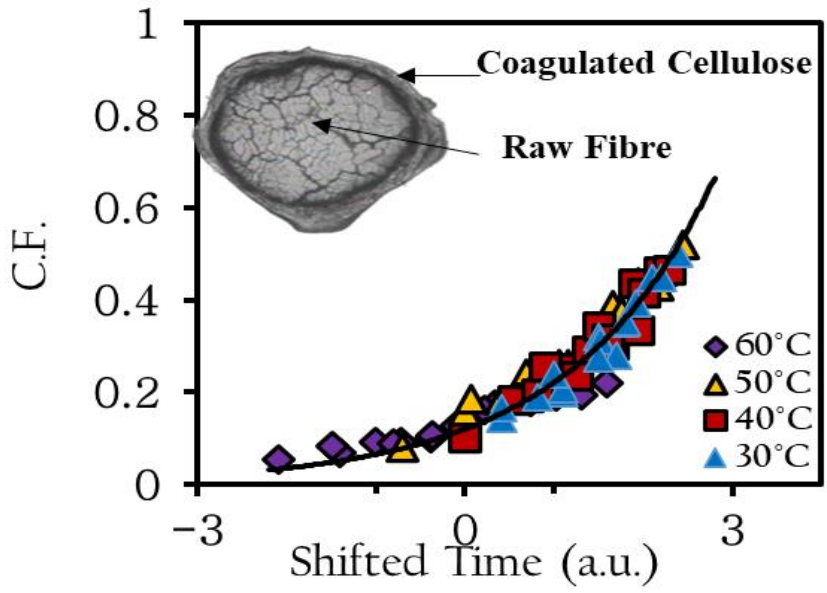

Graphical Abstract

Contents

List of Tables

List of Figures

Abbreviations

ACC, all- cellulose composite

CF, coagulated fraction

D, (self)- diffusion coefficient

IL, ionic liquid (defined as MP< 100 °C

NMMO, N- methylmorpholine N-oxide

OM, optical microscopy

RT ILs, ionic liquid at room temp.

TTS, time-temperature superposition

C2mim, 1-ethyl-3-methylimidazolium [also uses **'Emim'** and **'C_2C_1Im'**]

C4mim, 1- butyl-3-methylimidazolium acetate [also uses **'Bmim'**]

[TMGH] EtCO2, N,N,N,N-tetramethylguanidium propionate

[TMGH] OAc, N,N,N,N-tetramethylguanidiumacetate

NFC, natural fibre composite

PFG, pulsed- field gradient

η, viscosity

KFT, Karl Fischer titration

Chapter 1

Introduction and literature review

1.1 Introduction

Biopolymer carbohydrates attract much attention as renewable materials of biomass based on products and applications, such as food, agriculture, material, and medicine [1-6]. The most common biopolymer is cellulose. It is the most abundant polymer on earth [7, 8], and is a key component of plant cell walls found in plants and algae. Cellulose provides researchers with fascinating alternatives to fossil fuel products. Lignocellulose, which includes cellulose, hemicellulose, and lignin from plants has great potential due to its huge annual production of around 10^{11} tons [9]. The interest in these naturally occurring biopolymers comes from their unique nanostructures composed of glucose units with amorphous and crystalline regions in their fibres [10]. Cellulose is an environmentally friendly and biocompatible material, known to be an almost inexhaustible source for raw materials. Nevertheless, several industrial pre-treatment methods require harsh chemical treatments and/or hazardous conditions, which raise environmental concerns and reduce the potential use of cellulosic materials [11]. Most of the solvents presently used in cellulose processing provide notable environmental difficulties. For example, the viscose process, which involves the production of by- products such as carbon disulfide. The use of N-methylmorpholine N-oxide (NMMO) as a direct dissolution solvent has increased in importance as it does not require any pre chemical reaction and does not produce unfriendly environmental by-products [12]. However, this process cannot fully replace the viscose process due to the reduction of the product performance and unstable thermal properties [13, 14]. Researchers are currently facing challenges in developing solvents that are both highly efficient and sustainable for the environment. Recently, the use of ILs as a direct solvent, which does not require any pre-treatment for dissolving cellulose has become a potential promising development. However, the high cost of the ILs due to their production is currently limiting scale up from laboratory scale processes. Therefore, understanding how cellulose is dissolved and how the properties of ILs affect this process at the microscopic level is essential. Furthermore, it is essential to conduct a study of new cellulose solvents that have the potential to

reduce the cost of using ILs by enhancing the dissolution time and temperature for cellulose dissolution, which is required for industrial purposes.

Currently, there are many waste products causing environmental difficulties cross the globe such as textile industry and plastic waste. In 2015, the textile waste disposal was 92 million tonnes around the world, with an estimated increase of 60% by 2030 [15]. Plastic waste also contributes to several environmental problems. Around 250,000 tonnes of plastic waste are drifting in the oceans [16], which causes a serious problem for wildlife. Most textiles, like other polymer composites, are made from petroleum-based materials and depend on fossil fuels, which are expected to run out within the next 100 years. At the end of their life cycle, textiles are rarely recycled efficiently. Instead, they are commonly disposed of in landfills or incinerated, releasing the carbon stored in these materials into the atmosphere and contributing to environmental harm. For these reasons, so called green composites are a class to create new materials that can replace the conventional materials and have less environmental impact as being derived from sustainable sources and also biodegrade over time. Hence the study of the dissolution process of cellulose is important to understand the transformation of natural materials into cellulose based composites [17]. Moreover, the dissolution of cellulose-based fibres in an ionic liquid is a highly dependable process, with the dissolution rate being influenced by variables such as time, temperature, and anti-solvent concentration in a predictable and controllable method. In contrast, traditional methods like using harsh chemical solvents (e.g., carbon disulfide in the viscose process) are more toxic, less environmentally friendly, and harder to control, often leading to greater environmental and health hazards.

1.1.1 Project aims and objectives

The purpose of this study is to investigate the dissolution of flax fibres in three different imidazolium-based ionic liquids. The ionic liquids were chosen such that two had the same acetate anion ($[OAc]^-$) but a different cation, either ethyl $[C2mim]^+$ or butyl $[C4mim]^+$. The third ionic liquid had the same ethyl cation $[C2mim]^+$ but a different anion, an octanoate $[Oct]^-$. These different combinations allowed the role of the anion and cation in cellulose dissolution to be investigated. The three ILs studied in this work ([C2mim][OAc], [C4mim]][OAc] and [C2mim][Oct]) are summarised in Table 1.1.

IL type	Cation	Anion
1-ethyl-3-methylimidazolium acetate	[C2mim]+	[OAc]-
1- butyl-3-methylimidazolium acetate	[C4mim]+	[OAc]-
1-ethyl-3-methylimidazolium octanoate	[C2mim]+	[Oct]-

Table1.1: The three ILs used on dissolving flax yarns in this study.

A range of experimental techniques were used to follow the dissolution of the chosen flax fibres in the three different ILs for a range of processing temperatures and times. Measurements were done using a combination of optical microscopy (OM), rheology, and nuclear magnetic resonance (NMR) and together these represent most of the collected experimental data. They provide the basis for further discussions and different chemical and physical insights. The effect of water on dissolution was also investigated (for ILs [C2mim][OAc] and [C4mim][OAc]) and Karl Fischer titration was used to measure water content of ILs both before and after any experiments. The study has also identified the importance of the presence of water on both the speed of dissolution of flax fibres and the activation energy for dissolution. For this reason, we are investigating the effect of water on these two important parameters for dissolution. This became apparent at the start of the project, when it was found that the ILs [C2mim][OAc] from two different suppliers, (Proionic GmbH, Grambach (0.2% water)), and Sigma- Aldrich (0.5%water)) contained different base amounts of water, which significantly change the speed of dissolution and the activation energy. For this reason, it was felt necessary to examine the effect of water, as well as to investigate the three potential anion/cation combinations in their as received state.

The dissolution of flax fibres in the IL [C2mim] [OAc] has been studied for four water percentages: as received (0.2%), 1%, 2%, and 4%. For the IL [C4mim][OAc], the dissolution of flax fibres has been studied for five water percentages: as received (0%), 1%, 2%, 4% and 8%. The same flax fibres studied in the first part of the work were chosen to be the cellulose source and their dissolution was studied, immersing in excess ILs at various temperatures and times.

Optical microscopy (OM) was employed to acquire morphological pictures of both natural and partially dissolved flax yarns and to directly follow the dissolution of the

flax fibres. This simple technique offers significant insights into the fundamental physics of dissolution, allowing the dissolution activation energy to be calculated along with the speed of dissolution by employing time- temperature superposition (TTS). Samples at various stages of dissolution (for a range of processing times and temperatures) were encapsulated into epoxy resin and then polished. Viewed in reflection under an optical microscope, two regions were always clear, a region of the original fibres surrounded by a ring of dissolved and coagulated cellulose. From the optical micrographs it was therefore possible to determine the amount (fraction) of dissolved yarn with time and temperature, which is termed the coagulated fraction (CF). Additionally, it was found that following the growth of the thickness of this coagulated fraction allowed important information on the diffusion of the various ionic liquids to be measured.

NMR is not only used in chemical characterization, but it can also determine diffusion characteristics, molecular structure, motion, and conformation. NMR experiments presented here will be limited to the measurement of the self-diffusion coefficients of each of the ILs at various temperatures to calculate the diffusion activation energy and the effective molecular size of each IL. Rheological methods offer a wide variety of approaches for examining the macroscopic flow characteristics of fluids, which can provide insight into the microscopic properties. The measurements here will be limited to focus on the viscosity of each ionic liquid as a function of shear rate and temperature to create a flow curve which then shows the rheological character of each ionic liquid to be compared and contrasted.

This study's focus is to understand and explore the underlying physics of preparing all-cellulose composites by investigating the dissolution of single flax yarns. The results obtained in this study will contribute to future research to consider preparing all-cellulose composites [18, 19]. Flax fibres, and their composites, provide a promising way of replacing traditional composite materials without environmental damage due to excellent mechanical performance, the material is fully bio-based and designed to be completely recyclable [20, 21]. Furthermore, we have studied flax fibre yarns, as this builds on previously published work in our research group [22], which studied the effects of a co-solvent DMSO on the same flax yarn material. It is also important to note that this work feeds directly into our ongoing work in our research group [23], on woven cloth made from the same flax source material.

1.1.2 Thesis structure

There are 6 chapters in this thesis. Following the **Literature Review**, the next chapter is **Chapter 2,** and this describes the experimental methods used to carry out the measurements. These are optical microscopy, rheology, and nuclear magnetic resonance (NMR) and together these represent the majority of collected experimental data. They provide the basis for further discussions and different chemical and physical insights. **Chapter 3** focuses on the detailed dissolution behaviour of flax yarns in the ionic liquid 1-ethyl-3-methylimidazolium acetate ($[C2mim]^+$ $[OAc]^-$). The use of optical microscopy enables the direct observation and analysis of the dissolution process at various stages, providing valuable insights into the behaviour of the flax yarns within the ionic liquid system. The systems were all found to exhibit TTS behaviour, where Arrhenius plots are constructed to investigate the relationship between temperature and dissolution rates. The activation energy for the dissolution process is determined through each of the experimental approaches. Additionally, the chapter documents the activation energies calculated from the TTS-based thickness method and the intercept method [24], further expanding the understanding of the physics of the dissolution dynamics. To complement the dissolution studies, NMR experiments are conducted to measure the self-diffusion coefficients of the pure ionic liquid [C2mim][OAc] at various temperatures, allowing for the calculation of the self-diffusion activation energy and the effective molecular size of the ionic liquid ions. Rheological studies were also performed to assess the viscosity of [C2mim][OAc] as a function of shear rate and temperature, from which a flow curve is generated. The viscosity activation energy of the ionic liquid is then calculated to understand its temperature-dependent flow behaviour. Together, these combined approaches provide a comprehensive view of the dissolution process, activation energies, and molecular dynamics within the [C2mim][OAc] system, helping to understanding the interactions between the flax yarns and the ionic liquid. **Chapter 4** building on the insights from the previous chapter, this chapter explores the dissolution behaviour of flax yarns in two additional imidazolium-based ionic liquids (ILs) with different cation/anion combinations. The same experimental approach is applied, using flax yarns and focusing on a range of processing temperatures and times. For the first ionic liquid, the cation is changed from 1-ethyl-3-methylimidazolium ($[C2mim]^+$) to 1-butyl-3-methylimidazolium ($[C4mim]^+$), while the anion remains acetate ($[OAc]^-$). In the second ionic liquid, the cation remains $[C2mim]^+$, but the anion is changed to octanoate ($[Oct]^-$). These variations allow for exploring how changes in the cation or anion impact the dissolution behaviour. The same dissolution methodology used in the previous chapter is employed here, with

dissolution experiments carried out at different temperatures and times. The systems again exhibit time-temperature superposition, and Arrhenius plots are constructed to assess the temperature-dependence of the dissolution process. The activation energy of dissolution for both ILs is obtained using each experimental approach. Additionally, NMR experiments are conducted to measure the self-diffusion coefficients of both ionic liquids at various temperatures, enabling the calculation of diffusion activation energy and the effective molecular size of each IL. These NMR studies provide valuable insights into the molecular dynamics of ionic liquids. Rheological studies are also performed to investigate the viscosity of each ionic liquid as a function of shear rate and temperature. A flow curve is generated for each IL, and the viscosity activation energy is calculated, enabling a detailed comparison of their temperature-dependent flow behaviour. By comparing the results from these two additional ILs with those from [C2mim][OAc], the analysis advances our understanding of the dissolution process and molecular behaviour across the three ILs. This comparative study offers a more comprehensive view of how variations in ionic liquid structure (both cation and anion) influence dissolution, diffusion, and viscosity, enhancing the understanding of these systems. **Chapter 5** investigates how the addition of small amounts of water to the ILs [C2mim][OAc] and [C4mim][OAc] affects the activation energy required for dissolution as well as the overall dissolution rate. The result analysis and discussion highlight the effects of water content on the dissolution characteristics of these ionic liquids, and builds on the insights from the results in this chapter, the final comparison evaluates the activation energies, as well as the relative and absolute dissolution rates for both ionic liquids. **Chapter 6** summarises the findings and suggests the potential future work for this research.

1.2 Literature review

1.2.1 Cellulose

The term “cellulose” was first introduced in 1839 in a study by the French Academy on the work of Anselm Payne. Payne found cellulose is made up of 44 to 45% carbon, 6 to 6.5% hydrogen, and the remainder is oxygen and its chemical formula is $(c_6H_{10}o_5)_n$ [25]. The straight-chain molecules in cellulose form hydrogen bonds with one another, making it a particularly strong material. Cellulose is a natural linear chain consisting of D- glucose units connected by a series of β (1-4) glycosidic bonds between C-1 and C-4 of adjacent glucose, and rotates 180 degrees in relation to its

neighbour. Each D- glucose unit possesses three hydroxyl (OH) groups at C-2, C-3 and C-6 positions, as shown in Figure 1.1 [26]. Cellulose has a strong structure reinforced by intermolecular hydrogen bonds; these bonds are formed from hydroxyl groups in glucose units. Cellulose has excellent properties, for instance high crystallinity, resistance to solvents, high temperature performance, water absorption and hence biodegradability and nontoxicity, all of which combine to make it attractive in many applications [27-29]. Cellulose has various polymorphs namely cellulose I, II, III and IV. Most of these crystalline allomorphs have been identified via dissolving, precipitating, treating with liquid ammonia or chemical modification cellulose I [30, 31].

The length of cellulose chains is determined by the number of repeating units of glucose, which is referred to as the degree of polymerization (DP). The source of cellulose has a significant impact on the value of DP. The DP of laboratory-synthesized cellulose is 20 and it can be greater than 10,000 for bacterial cellulose [32].

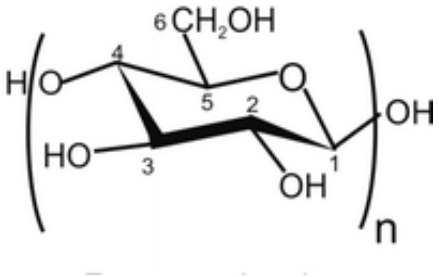

Figure 1.1: Chemical structure of cellulose polymer chain [26].

Cellulose, in its natural form, consists of microfibrils of stacked sheets of parallel chains that form three-dimensional crystals with varying lengths (0.1 to 100 micrometres) and diameters (2 to 20 nanometres), and the chains are attracted to each other via H-bonds and van der Waals forces [9, 33, 34]. Figure 1.2 represents the inter and intra molecular H-bond network of native cellulose. This H-bonding plays a significant role in solubility, thermal stability, and mechanical properties [35].

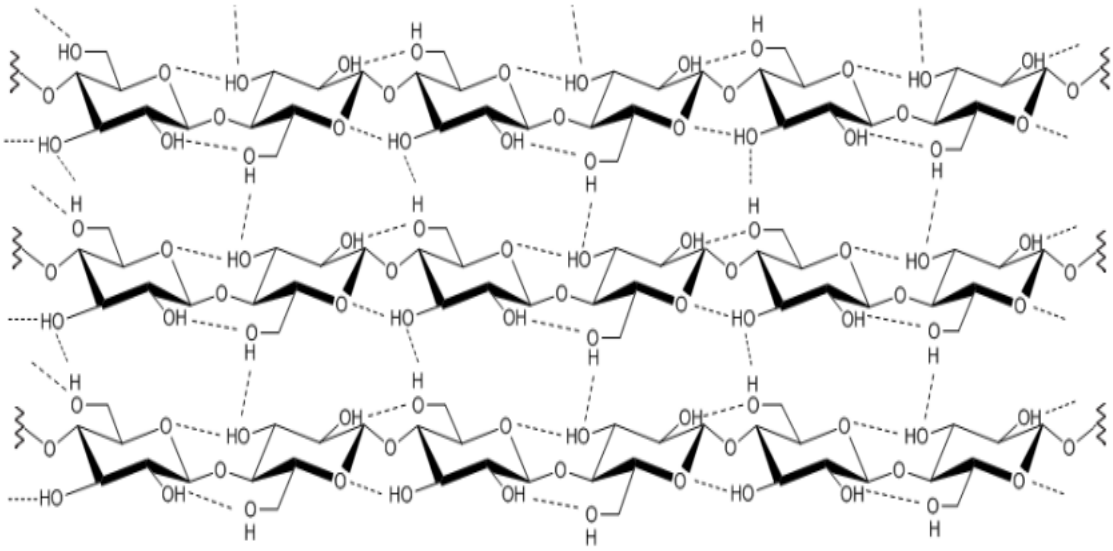

Figure 1.2: Schematic of the intra- and intermolecular hydrogen bonding network in native cellulose. Taken from [35].

Another important feature reported is that the cellulose molecule's shape and the arrangement of its hydroxyl groups and hydrogen atoms generate regions with varying degrees of polarity: hydrophilic regions parallel to ring plane and hydrophobic regions perpendicular to the ring. The side view of the glucopyranose ring plane reveals the hydrophobic sites on the cellulose molecule, with the hydrogen atoms of the C–H bonds on the axial locations of the ring, and the top view of the glucopyranose ring plan reveals the hydrophilic sites, with the hydroxyl groups located on the equatorial positions of the rings, as shown in Figure 1.3 [36-39]. These features are expected to influence both the interactions and solubility of cellulose.

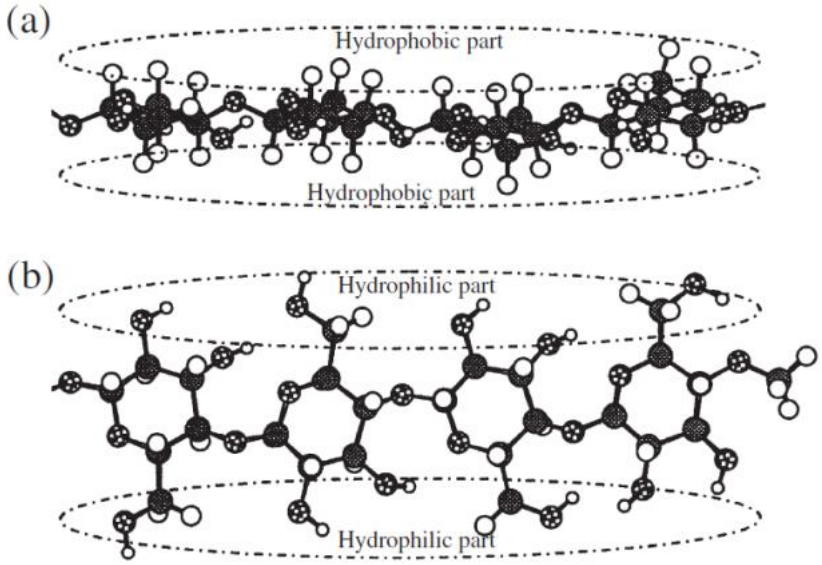

Figure 1.3: The cellulose molecule's hydrophilic and hydrophobic parts. Taken from [36].

1.2.2 The structure of cellulose I and cellulose II

The native form of cellulose is cellulose I, usually found in plants and certain bacteria. The crystalline structures of the two allomorphs of cellulose I, Iα and Iβ, are slightly different. Iα is triclinic and is mostly found in bacteria and algae, whereas Iβ is monoclinic and is more frequently found in higher plants [40]. Cellulose I is essential for keeping the structural integrity of plant cell walls since these differences in crystalline structure have a substantial influence on the physical characteristics of cellulose, such as its resistance to hydrolysis and its insolubility in water [41]. Conversely, cellulose II is the more thermodynamically stable form that is produced by regeneration (dissolution and reprecipitation) or mercerization (alkaline treatment). Cellulose II's crystalline structure and characteristics are different from those of cellulose I due to its antiparallel chain arrangement [42]. Because of this rearrangement, cellulose II is more soluble and reactive than its native counterpart due to a reduction in crystallinity. Other differences include the locations of intra molecular H- bond and the packing orientation can be seen in Figure 1.4 [43]. This figure shows that the orientation of the glucose units in cellulose I is such that the O6 and O3 atoms are able to form intermolecular hydrogen bonds between one glucose unit and a neighboring chain, as well as with the adjacent glucose units of O3 and

O5 atoms help to stabilize the linear arrangement of cellulose chains, while the orientation of the glucose units on the cellulose II is such that the O2 and O6 atoms are not able to form intermolecular hydrogen bonds with each other, instead the O3 and O5 atoms of adjacent glucose units are able to form hydrogen bonds [44]. Significant alterations in the material's physical and chemical characteristics occur during the conversion of cellulose I to cellulose II. The transformation of cellulose I into cellulose II is associated with notable alterations in the material's physical and chemical characteristics, which have been extensively utilized in industrial uses such as the manufacture of films, textiles, and bioplastics [45].

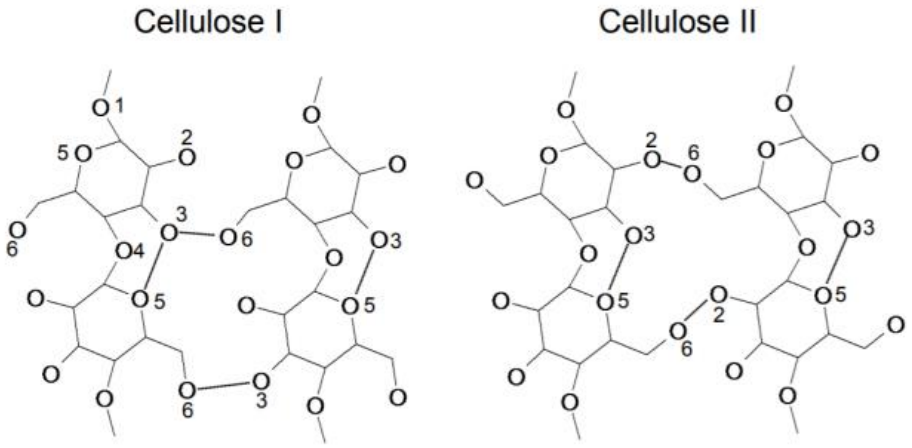

Figure 1.4: The structure of cellulose I and cellulose II, with hydrogen bond locations indicated by solid dark line. Taken from [44].

Cellulose is classified as a semi-crystalline polymer because it has both crystalline and amorphous parts namely a two-phase system [46]. These systems in the microstructure of the cellulose microfibril show the highly order crystalline regions and less organized amorphous regions, see Figure 1.5.

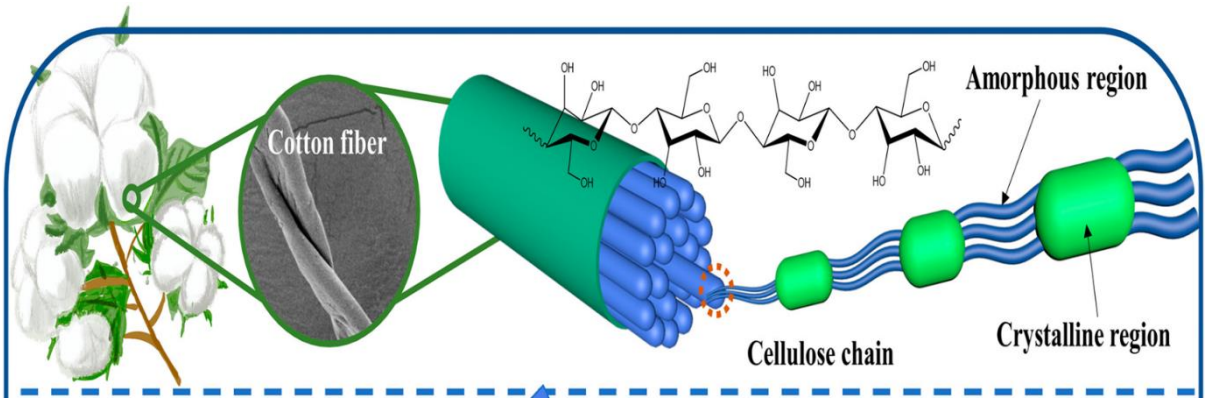

Figure 1.5: Schematic diagram of cellulose microfibrils showing the crystal regions and amorphous region. Taken from [46].

1.3 Natural Fibre

Natural fibre are materials made by combining natural plant-based fibres come from renewable sources such as flax [47], cotton [48], jute [49], and wood [50] with a polymer matrix (which can be either synthetic or bio-based). All can be used as natural reinforcement, to form biomaterials with good physical and chemical properties. Natural fibres are a promising alternative to traditional fibres such as glass and carbon, as

A common natural fibre classification is shown in Figure 1.6. There is an increasing demand for natural fibres as eco-friendly materials due to a growing concern to produce sustainable materials and looking for more renewable products from plant resources [51]. As environmental awareness grows, natural fibre composites are becoming increasingly common. Natural fibres have been widely used as a green alternative to replace synthetic materials [52, 53]. The composition of plant fibres can include cellulose, lignin, hemicellulose, pectin, and waxes [51, 52]. They have been proposed to be used in many applications such as automotive, building and construction [51]. They can be employed as reinforcing fibres in polymer matrix composites, providing a more cost-effective approach compared to synthetic polymer fibres [53, 54].

Natural fibres can have a problem of adhering to a different matrix phase, which can be a drawback of employing them as reinforcing fibres in composite materials because of their hydrophilic nature [55]. As result, this can give the composites poor mechanical properties [52]. Therefore, the chemical modification of natural fibres is required to improve the adhesion between the fibres and matrix and enhance the

mechanical properties of the composites. In 2004, Nishino et al. first reported the term all-cellulose composites (ACCs). These materials comprised cellulose fibres together with a cellulose matrix from the same source of cellulose to give a better adhesion at the interface between the fibre and the matrix, allowing efficient stress transfer. These types of ACCs are known to be recyclable, bio-based, bio-degradable, and show good fibre-matrix adhesion [19, 56].

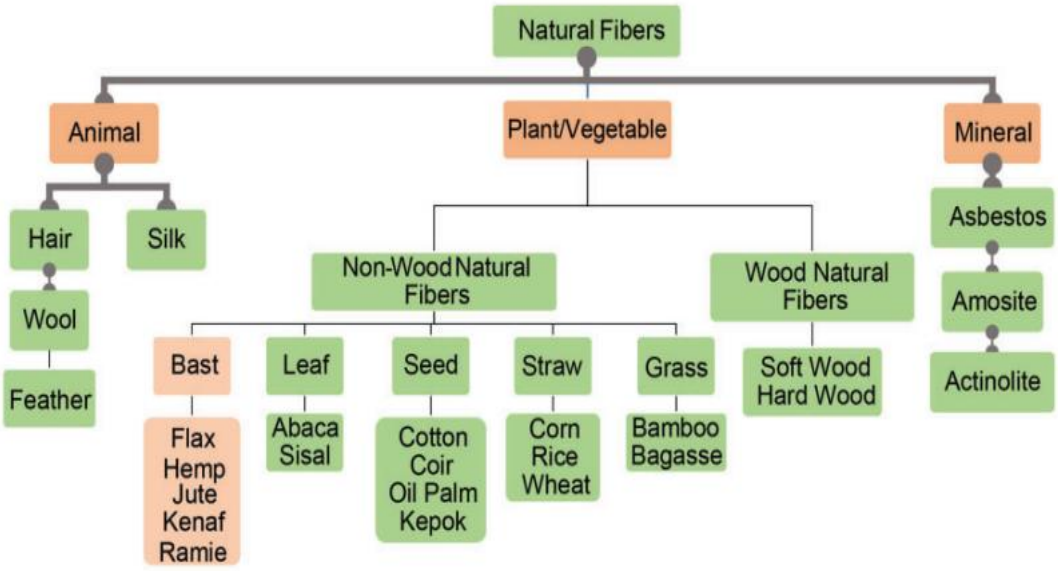

Figure 1.6: Classification of natural fibre sources. Taken from [57].

1.3.1 Flax

Flax is the cellulose source used during this study which is a bast fibre that occurs naturally. For over 30,000 years, the flax plant has been grown all over the world and used for its unique properties [58, 59]. With a degree of polymerisation of over 4,000, it is also one of the longest known linear fibres [60, 61]. The use of flax fibres has gained a lot of attention recently for developing renewable materials due to the natural ability to be bio-degradable and have excellent mechanical properties, low density as well as low cost, [20, 21]. Flax consists of typically 70% cellulose and 27% hemicellulose, with a small amount of lignin 3% [49]. Flax fibres are also considered an eco-friendly material which can potentially replace some synthetic materials such as in automobile interiors, boat and bicycle frames and furniture [62].

A single flax fibre structure has several sub-layers, as shown in Figure 1.7 [63] [64]. In a single flax fibre, there are two cell walls called the primary and secondary cell walls and the lumen layer. The secondary cell wall is a major part of the fibre diameter and contains three layers; the first secondary cell wall layer is S1 which is known as the outer layer of the fibre. The second layer of the secondary cell wall is S2 which is known as the middle, or the inner layer and the third layer is S3. The middle layer S2 is thicker than both the primary cell wall and the third layer S3, also it contributes to the strength of the fibre.

The inner layer S2 is the dominant constituent and plays a fundamental role to provide better mechanical performance of the fibre due to the highly crystalline cellulose microfibrils bounded by lignin and hemicellulose [57]. On the other hand, the primary cell wall and the first layer of the secondary cell wall S1 are the outer layers, they are thin and deposited during plant growth. The outer layers can have a lower orientation of cellulose, hemicelluloses, and pectin [64] [65].

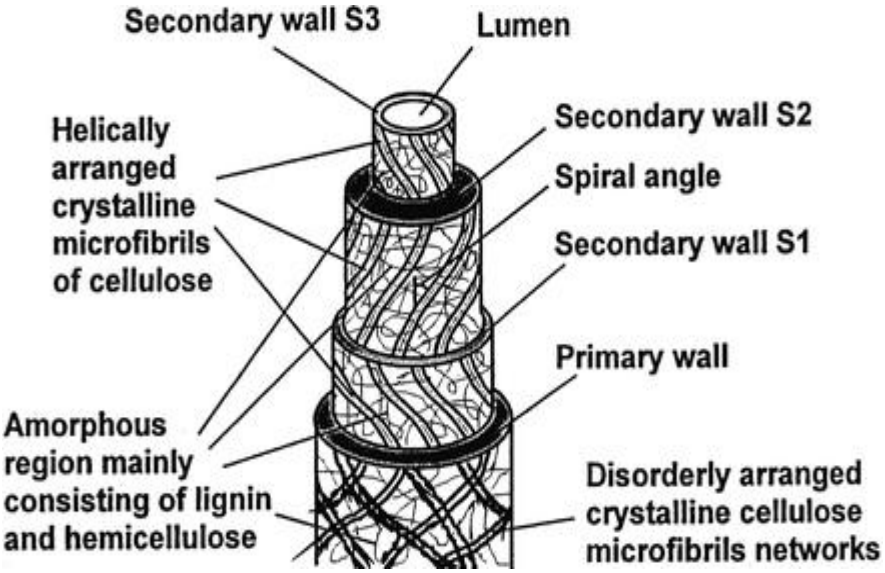

Figure 1.7: Structural constitution of flax elementary fibre. Taken from: [66].

1.4 Ionic Liquids

1.4.1 Conventional solvent systems

The dissolution of cellulose can be a challenge due to the extensive intra and inter hydrogen bonds and its highly crystalline structures. Common solvents used in cellulose processing often contain properties harmful to the environment. For example, the Viscose process is the oldest technique used to dissolve cellulose and is still currently used. It uses carbon disulfide dissolved in sodium hydroxide to form cellulose xanthate [67]. However, this process involves unfriendly environmental by products such as carbon disulfide, which must be thoroughly removed or chemically disposed of prior to being released into the environment. Therefore, numerous cellulose solvent systems, such as NaOH/CS_2, NaOH/urea, and N-methyl morpholine-N-oxide (NMMO), have been investigated by researchers, with commercial success in a variety of NMMO systems [68-70]. However, these traditional cellulose dissolving methods have a number of disadvantages, including damage to the environment, high energy and reagent consumption, solvent evaporation, and complex operating processes [71-74]. N,N-Dimethylacetamide (DMAc) with lithium chloride (LiCl) has also been used to dissolve cellulose at a temperature higher than 100 °C [75]. Sodium hydroxide (NaOH) aqueous solution at low temperature is also used for dissolution with or without any additive [76-78]. However, these solvent systems have limited potential to be scaled up to an industrial level due to high toxicity, high vapour pressure, low thermal stability, and slow dissolution speed [79, 80]. In order to address these issues, there is an increasing demand for the development of environmentally friendly substitutes for these commonly used cellulose solvents. Recently, there has been increasing interest in a new family of cellulose solvents called "ionic liquids". Nevertheless, the mechanism of cellulose dissolution in ionic liquids is still not fully understood.

1.4.2 History of Ionic Liquids

It is widely acknowledged that the breakup of the intra- and intermolecular hydrogen bonds in cellulose is the crucial point in the dissolution of this polymer [81]. Since cellulose does not dissolve in common solvents such as water, there has been a need to find alternative solvents. One of these solvent groups are ionic liquids (ILs), which have a huge potential to be ‘green’ solvents for dissolving cellulose and making

ACCs [82, 83], due to their notable excellent properties and the ability to dissolve cellulose without any pretreatment [84]. ILs are organic salts and have a low melting point below 100 °C [85], low vapor pressure, high thermal stability, and recyclability [86]. Over the last decades they have shown great potential as green cellulose solvents [86-89]. From 1914, the ILs were identified as playing an important role in the dissolution process, for example by Paul Walden, who first discovered the IL of ethyl ammonium nitrate ([EtNH3] [NO3]) with a melting point 13 - 14 °C. In 1934, Graenacher dissolved cellulose in a molten salt (N-alkyl pyridinium chloride) at melting point 118 °C, so not strictly an IL according to the prior Walden's definition with a melting point below 100 °C [90]. In 2002, Swatloski et. al. discovered the first IL imidazolium - based ionic liquid with a low melting point below 100 °C, which is considered as a green solvent to dissolve cellulose [91]. Since then, the dissolution of cellulose in ionic liquids has interested a number of researchers in studying cellulose solutions [92, 93].

ILs contain many different cations/anions that play a significant role in dissolving cellulose as a direct solvent [94]. Brehm et al. stated that the determination of the solubility of cellulose in ILs was affected by the capacity of anions from ILs to interact with the hydrogen bond [95]. Additionally, the effect of cations in the dissolution of cellulose is minor, and many studies tried to prove this by NMR measurements and the molecular simulation studies [96-98]. ILs have been demonstrated to have the capacity to dissolve a variety of materials that are typically difficult to dissolve, including wood fibre and other lignocellulosic materials such as flax [99]. However, it is worth noting that the purity of the IL (98% in our case) may have also impacted the dissolution due to derivatizing reactions or additional side reactions [100]. Within their work, they cautioned that if the IL contains significant impurities, additional side reactions with cellulose can occur. Furthermore, Zweckmair et al. reported that acetylating action of ILs (1,3-dialkylimidazolium acetate) with cellulose may occur with resultant impurities. They also note that ILs that are pure do not exhibit this reaction [101].

The potential of dissolving cellulose was investigated for many ILs, particularly room temperature ionic liquids (RT-ILs) where higher cellulose solubility has been documented. For example, Zhang et al. used 1-allyl-3-methylimidazolium chloride ([AMIM][Cl]) in order to produce solutions that contained up to 5 wt.% of cellulose [102]. Ohno et al. used 1-ethyl-3-methylimidazolium methylphosphonate ([EMIM][CH3PO3]) to prepare solutions containing 10 wt.% of cellulose [99].. In addition to the examples given, there are certain ILs that have a solubility of up to 22% wt. of cellulose (Fukaya et al. 2006).

There are four main groups of the ILs based on their cation: alkylammonium, alkyphosphonium, N,N'-dialkylimidazolium and, N-alkylpyridinium. The imidazolium-based are the most studied of these groups [103-105].

The significant drawback of pure ILs can be a high viscosity as compared to most solvents [106]. The viscosities of ILs depend on their interionic interactions, such as hydrogen bonding and van der Waals forces [107]. Thus, ILs viscosity varies with the composition, temperature, and the chemical structure [108]. One of the ways to reduce the viscosity of ILs is by adding a small amount of water or co-solvent [109] [110]. In addition, incorporating low-viscosity solvents into ILs is an effective approach for overcoming these challenges, which leads to the formation of binary solvents that facilitate the dissolution of cellulose [111, 112]. These studies found that mixing the ionic liquid [Emim]OAc with the low-viscosity, biomass-derived solvent γ-valerolactone (GVL) significantly improved cellulose dissolution. For example, 15 wt% α-cellulose was rapidly dissolved in the [Emim]OAc/GVL mixture at 80 °C within 1 hour. Other approaches can be to change the size of the anion [113] or via using a co-solvent such as DMSO, polyethylene glycol, dimethyl sulfoxide, dimethylformamide and 1,3-dimethyl-2-imidazolidinone, etc. [114] [115] [116]. Other organic co-solvents such as dimethyl sulfoxide, dimethyl formamide and 1,3-dimethyl-2-imidazolidinone were also effectively used to reduce viscosities [116].

1.4.3 Imidazolium- based ionic liquids for cellulose dissolution

The ionic liquids used within this study were listed in Table 1.1. They are an organic salt and have a melting point below 100 °C. In addition, many studies proved that the ILs [C2mim][OAc] and [C4mim]OAc] can effectively dissolve cellulose [117-119]. They have shown high solvation efficiency, due to the advantage of being a liquid at room temperature, which simplifies the handling and requires lower process temperatures (30 °C, 40 °C, 50 °C, and 60 °C) for [C2mim]OAc], and (40 °C, 50 °C, 60 °C, and 70 °C) [C4mim][OAc]. However, the IL [C2mim][Oct] requires higher process temperatures (80 °C, 85 °C, 90 °C, and 100 °C) due to the long chain and higher molecular weight. Several studies found that the solubility power of ILs to dissolve cellulose depended on their physiochemical properties [99, 120, 121].

1.4.3.1 1-Ethyl-3-methylimidazolium acetate [C2mim][OAc]

1-Ethyl-3-methyl-imidazolium acetate, [C2mim][OAc], with the molecular formula ($C_8H_{14}N_2O_2$), is formed of two ions, which are the larger positively charged imidazolium [C2mim]+ cations seen on the left in Figure 1.8, ($C_6H_{11}N_2$), and the smaller negatively charged acetate [OAc]- anions on the right, ($C_2H_3O_2$), [122]. The molecular structure of [C2mim]+ consists of a 5-membered ring with 2 nitrogen and 3 carbon atoms while the $[OAc]^-$ consists of an acetate ion, as shown in Figure 1.8.

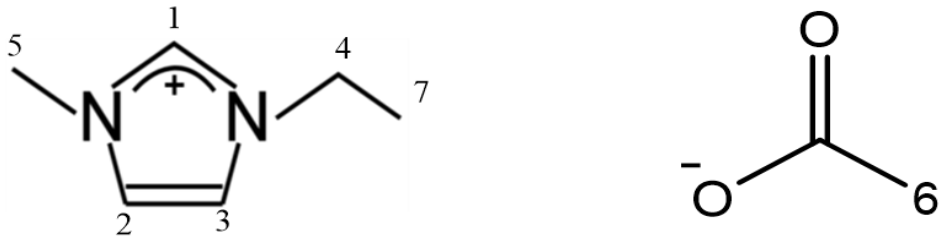

Figure 1.8: Chemical structure of the IL 1-ethyl-3-methyl-imidazolium acetate [C2mim] [OAc].

[C2mim][OAc] has a high solvation efficiency due to its liquid state at ambient temperature, thermal stability, low vapor pressure and the potential for recyclability [123, 124]. In addition, [C2mim][OAc] is one of the most common solvents used for cellulose dissolution and has been used to prepare ACCs due to its capability of dissolving a high concentration (20 wt.%) of cellulose [125, 126]. ILs based on the acetate anions [OAc], have proved to be more effective in dissolving cellulose than chloride $[Cl]^-$ based ILs [127]. Schuermann and Cosby groups found that the IL [C2mim][OAc] is an excellent green solvent that can dissolve a high polymer concentration and has a good dissolving capability for cellulose, when compared with other solvents such as 1-butyl-3-methylimidazolium chloride [C4mim] [Cl] [128, 129]. Cellulose with the IL [C2mim][OAc] has diverse applications, such as man-made fibres, films, and composite materials [130].

1.4.3.2 1-Butyl-3-methylimidazolum acetate [C4mim][OAc]

[C4mim][OAc], bearing a molecular formula ($C_{10}H_{18}N_2O_2$), sits at the forefront of ILs widely studied within the realm of cellulosic biomass processing research. The cation ($C_8H_{15}N_2$), carries within its structure a five-membered ring housing two nitrogen and three carbon atoms, whereas an acetate ion constitutes the anion within ($C_2H_3O_2$), as shown in Figure 1.9. With unique properties that favor its role as a solvent, [C4mim][OAc] has a low viscosity at room temperature which decreases with increasing temperature [131]. However, compared to the IL [C2mim][OAc] it has a higher viscosity at room temperature.

[C4mim][OAc] displays a strong potential in dissolving biomass and lignocellulosic materials due to its higher thermal stability compared to [C4mim][Cl] [132]. Numerous studies have documented its physicochemical properties including density and viscosity (Lefroy et al., 2021). The presence of hydrogen bond acceptors in this IL allows acetate to form a strong interaction with hydrogen bond donors in cellulose to break down the cellulose structure; because of this strong interaction [C4mim][OAc] has prospects as an ideal cellulosic biomass solvent [133].

Studies have analyzed the refractive index of 1-butyl-3-methylimidazolium acetate to measure how it interacts with light. They found that it linearly decreases in the temperature range 25°C – 55°C [131]. The longer chain length of the [C4mim] cation contributes the interaction with the polysaccharides and enhances the dissolution potential of [C4mim][OAc] in lignocellulosic biomass processing.

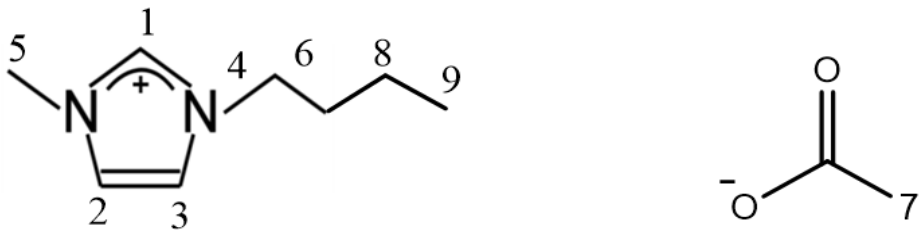

Figure 1.9: Chemical structure of the IL 1-Butyl-3-methylimidazolum acetate, [C4mim][OAc].

1.4.3.3 1-Ethyl-3-methylimidazolium octanoate [C2mim] [Oct]

Only one study has mentioned the IL 1-Ethyl-3-methylimidazolium octanoate [C2mim] [Oct] [113]. It is an ionic liquid composed of a cation and an anion, each contributing unique structural features with the molecular formula ($C_{14}H_{26}N_2O_2$), as shown in Figure1.10. This illustrates the cation and anion of the IL, the cation, 1-Ethyl-3-methylimidazolium [$C_6H_{11}N_2$]+, features an imidazolium core, a five-membered ring comprising three carbon atoms and two nitrogen atoms at positions 1 and 3. The nitrogen atom at position 1 is bonded to an ethyl group (C2H5), and the nitrogen atom at position 3 is bonded to a methyl group (CH3). These substitutions contribute to the cation's positive charge. On the other hand, the anion, Octanoate [$C_8H_{15}O_2$]−, is derived from octanoic acid, characterized by a long-chain alkyl group consisting of eight carbon atoms. Furthermore, it is an ambient temperature ionic liquid that is stable throughout a wide temperature range, making it suitable for high-temperature applications without risk of the decomposition or evaporation [113]. Physical properties of the three ILs studied in this work; [C2mim][OAc], [C4mim][OAc] and [C2mim][Oct]are summarized in Table 1.2.

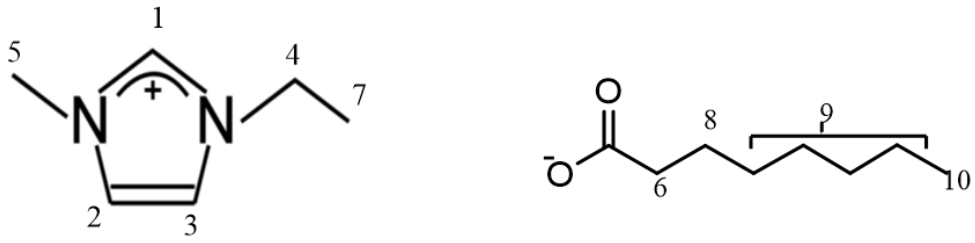

Figure 1.10: Chemical structure of the IL 1-Ethyl-3-methylimidazolium octanoate, [C2mim][Oct].

Physical properties	[C2mim][OAc]	Ref.	[C4mim][OAc]	Ref.	[C2mim][Oct]	Ref.
Molecular mass (g/mol)	170.21	-	198.26	-	254.38	-
Density (g/cm^3) at 25 °C	1.09903	[134]	1.05259	[135]	-	-
Melting point (℃)	<-20	-	<-20	-	<-20	-
Viscosity at 25 °C (Pa.s)	0.15	[23]	0.4475 0.390	[135] [133]	-	-
Price £ /100 g	318	Proionic	285	Proionic	153	Proionic
solubility	fully miscible	-	fully miscible	-	fully miscible	-

Table 1.2: Physical properties of ILs studied in this work; [C2mim][OAc], [C4mim][OAc] and [C2mim][Oct].

1.5 Dissolution process of dissolving cellulose

The dissolution mechanism of cellulose is not fully understood, even though it is a crucial stage in the processing of cellulose, which occurs prior to its transformation into high-value products through the use of anti-solvents for coagulation [136]. The dissolving processing of cellulose can work by only disrupting of the hydrogen bond network between the interactions between and within molecules [26, 137-139]. Most of the current experiments found that the breaking of the hydrogen bonds occurs via the interaction between the hydroxyl groups of cellulose and ions of the IL [140]. Based on Feng et al. the dissolution of cellulose occurs predominantly through the interaction between the anion of the IL with the hydrogen atoms of the hydroxyl groups of cellulose and whilst cation associates with the oxygen atoms of hydroxyl

groups [141]. Figure 1.11 illustrates the mechanism of dissolution cellulose in ILs, and it states that the individual cellulose chains are peeling away from the crystal lattice during the dissolution [142]. The dissolution of cellulose in the solvent occurs in three main steps: the swelling of the polymer network at the polymer-solvent interface is the initial step. Then, the swelling allows separating of chains and finally, chains becomes able to migrate into the solvent [143, 144]. Moigne et al. reported that these chains started to separate and move into the solvent in the early stage of the dissolution process [145]. Dissolution begins outside and moves within, and the dissolution mechanism is comparable in crystalline and amorphous areas, although the speed is occurs more faster in the amorphous regions [146].

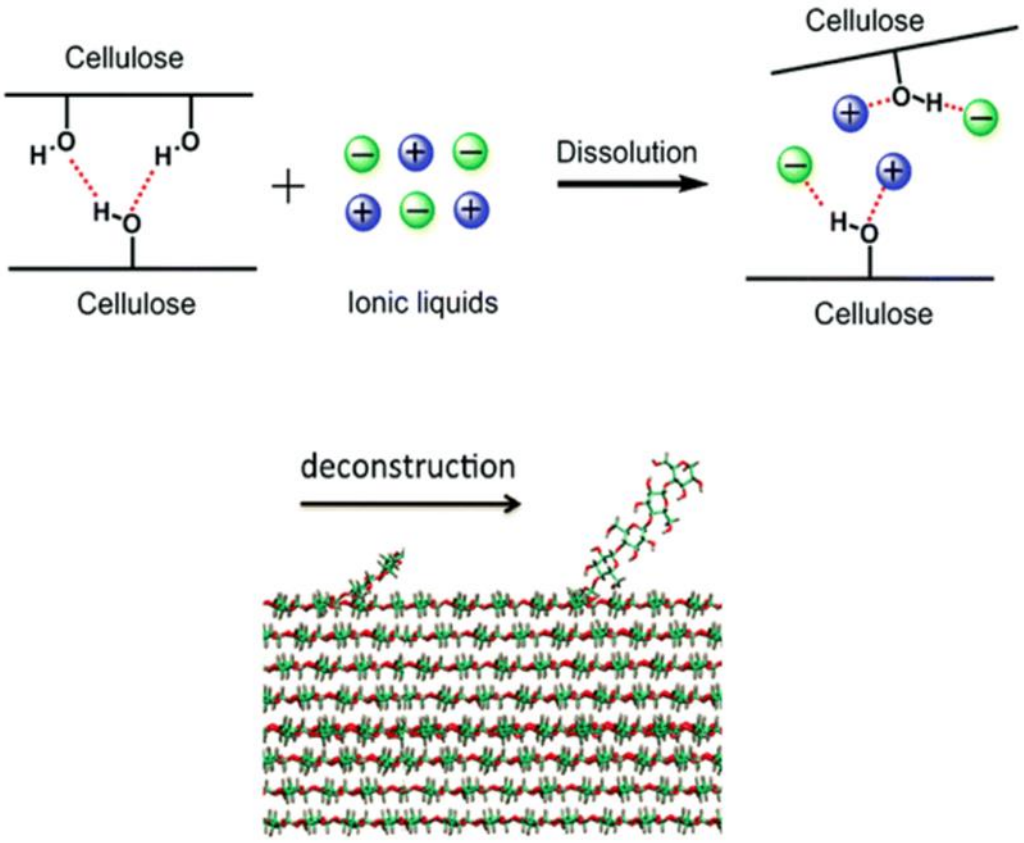

Figure 1.11: The diagram of the dissolution process for dissolving cellulose in the ILs and a glucan chain peeling away during the dissolution process. Taken from: [142].

The literature generally agrees that dissolution is based on a solvent's capacity to effectively destroy hydrogen bonding within cellulose [147]. The Lindman hypothesis, introduced by Björn Lindman in 2010, claims that the hydrophobic interaction in cellulose dissolution is exceeding the importance of hydrogen bond disruption [137]. This hypothesis is not consistent with the traditional view that H-bonds are the primary role of dissolving cellulose. Lindman’s hypothesis focuses on why cellulose is insoluble in water, is the insolubility of cellulose in water solely due to the hydrogen bonding between cellulose molecules?. Cellulose is an amphiphilic polymer, with both hydrophobic and hydrophilic groups. Hydrophobic interactions are crucial for understanding the solubility pattern of cellulose due to its amphiphilic property.

Despite water's hydrogen bonding ability, cellulose's non-polar hydrophobic interactions play a significant role in its insolubility in water.

Lindman's investigation highlights contradictions in the hydrogen bonding explanation. For example, cellulose should dissolve well in water if the hydrogen bonds were the primary factor which is similar to the hydrogen bonds in dextrin. Instead, Lindman postulates that cellulose's amphiphilic properties, the enhancement of aggregation and reduction of solubility, are due to hydrophobic interactions between cellulose molecules in water. Solvents such as ILs and NMMO have been used to dissolve cellulose in order to investigate this hypothesis. They are amphiphilic solvents and can dissolve cellulose effectively due to the disruption of hydrophobic interactions that contribute to its insolubility. Instead of focusing on the dissolution due to breakage of hydrogen bonding, the Lindman study presents a fresh perspective on cellulose dissolving by emphasizing hydrophobic interactions.

Recently, the importance of hydrophobic interactions has received considerable attention in several studies, supporting the Lindman hypothesis. Norgren et al. reported that the amphiphilic properties of cellulose have been shown to improve its interactions with solvents, particularly hydrophobic molecules, hence facilitating the dissolution of cellulose [148]. Similarly, Alvse et al. found that solvents containing hydrophobic molecules effectively disrupted interactions between cellulose chains, supporting the idea that hydrophobic forces play a significant role in the dissolution process [149].

There are numerous counter arguments against the Lindman hypothesis that need to be considered. A study conducted by Glasser et al. claimed that hydrophobic interactions may only become an important factor after breaking the H-bonds. They have claimed that the main reasons of cellulose's insolubility are its crystallinity, which Lindman hypothesis neglected the importance of the modification in the crystalline structure to improve solubility, rather than just hydrophobic interactions [150]. This summary of the key published works shows the complexity involved in the dissolution process of cellulose, and it is clear that the cellulose dissolution is still not completely understood.

1.6 Coagulation process and anti-solvents

Cellulose must be regenerated from the cellulose/IL mixtures after dissolution in ILs. Swatloski et al. conducted an experiment to examine the regeneration of cellulose that was dissolved in [BMIM][Cl]. They observed that by adding anti-solvents such water, ethanol, and acetone, the dissolved cellulose could be precipitated quickly [151]. Anti-solvents play a crucial role in transforming dissolved cellulose into usable products. They are excellent for regenerating dissolved cellulose, which has led to much scientific research on these substances [152]. Hauru et al. investigated the role of the solvent in the regeneration of cellulose from its solution in the presence of ILs ([BMIM][Ac], [TMGH][EtCO2], and [TMGH][Ac]) and NMMO [153]. These findings illustrate the ease with which cellulose may be recovered and have motivated researchers to examine the full potential of ILs for cellulose dissolution and regeneration. This coagulation process includes two steps: the first is when the IL has been sufficiently removed from a suitable anti-solvent, then followed by a drying process. Water molecules stop the dissolving by breaking the H-bonds between cellulose and solvent, and subsequently form new h-bonds with solvent as well as with the water molecules resulting a new crystal structure known as “Cellulose II” [36, 154, 155]; this mechanism is known as “coagulation” [156]. The coagulation process in cellulose-IL solutions involves reforming the cellulose molecules into amorphous and crystalline “cellulose II” [157]. Figure 1.12 shows the procedure of this mechanism, which shows the solvent molecules are observed to separate from the hydroxyl groups of cellulose and then attach to the anti-solvent water. This mechanism has been found to be influenced by the coagulation conditions such as degree of polymerization, cellulose molecules, cellulose concentration in the solution, the coagulating temperature, and the coagulant type [156, 158-164]. The complete

understanding of the process of dissolution and regeneration in ILs is not well-known, which is a challenge in developing novel ILs for efficient cellulose pretreatment and processing. In this study, water was used as a coagulating antisolvent to demonstrate the disruption of solvent–cellulose bonds formed during dissolution, and it can display a far higher degree of crystallinity 43% compared to the ethanol as coagulant 21%, thus, the resultant cellulose structure has been found to be affected by the type of antisolvent used [152]. As an illustration, Zeng et al. conducted a comparison of the anti-solvent capabilities of water and ethanol. They observed that water exhibited better efficiency in disrupting cellulose-IL bonds [165]. Moreover, another study conducted by Taokaew and Kriangkrai found that the thermal stability of cellulose regeneration using water is greater than that of regeneration using ethanol [166]. Subsequently, the anti-solvents can be removed from the cellulose-IL solutions using a drying process to evaporate the coagulants [78].

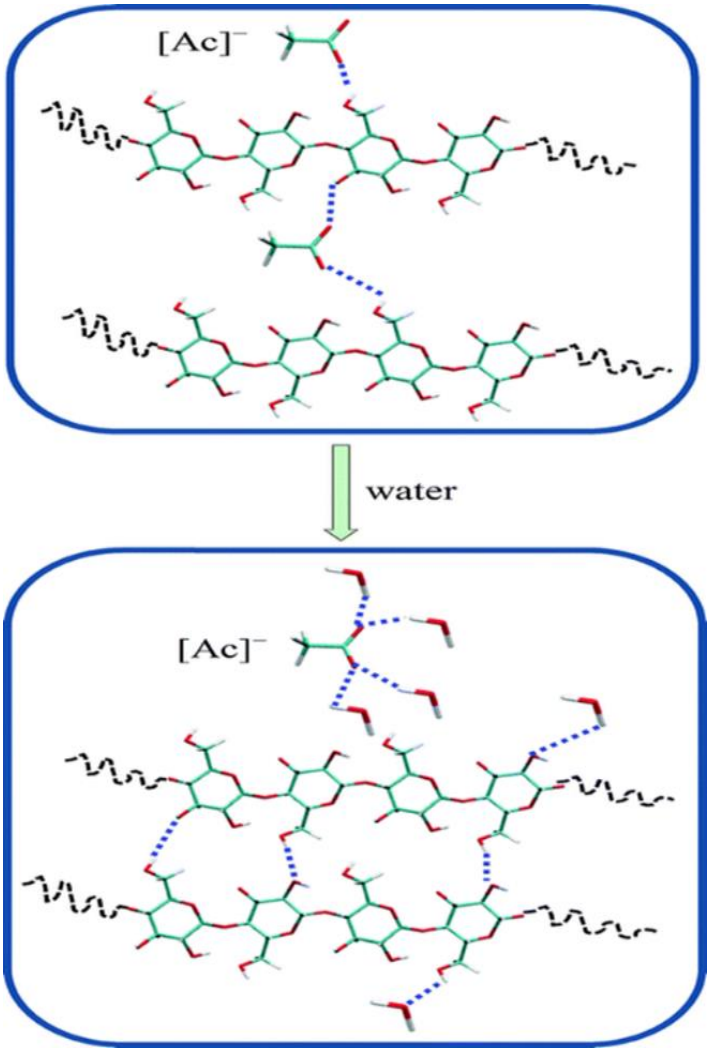

Figure 1.12: A diagram of coagulation mechanism for cellulose regeneration by adding water to the cellulose/IL mixture with h-bond shown as dashed lines. Taken from [156].

1.7 Activation energy and dissolution kinetic factors

Molecules are constantly in motion and moving randomly in all directions. This motion becomes faster with increased thermal energy that can then be used to break bonds leading to chemical reactions due to the kinetic energy increases. According to collision theory, molecules must collide with each other for the reaction to occur, and the colliding molecules need a sufficient energy to overcome the activation energy (Ea) barriers, which is the minimum energy required for the react to occur from the initial state (reactants) to the final state (products), as shown in Figure 1.13 [167]. The reactants are ready to climb over the peak, the highest energy (transition state), to produce new products [168]. The new products will be on a lower enthalpy (ΔH) by overcoming the energy barrier to reach a more stable energy level than the reactants level: if this happens then the reaction is called exothermic. In this system, the enthalpy change (ΔH) is negative, which means that the products have a lower energy than the reactants, leading the reaction to release energy to the surroundings. Thus, the energy required to break the bonds in the reactants is less than the energy release when new bonds are form in the products; as result, this reaction loses energy which is transferred to the surroundings. However, in the endothermic system, the new products will be in a higher enthalpy, and the enthalpy change (ΔH) is positive, which means the products have higher energy than the reactants, leading to absorb energy from its surroundings. Thus, the activation energy required for the reactants to climb over to the transition level is still the minimum amount of energy which is similar to above system, the old bonds are half broken, and the new bonds are half made [169].

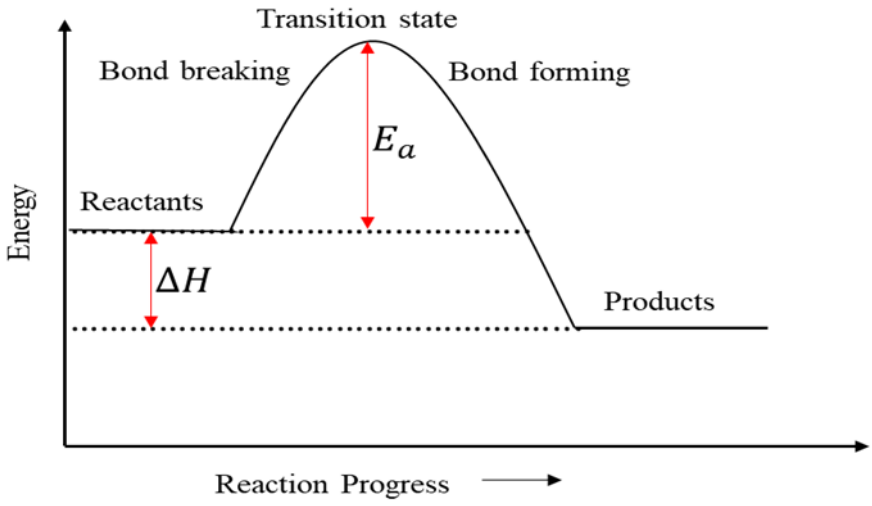

Figure 1.13: Changing in the thermodynamic and kinetics during the dissolution.

The Arrhenius equation is frequently used throughout this work, and this describes a relationship between the rate of a chemical reaction and the corresponding activation energy and reaction temperature, see equation 1.1.

$$\alpha_T = \alpha_0 \, e^{\frac{-E_a}{RT}} \tag{1.1}$$

where α_T is the scale factor, E_a is the Arrhenius activation energy, R is the gas constant, T is the temperature in Kelvin and is α_0 the pre-exponential factor (a reaction based constant).

If the scale factor (α_T) obeys the Arrhenius equation via applying the natural logarithmic form in both sides, then a plot of ln (α_T) vs. T^{-1} will reveal a straight line with a gradient $-E_a/R$ and intercept $Ln\alpha_0$, as evident in equation 1.2.

$$Ln\alpha_T = \left(\frac{-E_a}{RT}\right) + Ln\alpha_0 \tag{1.2}$$

This shift factor ($Ln\alpha_T$) specifies how much data must be moved in Ln time to overlay time-dependent behaviour at different temperatures onto a master curve, so how the rate of the reaction changes with temperature. TTS is used to align data collected at various temperatures by shifting it to a reference temperature, creating a master curve that represents the material's behaviour over a range of times and temperatures. In addition, the kinetic energy of the molecules increases as the temperature increases, according to the Maxwell-Boltzmann distribution, as shown in Figure 1.14. This implies that more molecules will possess sufficient energy to overcome the activation energy barrier. Moreover, at low temperatures (the red curve) illustrates the molecule has less energy and move slow, which allow fewer molecules to overcome the activation energy, resulting a slower reaction. Inversely, molecules move faster with higher energy leading to higher reaction rate, at higher temperature (the blue curve).

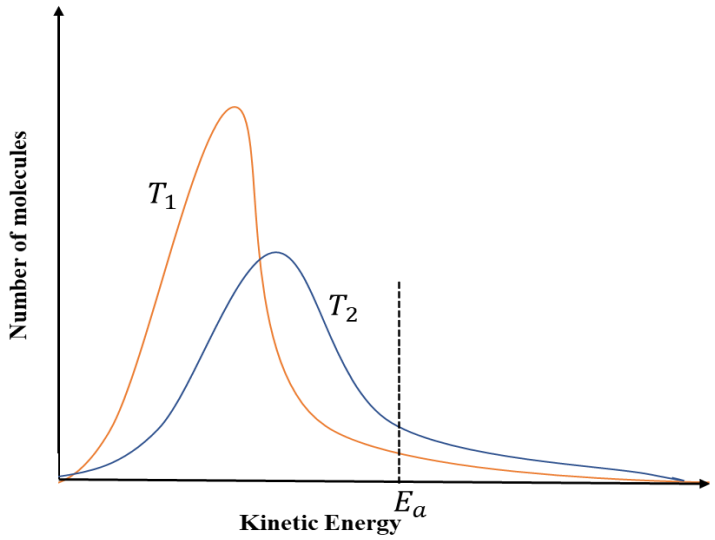

Figure 1.14: Energy distribution of molecules that exist in a solution at two different temperatures. As the temperature is increased ($T_1 < T < T_2$), a corresponding increases in the number of molecules with energy Ea.

1.8 Influence of water on dissolution process

ILs are commonly used as a solvent for cellulose, but the dissolving capability of most ionic liquids is reduced by the addition of even small amounts of water [170]. ILs are extremely hygroscopic in nature, and they absorb atmospheric moisture [171]. Several researchers have studied their interaction with water. This interaction could cause several alterations, such as the structural and dynamical alterations in the ILs that may change with the type of ILs and concentration of water. The concentration of water could also affect the ion-water interaction, especially in the case of hydrophobic ILs [172]. The differences in the ion-water interaction between hydrophobic ILs and hydrophilic ILs are attributed to the activity of water molecules. For instance, the water molecules in hydrophilic ILs are stabilized through dipole-dipole forces and H-bonding, allowing them to remain in the IL system and contribute to a stable and effective solvent environment. On the other hand, in the case of hydrophobic ILs, the ILs are reoriented at the interface between the hydrophobic IL and water leading to the differences in the properties of the solutions [173]. The presence of water in the ILs alters the nanostructure of the ions [174]. The sizes of

the alkyl chains of the cations of ILs play a key role in the micelle formation because of an interaction of ILs with water. Ficke and Brennecke reported that the interactions between IL and water are stronger than the respective IL-IL and water-water interactions [175], due to the strong interaction between anion and water molecules by h-bond forming an anion H-bond structure [176]. The interaction between ILs and water leads to structural changes that also affect the dynamic properties of the ions. For instance, the reorientation and diffusion dynamics of the ILs are altered upon the interaction between ILs and water [173].

Among ionic liquids, imidazolium based ILs are prone to water absorption [177]. The absorption of water can reduce the available bond on the anion, and as a result, decrease the capability of dissolving cellulose [178]. According to several studies, even small amounts of water can reduce the effectiveness of ionic liquids in dissolving cellulose, due to the impact of moisture content [170, 179, 180]. The water content can modify the diffusion of the cation and anion. In pure ionic liquids, cations typically diffuse faster than anions; however, this trend can be reversed in the presence of water [170, 181].

The presence of water can also reduce the interaction between ions due to the interaction between water molecules and the anion. Liu et al. found that interactions between cation-anion in the pure ionic liquid are stronger than in the aqueous solution. The average interaction energies in the pure IL are approximately -1309.08 kJ/mol and - 6725.87 kJ/mol, which are lower than those in solution. This suggests that the pure IL exhibits a higher ion-to-ion interaction than the mixed IL [182]. Most investigations focus on cellulose regeneration yield and properties. However, the microscopic processes of cellulose regeneration, anti-solvent roles, and ionic liquid-anti-solvent interactions are unrevealed yet.

1.9 Composites

It is important to end this introduction with directions on how the discoveries in this thesis will feed into the field of composite science and in particular the manufacture of all cellulose composites. In the 1940s, composite materials were first developed by reinforcing fibres [183]. Composites comprise two or more discrete constituents that maintain their separateness in terms of their physical and chemical properties but, when combined, yield a material with improved properties over its constituent parts [184]. These constituents often have a matrix that binds and supports the reinforcement, and a reinforcement, enhancing the composite's mechanical

properties [185]. A common example of composite material is wood, composed of cellulose fibres organized in a matrix of lignin and hemicellulose. This structure gives the wood strength and flexibility, making it the appropriate choice to support the plant structures. This is mostly applied in construction due to the strength/weight ratio [186]. They are classified into several divisions, particularly polymer matrix composites (PMCs), metal matrix composites (MMCs,) and ceramic matrix composites (CMCs). Currently, PMCs are highly effective and flexible [187], and their way of production is simple.

1.9.1 All-Natural Fiber Composites

The interest in natural fibre composites (NFCs) is rapidly increasing in the present market due to their sustainability and environment-friendly material, and they are used in automotive industries, construction and packaging industries, and several other industries [188, 189]. These composites can replace some synthetic fibre-reinforced polymer matrices as an environmentally friendly replacement by incorporating natural fibres such as sisal, hemp, jute, and flax [190]. Recent works that have been carried out highlight the mechanical behaviour of NFCs and infer that natural fibres might well be as strong and stiff as those manufactured synthetically. For instance, the study by Koronis et al. has shown efforts in the natural fibre to increase the composites' polymer matrices and tensile and flexural properties [191]. Fiber surface treatment, which improves the bonding of the resulting composite by enhancing the interface between the fibre and polymer matrix, can retain these qualities [192]. In addition to the purely mechanical aspects, NFCs present a string of advantages from the environmental sustainability standpoint. The synthesis of these composites usually involves a reduced carbon footprint and the use of environmentally friendly materials as Pickering et al. (2016) stated. Due to properties such as renewability and biodegradability of natural fibres, it enhances the aims of reducing resource depletion and waste [193]. Moreover, NFCs offer many advantages, such as thermal stability, renewability, biodegradability, nontoxicity, and sound insulation, which increases NFCs’ applicability in areas such as construction materials and automotive interiors [194].

However, NFCs have encountered several challenges. Such drawbacks include the variability of the mechanical properties of natural fibres, which, in turn, cause the inconsistencies of the composite’s performance. This heterogeneity is ascribed to the unfavorable characteristics of natural fibres, which limit their application in the industrial sector. These characteristics include excessive water absorption, poor

bonding, low durability, and low mechanical and thermal properties compared to synthetic fibres [195]. Another issue is that natural fibres are hydrophilic in nature as most of them originate from crops, leading to fluctuations in mechanical properties and swelling of the composites over time. Several scientists have endeavored to develop chemical modifications and compound materials to improve moisture resistance and comprehensive performance [196].

1.9.2 All cellulose composites

All-cellulose composites (ACCs) are one of the versatile and novel green materials synthesized solely from cellulose – Earth's most abundant natural polymer. In recent years, among plant fibres, flax fibre has been considered one of the most important natural reinforcements for composite materials. Flax fibre with cellulose content found to be 70%, and other substances of about 30% have been used as cellulose sources in ACCs. The tensile strength and the Young's modulus of the single flax fibre were 1.2 GPa and 60 GPa, respectively [197], which suggests a significant potential for application in ACCs. Flax-based materials such as flax nonwoven textile [47], linen textile [198], flax yarn [199], are reported to make ACCs when [C4mim][Cl], [C4mim][OAc] and [C2mim][OAc] were used as solvent. As reported on the flax yarn-based ACCs made with partially dissolved process, the highest tensile strength and Young's modulus are found to be 151.3 MPa, and 10.1 GPa, respectively [199]. Compered to cotton, with the highest cellulose in plants of 90%, the highest tensile strength and Young's modulus were found to be 68 MPa and 134 MPa, respectively which suggests hug potential as cellulose sources in ACCs [200, 201]. Therefore, flax fibre ACC is two times stronger than cotton fibre ACC [85, 202].

Composites are also advantageous in being biodegradable and renewable, thus providing a green solution to the problem. ACCs are made using cellulose fibres and a cellulose matrix. There is good compatibility between the fibres and the matrix since they are chemically related commonly through the partial dissolution of cellulose fibres. This improves interfacial bonding, which leads to enhanced mechanical features such as high tensile strength and modulus, allowing them to rival synthetic fibre composites (Nishino et al.2004).

The significant study conducted by Nyshano et al. (2004) came up with a new approach of thought that involved the creation of composites from a single type of fibre. This study demonstrated it was beneficial that a uniform fibre type was employed in the given research so that the mechanical properties of composites could be more easily and uniformly predicted. Nyshano's research focused on

determining how chemical treatments and single-fibre composite processing techniques may enhance the fibres' interfacial adherence to the matrix while lowering moisture absorption (Nishino et al.2004). They proved that by choosing one kind of fibre and then controlling the processing parameters, the mechanical characteristics could be increased up to the level of multi-fibre composites. This approach helps solve the variability problem, as it minimizes fluctuations in fibre properties and creates a more reliable foundation for future research and industry application. Additionally, all-cellulose composites are completely bio-based and biodegradable according to the all-polymer composites concept; there eliminate the poor fibre/matrix interaction when fibres and matrix are made up of dissimilar material [203, 204].

The solvent used, the temperature, and the natural fibres' composition, kind, and form all affect how they dissolve [205]. As a result, understanding the kinetics of dissolving a certain fibre in a cellulose solvent is critical for determining the relationship between the fibre's form. This will help in deciding the best processing conditions that can be used to create better ACCs in terms of their mechanical properties.

Among these, the ACCs that are produced include those produced through the impregnation method (two-step method) or systematically dissolving partial method (one-step method), as shown in Figure 1.15. The two-step method called the impregnation method, is used to produce ACCs, all-cellulose composites. In this process, cellulose fibres are first treated using a solvent system that selectively dissolves the cellulose and any hemicellulose. The main feature of the method is that the dissolved cellulose can penetrate through the layers and get onto the surface of undissolved cellulose fibres. This interaction results in the development of a further embodiment whereby the dissolved cellulose surrounds the fibres. Then, adding cellulose fibre to the solution and the cellulose leaves to precipitate or coagulate to form a strong shell between matrix and fibre composite [78, 206]. This procedure optimizes the mechanical features of the composite by strengthening the interfacial adhesion between the fibres and the matrix: the outcome is a strong, eco-friendly material. The technique above has used solvents such as NaOH/urea systems, ionic liquids, and NMMO [207, 208].

The one-step method, also known as the partial dissolution of cellulose, used to obtain all-cellulose composites since the dissolution and regeneration processes are a single process. It is more of a solvent that swells the cellulose fibre; the soluble part also works as a matrix for the insoluble part of the fibre [83]. This results in improved interfacial adhesion and a reinforcement of the mechanical properties of the final

composite material [19, 78, 209]. This approach also abolishes the need for additional processing stages, lowering production costs and increasing efficiency.

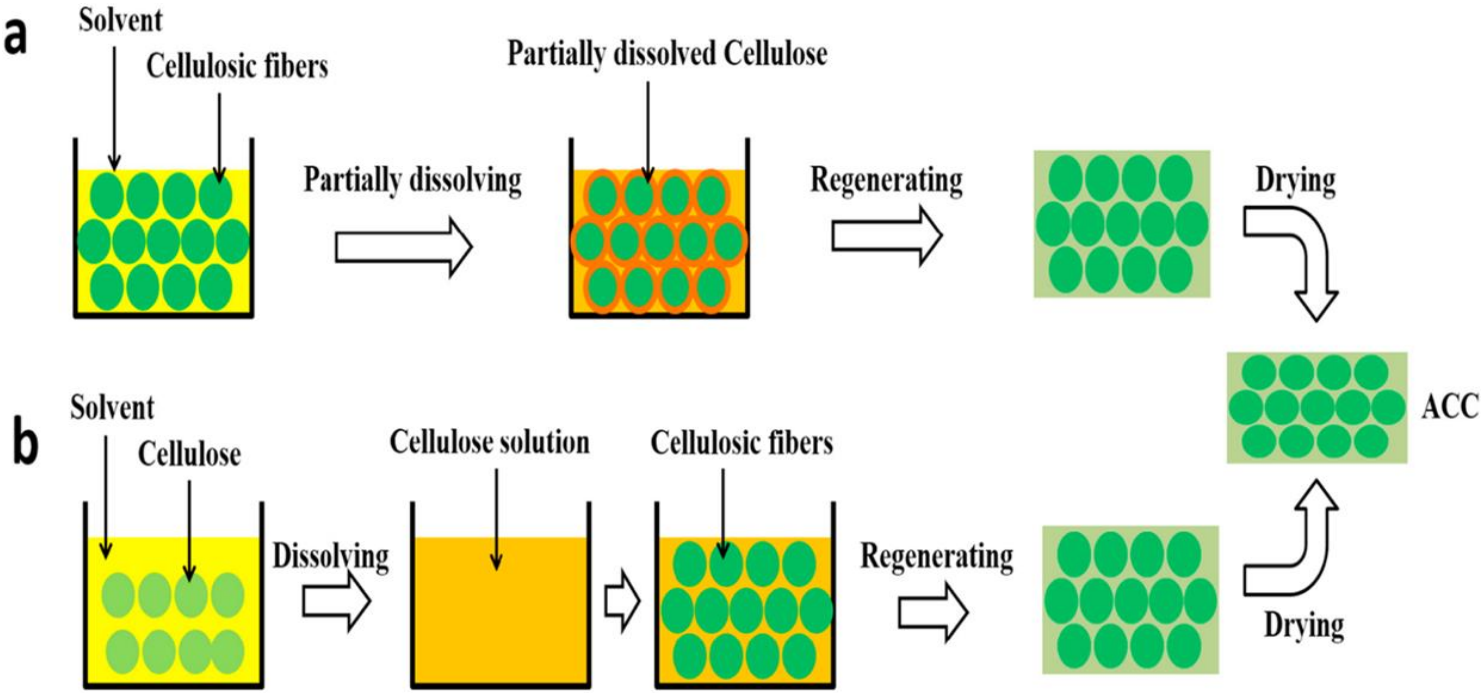

Figure 1.15: Schematic of ACCs preparation: (a) one-step method and (b) two-step method. Taken from [209].

The work presented in this thesis would help in the development and production of ACCs, which requires improving flax yarn dissolving conditions in (ILs) to obtain particular coagulated fractions and establish the best IL to use and the optimum processing conditions (temperature and time). Specifically, a woven ACC usually requires ~30% matrix (coagulated fraction) so the data in this study collected from various temperature and time combinations illustrate the impact of these variables on the dissolution process and have been published [210-213], their effects thereby establishing a precise guideline for the conditions required to achieve the optimal ratio which is 70% reinforcing fibres (cellulose) to 30% matrix (coagulated fraction) [83]. The results of this study indicate that manufacturers are now able to predict the required temperature and dissolve time to obtain the right matrix fraction, increasing

the accuracy as well as effectiveness of ACC production. It is known that an appropriate fibre-to-matrix ratio is needed to create a high-performance composite material with higher strength, low density, and deformation resistance [82, 214]. Controlling temperatures throughout production is essential for maintaining this ratio and producing a better composite material. The results of this study indicate that manufacturers are now able to predict the required temperature and dissolve time to obtain the right matrix fraction, increasing the reproducibility as well as effectiveness of ACC production.

Chapter 2

Experimental Methods and Materials

2.1 Introduction

This chapter will present the different experimental techniques used throughout the project, the purpose of which is to investigate the dissolution mechanism of flax yarns in three distinct ionic liquids. The ionic liquids were chosen such that two had the same acetate anion $[OAc]^-$ but a different cation, either ethyl $[C2mim]^+$ or butyl $[C4mim]^+$. The third ionic liquid had the same ethyl cation [C2mim] but a different anion, an octanoate $[Oct]^-$. These different combinations allowed the role of the anion and cation on cellulose dissolution to be investigated. Measurements were carried out using a combination of optical microscopy, rheology, and nuclear magnetic resonance (NMR) and all of these represent the majority of the collected experimental data. They provide the basis for further discussion and different chemical and physical insights. The effect of water on dissolution was also investigated for ILs and Karl Fischer titration was used to measure water content of ILs both before and after any experiments.

Optical microscopy (OM) captures flax yarn morphology and allows to directly follow the dissolution of the flax fibres. This simple technique offers significant insights into the fundamental physics of dissolution, allowing the calculation of both the dissolution activation energy and the dissolution rate. Samples at various stages of dissolution (for a range of processing times and temperatures) were encapsulated into epoxy resin and then polished. Viewed in reflection under an optical microscope, two regions were always clear, a ring of dissolved and coagulated cellulose surrounding the original fibres. From the optical micrographs it was therefore possible to measure the amount of dissolved yarn with time and temperature, which is termed the coagulated fraction. Additionally, it was found that following the increase of the thickness of this coagulated fraction allowed important information on the diffusion of the various ionic liquids to be measured.

NMR is an efficient technique, due to its ability to explore a wide range of chemical information. In addition, it is not only used in chemical characterization, but it can also determine diffusion characteristics, molecular structure, motion and conformation. The NMR studies here will measure the self-diffusion coefficients of each ionic liquid at different temperatures to determine its diffusion activation energy and effective molecular size.

Rheological methods offer a wide variety of approaches for examining the macroscopic flow characteristics of fluids, which can provide insight into the microscopic properties. The measurements here will be limited to focus on the viscosity of each ionic liquid as a function of shear rate and temperature to create a flow curve which then shows the rheological character of each ionic liquid to be compared and contrasted.

2.2 Materials

Flax yarns have been purchased from Airedale Yarns, Keighley, UK. The chosen flax fibres were in the form of continuous yarn and had a diameter of 0.5 mm. These flax fibres have been chosen to build on the first work of our research group [22] using a single ionic liquid [C2mim] [OAc]. The ionic liquids used in this study were [C2mim] [OAc] with a purity of 98%, [C4mim][OAc] with a purity of 98%, and [C2mim] [Oct] with a purity of 98% which were all purchased from Proionic GmbH, Grambach, Austria. As described above, these three were chosen so that each pair has a common anion or cation, enabling the role of cation and anion to be studied. In order to investigate and determine the dissolved coagulation fraction at each processing condition, epoxy resin was used to embed the samples (Epoxicure, Cold Cure Mounting Resin from Buehler, UK) and then examined using optical microscopy (OM) in reflection to allow for clear images. Water was used as the coagulant as it has been reported to perform effectively in regenerating dissolved cellulose [165]. A nitrogen vacuum was employed to prevent moisture contact with the ILs that were used for water experiments. An MBraun Labmaster 130 glove box was used to prevent water contamination in the IL samples for NMR and density measurements. Karl-Fischer titration using a Metrohm 899 Coulometer was employed to determine the water content in ionic liquids as received, giving the water content in the experiments of [C2mim][OAc], [C4mim][OAc], and [C2mim][Oct] were 0.2 wt.%, 0 wt.%, and 0.1wt.% respectively.

2.3 Dissolution Procedure

The various stages to perform the dissolution experiments and analyse the partial dissolved yarns are shown in Figure 2.1. Flax yarns were first wrapped individually around a polytetrafluoroethylene (PTFE) Teflon picture frame of 5 cm × 5 cm, binding both ends of each yarn. Repeated measurements were taken at the chosen temperatures and timings during processing by winding four separate yarn samples onto each frame for testing. Next, the IL (approximately 50 ml) was preheated in a PTFE tray for 1 hour before starting the dissolution experiments to ensure that it was stable at the selected target temperature. Then, submerging the frames in a Teflon plate filled with preheated IL in a vacuum oven, the flax samples were dissolved at various temperatures and times (Shellab 17L Digital Vacuum Oven SQ-15VAC-16, Sheldon Manufacturing, Inc., Cornelius, OR, USA). Subsequent to the dissolution of the composite, it was immediately removed from the ionic liquid and its cellulose was allowed to coagulate in a water bath maintained at the room temperature for 24 hours. Following the removal of the partially dissolved composites from the water bath and allowing them to dry at room temperature for 48 hours, a drying method was employed. The composite yarns were finally removed from the frame and ready for embedding in epoxy resin, see Figure 2.1.

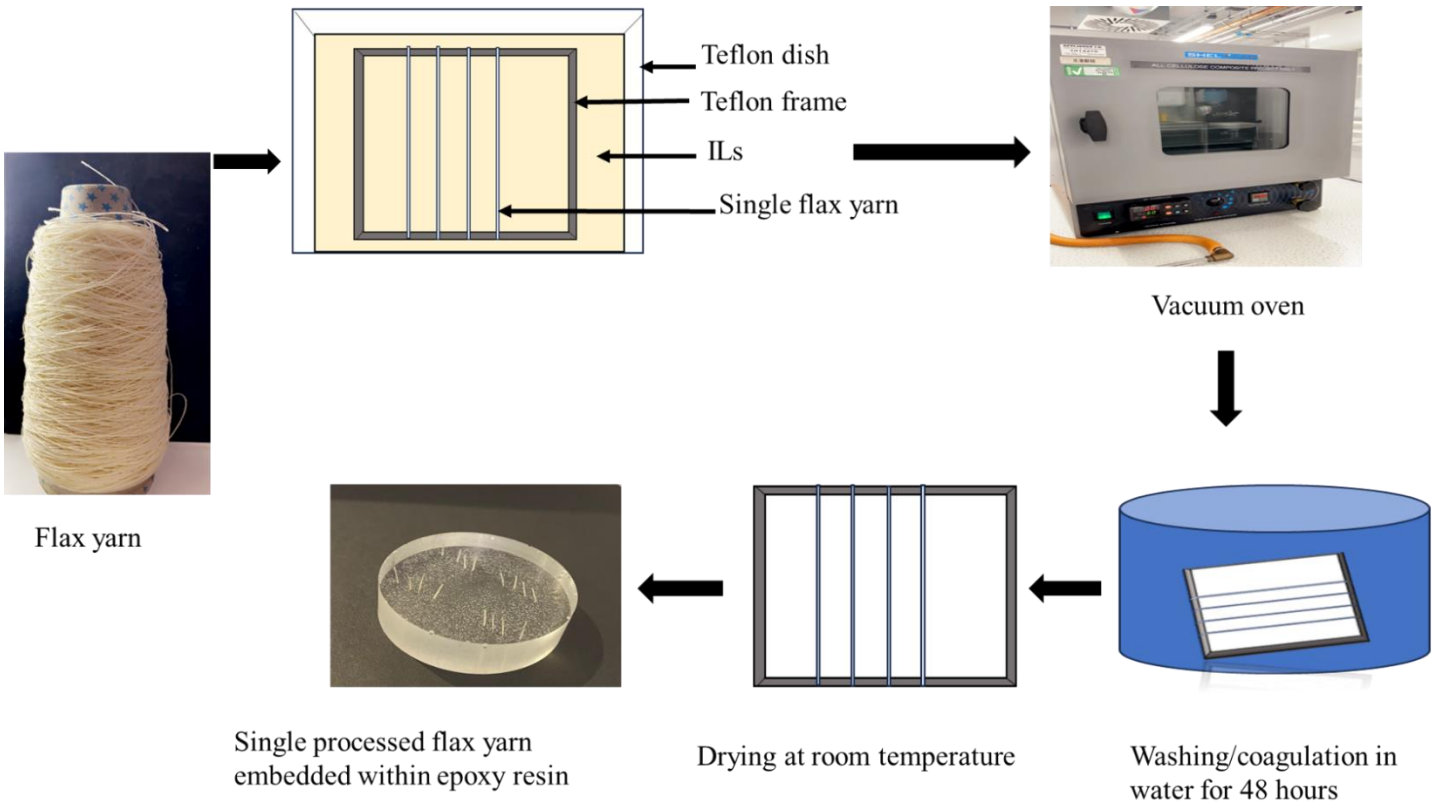

Figure 2.1: Schematic diagram of the process of dissolving flax yarns in pure ILs.

2.4 Optical Microscopy

Optical microscopy (BH2-Olympus Corporation, Japan) at various magnifications (x50, x100, and x200) was used to examine partially dissolved flax yarn morphology, alongside a CCD (charge-coupled device) camera with a resolution of 1920 x 1200 for the capture of clear cross-sectional images. Samples were encapsulated with epoxy resin for optical microscopy. Each of the four processed samples was vertically embedded in epoxy resin after the resin and hardener (EpoxiCure 2, BUEHLER) were mixed at a 4:1 ratio, then the Teflon circular container was left at room temperature for 48 hours. After that, a grinding and polishing process was applied to the yarns surface via a polishing machine (STRUERS ROTOPOL-11/ROTOFORCE-1, Struers Ltd., UK) on the resin to produce a 1 to 2 cm thick sample prior to reflection analysis, enabling for taking high-resolution images, as shown in Figure 2.2. The polishing procedure was as follows: 2 minutes using an 800 grit SiC paper, then 4

minutes using a 1200 grit SiC paper and then finally 6 minutes using a 1-micron alumina suspension.

To measure the ratio of undissolved core (inner region) to the dissolved and coagulated fraction (outer region) of the processed yarns, 'ImageJ 1.52d' processing software was used to measure these two regions, as shown in Figure 2.3. A mouse was used to draw round the outer perimeter (the orange line shown in the Figure) which is the area of both the original remaining yarns and the outer dissolved and coagulated region. A mouse was then used to draw round the inner area, which is just the remaining raw yarn.

Figure 2.4 shows a set of optical micrographs for samples all processed at 60 °C for a range of processing times from 15 minutes to one hour. On the left is shown the drawn outer area and, on the right, the drawn inner area. One interesting aspect is that the overall size decreases as the coagulated fraction increases as this has a higher density compared to the original plant fibres, that have some internal voids.

Figure 2.2: The epoxy resin embedding method. a) Flax yarns were embedded in an epoxy resin, b) Yarn threads before grinding down and polishing, (c) Complete curing of yarns allows clear image capture.

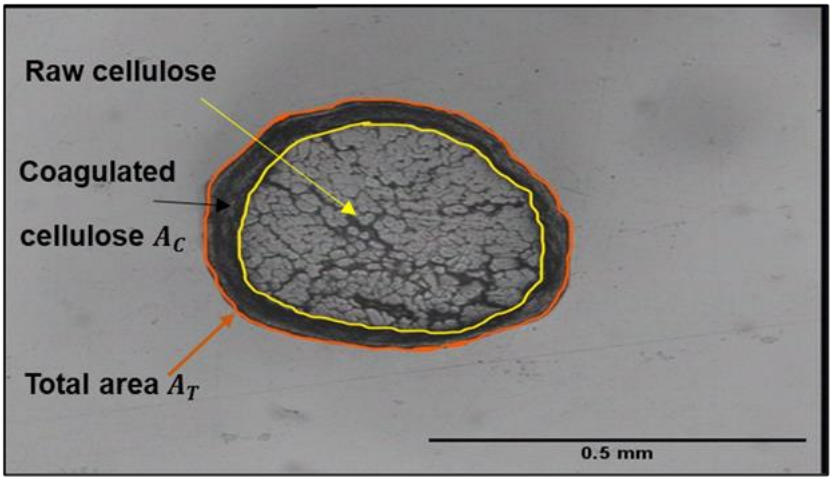

Figure 2.3: A partially dissolved yarn shows the raw cellulose (inner core), the coagulated cellulose area and the total area of both raw and coagulated fibre (outer layer).

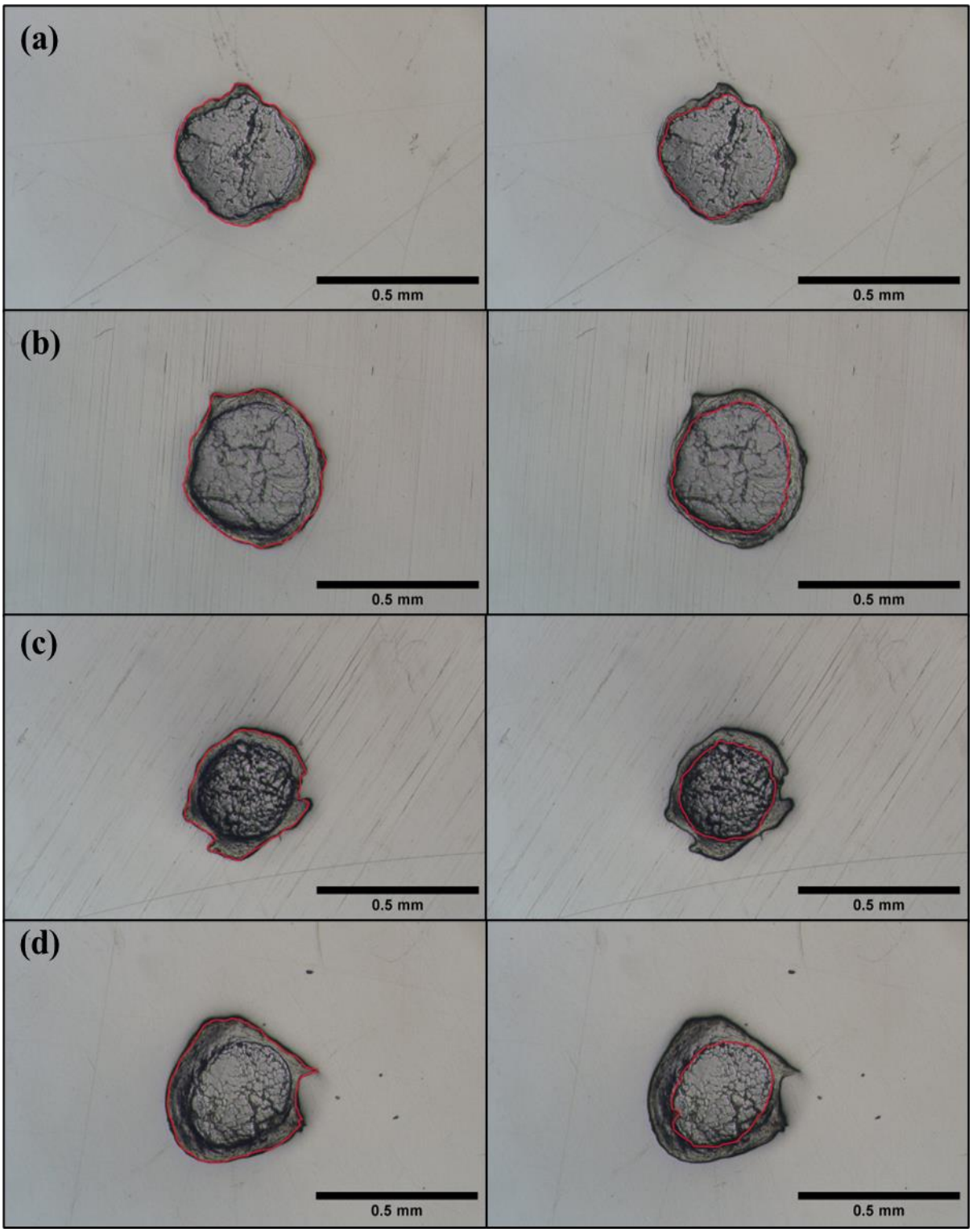

Figure 2.4: Microscopy images showing how the boundaries between raw and partially dissolved cellulose were determined. The outer boundary is shown on the left and the inner on the right. Yarns shown were dissolved at 60 °C for a) 15 min, b) 30 min, c) 45 min and d) 1h. Scale length 0.5 mm.

The boundaries between the inner core and the partially dissolved region, as well as between the partially dissolved region and the outside area, can be determined and established as shown in Fig.2.4. The coagulated fraction CF was calculated using,

$$CF = \frac{A_{outer} - A_{inner}}{A_{outer}} \quad (2.1)$$

where A_{inner} is the area of the remaining fibre core and A_{outer} are coagulated and raw cellulose cross-section outer area.

2.5 Viscosity

The viscosity of the three different ionic liquids, as a function of shear rate, was studied using an Anton Paar 302 rheometer (Anton Paar GmbH, Graz, Austria), which was equipped with a water bath temperature control system and a Peltier cover. The Peltier hood was used to prevent water uptake by covering the edges of the plates from air. A plate- plate geometry with a diameter of 25 mm, and a gap size of 0.3 mm was used with temperature increasing from 30 °C to 100 °C. Newtonian behaviour was observed in all solvents at all temperatures, as evidenced by steady shear experiments conducted at shear rates ranging from 1- 100 s^{-1}. The suggestions of Ewoldt et al. (2015) were followed to, including testing the air check to prevent the data being scattered; this was done before the measuring process started [215]. Each sample was heated to the chosen temperature for one minute, and the measurements were conducted three times to determine an average viscosity value. The standard deviation in the measurements was found to be less than 10%.

2.6 Controlling water content

ILs have a tendency to absorb moisture exposed to humidity and ambient conditions (Seddon et al., 2000). Therefore, it is important to protect ILs from atmosphere and minimize their exposure to humidity. Additionally, it is advisable to limit exposure as much as possible during sample preparation, measurement and storage.

We employed an MBraun Labmaster 130 glove box to prevent water contamination in the IL samples. The glove box maintained a dry nitrogen atmosphere with a dewpoint level ranging between -40 °C and -70 °C. All ILs used for NMR and density measurements were kept in a controlled atmosphere to minimize humidity exposure. Karl-Fischer titration using a Metrohm 899 Coulometer was employed to determine the water content in pure ionic liquids. In cases if storing the ILs in a glove box was not feasible, pure ionic liquids were carefully sealed and stored in a desiccator.

2.7 NMR Method

The self-diffusion coefficient measurements of $[C2mim]^+$, $[C4mim]^+$, $[OAc]^-$ and $[Oct]^-$ ions were determined using a Bruker Avance II 400 MHz spectrometer. To measure the diffusion a Diff50 diffusion probe and a ^{1}H coil was utilized. We were able to achieve gradient strengths of, up to 20 Tm^{-1}. The gradient field strength was calibrated by measuring the self-diffusion coefficient of water at a temperature of 20 ± 0.1°C. This measurement involved using a heating element and dry airflow. Samples were given a minimum equilibration period of 10 minutes prior to each measurement.

The measurements, at high field were conducted on samples that were carefully prepared in a controlled environment in a glove box. These samples were sealed before being taken out as mentioned earlier. We followed the advice of Annat et al. which included maintaining a sample height of less than 1 cm to minimise any disturbances caused by convection currents [216]. Additionally, maintaining the water-cooling system for the gradient coils at 15 °C below the measurement temperature. This was done in order to reduce the convection currents that were caused by temperature differences across the sample.

In this work, the pulsed-field gradient (PFG) technique was employed to measure self- diffusion coefficients, D. A stimulated echo pulse sequence with bipolar

gradients was used [216]. Gradient strength was varied stepwise, and D was obtained by applying the Stejskal-Tanner equation [217]. The gradient pulse lengths, δ, ranged from 1 to 4 ms, whereas the diffusion times, ∆, varied from 10 to 100 ms. The uncertainty in the measurements was found to be 10%.

2.8 Anti-solvent distilled water

To investigate the effect of water on the dissolution, amounts of (distilled water) were mixed into the pure ILs [C2mim][OAc] and [C4mim][OAc] with a magnetic stirrer for 10 minutes prior to use. Three water concentrations were used for the IL [C2mim][OAc]: 1%, 2%, and 4% by weight. We chose 4 wt.% water as our maximum limit, as exceeding this concentration results in a dissolving process that becomes impractically slow for observation within a reasonable time. Four water concentrations were used: 1%, 2%, 4% and 8% by weight for the IL [C4mim][OAc].

The water content in the ionic liquids was measured using Karl Fischer titration (KFT) before to and after the dissolving process. The KFT results for the ILs provided by the manufacturers Proionic indicated that they contained 0.2% water and 0% water for [C2mim][OAc] and [C4mim][OAc], respectively. The following equation was applied to determine the amount of water for ILs [C2mim][OAc] and [C4mim][OAc] in order to investigate the dissolving power and its effect of adding water.

$$C_{water}, wt\% = W_{water} \times 100\% \,/\, (W_{IL} + W_{water}) \qquad (2.2)$$

where C_{water} is water concentration and W_{IL} , W_{water} are the total weights of the water and IL, respectively.

The IL/water mixture has a significantly higher vapor pressure compared to pure IL and may therefore evaporate under a vacuum environment. Consequently, the vacuum oven environment was replaced with nitrogen to prevent evaporation during dissolution in the Leybold Sogevac vacuum oven. Many studies have examined the interaction between ionic liquids and water, revealing that their properties may be significantly modified in the presence of water. The melting point, polarity, viscosity, and surface tension of ionic liquids are modified [218].

2.9 Uncertainties

The equation below is frequently used throughout this thesis to determine the standard error of the mean (also called the uncertainty in the mean) of the number of measurements conducted, see equation 2.3.

$$SE = \frac{\sigma}{\sqrt{N}} \tag{2.3}$$

where SE is the standard error, σ is the standard deviation of the population, and N is the number of measurements taken. The standard error is used to plot error bars on all the graphs in the following three chapters, where the number of measurements, *N*, is usually 4.

Chapter 3

The Dissolution of Flax Yarn in the Ionic Liquid 1-ethyl-3-methylimidazolium acetate $[C2mim]^+[OAc]^-$

The significant work of this chapter has been published as follows; Albarakati, F.A., Hine, P.J. & Ries, M.E. Effect of water on the dissolution of flax fiber bundles in the ionic liquid 1-ethyl-3-methylimidazolium acetate. *Cellulose*. 30, 7619–7632 (2023). https://doi.org/10.1007/s10570-023-05394-3

The remaining work of this chapter is under review now as follows; Albarakati, F.A., Hine, P.J. & Ries, M.E. The Role of Cation and Anion on The Dissolution Rate of Flax Yarns in Ionic Liquids. *Cellulose*.

3.1 Introduction

For over 30,000 years, the flax plant has been grown all over the world and used for its fabric, mechanical, and culinary characteristics [59]. Over 2.7 million tons of flax were produced in 2017, making it cheap and abundant [219]. This plant thrives in a variety of climates and soil conditions [220, 221]. It is documented as one of the oldest textile cellulose, and has a typical polymerization degree of approximately 4,000 [60]. Flax fibre-based composites, with their superior mechanical performance, complete biobased composition, and possibility for recycling, provide a viable alternative to traditional production materials without causing considerable environmental harm [20].

The work presented in this chapter investigates a flax yarn and its dissolution process in an ionic liquid (IL) 1-ethyl-3-methylimidazolium acetate [C2mim][OAc]. Our group and other research teams have extensively used this ionic liquid as a solvent for dissolving cellulose materials, such as films, textiles, and composites [22, 113, 126, 171, 222-227]. The dissolving of the chosen flax yarns was examined across various dissolution temperatures and times, the method being explained previously in Section 2.3. The structure of the partially dissolved fibres was then examined using optical microscopy. In all of the partially dissolved composite yarns, a central undissolved yarn was seen to be surrounded by an outer ring of dissolved and

coagulated cellulose. From these optical images, two specific parameters were used to measure the increase in the fraction of this outer material. First, the area fraction of the dissolved and subsequently coagulated material, called the coagulation fraction (CF), was determined and then secondly, the growth in thickness of the outer coagulated layer (T_H). Both parameters have been examined at different processing temperatures and times. Firstly, the coagulated fraction's growth in the partially dissolved flax fibre within IL [C2mim][OAc] was shown to follow TTS, enabling the determination of the dissolution activation energy. Secondly, the growth of the outer coagulated ring's thickness of the coagulated material was investigated and it was found that the thickness grew with the square root of the processing time, indicating a dependence on some aspect of diffusion. The NMR studies given here will measure the self- diffusion coefficients of each ion of the IL at different temperatures to determine the diffusion activation energy and effective molecular size of each IL. Rheology measurements were also carried out to determine the pure ionic liquid's viscosity as a function of shear rate and temperature.

3.2 Experimental Methods and Materials

3.2.1 The procedure of dissolving the flax samples with [C2mim][OAc]

The dissolution process described in Section 2.3 is used throughout this chapter. It should be noted that this ionic liquid as received contains 0.2% of water as measured by Karl Fischer titration.

3.2.2 Optical Microscopy

Optical microscopy was used as detailed in Section 2.4. The dissolution progress of the flax yarn sample in the IL is determined using two different measurement parameters, the coagulation fraction (CF) and the thickness of the outer coagulated cellulose ring, called the ring thickness (T_H). The CF was obtained from OM by measuring the total area and coagulated cellulose area using Eq. 2.1. We used this approach to assess the applicability of our TTS analysis method. The results obtained from the TTS analysis allowed us to track the increase of the dissolved and coagulated fractions, as well as the absolute thickness of this outer layer, for each combination of time and temperature. A second set of observations were made from the optical images, by determining the difference in the diameters of the two regions.

This growth of the thickness of the dissolved and coagulated region has enabled us to calculate the IL's diffusion, as the thickness growth was found to depend on the square root of the processing time. The red double-arrow (T_H) indicates the average ring thickness of the flax samples, as shown in Figure 3.1, and was calculated after repeating the two diameter measurements four times from multiple directions for each sample via Eq. 3.1:

$$T_H = \frac{DT - DC}{2} \qquad (3.1)$$

Here DT is the outer ring diameter and DC the dimeter of the undissolved yarn fraction.

As there are four samples analysed for each time and temperature, this leads to a total of 16 measurements for each condition, giving an accurate calculation of the average thickness of the dissolved and coagulated layer. Then, we plot the average layer thickness against time (t) and then the root of the dissolution time (√t).

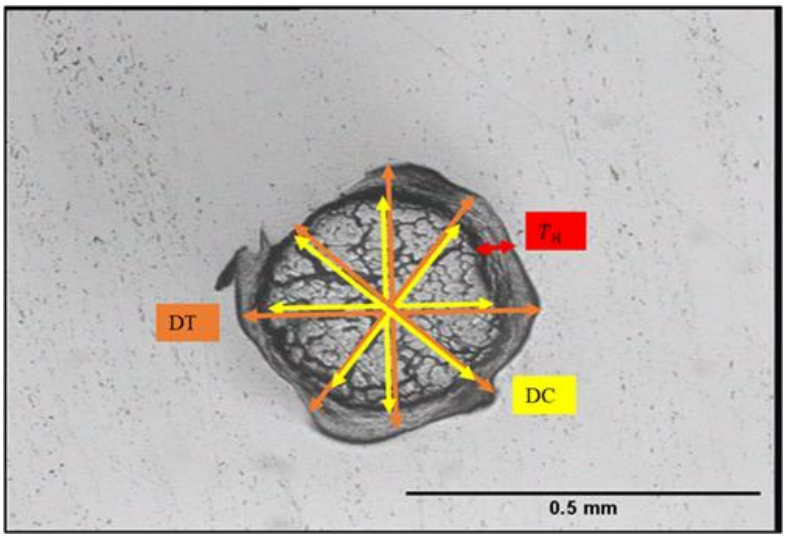

Figure 3.1: Optical microscopy images of the cross section of the flax yarn, in which the total sample, the undissolved section, and the outer ring are indicated in orange (DT), yellow (DC) and red ($\boldsymbol{T_H}$) double-arrow lines, respectively.

3.2.3 The growth of the dissolved and coagulated region for [C2mim][OAc]

We can further investigate the data presented in the Arrhenius plots at a particular chosen reference temperature to gain insights into the how the thickness of the outer coagulated area increases over time for dissolution in the IL. By analysing the (TTS) data it became clear that the growth rate of this region slowed down as time progressed. Additionally, a linear dependence is observed when the root of dissolution time ($\sqrt{t}$) is plotted against layer thickness. The results indicate that diffusion governs the growth of coagulated region. The observed linear correlation between thickness and the square root of time is a strong indicator that the process in these systems follows Fick's law for diffusion see Eq. 3.2.

$$r \sim < r^2>^{1/2} = (2D)^{1/2} * t^{1/2} \quad (3.2)$$

where r represents the root mean squares of the distances that particles have moved from their original position, diffusion time t, with self-diffusion coefficient D.

The average thickness was then plotted first against linear time and then against the root of the dissolution time ($\sqrt{t}$). Then, fitting it to a linear dependence, it is possible to determine the diffusion coefficient D from the slope of the line, which will be $(2D)^{1/2}$ according to the equation. Further, the gradient of the $\ln D$ vs $1000/T_{ref}$ is used to give the diffusion activation energy, and the gradient of this method gave an activation energy similar to gradient that exhibited by following the growth of the area of the coagulated fraction. Our hypothesis is that because the coagulated region grows as the square root of the dissolution time, then the controlling factor for dissolution is the diffusion of the IL through the outer region which comprises dissolved cellulose and IL.

3.2.4 Viscosity

The method and equipment described in Section 2.5 were used to measure the viscosity of the pure IL [C2mim][OAc].

3.2.5 NMR diffusion

The self-diffusion coefficients of the anion and cation in the pure IL were determined using the pulse sequences and equipment detailed in Section 2.7. The diffusion coefficient measurements of each ion were averaged over the relevant peaks for the cation $[C2mim]^+$ peaks (1-5, 7) and the anions $[OAc]^-$ (6), as determined by the spectral assignment of each peak, as shown in Figure 3.3. The cation proton resonances for each measurement were determined to have similar diffusion coefficients, which was to be expected since they were connected to the same ion. For the diffusion coefficient of cation, this means that only one average number will be used. Regarding the anion, its diffusion coefficient was determined based on the resonance of only one proton for [OAc]. ^{1}H spectra for the IL $[C2mim]^+[OAc]^-$ is shown in Figure 3.3. All NMR samples were measured at temperatures ranging from 30 °C to 60 °C.

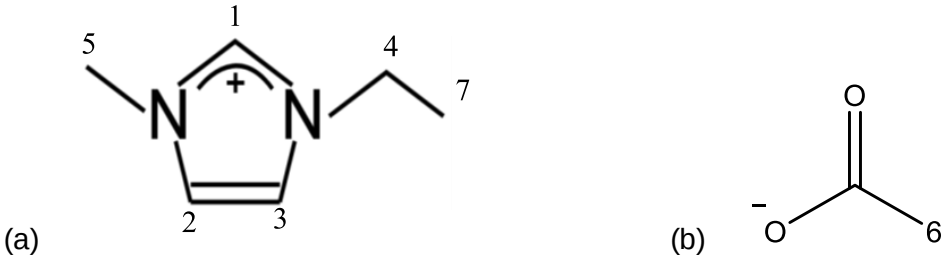

Figure 3.2: The ionic liquid investigated in this study: (a) [C2mim]+, and (b) [OAc]-. 1H NMR resonances are labelled for each cation-anion pair according to the spectral assignment and previous published by [110, 113].

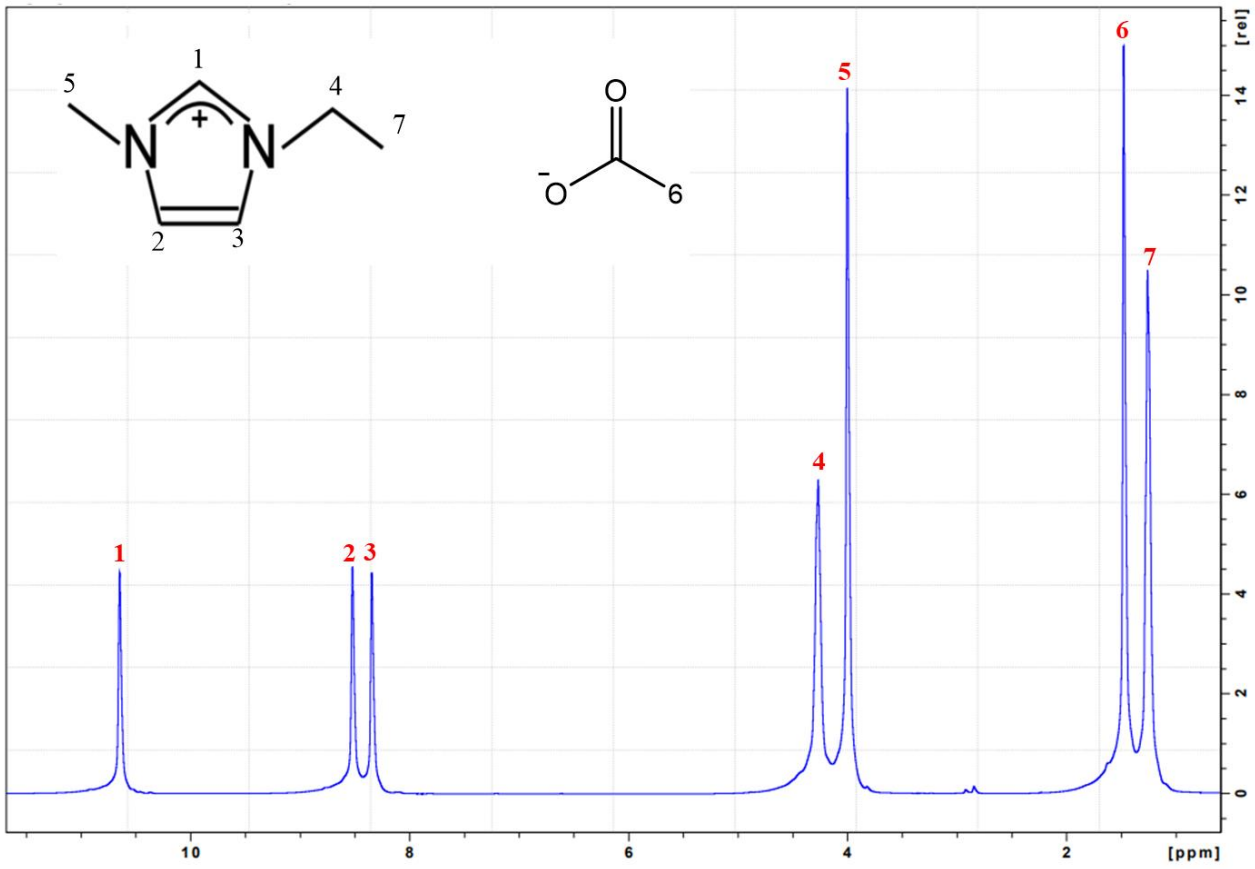

Figure 3.3: High field 1H NMR spectrum (400$\boldsymbol{MH_Z}$) of pure IL [C2mim][OAc] at 30 °C, with peak assignments given in red for protons labelled 1-7. The chemical structure is shown, and the inset includes corresponding labels.

3.3 Results and discussion

3.3.1 Optical data

A number of typical images representing raw yarns can be seen in Figure 3.4. Figures 3.5 and 3.6 show further higher magnification pictures of the internal structure of the raw flax yarns. Figure 3.7 is a representation of typical micrographs of both raw yarns and partially dissolved yarns that were processed at various times at 50 °C. These are very similar to a previous study in this group investigating the dissolution of flax yarns in the IL [C2mim][OAc] as manufactured by Sigma Aldrich [22]. As shown, a yarn is made up of various bundles which are tightly packed together with minimal internal free space. This appears to prevent the ionic liquid from penetrating the core, and so the dissolution proceeds from the outer edges inwards. The micrographs suggest that we can consider the partially dissolved composite yarns to be comprised of an inner undissolved core surrounded by a ring of dissolved and coagulated cellulose. The coagulation fraction (CF) is calculated by Eq. 2.1.

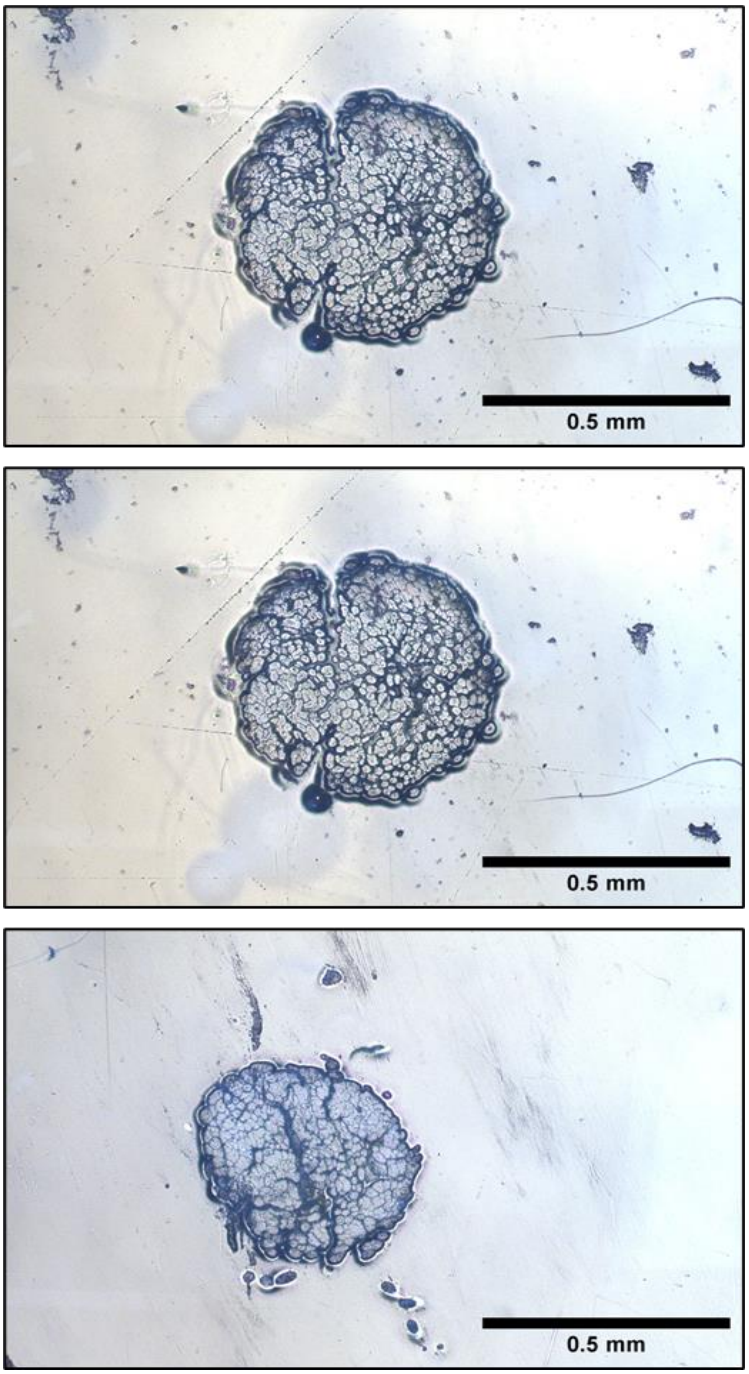

Figure 3.4: Microscopy cross- sectional images of multiple raw yarns embedded in an epoxy, observed at 10 times magnification. Scale length 0.5 mm.

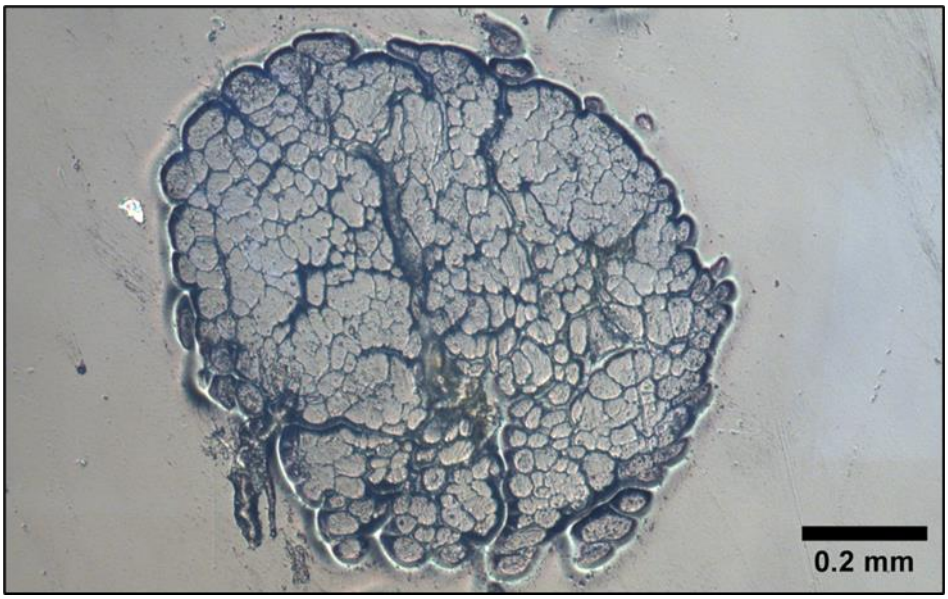

Figure 3.5: Cross sectional of a raw yarn at 20 times magnification.

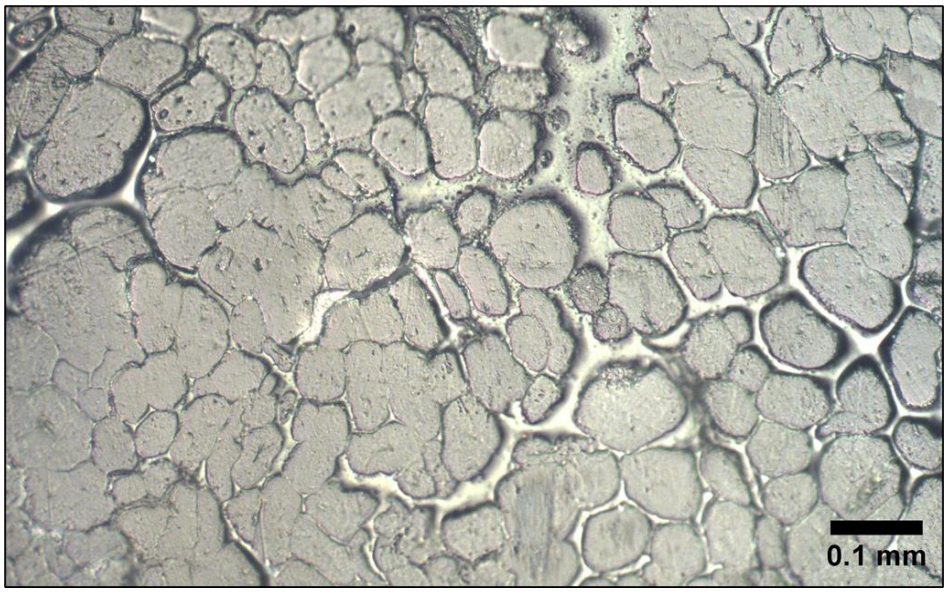

Figure 3.6: Cross sectional of a raw yarn at 50 times magnification.

The average raw flax yarn was calculated using the area determined via ImageJ software to be 0.442 ± 0.002 mm^2. Optical micrographs of typical partially dissolved fibres are shown in Figures 3.7 and 3.8. The CF's growth is illustrated in these figures as a function of temperature and time, and this growth in CF from 30 °C to 60 °C suggests that higher temperatures lead to larger size of coagulation material, due to the diffusion progressing at a higher rate. Figure 3.7 shows samples processed for 1 hour at temperatures of 30, 40, 50 and 60 °C while Figure 3.8 shows samples processed at 50 °C for times of 0.5, 1, 1.5 and 2 hours. It can be seen how the inner undissolved area is surrounded by an outer layer whose size depends on the processing time and that this increases as time increases. These outer layers are the result of cellulose that went through the dissolution and coagulation process. It can be seen that the size (and thickness) of the outer ring of coagulated material increases with both time and temperature.

To measure the boundaries between the inner core and partially dissolved area, as well as the partially dissolved area and the outer area, a software (Image J) was used to trace out each boundary by eye and the ratios between inner and outer boundaries were averaged across four repeat samples made at each set of processing conditions. The area enclosed within these boundaries is used to determine the coagulated fraction and the raw material.

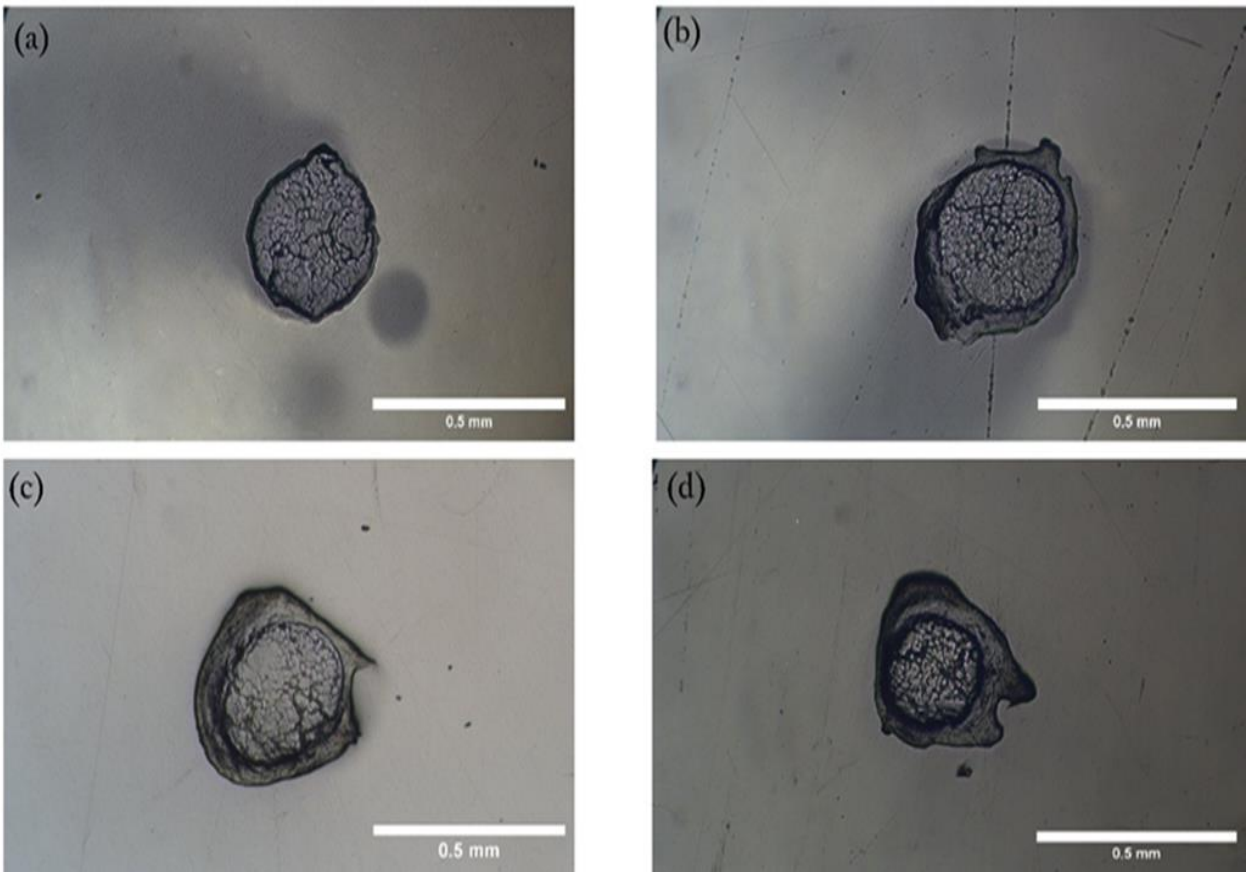

Figure 3.7: Microscopy cross sections of fibre after 1 hour at various temperatures; a) 30 °C, b) 40 °C, c) 50 °C and d) 60 °C. CF can be growing as a function of temperatures. Scale length 0.5 mm.

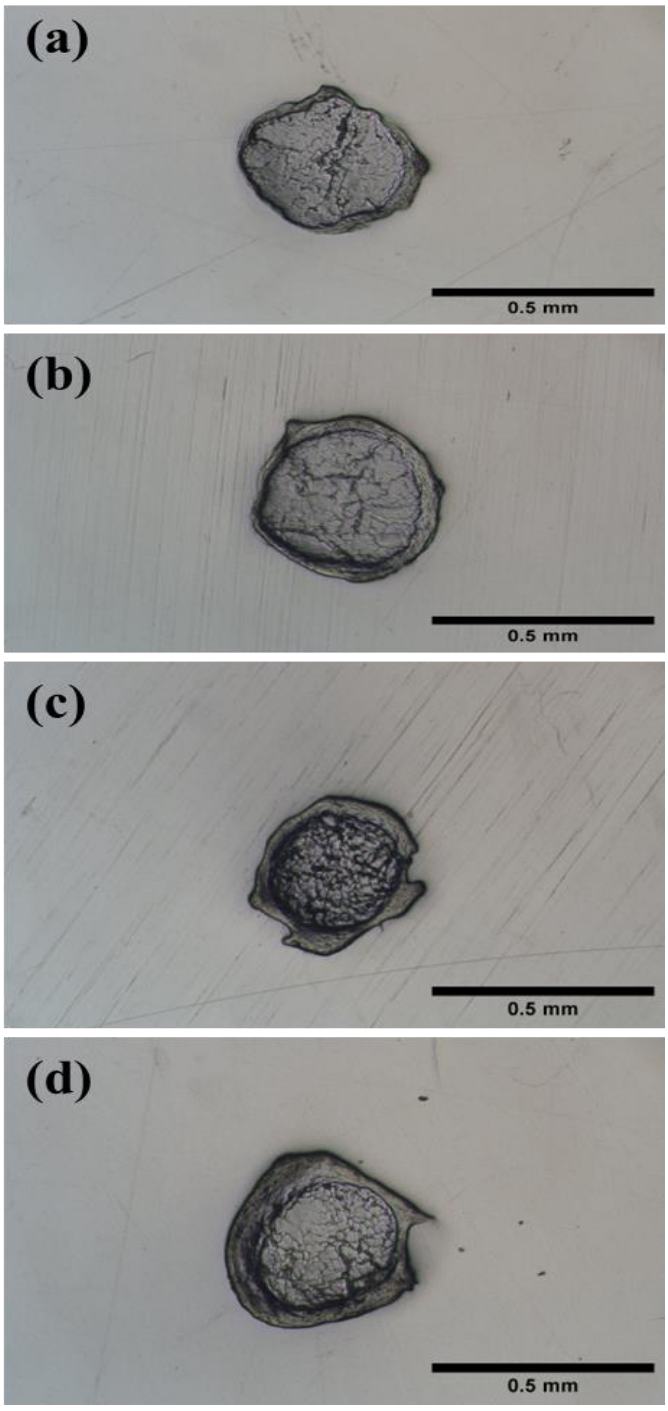

Figure 3.8: Microscopy images showing how the boundaries between raw and partially dissolved cellulose were determined. Yarns shown were dissolved at 50 °C for a) 0.5 h, b) 1h, c) 1.5 h and d) 2h. Scale length 0.5 mm.

3.3.2 Analysis of the dissolution of flax yarn in [C2mim][OAc] with TTS

In Figure 3.9 is shown the results of the growth of the coagulation fraction of the fibres processed at different temperatures and times. On this figure, the data represents the average value of the coagulation fraction taken from the four cross-sectional fibres processed under the same time and temperature, and the error bar is the standard error. The CF is seen to increase as a function of both processing time and the processing temperature.

In Figure 3.9 it can be seen that the CF grows with time at each processing temperature and grows faster as the processing temperature is increased. Figure 3.10 (a) shows the results for the four temperatures plotted together against linear time while Figure 3.10 (b) shows the same results plotted against logarithmic time (ln time). The results in Figure 3.10 (b) show a similar gradient in logarithmic time but appear to be shifted in time, suggesting (TTS) could be applied. The process used to form a master curve by TTS is to shift different temperature curves horizontally along the logarithmic time (ln time) x- axis in order to achieve the best overlap via eq. (3.3) and (3.4):

$$t' = t \times \alpha_T \tag{3.3}$$

Taking the natural log of both sides of the equation (3.3) yields the following:

$$\ln(t') = \ln(t) + \ln(\alpha_T) \tag{3.4}$$

where t' is the shifted dissolution time, t is the dissolution time and $\ln(\alpha_T)$ is the shift factor to move the data from temperature T to the reference temperature T_{ref}.

Figure 3.10 (c) shows schematically the creation of the master curve, by using the middle temperature, T_{ref}= 50 °C, as the reference set with therefore scaling factor α_{50}= 1. The 50 °C data was fitted with an exponential function used to guide the eye in order to provide the best shifting of further data sets, then each of the other data curves 30 °C, 40 °C and 60 °C was horizontally shifted separately along the x-axis (ln time) by a shift factor equal to $\ln(\alpha_T)$ towards the reference temperature to make them overlap, as shown by the arrows. After shifting of the data sets, the master curve is formed (at 50 °C), as shown in Figure 3.10 (d). The temperature dependent shift factors $ln\alpha_T$ used to form Arrhenius plot of different temperatures at $T_{ref.50℃}$ are summarised in Table 3.1 and also plotted in Figure. 3.10 (e). These shift factors describe the dissolution rate of the process at the reference temperature. When the

value of the ln$\boldsymbol{\alpha_T}$ is greater than zero, the dissolution rate is faster than at the reference temperature 50 °C; as a result, data require to be shifted to the right in ln time to insure overlap. Conversely, a negative value of the lnα_T shows the dissolution rate is slower, and therefore data require to shift to the left in ln time to overlap with the reference.

This exponential master curve shows superimposed data set with R^2 > 0.98, the R^2 value was maximized via adjusting the shift factors at the other temperatures (α_{30}, $\alpha_{40}$and α_{60}) to provide the best fit between the shifted points and the exponential fitted.

We can now plot the four shift factors $\ln(\alpha_T)$ for the data against the inverse of temperature (T^{-1}), as shown in Figure 3.10 (e). The linear nature of these data indicates that the dissolution process follows Arrhenius behaviour. The activation energy (E_a) in the equation below describes the energy barrier required for the dissolution of flax fibres in [C2mim] [OAc] that needs to be overcome for dissolution to occur. The dissolution activation energy of the flax fibre in [C2mim] [OAc] was calculated, using the slope shown in Figure 3.10 (e), to be 64 ± 5 kJ/mol. The uncertainty comes from the uncertainty from the linear regression fitting and is found using (LINEST in EXCEL).

$$\alpha_T = \alpha_0 \, e^{\frac{-E_a}{RT}} \tag{3.5}$$

$$\ln(\alpha_T) = \left(\frac{-E_a}{RT}\right) + \ln\alpha_0 \tag{3.6}$$

where α_T is the scaling factor, E_a is the Arrhenius activation energy, R is the gas constant, T is the temperature in Kelvin and is α_0 the pre-exponential factor.

The Arrhenius equation is frequently used throughout this work. This expression relates to the rate of a reaction to the temperature at which the reaction is occurring, and the rate of reaction typically increases as the temperature increases. This is because higher temperatures provide the reactant molecules with more kinetic energy, increasing the chances that collisions between molecules will have enough energy to overcome the activation energy barrier, leading to a successful reaction, as detailed in chapter 1.

Using the Arrhenius equation with the TTS principle enables predicting how a system will act over time at different temperatures by looking at how reaction rates change

with temperature. The shift factor $\ln(\alpha_T)$ is employed to build a correlation between the response of a system at a reference temperature (T_{ref}) and its response at a different temperature (T). The scale factor (α_T) can be calculated from the temperature dependence of the rate constant, which show the relationship between (α_T) and the Arrhenius equation. It can be used to create a master curve that predicts the system's behaviour under different conditions of dissolution time and temperature. So, we can then finally plot the dissolution master curve at any particular temperature (e.g. 50°C) against linear time which then describes how the dissolution rate is initially fast and then slows down as time progresses, as shown in Fig. 3.11.

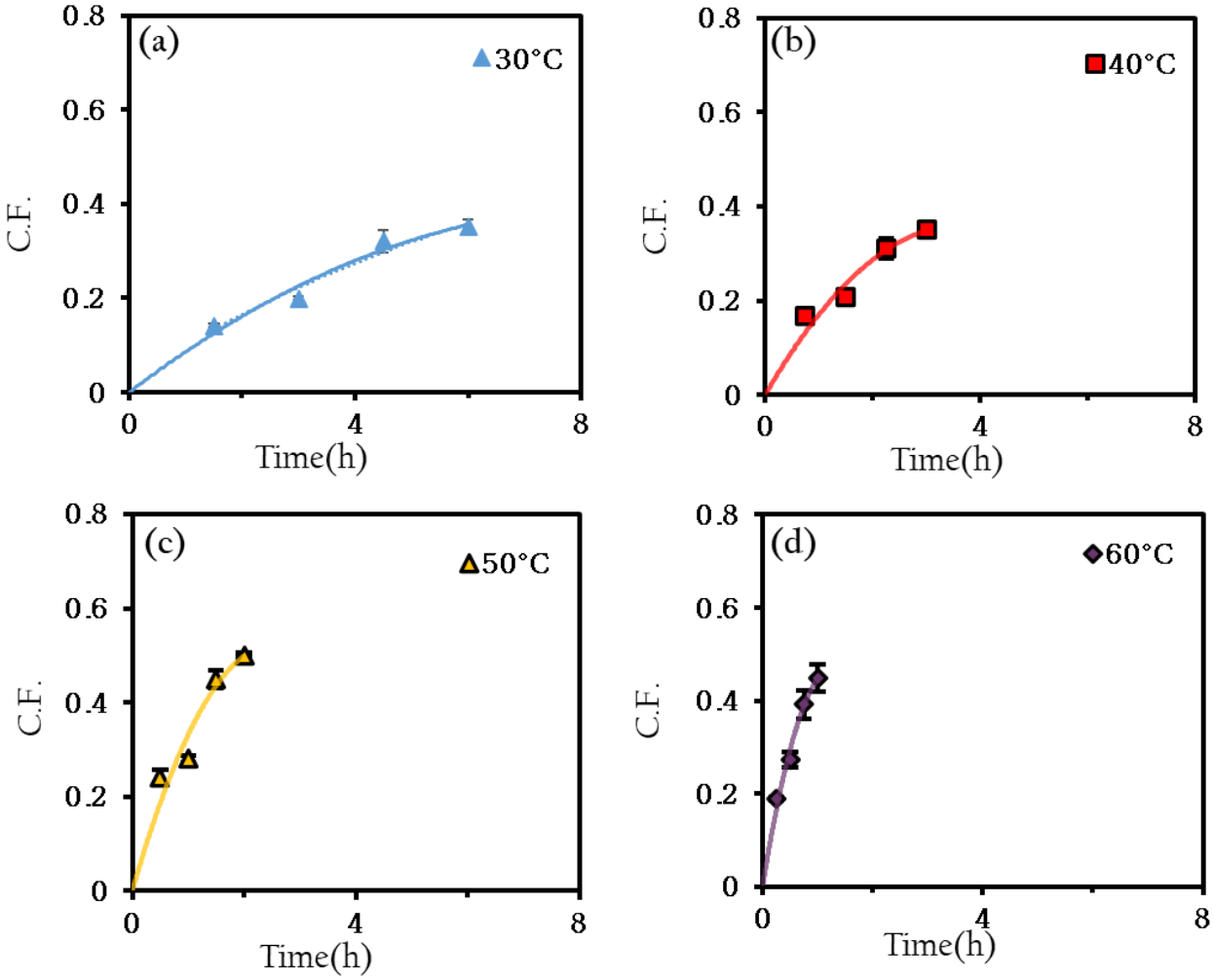

Figure 3.9: Coagulated fraction as a function of dissolution time at different temperatures. Polynomial function is used in order to guide the eye and error bars included.

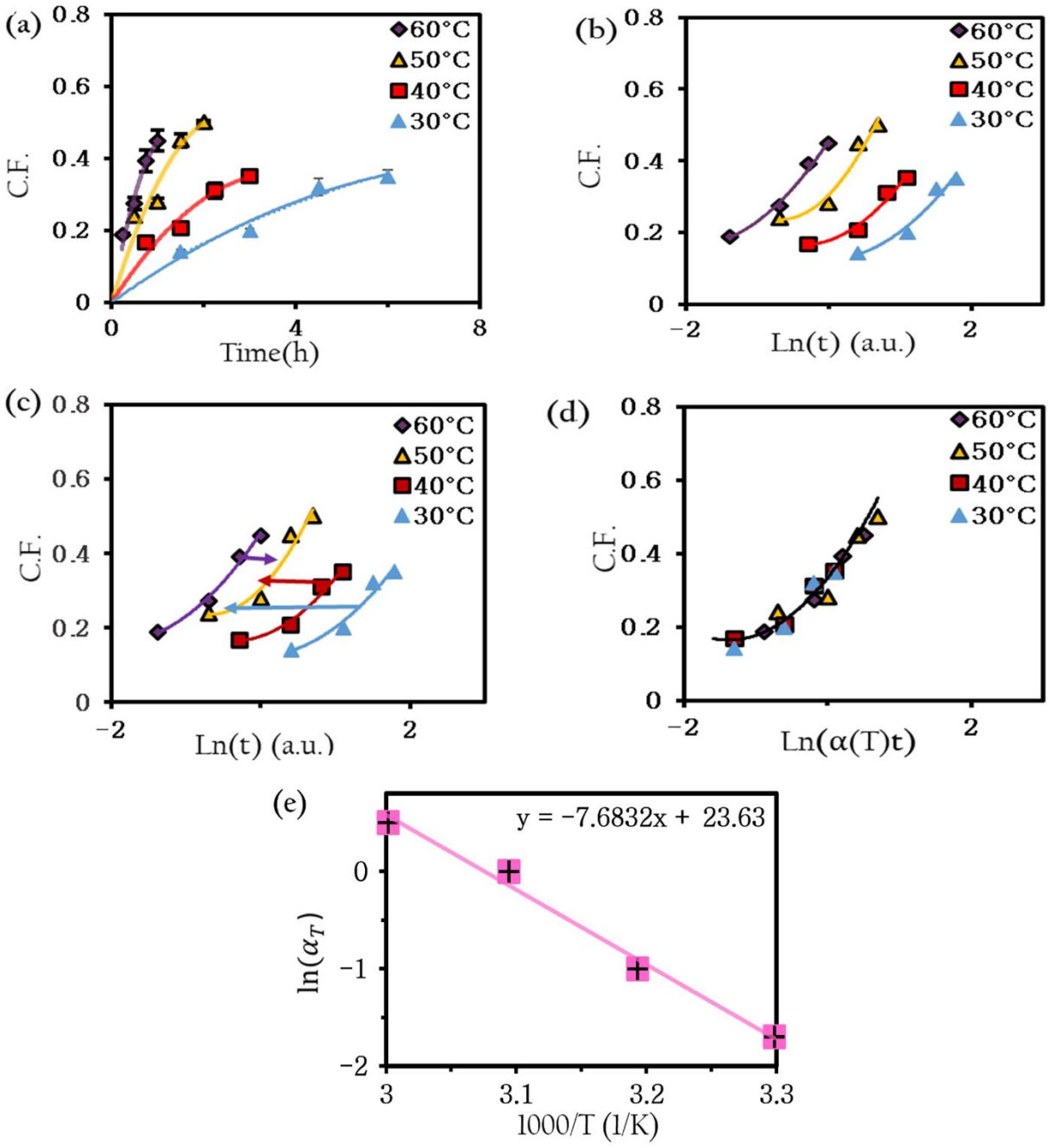

Figure: 3.10: (a) CF as a function of both dissolution time and temperature. (b) CF at various times and temperatures expressed in $\mathbf{ln}(\boldsymbol{time})$. (c) The shifting process, by moving the 30 °C, 40 °C and 60 °C data towards the 50 °C data. (d) The final master curve shows the effect of dissolution time and temperature on the coagulation fraction. (e) The linear nature of the data showing shift factors $\mathbf{ln}(\boldsymbol{\alpha_T})$ as a function of temperature, an Arrhenius plot and error bars included.

Temperature T (°C)	$\ln\alpha_T$	Regression Coefficient R^2
30	-1.7	
40	-1	0.98
50	0	
60	0.5	

Table 3.1: Shift factors obtained from TTS analysis of different temperatures at reference temperature (T_{ref}) of 50 °C , used to plot Fig. 3.10 (d).

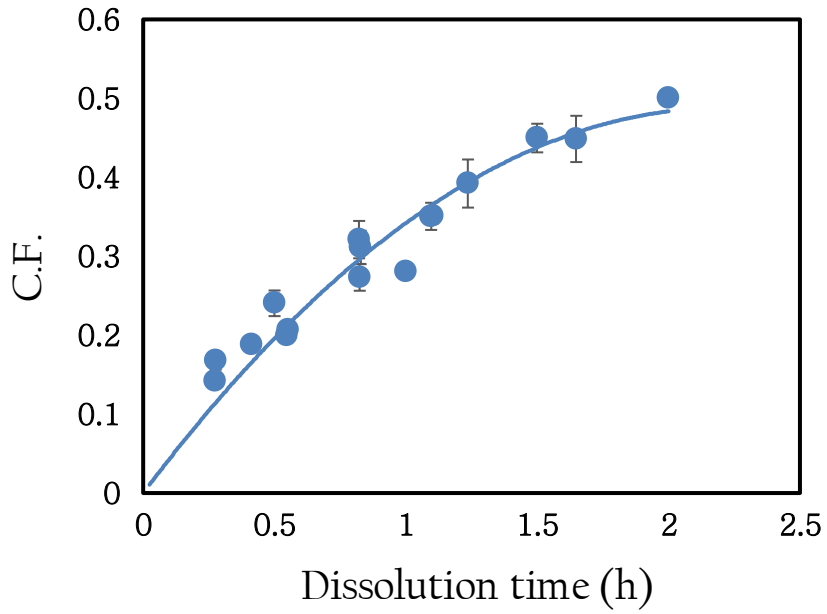

Figure 3.11: CF master curve against linear time at a reference temperature of 50 °C showing the dissolution process, and the line is a polynomial of order two fit to the data.

3.3.3 Intercept analysis (ln α_0)

The intercept method uses the other parameter from the Arrhenius plots of the shift factors versus inverse temperature, namely the intercept $\ln \alpha_0$ from Eq. 3.6. The process used to obtain the intercept from the Arrhenius plot curve was described in detail for a reference temperature of 50 °C. Fig. 3.10 (e) showed that this gave a gradient of -7.6832x and an intercept of 23.63.

If all of the above analysis is carried out again three times, now using the other three temperatures as reference temperatures (T_{ref}), so shifting all data to 30 °C and 40 °C and finally 60 °C in order to create a master curve for each set of data at each of these temperatures. The shift factors, from 30 °C, 40 °C and 60 °C TTS shifting, can be plotted separately as a function of reference temperature as before for the 50 °C TTS shifting results. Each set of shift factors for each of the reference temperatures is again found to display an Arrhenius behaviour, each giving a dissolution activation energy, see Fig.3.12 (a-c). These plotted graphs give similar gradients, leading to similar E_a as calculated from 50 °C (64 ± 5 kJ/mol). The important result is that intercept $\ln \alpha_0$ in each of these graphs is itself temperature dependent $\ln \alpha_{30}$, $\ln \alpha_{40}$, and $\ln \alpha_{60}$. The shift factors $ln\alpha_T$ used to form these three Arrhenius plots of each temperature in the process as a reference temperature are summarised in Table 3.2.

The intercepts are 25.33, 24.63, and 23.13 for 30 °C Fig.3.12 (a), 40 °C Fig.3.12 (b), and 60 °C Fig.3.12 (c), respectively. These intercepts can then be checked to further verify the Arrhenius behaviour, as follows.

Firstly, we set the temperature T as the reference temperature T_{ref}, in Arrhenius Eq. (3.6), this then gives,

$$\ln(\alpha_{T_{ref}}) = \left(\frac{-\mathrm{E_a}}{\mathrm{R}T_{ref}}\right) + \ln \alpha_0 \qquad (3.7)$$

The shift factor at the reference temperature has to equal zero $\ln(\alpha_{T_{ref}})$= 0, since the reference temperature data itself needs no shifting $\alpha_{T_{ref}}$=1. Next, by substituting the value of $\ln(\alpha_{T_{ref}})$= 0 in eq.3.7, rearranging Eq. (3.7) to be Eq. (3.8),

$$0 = \left(\frac{-\mathrm{E_a}}{\mathrm{R}T_{ref}}\right) + \ln \alpha_0 \qquad (3.8)$$

$$\ln \alpha_0 = \left(\frac{\mathrm{E_a}}{\mathrm{R}T_{ref}}\right) \qquad (3.9)$$

This expression above shows that the intercepts $\ln \alpha_0$ determined at each reference temperature themselves will follow an Arrhenius law, being directly linearly dependent on the inverse of the reference temperature. The gradient of the $\ln \alpha_0$ vs 1000/T_{ref} is predicted to give the activation energy, and this is a further confirmation that the system is exhibiting Arrhenius behaviour, see Fig.3.8 (d). In our work we have found that this analysis is very sensitive to any curvature or non-Arrhenius behaviour.

This 'intercept' method was applied as another method to determine the activation energy and was then compared with the activation energy for each master curve. The gradient of the line in Fig.3.12 (d) shows a very similar gradient as the Arrhenius plots in Fig.3.10 (e) and Fig.3.12 (a-c) and hence gave a fifth value for the activation energy of 64 ± 5 kJ/mol, very consistent with our previous determined values.

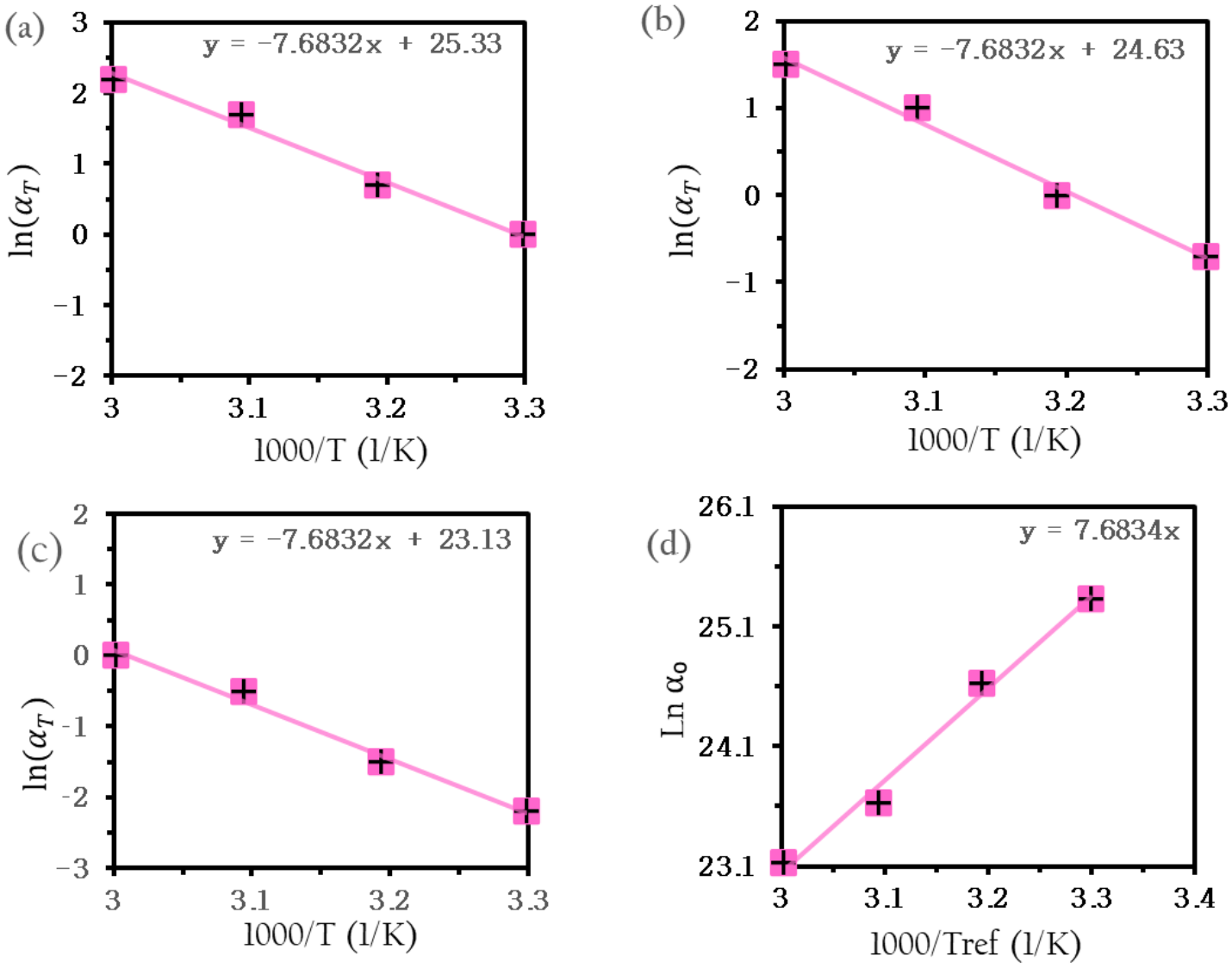

Figure 3.12: Shift factors $\ln(\alpha_{T_{ref}})$ as a function of inverse temperature, indicating Arrhenius plot. Reference temperatures of (a) 30 °C, (b) 40 °C, (c) 60 °C and (d) Plot of the Ln α_0 of the four intercepts vs the inverse of the reference temperature α_0. Intercept process, showing shifting to all temperatures indicating Arrhenius dependence, and error bars included.

Temperature T (°C)	lnα_T	Regression Coefficient R^2
30	0	0.98
40	0.7	
50	1.7	
60	2.2	
30	-0.7	0.98
40	0	
50	1	
60	1.5	
30	-2.2	0.98
40	-1.5	
50	-0.5	
60	0	

Table 3.2: The fitting results for flax yarns dissolution in IL [C4mim][OAc] at $T_{30℃}$, $T_{40℃}$, and $T_{60℃}$ used to plot Figure 3.12 (a-c).

A number of other studies have shown that the dissolution process follows an Arrhenius behaviour. Dissolution activation energies of cotton in [C2mim][OAc] of 96 ± 8 kJ/mol was reported by Liang et al. (2021) [228]. Xin Zhang et al. (2021) reported that the activation energy needed to dissolve silk via [C2mim][OAc] as 138 ± 13 kJ/mol [229]. The dissolution rate of cellulose yarns was in a linear relation with the viscosity of [C2mim][OAc] when both are expressed in natural logarithmic form indicated that the dissolution process is found to follow Arrhenius behaviour [18]. The kinetics of cellulose dissolution in ILs have been reported to be dependent on the IL used and the concentration of cellulose [171, 230, 231]. These studies found that the rheological activation energy to be from 46 kJ/mol to approximately 70 kJ/mol. Villar et al. (2023) reported that the activation energy needed to dissolve lyocell yarn via [C2mim][OAc] is 46.8 kJ/mol, this result was reduced by 70% when DMSO was added [232].

3.3.4 The growth of the dissolved and coagulated region for [C2mim][OAc]

Further analysis was conducted on the optical micrographs, using the same technique as described above for the TTS for the dissolution of flax yarn in the IL [C2mim][OAc], but this time measuring the difference in the diameters of the two regions and hence the thickness growth with time. The same technique was used as described above for following the coagulation fraction, by constructing master curves at each temperature (30 °C- 60 °C). Figures 3.13 (a-c) show an example of this procedure for a reference temperature of 50 °C. First the thickness results were plotted on a single graph against linear time, as shown in Figure 3.13 (a). Then, the thickness measurements were plotted against logarithmic time Ln (time) and then shifted with time to form a master curve using the temperature of 50 °C as a reference temperature, so all the data points fit into a new exponential function as shown in Figure 3.13 (b). After that, a relationship set between the thickness values and their real dissolution time showing the dissolution rate is relatively fast in the initial period, and then slows down gradually with increase in time, as shown in Figure 3.13 (c). A linear relationship between the ln (α_T) against the inverse of all temperatures, thus, an activation energy calculated, as shown in Figure 3.13 (d). The same results were found for the other three temperatures of 30 °C, 40 °C, and 60 °C after applying the TTS shifting process separately. The slope from this process is similar to the slope from the dissolution process of the curve in Figure 3.10 (e) and R^2. The value of the activation energy was found to be a 64 ± 5 kJ/mol, identical to that found from following the growth of the coagulation fraction.

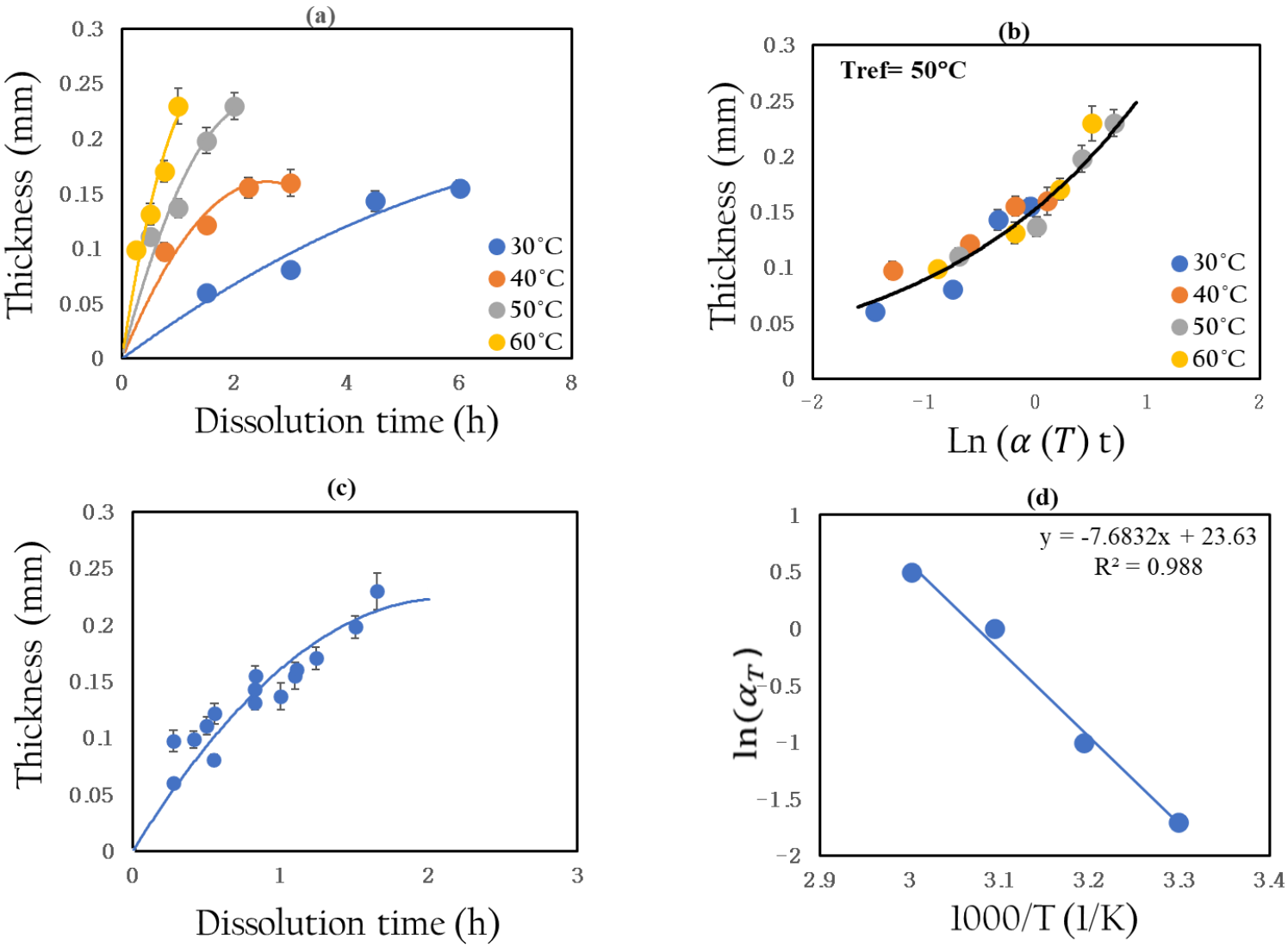

Figure 3.13: (a) The thickness values of the dissolved outer ring as a function of dissolution time and temperature. (b) A master curve of thickness as a function of shifted time at various temperatures by using 50 °C, as a reference temperature. (c) The thickness as a function of real dissolution time. (d) The ln($\boldsymbol{\alpha_T}$) as a function of inverse temperature and resulting an activation energy and error bars included.

It is seen that Figure 3.13 (c) shows a non-linear relationship with the thickness growth slowing down as time increases. Figure 3.14 presents an alternative way to present data, by plotting the thickness against the square root of time for the four reference temperatures. It is seen that there is linear relationship between the growth of the thickness and the square root of time, indicating importantly, that the dissolution could be diffusion controlled. Our hypothesis is that this could be due to the diffusion of the IL ions through a mixture of IL and dissolved cellulose around each fibre, rather than the interaction of the IL with the undissolved fibre surfaces. Furthermore, the slope of each master curve used to calculate the self-diffusion coefficients by an Arrhenius equation was used to model the temperature dependence of the self-diffusion coefficient of the ions D,

$$\ln D = ln\ D_0\ e^{(\frac{-E_{A,D}}{RT})} \qquad (3.10)$$

where $E_{A,D}$ is the activation energy of diffusion for the ions, T is the temperature, R is the gas constant, and D_0 is represented the pre-exponential factor.

The gradient of each straight line gives the value of self-diffusion coefficient of the IL [C2mim][OAc] $(6.2 \pm 0.3) \times 10^{-13}\ m^2/s$, $(1.2 \pm 0.1) \times 10^{-12}\ m^2/s$, $(3.4 \pm 0.1) \times 10^{-12}\ m^2/s$, and $(5.6 \pm 0.2) \times 10^{-12}\ m^2/s$ at reference temperature of 30 °C, 40 °C, 50 °C and 60 °C, respectively. The linear fit to the data with a high coefficient of determination R^2= 0.98 indicates a very good correlation between the thickness and the square root of time at each reference temperature. Interestingly, measuring the diffusion from the growth of the thickness of this outer coagulated layer by optical microscopy is explored for the first time in our group by [233].

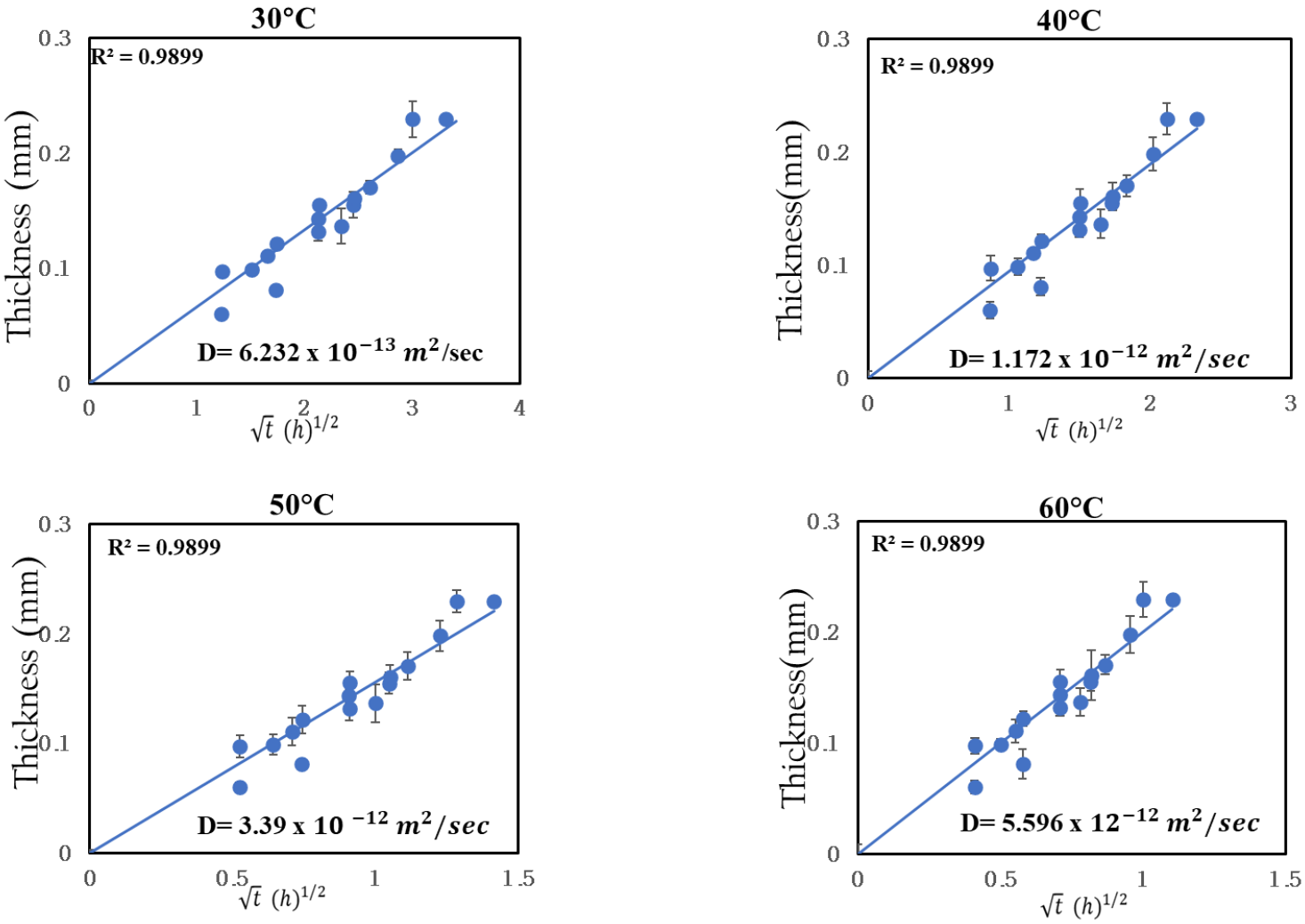

Figure 3.14: Plots of the thickness vs. the square root of time for IL[C2mim][OAc] at 30 °C, 40 °C, 50 °C, and 60 °C and error bars included.

The diffusion activation energy from the thickness measurements for IL [C2mim][OAc] was evaluated by using the D values for each temperature as shown in Figure 4.14. These linear fits indicate that the system follows Arrhenius behaviour. Then Eq. 3.10 was used to calculate the diffusion activation energy for the IL. Interestingly, the value of the diffusion activation energy of 64 ± 6 kJ/mol determined from Figure 3.15 was found to be very similar to that of the dissolution activation energy that calculated earlier from the investigation of the coagulated fraction.

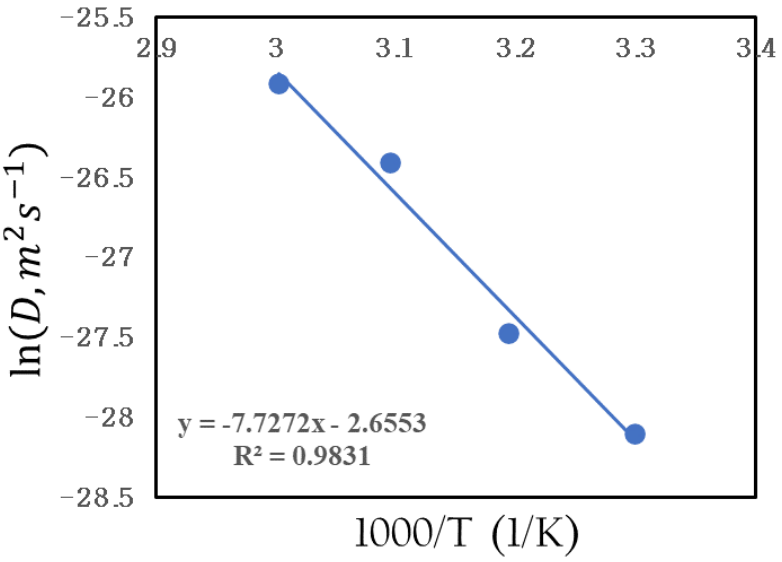

Figure 3.15: Natural logarithm of diffusion as a function of inverse temperature of flax fibre, indicating Arrhenius plot of [C2mim][OAc].

Numerous investigations have been conducted using the Fick method to quantify and understand the dynamics of the process across various conditions [233-238]. The kinetics of cellulose regeneration from cellulose-NMMO-water solutions and cellulose-NaOH-water solutions were found to follow Fick's law when applied to NaOH and NMMO in time t as a function of $\sqrt{t}$, so the experimental data were fitted with a straight-line approximation, suggesting the presence of a diffusion-controlled mechanism [236, 237]. Another study evaluated the relative thickness as a function of square root of time to measure the diffusion coefficients, as far as the thickness is one of the main parameters in Fick equation. Thus, the study was performed in order to understand time dependence of the dimensions of regenerating cellulose–NaOH–water gel in the acid bath [238]. The same procedure was applied for EmimAc and BMIMCl for 5% cellulose solutions at various temperatures to measure the diffusion coefficients [234]. The activation energy was determined by analysing the relationship between temperature and the diffusion coefficients of EMIMAc and BMIMCl. The determined activation energy was found to be in the range of 15-20 kJ/mol, which is similar to the activation energies measured for the diffusion coefficients of NaOH and NMMO at this concentration of cellulose [234]. Recently, the same method was applied for IL [C2mim][OAc] at various temperatures to measure the self- diffusion coefficient. For hemp yarn, the self- diffusion coefficient activation energy was found to be 69 ± 2 kJ/mol [233]. For wool yarn, the rate-limiting

factors in the two competing dissolution processes appear to differ by temperature: at low temperatures, disulfide bonds dominate, while at high temperatures, hydrogen bonds are more influential. Additionally, the diffusion activation energies were found to be 127 ± 8 kJ/mol in the low-temperature regime and 34 ± 1 kJ/mol in the high-temperature regime [235].

3.3.5 Viscosity

Viscosity - shear rate dependence for pure [C2mim][OAc] at temperatures ranging from (30 °C to 80 °C) was measured. Figure 3.16 shows the viscosity of the IL [C2mim][OAc] as a function of shear rate, indicating a Newtonian flow over the chosen range of shear rates. The average value of viscosity calculated from the Newtonian shear rate of each temperature was calculated by repeating the measurements three times in order to calculate an average and a standard error.

As expected, the IL viscosity decreased as the temperature increased. This tendency is explained by the fact that when temperature is increased the molecules with more thermal energy can overcome the intermolecular force to move more easily, reducing viscosity [239, 240]. Data of viscosities are in good agreement with the published data in [23, 113, 241, 242]. Viscosity values from experiments are summarised in Table 3.4.

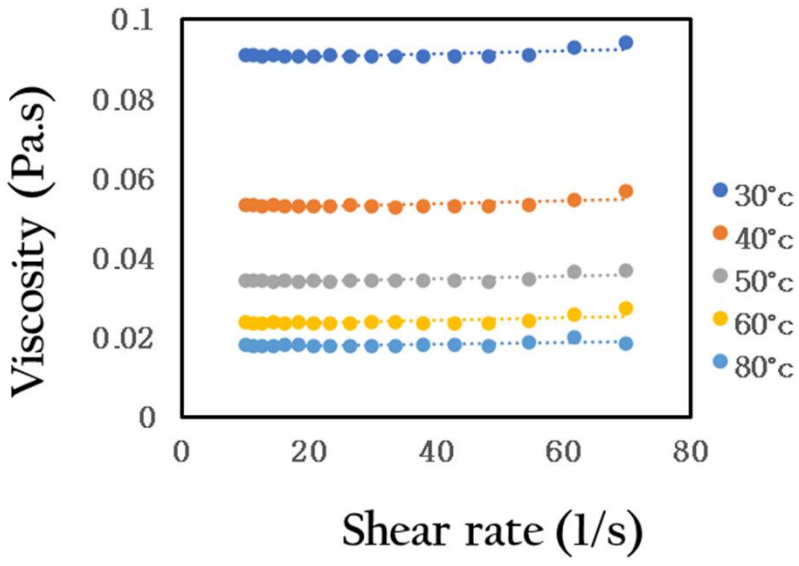

Figure 3.16: Viscosity as a function of shear rate at temperatures of 30, 40, 50, 60 and 80 ˚C for pure IL [C2mim][OAc].

T (°C)	η (Pa.s)	Error in η
30	0.090	0.030
40	0.053	0.040
50	0.034	0.025
60	0.023	0.031
80	0.011	0.027

Table 3.4: The zero shear rate viscosity measurements of pure IL [C2mim][OAc].

The activation energy for viscous flow was measured from the obtained value of viscosity at each temperature once again plotted against the inverse temperature. The activation energy was found by using the slope of this Arrhenius plot for the viscosity data. The plot of ln (η) inverse temperature is linear in the range of temperatures studied, as seen in Figure 3.17. The corresponding $E_{a,\eta}$ value was found to be 37 $\pm$ 2 kJ/mol. Very interestingly, this is lower than the value found from the above studies on the growth of the coagulated fraction and the growth of the thickness of the coagulated layer. In addition, the obtained $E_{a,\eta}$ value of 37 $\pm$ 2 kJ/mol, is slightly lower than the activation energy 40 ± 1 kJ/mol reported by Green et al. 2017 [113].

Our hypothesis for the difference in these two activation energies is that the viscosity measurements are for the pure IL, whereas the thickness measurements are controlled by the diffusion of the IL ions in a mixture of IL and dissolved cellulose that surrounds each partially dissolved flax fibre.

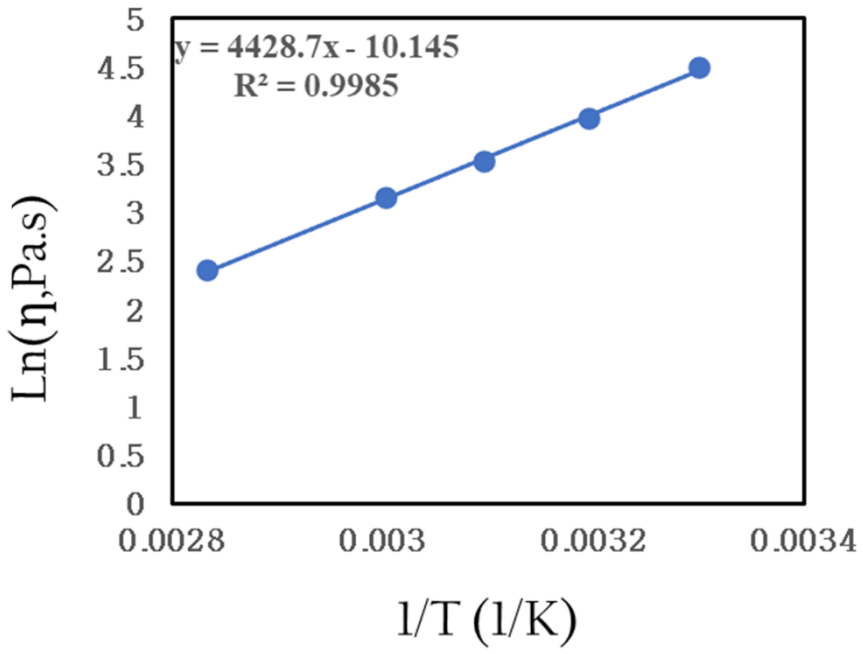

Figure 3.17: Shows ln (η) viscosity verses inverse temperature.

3.3.6 Self- diffusion coefficient (NMR)

It can be observed how the self-diffusion coefficient of the anion and cation of pure IL [C2mim][OAc] changes with temperature (30 °C, 40 °C, 50 °C and 60 °C) using ^{1}H NMR spectroscopy. This method allows the molecular mobility of the ionic liquid to be studied, offering insights into its dynamic behaviour. Importantly, each ion (cation and anion) can be studied separately. The spectrum with full peak assignments, which correspond to the various proton environments (H1–H7) was shown above in Figure 3.3. In our work, we used the N-methyl proton resonance (peak 5) as a reference point to determine the chemical shift of all the other resonances by measuring their distances from this peak. Previous studies have demonstrated that the chemical shift position of the methyl group (peak 5) is least affected [243] by external factors. The self-diffusion coefficients of [C2mim][OAc] generally increase with temperature in the range of 30 to 60 °C. The reason for this behaviour is the increased thermal motion of the ions, which decreases the viscosity of the ionic liquid and allows for more movement of the ions.

The resulting self-diffusion coefficients, D, as a function of temperatures ranging from 30 °C to 60 °C were studied for both ions [C2mim]+ and [OAc]- are presented in Table 3.5. Again, it is interesting to see that this value agrees well with the value determined from the viscosity measurements, and lower than that from the coagulated region studies. These NMR diffusion coefficients calculated at different temperatures also provide information on the diffusion mechanism. The results of self-diffusion coefficients as a function of temperatures in Table 3.5 show that both ions are increased in diffusion coefficient with increasing temperature. However, the facts may be obtained by comparing the cation and anion diffusion coefficients at each temperature. The cation [C2mim]+ has a higher diffusion coefficient than the anion [OAc]- at all temperatures. The data are consistent with previously reported diffusion coefficients for [C2mim][AOc] [110, 181, 223]. The temperature dependence of diffusion coefficients can be described with an Arrhenius analysis. Figure 3.18 shows the natural logarithm of self-diffusion coefficient inverse their temperatures of [C2mim]+, cation and [OAc]-, anion is plotted following Arrhenius equation, see Eq. 3.10. The diffusion activation energies, E_a, for each ion [C2mim]+ and [OAc]- are given in Table 3.6. The value of activation energies for self-diffusion for both ions are agreement with published data (refer to Table 3.6).

T (°C)	**diffusion coefficient (10^{-11} m2/s)**	
	$[C2mim]^+$	**$[OAc]^-$**
30	1.65	1.37
40	2.64	2.18
50	4.27	3.66
60	7.49	6.42

Table 3.5: NMR self-Diffusion Coefficients of $[C2mim]^+$ and $[OAc]^-$ as a function of temperatures.

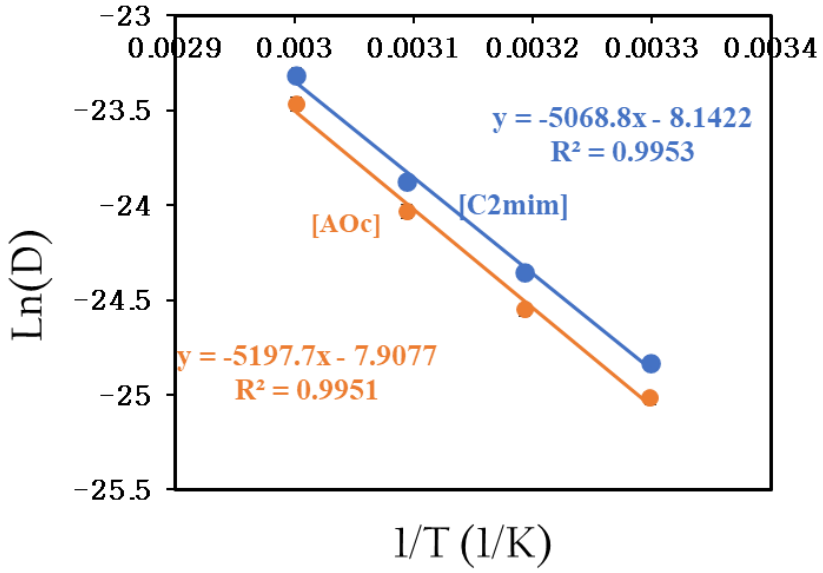

Figure 3.18: Arrhenius plots of the self-diffusion coefficient for the anion and cation of the IL as a function of the inverse temperature. Uncertainty in ln(D) of 4% is approximately the size of point.

Activation Energy, kJ/mol	**Experiment**	**Literature review**	**References**
$E_{a,D}(cation)$	42 ± 2	40.6	[113]
$E_{a,D}(anion)$	43 ± 2	41.5	

Table 3.6: Self-diffusion activation energy for the ions [C2mim]+ and [OAc]- obtained from experiment and compared with previous publication.

3.3.7 Stokes-Einstein Analysis

The relationship between viscosity and diffusion is crucial in studying the dynamics of fluids. It has long been a goal to quantitatively understand this connection as it helps explain how molecules move, and transport momentum collectively is related to the hydrodynamic size. By exploring diffusion in solutions, we can gain insights into various physical properties such, as molecular size, shape, aggregation, and hydrogen bonding. The Stokes-Einstein relation states:

$$D = \frac{k_B T}{6f\pi\eta R_{h,i}} \tag{3.11}$$

where k_B is the Boltzmann constant, $R_{h,i}$ is the hydrodynamic radius. The value of "f" is a correction factor [244].

The Stokes-Einstein relationship can be modified by introducing a correction factor f (recall to Eq. 3.11). The factor f is unity in classical Stokes- Einstein; however, it can be modified from unity under certain conditions. The deviation can be attributed to four conditions: 1) size of the diffusing molecule in comparison to the mixture, which leads to a decreased f. 2) The diffusing molecule is small compared to the mixture, which again reduce f. 3) The interaction between diffusing molecules and their surroundings, such as through hydrogen bonding, leads to a rise in f. 4) The creation of aggregates results in an enhanced effective hydrodynamic radius of diffusing molecules, which therefore leads to a rise in f [181]. The correction factor f in this study depends on the specific circumstances of the diffusion process, which is the size of the diffusing molecule is similar size to the mixture, which reduce f. Various studies have shown that a pre-factor of f=2/3 is suitable for a variety of molecular liquids [113, 181, 245, 246], so this value has been applied to the Stokes−Einstein analysis in this study.

The plot of D against T/η for all species in [C2mim][OAc] is presented. It was found that, the plots of D against T/η showed linear relationships, as given in Figure 3.19. The linear correlation in the experimental data demonstrates that the Stokes-Einstein equation provides a suitable description of the relationship between D and T/η for the system of [C2mim][OAc]. The gradients from the Stokes-Einstein fitting are used to calculate the values of $R_{h,i}$, refer to Eq. 3.11. The values of the $R_{h,i}$ are 2.19 Å and 2.57 Å, for the cation and anion of [C2mim][OAc], respectively.

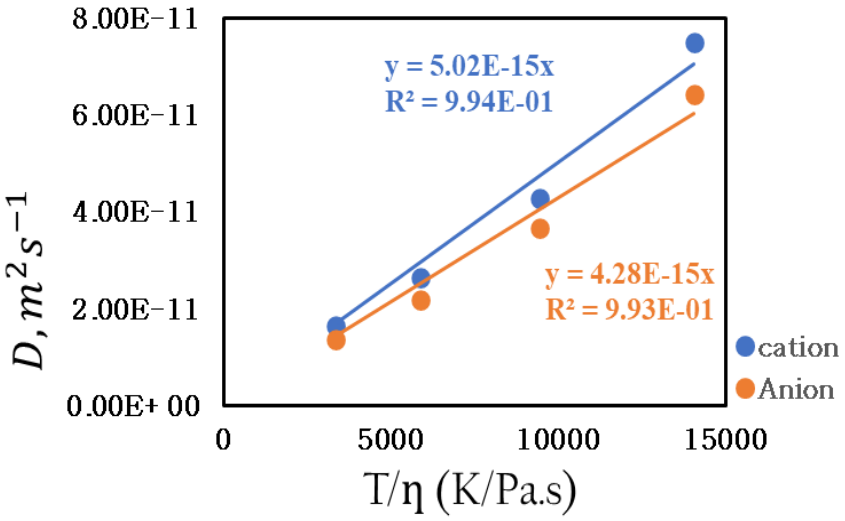

Figure 3.19: Correlation between D and T/η for the cation and anion in the IL [C2mim][OAc]. The solid lines are fits to the Stokes-Einstein equation calculated from Eq. 3.11.

The hydrodynamic radius, $R_{h,i}$, can be related to the molar mass of the liquids by the approximation:

$$R_{h,i} = \frac{1}{2}\left(\frac{M}{\rho N_A}\right)^{1/3} \qquad (3.12)$$

where N_A is the Avogadro number; M the molar mass of the liquid; and ρ the density.

The hydrodynamic radius depends on the size and it is important to note that the size of the diffuser, not its mass, is what matters for diffusion [247]. To calculate the hydrodynamic radius $R_{h,i}$ theoretically by measuring the density refer to Eq. 3.12, the values of $R_{h,i}$ for the IL [C2mim][OAc] is 3.13 Å. It has been demonstrated that the effective values of $R_{h,i}$ were found to be 2.72 Å and 2.20 Å for the [C2mim] and [OAc], respectively, which are close to previously published values of 2.74 Å and 2.24 Å [113, 133, 181, 248].

3.4 Conclusion

The dissolution of flax fibres in the ionic liquid [C2mim] [OAc] has been studied as a function of dissolution time and temperature. The dissolution process allowed the partially dissolved flax composite fibres to be created, after which OM was used to analysis the morphology of the partially dissolved fibres and it was found that the core, undissolved, fibre is surrounded by a coagulated flax matrix phase as dissolution proceeded. The coagulation fraction became larger as a function of time and temperature which was found to follow (TTS). The shift factors used to obtain the master curve across their dissolution temperatures was found to show an Arrhenius behaviour in this system. As a result, an activation energy was measured to be 64 ± 5 kJ/mol. An “intercept method” was introduced, which is highly sensitive to any curvature in an Arrhenius type plot and confirmed the Arrhenius behaviour of our data. This method confirmed an identical activation energy of 64 ± 5 kJ/mol.

Further analysis used the same techniques to measure the growth of the thickness of the outer coagulated cellulose ring at various temperatures and times. Thickness was calculated at each temperature, as a reference temperature, and a linear relationship was found between the thickness and square root of the processing time, indicating that the system is diffusion limited. Furthermore, the slope of each master curve was used to calculate the diffusion coefficients and the gradient of each straight line gives the value of diffusion coefficient of the IL [C2mim][OAc]. By plotting a relation between the natural logarithm of diffusion against the inverse of temperatures to calculate the diffusion activation energy for the IL. Interestingly, the value of the diffusion activation energy based on thickness measurement of 64 ± 6 kJ/mol was found to be very similar to the dissolution activation energy from following the growth of CF.

The pure IL [C2mim][OAc] solution viscosity was measured for all our samples. As it is expected, this decreases when temperature is increased. The activation energy for viscous flow was measured form the obtained value of viscosity at each temperature as function of inverse their temperature as fitted with the logarithmic form of Arrhenius plot. The activation energy was found by using the slope of this Arrhenius plot for the data of viscosity. The plots of ln(η) vs inverse temperature is linear in the range of temperatures studied and the corresponding $E_{a,\eta}$ value was found to be 37$\pm$ 1 kJ/mol which is lower than that from the coagulated region studies.

The NMR self-diffusion coefficient for each component ([C2mim]+,[OAc]- in the mixtures was measured using high field NMR (400 MHz). It was found that larger [C2mim]+ diffuses faster than its counterpart [OAc]- in the pure [C2mim][OAc]. The activation energy values of both ions [C2mim] and [OAc] obtained from NMR diffusion measurement are very close to the activation energy value of viscosity, so the IL follow a Stokes-Einstein relationship. Natural logarithm of self-diffusion coefficient inverse their temperatures of [C2mim]+, cation and [OAc]-, anion is plotted flowing Arrhenius equation. The diffusion activation energies are 42 $\pm$ 2 kJ/mol and 43 $\pm$ 2 kJ/mol for [C2mim]+ and [OAc]-, respectively.

This work provides further insight into the mechanism of cellulose dissolution in ILs. Ries et al. (2018) highlighted that the factors affecting the macroscopic and microscopic properties of cellulose/[C2mim][OAc] solutions are different [109], and therefore, it is useful to investigate both when considering the dissolution of cellulose. Since the viscosity of the IL is very sensitive to changes in its degree of dissolution and aggregation, rheological investigation was selected as the most effective technique for discovering solution differences which offered insights into bulk properties of solutions. self-diffusion coefficients (D) obtained from NMR can be used to study the ion interactions. Therefore, using the two techniques, can compare the macroscopic and microscopic environment experienced by solvent molecules. This knowledge will be helpful in designing more appropriate cellulose solvents for larger-scale processing by better understanding the mechanism of cellulose dissolution in ILs.

Chapter 4

The Role of cation and anion on the dissolution rate of flax Yarns in ionic liquids

This chapter is submitted and under review now as follows; Albarakati, F.A., Hine, P.J. & Ries, M.E. The Role of Cation and Anion on The Dissolution Rate of Flax Yarns in Ionic Liquids. Cellulose.

4.1 Introduction

The previous chapter focused on the study of the dissolution of flax yarns using the IL [C2mim][OAc] via a range of different experimental techniques. Ionic liquids possess a range of properties and can be employed in various applications. However, it is crucial to have a comprehensive understanding of the links between chemical structure and attributes of any given liquid in order to tailor it for specific purposes. Gaining knowledge, about properties such as the dissolution rate for cellulose, viscosity, density, and diffusion rates is vital for optimising its use in practical applications. Additionally, understanding the characteristics of these liquids can aid in the modification of experimental techniques and might even prove significant in more intricate uses such, as fractionation or catalysis. The effects of changing the cation and anion in these ionic liquids can be significant. Altering the length of the alkyl chain on the imidazolium ring can affect the solvent's physical properties such as the viscosity, the melting point, and the ability to disrupt hydrogen bonds in cellulose. The choice of anion and cation also play a crucial role in determining the efficiency of cellulose dissolution. So, understanding the impact of the ion type, cation/anion combination and size is crucial for creating ILs with specific features. Furthermore, the [C2mim] and [C4mim] cations are the efficient cations in ILs for dissolving cellulose [142]. To the best of our knowledge, this is the first study to use TTS analysis to examine the impact of both ILs' dissolving capacities. It also demonstrates how altering the length of the cation/anion chain can have an impact

on the dissolution behaviour, highlighting the need for additional re-evaluation of established mechanisms for cellulose dissolution in ILs, Furthermore, only one study by Lefroy et al. (2021) has been performed on the rheological experiment with 1-butyl-3-methylimidazolium acetate (C4mim][OAc] [133], and only one study of rheological and NMR diffusion experiments by Green et al. (2017) have been performed with 1-ethyl-3-methylimidazolium octanoate [C2mim][Oct]) [113]. In addition, ILs [C4mim][OAc] and [C2mim][OAc] have displayed similar cellulose dissolving capacities [224, 249]. Wendler et al. (2012) state that the onset temperature (T_{on}) - the point at which these chemicals start to break down or reacts- unaffected by the length of the alkyl chain in both ILs [C4mim][OAc] and [C2mim][OAc]. As a result, these ILs with various alkyl chain lengths show comparable safety with respect of industrial applications, as the onset temperature is a crucial factor in determining the safety of materials in industrial processes [124].

This following chapter will study the dissolution behaviour in two further imidazolium based ILs in their pure form. For the first, the anion is kept the same as in the work described in the previous chapter (acetate $[OAc]^-$) but the cation is changed to (1-butyl-3-methylimidazolium) $[C4mim]^+$. For the second the cation is kept the same (1-ethyl-3-methylimidazolium) $[C2mim]^+$, but the anion is changed to an octanoate $[Oct]^-$. The same partial dissolution method is employed, also using the same flax yarns as in the previous chapter with dissolution carried out at a range of temperatures and times, using the ILs as the dissolving solvents, and water as the coagulant. For the two new ILs studied in this chapter, the dissolved and coagulated material produced an outer ring of a matrix phase as seen previously. Techniques used to study the dissolution included TTS (using Arrhenius plots and the intercept method), rheology, density, use of the growth of the matrix thickness with time to determine diffusion constants together with using NMR data and Stokes-Einstein analysis. These two ILs were chosen to highlight how changing the cation/anion chain length might affect the dissolution behaviour compared to [C2mim][OAc].

4.1.1 Role of the anion on the dissolution of cellulose

Previously reported literature has suggested that the IL anion mostly controls the dissolution of cellulose [250-253]. Anions' activity highly depends on their charge, size, and polarity while dissolving [254]. The anions, acetate, and octanoate, have specific characteristics that impact their performance in solubility practices; their chemical structures are shown in Figure 4.1. The dissolution rate of 1-ethyl-3-

methylimidazolium and in different ionic liquids (ILs) was investigated by Villar et al. (2023) with a focus on various anions, including acetate ([OAc]), diethyl phosphate ([DEP]), and dimethyl phosphate ([DMP]). They found that [OAc] significantly increases the rate of the dissolution compared to [DEP] or [DMP]. This enhanced dissolution efficiency was attributed to the strong interaction between [OAc] and cellulose, which effectively disrupts the hydrogen-bond network. Consequently, the results demonstrate that the dissolution rate of cellulose in ILs is highly dependent on the type of the anion [232]. The interaction between anion and cellulose made up of glucose units holds great interest. The glucose chains in cellulose are held together by hydrogen bonds, these bonds are important in maintaining the material's strength and stability [255]. There have been investigations reported previously on anion chain lengths of *m* = 0 - 3, where *m* represents the alkyl chain length of anion: formate ($[HCOO]^-$) (m= 0), acetate ($[CH3COO]^-$) (m= 1), propionate ($[CH3CH2COO]^-$) (m= 2), butyrate ($[CH3(CH2)2COO]^-$) (m = 3) [256-258]. However, to the best of our knowledge, no solubility experiments with cellulose and the [Oct] group has been investigated. The octanoate $[Oct]^-$ anion with the longer chain length of m= 7 would be expected to influence the dissolution process in the similar way by disrupting the H-bonds. A molecular dynamic study by Hua et al. (2024) reported that shorter alkyl chains reduce steric hinderance which allow higher efficiency of the interaction between anion and cellulose. While longer chain length increases steric hinderance, decreasing the efficiency of the interaction [259]. Therefore, the H-bond is harder to form in the longer alkyl chain, making the cellulose hard to dissolve [260, 261].

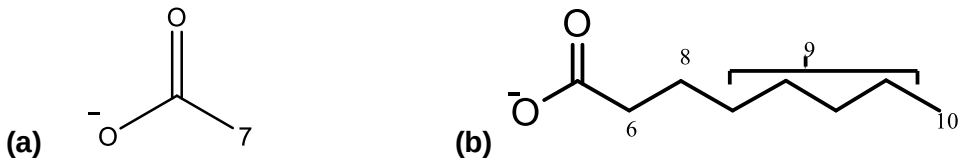

Figure 4.1: ^{1}H NMR resonances of anions (a) the acetate $[OAc]^-$ is labelled according to the spectral assignment and previous publication by [133], and (b) the octanoate $[Oct]^-$ is labelled according to the spectral assignment and previous publications by [113].

4.1.2 Role of the cation on the dissolution of cellulose

Most researchers acknowledge the role of cation in the solubility of cellulose as only secondary and that their function remains less significant compared to the anions, nevertheless it is imperative for one not to dismiss its role. A review of various research works indicates a weaker interaction between cations and cellulose in the dissolution [262-265]. Researchers such as Lu et al. (2014) noted that the interaction between the imidazolium cation and glucose rings occur through only a minor actions of van der Waals interactions [251]. Furthermore, the need to understand the complex interactions between cellulose and cations remains valid for a detailed review of the mechanisms for cellulose solubility. A study by Mezzetta et al. (2019) investigated the significant changes in the ILs solubility power after various cations are combined with the anion. They also examined the cation characteristics, with a focus on the alkyl chain length for the charge-carrying component of the cation [266]. Extensive research by Zhao et al. (2012) investigated the effect of cationic structures on cellulose dissolution in ionic liquids. A simulation was performed by the authors for a variety of chloride based ILs that were attached on imidazolium and pyridium and contained alkyl chains of varying lengths. In addition, this investigation examined the dissolution of cellulose in [C4mpy]Cl (Butyl-3-Methylpyridinium Chloride) and 1-butyl-3-methylimidazolium chloride [C4mim]Cl. It was determined that [C4mpy]Cl dissolves cellulose more effectively than [C4mim]Cl. The findings were significant as they demonstrated that IL [C4mpy] with shorter alkyl chains have a greater ability to dissolve cellulose compared to those with longer chains [C4mim] [261]. The research also explored the effect of incorporating an electron-withdrawing group within the alkyl chain of the cation using AMIM+, which was adopted as a model that demonstrated the electron-withdrawing group present within the alkyl chain of the cation led to more enhanced interactions between the cellulose and the cation as result, the interactions led to more dissolution efficiency for the cellulose. Furthermore, they demonstrate the value and role of alkyl chain characteristics, cationic properties, and electron-withdrawing groups within the above process. Gaining insight into the cationic structural function can help in the development of ionic liquids that have enhanced ability to dissolve cellulose.

4.1.3 Effects of Modifying Side-chain Lengths of cation and anion

Many studies have investigated the influence of the effect of anion/cation chain length on cellulose dissolution performance. However, the exact role of the anion/cation is still an open question [9, 56, 267, 268]. Researchers have reported that the formation of hydrogen bonds between anions and cellulose is the primary mechanism by which cellulose dissolves in ILs [96, 269]. However, it has been concluded that cations have an indirect role in the dissolving process, rather than creating direct and strong hydrogen bonds with cellulose [265]. Xu et al. (2014) investigated how the length of the alkyl chain influences the solubility of cellulose in [C4mim], employing various anions such as acetate and formate. They found that the acetate is the more effective for the cellulose solubility compared to the formate [258]. Moreover, the longer alkyl chain in $[C4mim]^+$ can impact the solvent's viscosity and its ability to penetrate the crystalline structure of cellulose [270]. Conversely, among the 13 cations investigated with a fixed acetate anion, the imidazolium cation was found to be the best for the interaction with cellulose, mainly by disrupting the hydrogen bonding network in the dissolution of cellulose [251]. The molecular dynamic simulation studies by Li et al. (2018) and Yao et al. (2015) found that the acetate $[OAc]^-$ anion has a good ability to disrupt hydrogen bonds in cellulose due to its ability to form three distinct types of H- bonds with the hydroxyl group attached to the second, third and sixth carbon atoms (C2, C3, and C6) of the glucose unit in cellulose which create the separation of cellulose chain easily compare to $[Cl]^-$ [9, 267]. The result is in line with the hypothesis that cellulose has a poorer solubility in ILs that contain cations with larger chain length profiles [267].

The structure of ionic liquids can have a significant influence on cellulose processing due to their capacity to disrupt the strong hydrogen bond network that forms between polymer chains. The first studies on IL-cellulose interactions mainly looked at 1-alkyl-3-methylimidazolium [$C_n$mim] cations with chain lengths from 4 to 8 and different anions. They found that [$C_n$mim] Cl (with n = 4) was the most efficient in increasing the dissolution rate among the ILs tested [84, 102, 271]. Another study demonstrated that the properties of the IL and its capacity to dissolve cellulose were significantly influenced by the length of the cation side chain [272]. ILs that contained different $[C_n\text{mim}]^+$ cations evidenced that the solubility of these ILs was influenced by the length of the cation chain, specifically demonstrating an odd-even effect. Interestingly, the ILs with a chain length as order of $[C_6\text{mim}]^+ < [C_4\text{mim}]^+ < [C_2\text{mim}]^+$ exhibited the highest solubility among a range of anions [249, 273, 274]. In a related work, they used molecular dynamics calculations to investigate how cellulose dissolves in [$C_n$mim]-based ILs. The patterns of bonding that existed between the

cations, anions, and cellulose chains were analysed. At the same time as increasing the length of the cation chain caused the dynamics of the system to slow down slightly, it was discovered that this change had only a marginal impact on the solvation process [94, 275].

4.2 Experiments and Methods

4.2.1 The procedure of dissolving the flax yarn samples with ILs [C4mim][OAc], and [C2mim][Oct]

This chapter uses the partially dissolving method to follow the dissolution for both ILs [C4mim][OAc] and [C2mim][Oct] which is identical to the method for the same flax yarns in IL [C2mim][OAc], which is described in our previous in Section 2.3. A Teflon dish was filled with IL [C4mim][OAc] or [C2mim][Oct] (approx. 50 ml) and preheated at the chosen desired temperature in an oven for 1h. Four separate yarn samples were wound around a Teflon frame. Then, the frame with the samples was submerged into the preheated IL, the dissolution experiments were then commenced at the various chosen times and temperatures in a vacuum oven under vacuum, after which the frame with samples was taken out from the IL and placed into a water bath for 24 hours at room temperature to coagulate the dissolved cellulose. A drying process then followed, by taking out the frame with the samples from the water bath to dry for more than 48 hours at room temperature. Karl-Fischer titration using a Metrohm 899 Coulometer was employed to determine the water content in ionic liquids as received, giving the water content in the experiments of [C2mim][OAc], [C4mim][OAc], and [C2mim][Oct] were 0.2 wt.%, 0 wt.%, and 0.1wt.% respectively.

4.2.2 Optical Microscopy

Optical microscope cross sections were obtained and analysed for the processed samples using the techniques outlined in Section 2.4. The partially dissolved composite yarns (for each set of four processed samples at the same processing time and temperature) after embedding in epoxy resin using the method detailed in Section 3.2.2. Each partially dissolved composite yarn cross section was analysed 4

times for each condition of dissolution time and temperature (from the four samples wound on the frame) and the average value and standard error were calculated. 'ImageJ 1.52d' software was used to measure the area of the cross section from multiple directions on each sample (e.g., Figure 3.1 in previous chapter). All the partially dissolved composites showed the same structure of a central undissolved yarn surrounded by an outer ring of dissolved and coagulated cellulose. From these optical images, two specific parameters were used to measure the increase in the dissolved fraction and hence follow dissolution. First of these was the area fraction of the dissolved and subsequently coagulated material, called the coagulation fraction (CF) and then secondly the growth in the thickness of this outer coagulated layer. Both parameters have been examined at different processing temperatures and times.

4.2.3 The growth of the dissolved and coagulated region for [C4mim][OAc], and [C2mim][Oct]

The growth of the dissolved and coagulated region of the two ILs were measured according to the method detailed in previous chapter section 3.2.3.

4.2.4 Viscosity

The viscosities of two ILs were measured according to the method and the equipment described in Section 2.5.

4.2.5 NMR Diffusion

To measure the self-diffusion coefficient of the anions and cations in each IL, the equipment and pulse sequences described in Section 2.7 were used. Based on the ^{1}H spectral assignment of each peak, diffusion coefficient measurements of each ion were averaged over the relevant peaks for cation $[C4\ mim]^{+}$ peaks (1-6, 8,9) and the anion $[OAc]^{-}$ (7), for cation $[C2mim]^{+}$ peaks (1-5, 7) and the anion $[Oct]^{-}$ (6,8,9,10), as shown in Figure (4.1) and (4.2). The cation proton resonances for each measurement were determined to have identical diffusion coefficients, as expected,

due to their attachment to the same ion. Thus, only one average value will be used for the diffusion coefficient of cation. Regarding the anion, its diffusion coefficient was determined based on the resonance of only one proton for [OAc], and four protons were determined to have similar diffusion coefficients for [Oct], therefore, only one average value will be used for the diffusion coefficient of anion. All NMR samples were measurements at temperature ranging from 30 °C to 60 °C.

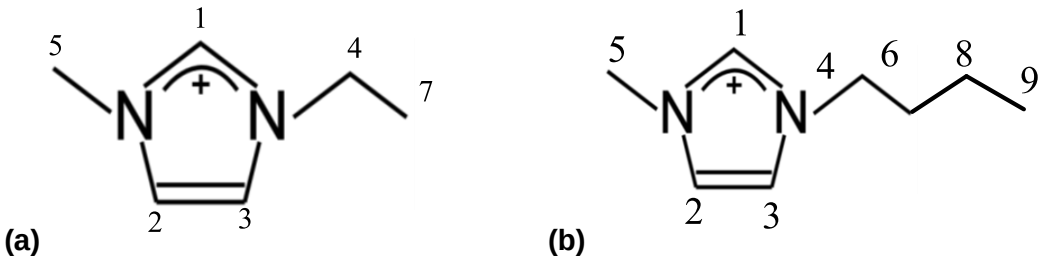

Figure 4.2: The cations investigated in this study: (a) [C2mim) and (b) [C4mim]. ^{1}H NMR resonances are labelled for each cation according to the spectral assignment published by [110, 113] for [C2mim], and [133] for [C4mim].

(a)

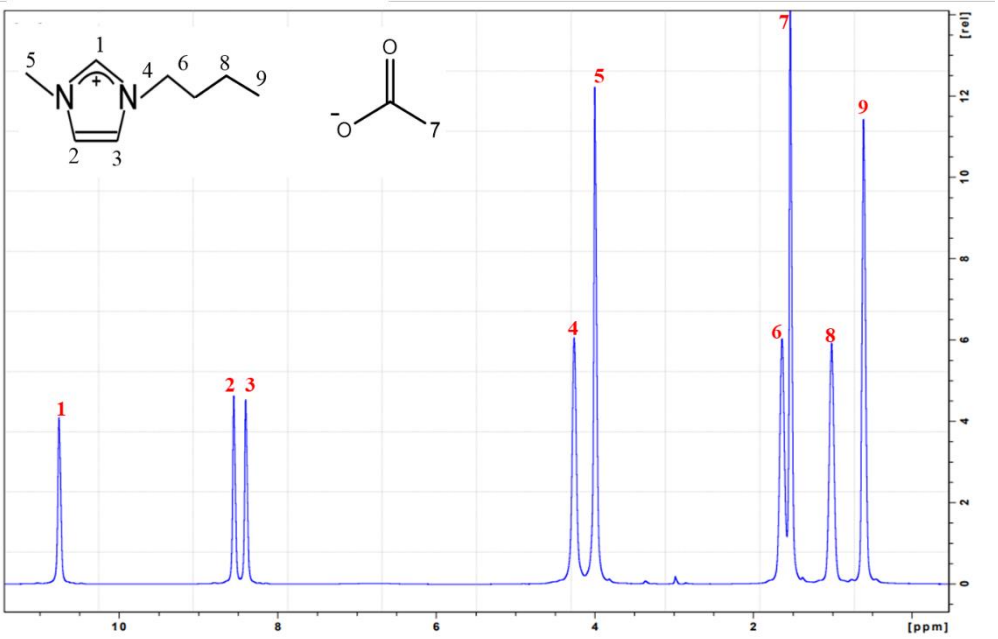

(b)

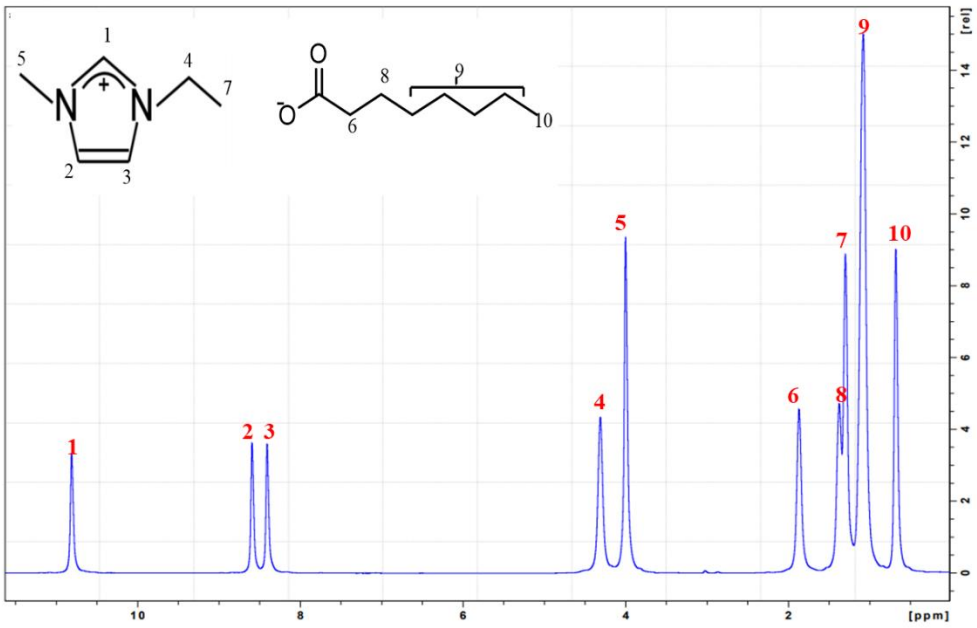

Figure 4.3: High field ^{1}H NMR spectrum (400$\boldsymbol{MH_Z}$) of pure ILs at 30 °C (a) [C4mim][OAc] with peak assignments given in red for protons labelled 1-9. (b) [C2mim][Oct] with peak assignments given in red for protons labelled 1-10. The chemical structure is shown, and the inset includes corresponding labels.

4.2.6 Density

The densities of the three pure ILs [C4mim][OAc], [C2mim][Oct], and [C2mim][OAc] were measured at 20 °C using a graduated cylinder in MBraun Labmaster 130 glove box maintained a dry nitrogen atmosphere with a dewpoint level ranging between -40 °C and -70 °C to prevent water contamination in the IL samples we utilized. The IL used for the density measurements, were stored within this controlled environment ensuring minimum exposure to humidity.

4.3 Results and discussion

4.3.1 Optical Microscopy

The dissolution mechanism found in the ILs explored in the chapter, [C4mim][OAc] at 40 °C, 50 °C , 60 °C, and 70 °C and [C2mim][Oct] at 80 °C, 85 °C, 90 °C and 100 °C was found to be very similar to that of the IL [C2mim][OAc], as detailed in the previous chapter. The flax yarns are dissolved from outside and on coagulation in water the coagulated material forms an outer layer around the inner undissolved core, which we call the coagulated fraction (CF). Figure 4.4 (a) and (b) shows the growth of this coagulated layer after various dissolution times and temperature for both ILs. Figure 4.5 illustrates optical microscopy images showing cross sections of processed yarn at 60 °C for arange of dissulotion times in the IL [C4mim][OAc]. From these images, it can be clearly seen that the growth of the coagulation fraction is dependent on the dissolution time and temperature, so as the appearance of the dissolution process is similar to that in the previous chapter, TTS master curve can be explored and constructed.

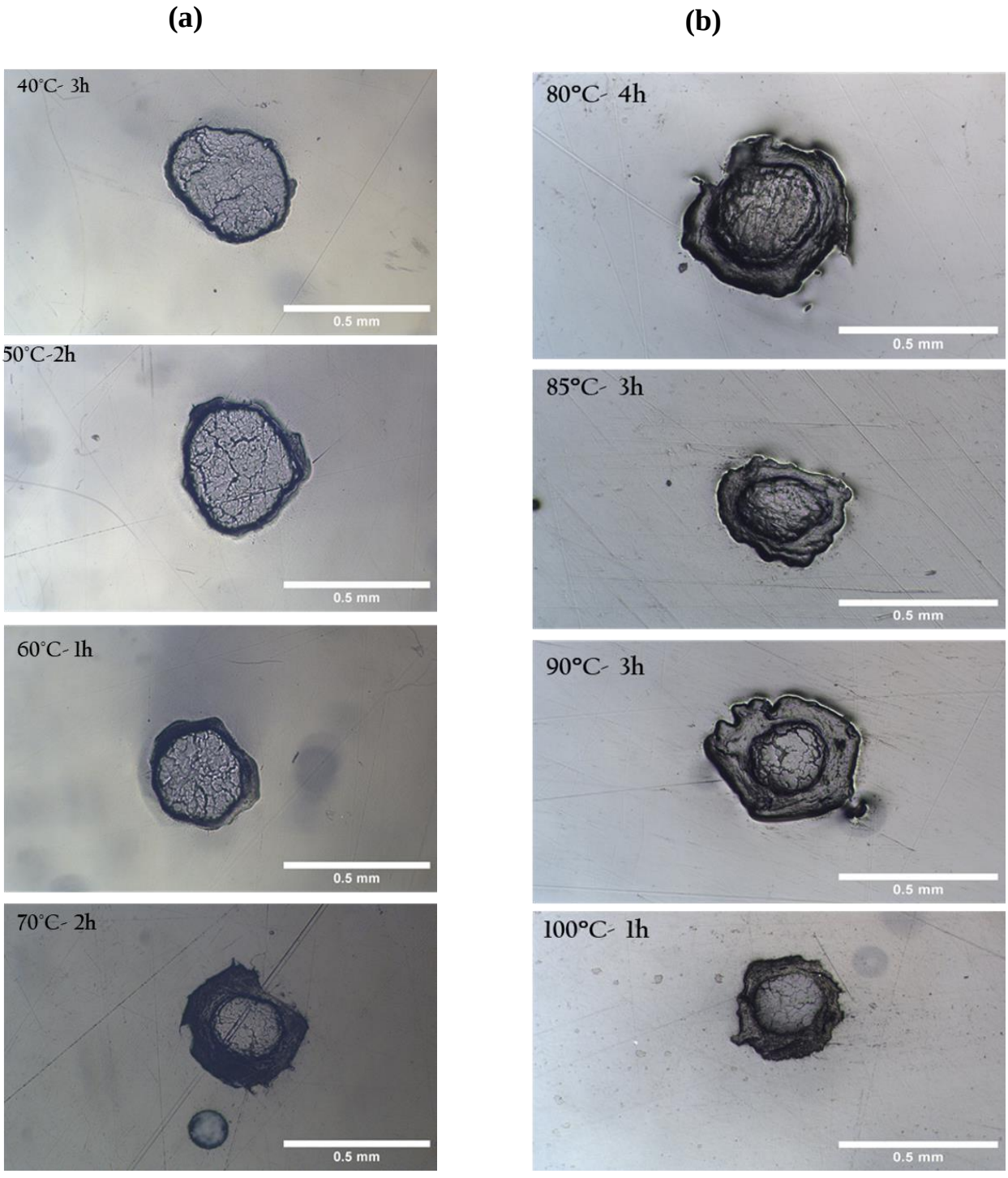

Figure 4.4: Microscopy cross section images for partially dissolved flax yarns for both ILs showing the growth of the CF at various temperatures and times (a) [C4mim][OAc] and (b) [C2mim][Oct]. Scale length 0.5 mm.

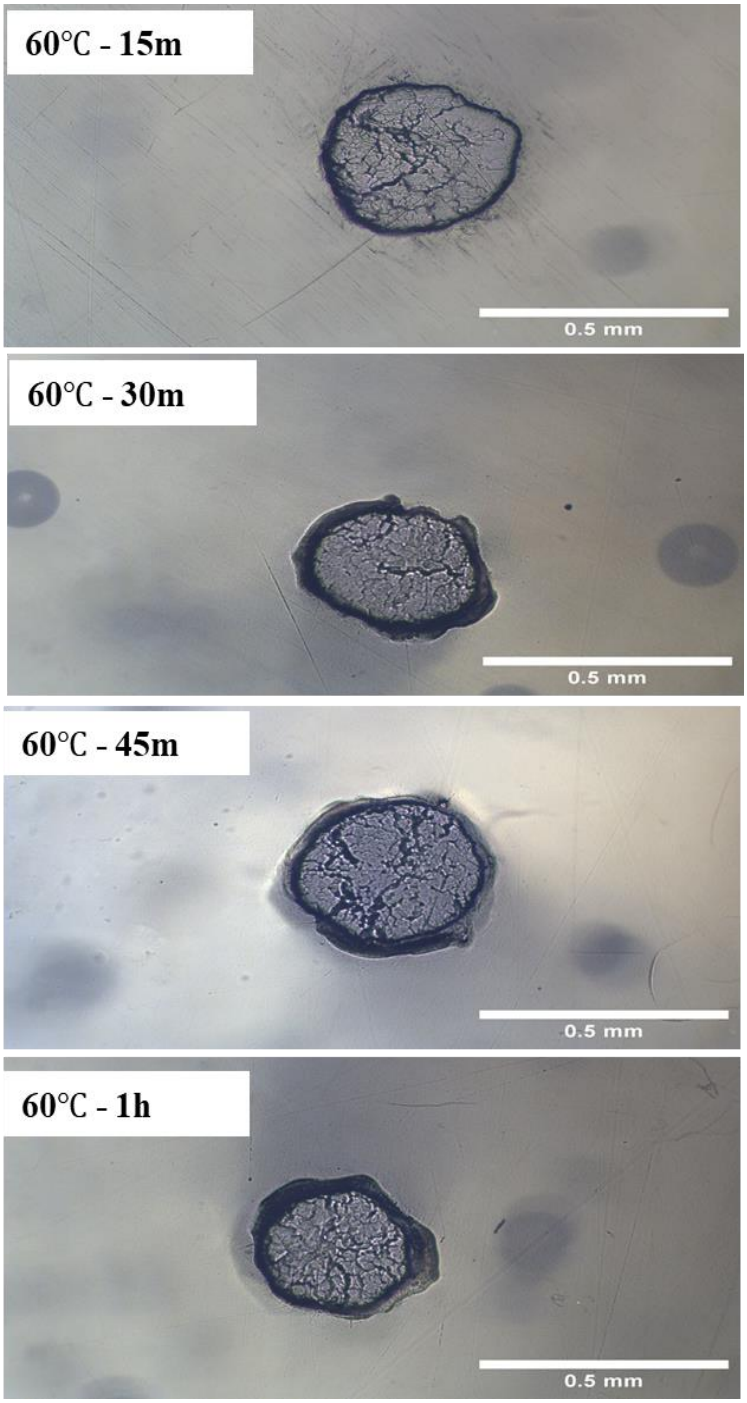

Figure 4.5: Optical microscopy images showing cross sections of processed yarn at 60 °C in arrange of dissulotion times 15 min, 30 min, 45 min and 1h of the IL [C4mim][OAc]. The CF growth with dissolution times, and the scale length 0.5 mm.

4.3.2 Analysis of the dissolution of flax yarn in [C4mim][OAc] using TTS

The growth of the CF as a function of processing time and temperature and the steps used to determine an activation energy of dissolution via TTS is shown in Figure 4.6.

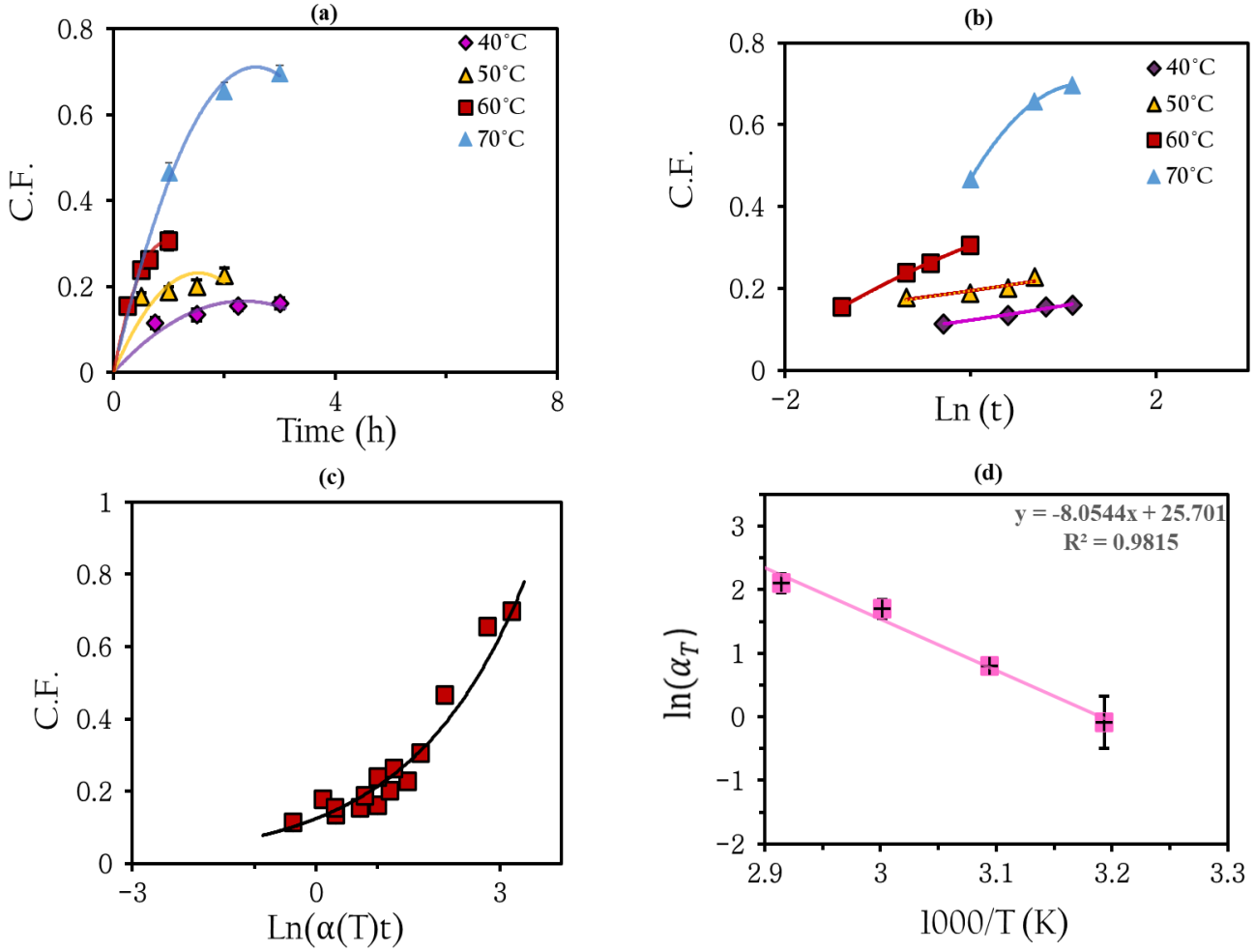

Figure 4.6: (a) CF as function of all dissolution temperatures and times in [C4mim][OAc]. Polynomial fits here are used to guide the eye, and in some cases error bars are smaller than data points size. (b) The CF is here plotted against the natural logarithmic time. Exponential fits are employed to visually represent the data. (c) master curve of the coagulation fraction for all dissolution temperatures, obtained by shifting the data to the reference temperature of 50 °C. (d) Arrhenius plot presenting the relation between the shift factors, and the inverse of the temperature. A linear best fit line fit to the data is shown, and error bars included.

Figure 4.6 (a) shows the calculated coagulation fractions at processing temperatures of 40 °C, 50 °C 60 °C, and 70 °C for times up to 3 hours calculated from Eq. (2.1) and then Figure 4.6 (b) shows this data plotted against ln(time). Next, Figure 4.6 (c) shows the data shifted in ln (time) to form a master curve using 50 °C, as a reference temperature, using a shift factor $\alpha_{50} = 1$ and their natural logarithm value $\ln\alpha_{50} = 0$, in order to shift the other datasets of different temperatures horizontally. Then, fitting the dataset at 50 °C with an exponentially function to provide a guide to the eye for other dataset shifting. Next, each dataset is shifted horizontally using a shift factor α_T with the aim for all data points to overlap to the reference data curve. To find the best fit, the coefficient of determination R^2 between the datasets and the exponential curve maximized by adjusting the shift factors $\ln\alpha_T$ of the final fitting at 40 °C, 60 °C and 70 °C. Finally, Figure 4.6 (d) shows these final shift factors used to form a master curve at 50 °C plotted against the inverse of the processing temperature. A straight line confirms that the data is again Arrhenius and so an activation can be determined by Eq. (3.6). For more detailed of the shifting process, refer to a previous chapter section 3.3.2. The shift factors $ln\alpha_T$ used to form Arrhenius plot of different temperatures at $T_{ref.50℃}$ and the E_a value are summarized in Table 4.1. So, we can then finally plot the dissolution curve at any particular temperature (e.g. 50 °C) against linear time which then describes how the dissolution rate of all shifted data are initially fast and then slow down with time progresses, as shown in Figure 4.7.

Temperature T (°C)	**$\ln\alpha_T$**	**Regression Coefficient R^2**	**Activation energy E_a (kJ/mol)**
40	-0.09	0.98	67 ± 1
50	0		
60	1.7		
70	2.1		

Table 4.1: Shift factors obtained from TTS analysis of different temperatures at reference temperature (T_{ref}) of 50 °C, used to plot Figure 4.6 (d).

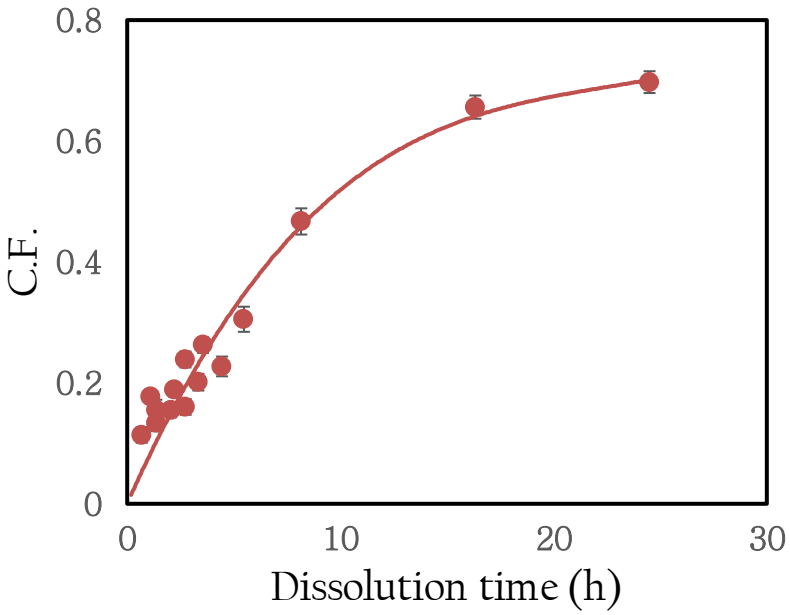

Figure 4.7: CF master curve against linear time at a reference temperature of 50 °C showing the dissolution process, and the line is a polynomial of order two fit to the data.

Now, all the above analysis is carried out again three times, using the other three temperatures as the reference temperatures (T_{ref}), so shifting all data to 40 °C and 60 °C and finally 70 °C in order to create a master curve for each set of data at each of these temperatures. The shift factors, from 40 °C, 60 °C and 70 °C TTS shifting, can be plotted separately as a function of temperature as before for the 50 °C TTS shifting results. Each set of shift factors for each of the reference temperatures is again found to display an Arrhenius behaviour, each giving a dissolution activation energy, see Fig.4.8 (a-c). These plotted graphs give similar gradients, leading to similar E_a as calculated from 50°C. The average activation energy required to dissolved flax yarn the IL [C4mim] [OAc] was found to be 67 ± 1 kJ/mol. The shift factors $ln\alpha_T$ used to form these three masters carves of each temperature in the process as a reference temperature and the E_a values are summarized in Table 4.2.

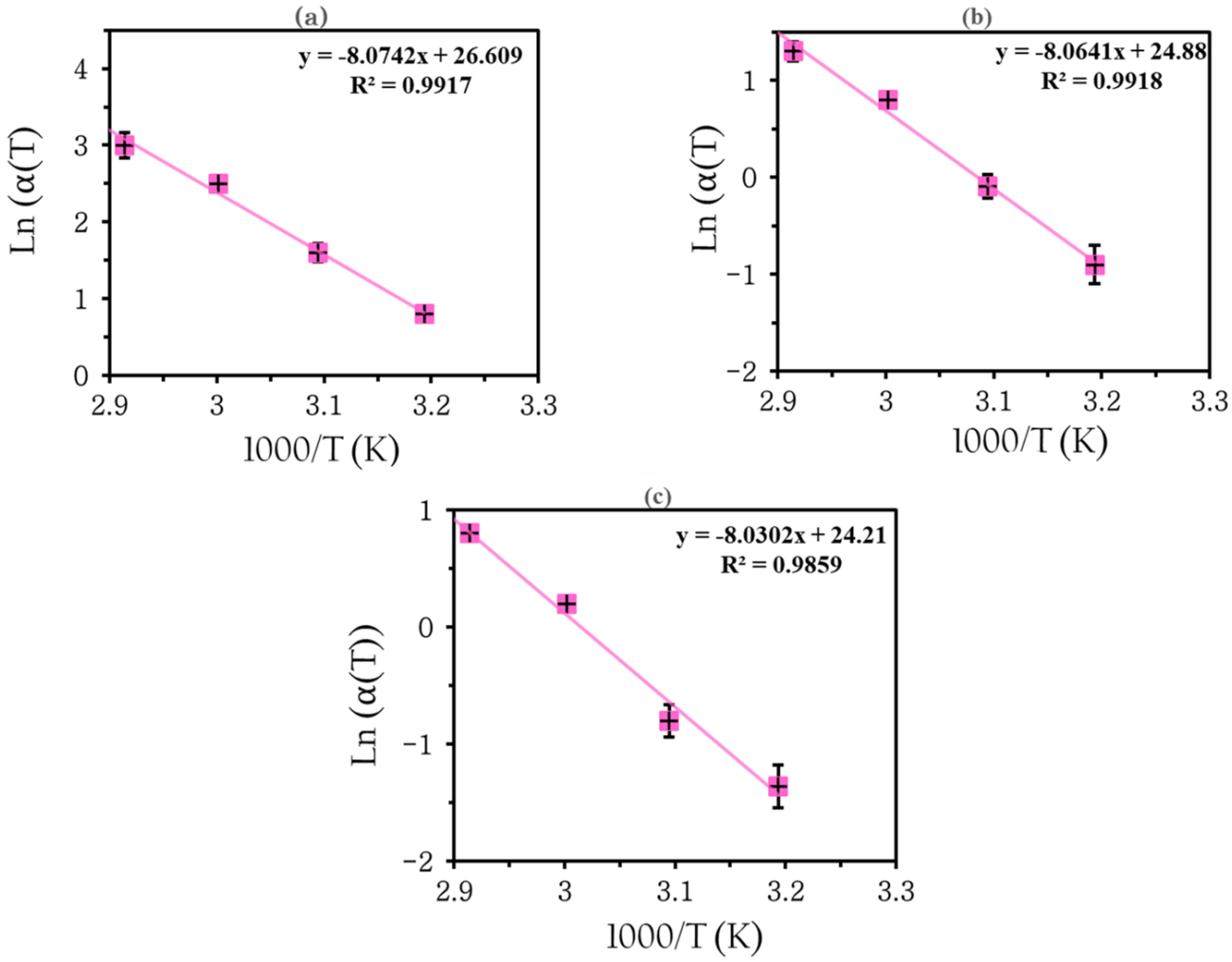

Figure 4.8: Shift factors $\ln(\alpha_{T_{ref}})$ as a function of inverse temperature, indicating Arrhenius plots in the IL [C4mim] [OAc]. Reference temperatures (T_{ref}) of (a) 40 °C, (b) 60 °C, (c) 70 °C, and error bars included.

Temperature T (°C)	lnα_T	Regression Coefficient R^2	Activation energy E_a (kJ/mol)
40 50 60 70	0 1.6 2.5 3	0.99	67 ± 1
40 50 60 70	-0.9 -0.09 0 1.3	0.99	67 ± 1
40 50 60 70	-1.36 -0.8 -0.2 0	0.98	67 ± 1

Table 4.2: The fitting results for flax yarns dissolution in IL[C4mim][OAc] used to plot Figure 4.8 (a-c).

4.3.3 Analysis the dissolution of flax yarn in IL [C2mim][Oct] using TTS

For the next IL, **[C2mim][Oct],** the dissolution process was started using a temperature of 50 °C within a specified time range (30 m, 1 h, 1.5 h, and 2 h), as used for two acetate anion ILs, but no observable signs of dissolution were detected even for 3 hours processing time. Subsequently, the temperature was elevated to 60 °C at different dissolution times, but again no outer coagulation layer was observed, as illustrated in Figure 4.9, whereas the outer coagulation layer was appeared at 60 °C for the [C4mim][OAc] as seen in Figure 4.5. In response to these outcomes, the temperature was further increased to 80 °C, resulting in the formation of a coagulated fraction layer around the undissolved core after 1h processing time, as seen in previously Figure 4.4(b). The growth of the CF as a function of processing time and temperature and the steps used to determine an activation energy of dissolution via TTS is shown in Fig. 4.10. This is already an indication that the processing

temperature has to be significantly higher for the IL [C2mim][Oct] compared to the two based on the acetate anion.

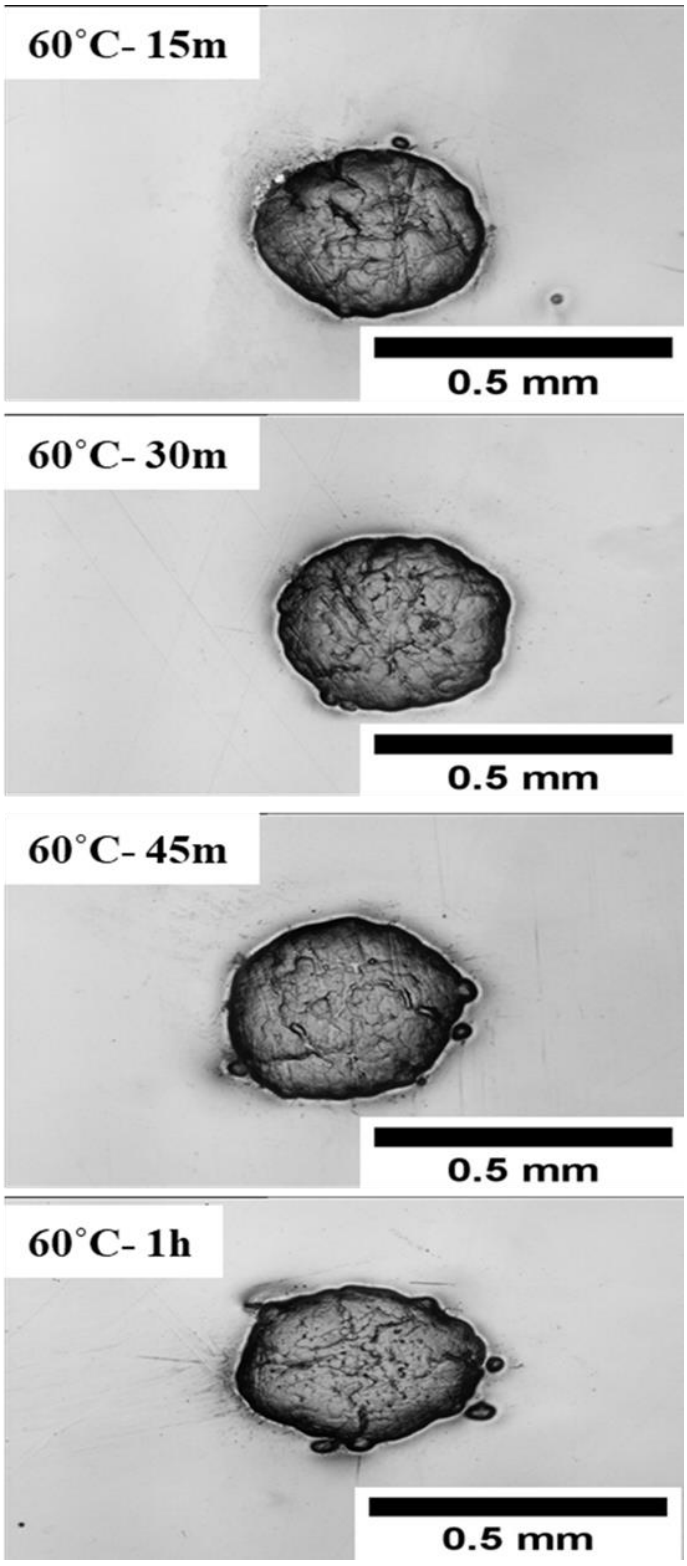

Figure 4.9: Images showing cross sctions of processed yarn at 60 °C ,in arange of dissulotion time 15 m, 30 m, 45 m and 1h of the for IL [C2mim][Oct], no coagulation fraction seen, and scale bars included.

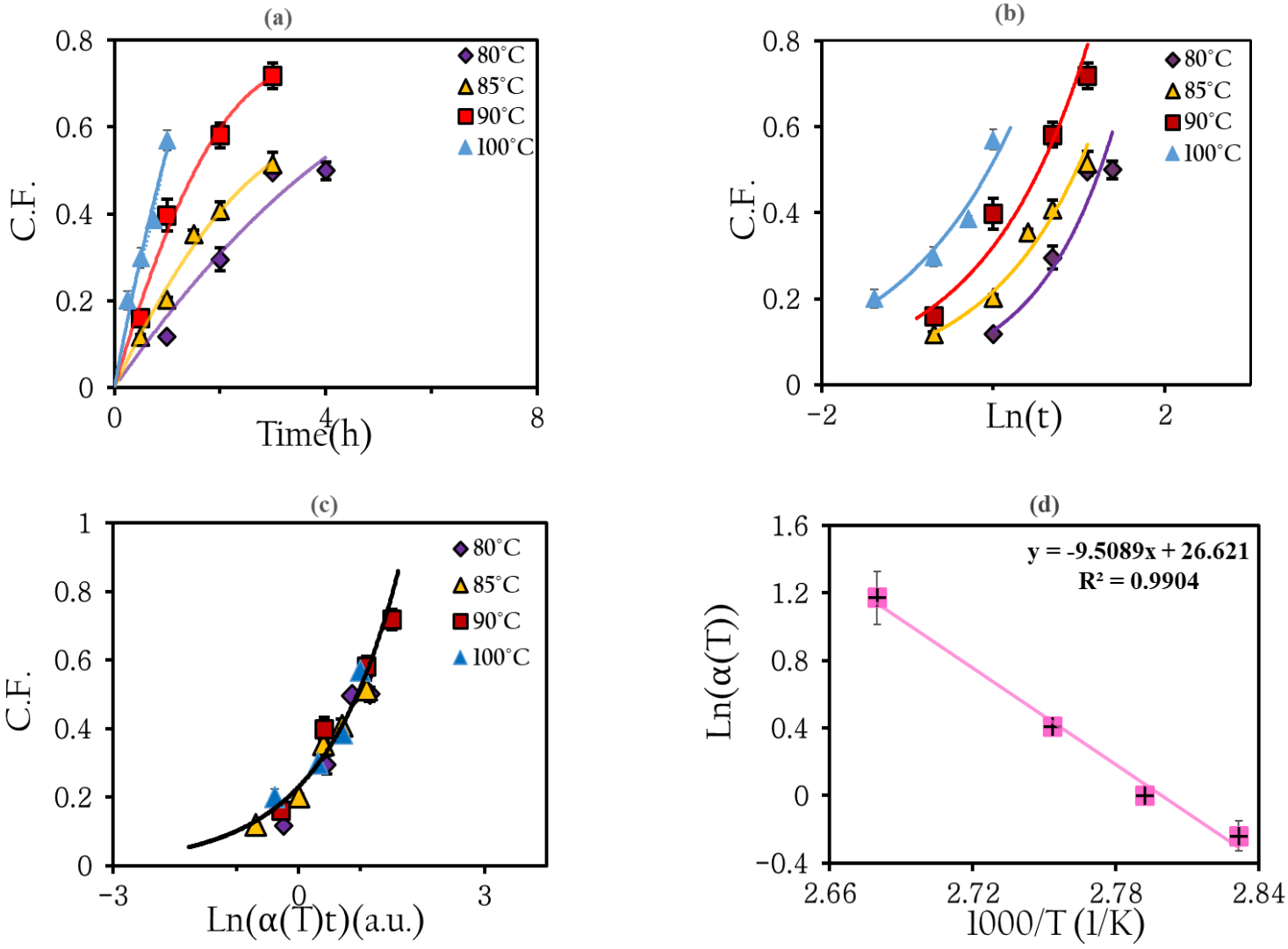

Figure: 4.10: (a) CF as function of all dissolution temperatures and times in [C2mim][Oct] at 85 °C, as reference temperature, polynomial fits used to guide the eye, and some error bars are smaller than data points. (b) CF as function of all dissolution time and temperature as expressed in natural logarithmic time. Exponential fits used to guide the eye, including error bars. (c) master curve of the coagulation fraction for all dissolution temperatures, exponential fit used to guide eye, and some error bars smaller than data points. (d) Arrhenius plot presenting the relation between temperatures and shift factors, linear line fit to the data, and error bars included.

To analyse the growth of the fraction of the coagulated layer (called the coagulation fraction CF), and to create a master curve at a chosen reference temperature (here at 85 °C for the [C2mim][Oct] IL) the following steps were carried out. First, all the datasets were plotted together in one graph to show the growth of CF with the increase of time and temperature, as seen in Figure 4.10 (a). Next, the x-axis (time data) was converted to a natural logarithm time scale (ln (t)) to provide a visual guide for the shifting process. Then, the reference dataset of 85 °C was given a scaling factor $\alpha_{85} = 1$ and hence a natural logarithm value $\ln\alpha_{85} = 0$. Next, the datasets at the other processing temperatures of 80 °C, 90 °C, and 100 °C were shifting horizontally left or right by eye using a number equal to $\ln\alpha_T$ to overlap with the reference data of 85 °C, creating a final master curve, as shown in Figure 4.10 (b). The final data points were all fitted to the same exponential function and the coefficient of determination R^2 for the datasets was maximized by adjustment of the shift factors α_{80}, α_{90}, and α_{100}. A subsequent plot of the shift factors ln α_T with the inverse of the processing temperature, showed a linear relationship which indicates an Arrhenius behaviour, allowing an activation energy to be determined by Eq. (3.6), as seen in Figure 4.10 (c). The average activation energy required to dissolved flax yarn in the IL [C2mim][Oct] was found to be 79 ± 1 kJ/mol. The shift factors used to create a master curve of different temperatures at ($T_{ref.85°C}$) as a reference temperature and the E_a value are summarized in Table 4.3. Then, we can finally plot the dissolution master curve at any particular temperature (e.g. 85 °C) against linear time which then describes how the dissolution rate is initially fast and then slows down as time progresses, as shown in Figure 4.11

Temperature (°C)	**lnα_T**	**Regression Coefficient R^2**	**Activation Energy E_a (kJ/mol)**
80	-0.24	0.99	79 ± 1
85	0		
90	0.41		
100	1.17		

Table 4.3: Shift factors obtained from TTS analysis of different temperatures at reference temperature (T_{ref}) of 85 °C to plot Figure 4.10 (d).

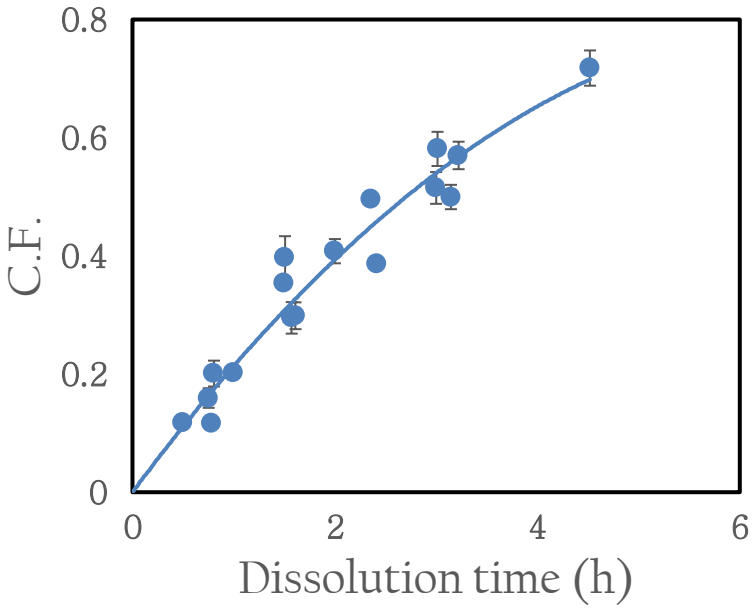

Figure: 4.11: C.F. master curve against linear time at a reference temperature of 85 °C showing the dissolution process, and the line is a polynomial of order two fit to the data.

Figure 4.12 (a-c) describes the Arrhenius plots of the other three temperatures as reference temperatures (T_{ref}), which is same analytical procedure above, emphasizing that the appearance of, and growth of, the coagulation layer is similar even at this elevated temperature, as reference temperature. The fitting results obtained from TTS analysis for $T_{ref.80℃}$, $T_{ref.90℃}$, and $T_{ref.100℃}$ for forming Figure 4.12 (a-c) are summarised in Table 4.4.

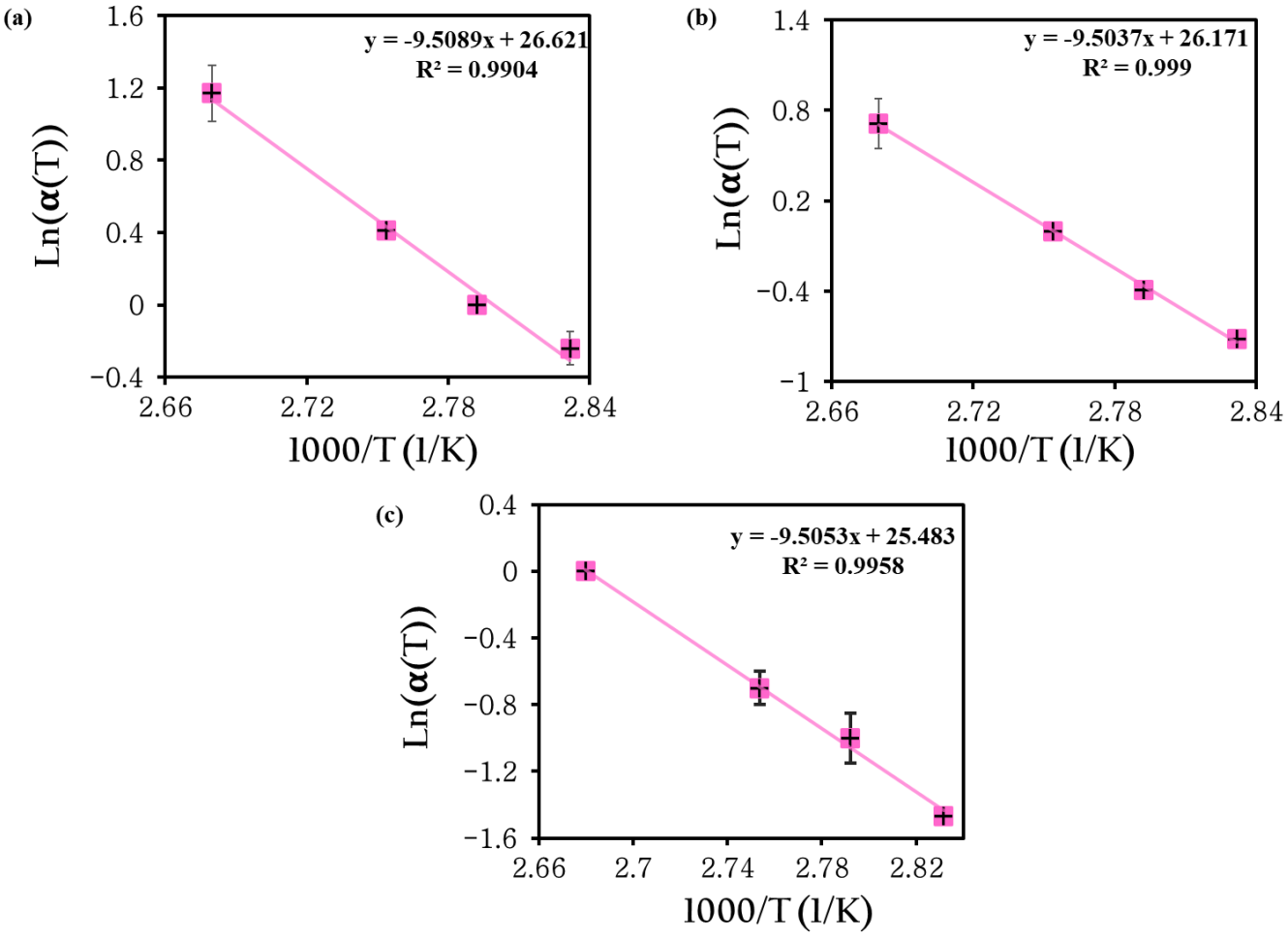

Figure 4.12: Shift factors $\ln(\alpha_{T_{ref}})$ as a function of inverse temperature, indicating Arrhenius plot in [C2mim][Oct]. Reference temperatures ($\boldsymbol{T_{ref}}$) of (a) 80 °C, (b) 90 °C, (c) 100 °C, and error bars included.

Temperature (°C)	**lnα_T**	**Regression Coefficient R^2**	**Activation Energy E_a (kJ/mol)**
80	0	0.99	79 ± 1
85	0.4		
90	0.75		
100	1.45		
80	-0.72	0.99	79 ± 1
85	-0.39		
90	0		
100	0.71		
80	-1.47	0.99	79 ± 1
85	-1		
90	-0.7		
100	0		

Table 4.4: The fitting results for TTS analysis of flax yarns dissolution in IL[C2mim][Oct] used to plot Figure 4.12(a-c).

4.3.4 Intercept analysis for both ILs [C4mim][OAc] and [C2mim][Oct]

A further analysis technique was employed on the coagulated fraction data (for both new ILs studied in this chapter), which was described above in section 3.3.3 and is termed the intercept method. This technique uses the intercept from each Arrhenius plot (e.g. Figures 4.6 (d) and 4.10 (d) but formed at each reference temperature for each IL to determine the intercepts $\ln \alpha_0$, and then these are plotted against the inverse temperature. For more details of the intercept process, refer to the previous chapter section 3.3.3. All the intercepts $\ln \alpha_0$ calculated at each reference temperature themselves follow an Arrhenius law, being linearly dependent on the inverse of the reference temperature, as seen in Figure 4.13 (a) and (b), allowing an activation energy to be determined. The intercepts $\ln \alpha_0$, plotted against the inverse temperature.

From the intercept method (Figures 4.13 (a) and (b)) the linear fit of $\ln \alpha_0$ vs. 1000/T_{ref} were determined to be 69 $\pm$ 2 kJ/mol and 79 $\pm$ 3 kJ/mol for [C4mim][OAc] and [C2mim][Oct] respectively. From Figures 4.6 (d) and 4.10 (d), the dissolution activation energies were found to be 67 $\pm$ 1 kJ/mol and 79 $\pm$ 1 kJ/mol for [C4mim][OAc] and [C2mim][Oct] respectively, Interestingly, the calculated activation energies from intercepts method are seen to be in excellent agreement to that obtained from TTS analysis. In addition, the fourth master curves obtained from TTS analysis give similar gradients, leading to similar $E_a$for each IL. Although [C4mim][OAc] and [C2mim][OAc] have comparable activation energies, they differ slightly, which may indicate that the length of the alkyl chain influences the dissolution process. Compared to the other ILs, [C2mim][Oct] was examined at lower temperature (30 °C - 60 °C), but it was not providing enough energy to dissolve, while higher temperature ranges (80 °C -100 °C), suggesting it provides sufficient energy to break down for the dissolution process compared to [C2mim][OAc] and [C4mim][OAc]. Summarising the activation energies measured through two different methods (dissolution method E_a and intercept method E_a) for the three ILs [C2mim][OAc], [C4mim][OAc] and [C2mim][Oct] are listed in Table 4. 5.

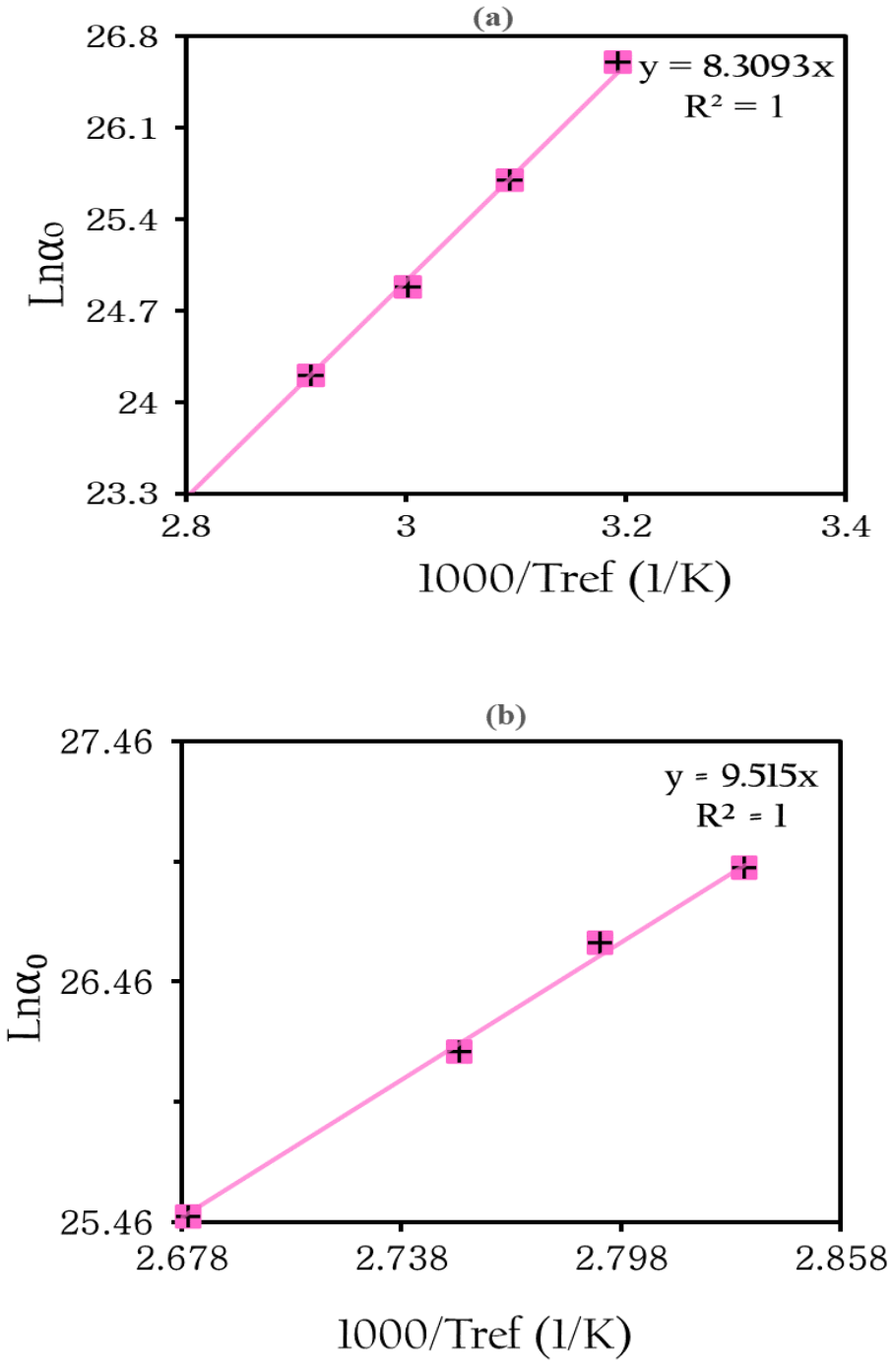

Figure 4.13: Intercept process showing shifting to all temperatures indicating Arrhenius dependence. [C4mim][OAc] (a), and [C2mim][Oct] (b).

IL	Temperature (°C)	Dissolution Ea (kJ/mol)	Intercept Ea (kJ/mol)
[C2mim][OAc]	30 40 50 60	64 ± 5	64 ± 5
[C4mim][OAc]	40 50 60 70	67 ± 1	69 ± 2
[C2mim][Oct]	80 85 90 100	79 ± 1	79 ± 3

Table 4.5: The activation energy measured through two different methods; dissolution process and intercept method for the three ILs.

4.3.5 The growth of the dissolved and coagulated region for [C4mim][OAc], and [C2mim][Oct]

The data collected above for the development of the coagulated fraction with time and temperature was analysed using Eq. (2.1), in a further way by calculating the growth of the thickness of this layer for both ILs as a function of time and temperature, as described in detailed in the previous chapter in Figure 3.13. For instance, the IL [C4mim][OAc] includes four processing temperatures, 40 °C, 50 °C, 60 °C and 70 °C; By using each temperature separately as a reference temperature, a master curve of the growth of the coagulation fraction at each temperature can be derived.

Accordingly, four master curves are constructed, (for example as shown in Figures 4.6 (c)) and the three master curves used to form Arrhenius plots in Figure 4.8 (a-c), at each reference temperature.

Then, the increase of the thickness of the coagulation layer with time was calculated, as detailed in sections 3.2.2 and 3.2.3, at each reference temperature using Eq. 3.1. As before, the results for increasing thickness were again plotted against the square root of time. Figure 4.14 (a) shows typical data for [C4mim][OAc] at a reference temperature of 50 °C and it is seen that the results fit well to a linear relationship between thickness and square root of time, indicating that the system is diffusion controlled/limited. Furthermore, the slope of each master curve can be used to calculate the self-diffusion coefficients by using Eq. 3.2. The gradient of the straight line gives the value of self-diffusion coefficient of the IL [C4mim][OAc] $(8.5 \pm 0.1) \times 10^{-13} \mathrm{m}^2/s$ at a reference temperature of 50 °C. The linear fit to the data with a high coefficient of determination R^2= 0.98 indicates a very good correlation between the thickness and the square root of time. The self-diffusion coefficient values at each reference temperature 40 °C, 60 °C and 70 °C are $(3.3 \pm 0.1) \times 10^{-13}\ \mathrm{m}^2/\mathrm{s}$, $(1.9 \pm 0.1) \times 10^{-12}\ \mathrm{m}^2/\mathrm{s}$, and $(3.3 \pm 0.3) \times 10^{-12}\ \mathrm{m}^2/\mathrm{s}$, respectively, as summarised in Table 4.6.

The same analysis was repeated for IL [C2mim][Oct] at temperatures of 80 °C, 85 °C, 90 °C and 100 °C. Figure 4.14 (b) shows again a typical result for a reference temperature of 85 °C and demonstrates that the thickness grows as a function of √t obtained from the master curve in Figure 4.10 (c) and from the three master curves used to form Arrhenius plots in 4.12 (a-c). The slopes were used to calculate the self-diffusion coefficients at each temperature as a reference temperature using Eq.3.10. The slope of the line in the graph can be related to the diffusion coefficient D of $(2.7 \pm 0.1) \times 10^{-12}\ m^2/s$ at a reference temperature of 85 °C. The obtained self-diffusion coefficients are $(1.9 \pm 0.1) \times 10^{-12}\ m^2/s$, $(4.2 \pm 0.2) \times 10^{-12}\ m^2/s$ and $(7.9 \pm 0.3) \times 10^{-12}\ m^2/s$ at 80 °C, 90 °C and 100 °C, respectively, as summarised in Table 4.7.

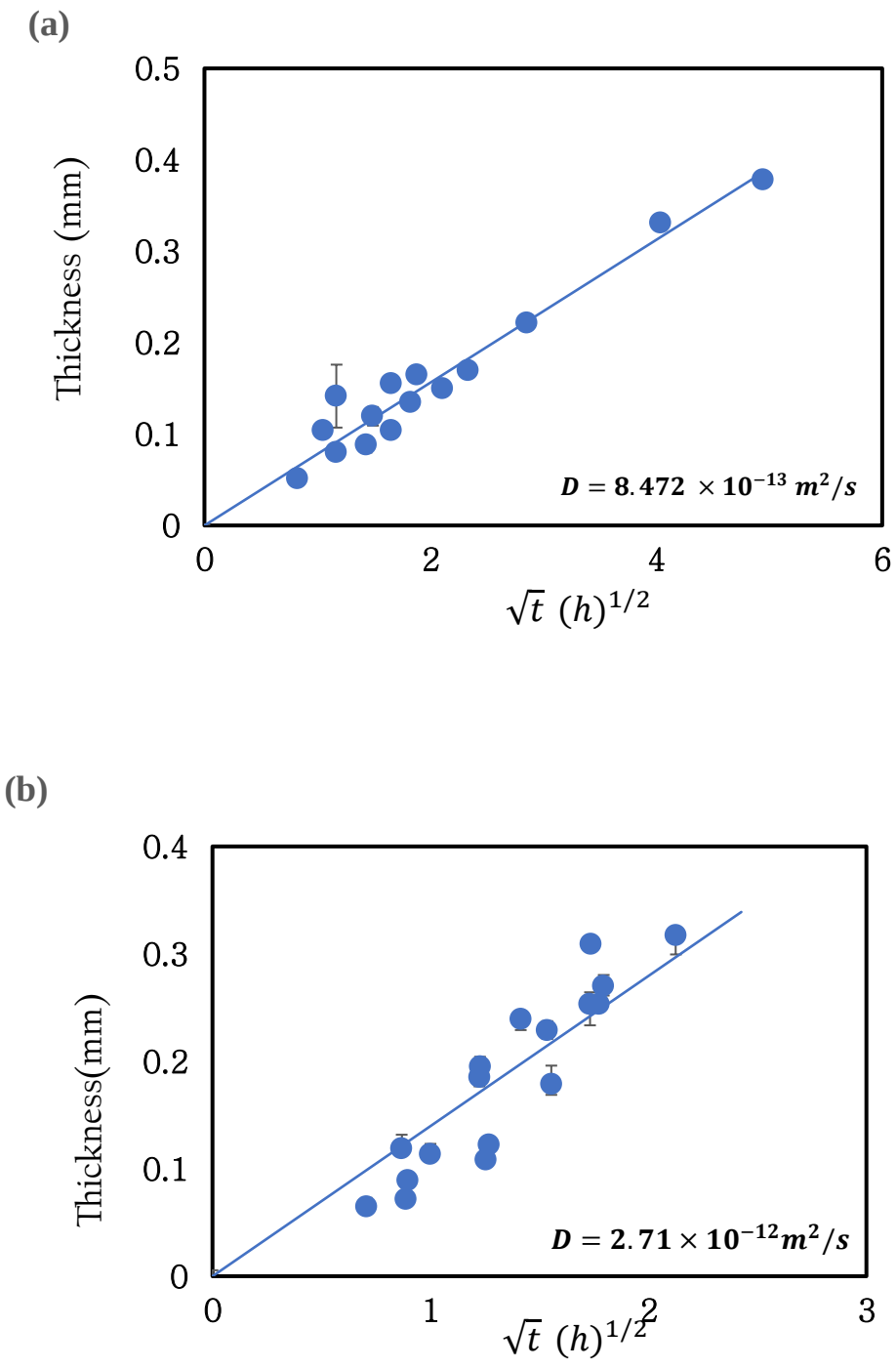

Figure 4.14: Plots of the thickness vs. the square root of time in hours (h) for ILs. (a) [C4mim][OAc] at 50 °C, and (b) [C2mim][Oct] at 85 °C, Error bars included.

Reference Temperature (°C)	$D_{[C4mim][OAc]}\ m^2/s$
40	$(3.3 \pm 0.1) \times 10^{-13}$
50	$(8.5 \pm 0.1) \times 10^{-13}$
60	$(1.9 \pm 0.1) \times 10^{-12}$
70	$(3.3 \pm 0.3) \times 10^{-12}$

Table 4.6: Self-diffusion coefficients from the thickness for [C4mim][OAc] at each reference temperature.

Reference Temperature (°C)	$D_{[C2mim][Oct]}$ ($10^{-12}m^2/s$)
80	1.9 ± 0.1
85	2.7 ± 0.1
90	4.2 ± 0.2
100	7.9 ± 0.3

Table 4.7: Self-diffusion coefficients from the thickness for [C2mim][Oct] at each reference temperature.

To determine the diffusion activation energy from the thickness measurements for both ILs, the data in Table 4.6 and Table 4.7 were used to set the relation between natural logarithm of diffusion against the inverse of temperature, as shown in Figure 4.15 (a) and (b). These linear fits indicate that the system follow Arrhenius behaviour. Interestingly, the values of the diffusion activation energies were found to be very close to those of the dissolution activation energies that found earlier in Table 4.5, with values of 77 $\pm$ 3 kJ/mol and 69 $\pm$ 5 kJ/mol for [C2mim][Oct] and [C4mim][OAc], respectively. A Table here comparing the two ways to determine the activation energy. Coagulation fraction and thickness/diffusion for the two ILs:

IL	Coagulation fraction E_a (kJ/mol)	Thickness/diffusion E_a (kJ/mol)
[C4mim][OAc]	67 ± 1	69 ± 5
[C2mim][Oct]	79 ± 1	77 ± 3

Table 4.8: Activation energy values from two ways; Coagulation fraction and thickness/diffusion for the two ILs.

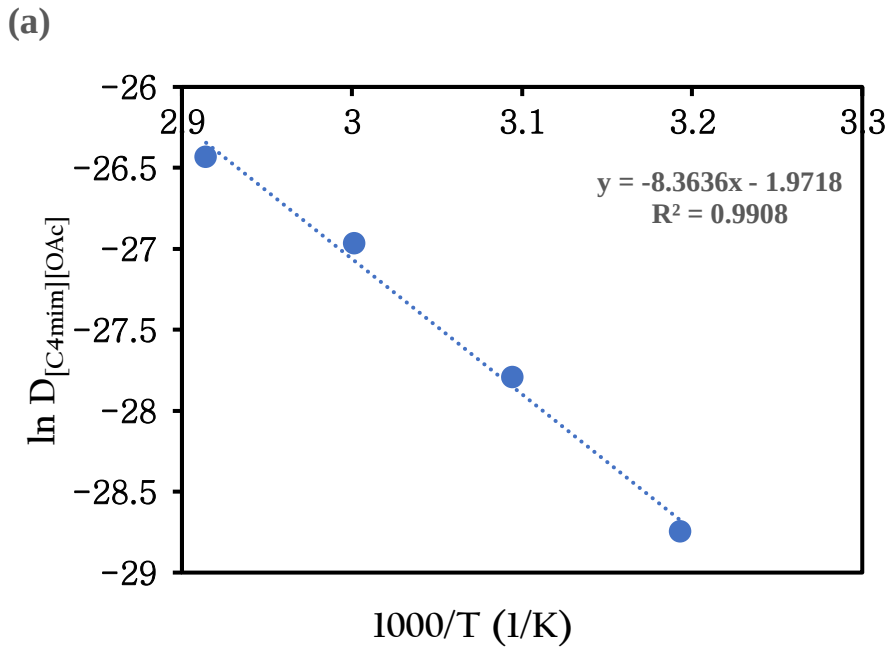

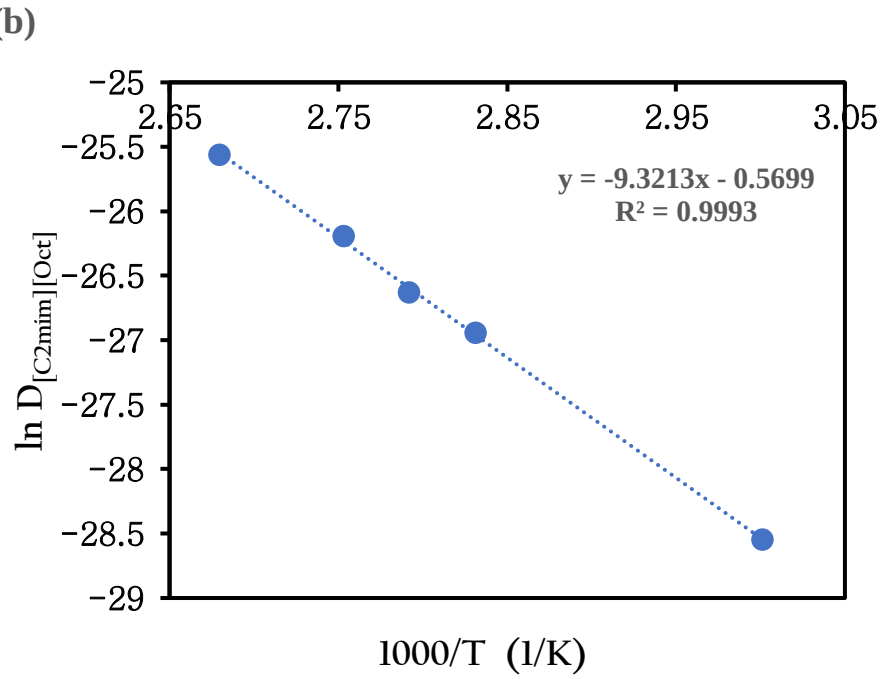

Figure 4.15: Natural logarthim of diffusion as a function of invers temperature of flax yarn, indicating Arrhunis plot. (a) [C4mim][OAc] and (b) [C2mim][Oct].

It is interesting at this point to compare the growth of the thickness, and the associated diffusion coefficients, for the three ILs all at the same reference temperature. A temperature of 60 °C was chosen for this comparison. As this temperature was below the measured temperature range for [C2mim][Oct], data had to be synthesised at 60 °C using TTS. First, using the Arrhenius equation again, but this time create the data at 60 °C by adjusting the values from Celsius to Kelvin according to the change in the previous data at 80 °C due to temperature change, so the linear equation at 80 °C is Y= − 9.5088x + 26.935, which represents the best fit line for this data, where Y is ln(α) and x is 1000/T. Then, calculate the temperature (1000/T) for 60 °C. Next, using this reciprocal values as x in the liner equation to solve for Y (which is ln(α)). The 1000/T value for 60 °C is given as 3.001651. Now, computing the ln(α) for that value, the recalculated ln(α) for 60 °C using the linear equation again is approximately -1.6071. By determining the difference between the calculated ln(α) at 60 °C and the actual ln(α) at 80 °C, then adjusting the ln(α) value at 80 °C by this difference to estimate what the ln(α) value would be if the temperature was 60 °C, so the calculated ln(α) for 60 °C is -1.6071, which used to shift the data from 80 °C to 60 °C. Now, these adjusted values form a new master curve at 60 °C,

which used to compare with other ILs. Figure 4.16 shows the relationship between thickness and square root of time √t, of each IL at 60 °C, showing a linear relationship in each case and the relative diffusion coefficients for each IL. As all three show a linear relationship with √t, our hypothesis is that dissolution of the flax yarns (in all three ILs) is controlled by the diffusion of each IL, most likely through a region of swollen cellulose/IL around each yarn. From the graph [C2mim][OAc] shows the faster growth rate followed by [C4mim][OAc], and [C2mim][Oct] shows the slowest rate.

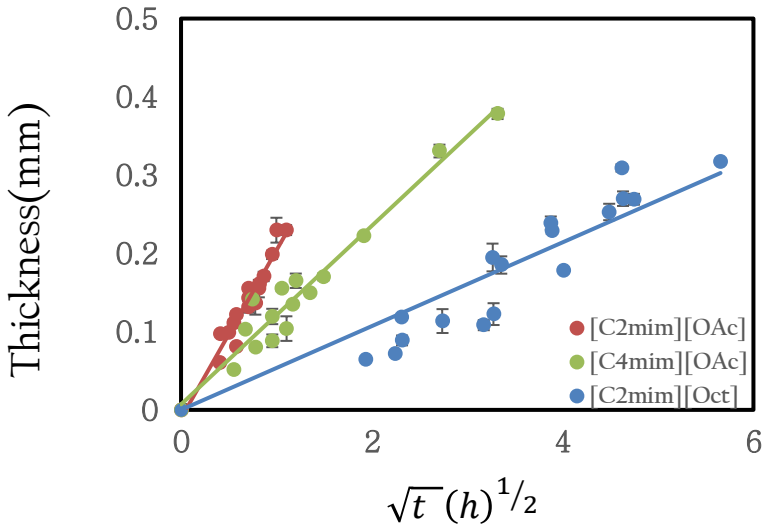

Figure 4.16: Thickness of coagulated regions as a function of square root of hours (mm/$(\boldsymbol{h})^{1/2}$) at 60 °C.

This growth rate of the thickness could be influenced by the viscosity of each IL, and molecular structure (i.e., the anion/cation combinations) of each IL. Moreover, the longer alkyl chain on the imidazolium cation (C4mim) in comparison to the ethyl chain on [C2mim] may be the cause of the decreased diffusion coefficient since it might result in reduced ion mobility and increased viscosity. [C2mim][Oct] has the lower value of the diffusion coefficient can be linked to the higher viscosity as showed in the graph. The larger size of the (Oct) can result in more significant interactions among ions, which can result in reduced mobility. The obtained self-diffusion coefficients of each IL at 60 °C are summarised in Table 4.9.

[C2mim][OAc] m^2/s	**[C4mim][OAc]** m^2/s	**[C2mim][Oct]** m^2/s
$(5.6 \pm 0.2) \times 10^{-12}$	$(1.9 \pm 0.1) \times 10^{-12}$	$(3.9 \pm 0.1) \times 10^{-13}$

Table 4.9: Diffusion coefficient of the ions at 60 °C.

Each factor that could control the different dissolution speeds for these three ILs is now investigated in turn.

4.3.6. Density

The density measurements at 20 °C for the three pure ILs [C4mim][OAc], [C2mim][Oct], and [C2mim][OAc] are given in Table 4.10 with a list of density values for ILs obtained from our experimental measurements and values from literature.

The density of each IL was determined as follow: first, using a glove box to minimise contamination, a small amount of the IL was carefully transferred into a graduated cylinder. Then, the mass of the IL was accurately measured using an analytical balance, while its volume was recorded from the graduated cylinder. After that, the density of the IL was calculated by dividing the measured mass by the recorded volume, yielding the density in units of g/cm³. Next, the molar mass of the IL was obtained from its chemical formula, and the molar volume was determined by dividing the molar mass by the calculated density. This step calculates the molar volume of the ionic liquid (IL) in cubic metres (m³), which is used to estimate the size of each IL molecule for later analysis.

Ionic liquid density (g/cm^3) at 20 °C	Experiment	Literature review	References
[C2mim][OAc]	1.14 ± 0.06	1.1014 1.1024	[113] [277]
[C2mim][Oct]	1.08 ± 0.04	0.9998	[113]
[C4mim][OAc]	1.03 ± 0.01	1.0557 1.040.6	[135] [276]

Table 4.10: Density of ILs [C2mim][OAc], [C2mim][Oct] and [C4mim][OAc] obtained from experiments and compared with references values at 20 °C.

4.3.7 Viscosity measurements of the pure ILs

Figure 4.17 shows a comparison of the viscosity of the three ILs [C2mim][OAc], [C4mim][OAc] and [C2mim][Oct] as a function of shear rate at a chosen temperature of 50 °C. The average value of viscosity for each IL calculated from the Newtonian shear rate for each temperature and the measurements were repeated three times to calculate an average value of viscosity, and the standard deviation in the measurements was calculated. The IL [C2mim][OAc] showed a noticeable decrease in viscosity compared to the two ILs [C4mim][OAc], and [C2mim][Oct], with the IL [C2mim][Oct] has a higher viscosity compared to other two and this might be due to the anion's longer chain (Oct). The length and also the structure of both cation and anion significantly affect viscosity as expected.

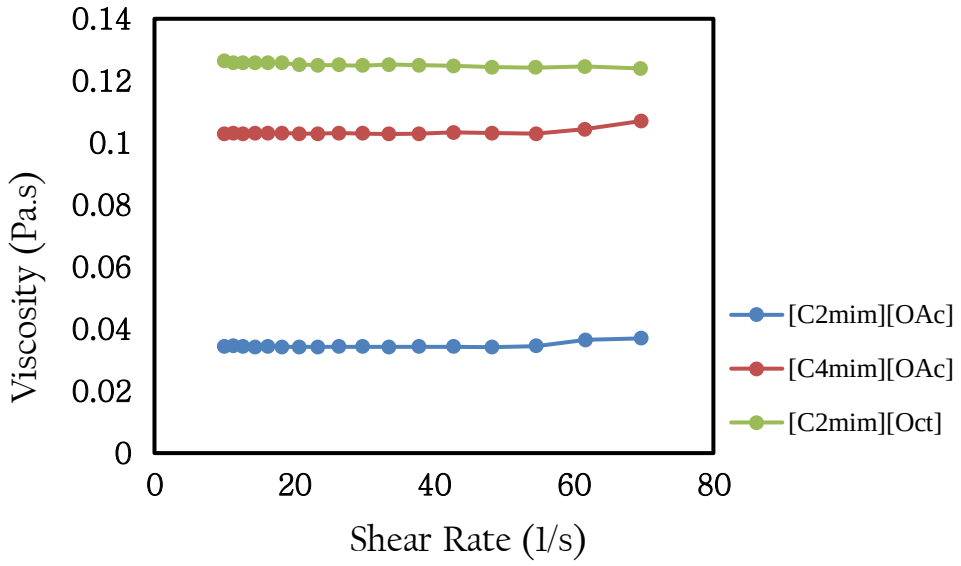

Figure 4.17: Viscosity at 50 °C verses shear rate of the three different ILs.

Seki et al. (2010) measured the viscosity of various room-temperature ionic liquids and analysed how different cations and anions affect these properties. They found that the viscosity of both cationic and anionic were significantly influenced by their molecular geometry (shape) rather than the molecular weight [278]. In addition, the study by Green et al. (2017) discusses how the presence of the acetate anion [OAc] in both [C2mim] and [C4mim] results in more powerful ionic interactions compared to the octanoate ([Oct]) anion in [C2mim][Oct], this difference in interactions leads to various viscosity attributes at different shear rates. Specifically, the acetate anion forms small, stable aggregates that are less sensitive to flow and temperature changes, whereas the octanoate anion forms larger, less stable aggregates that decrease in size with increased flow and temperature [113]. Yadav et al. (2018) discussed the densities and dynamic viscosities of ionic liquids with different cations and anions. They observed that the anion type significantly controls the density and viscosity [279]. The molecular weight and therefore the size of IL is expected to increase the viscosity of the IL. An extensive study by Tatiana Budtova and Patrick Navard (2015) found that the viscosity of cellulose solutions increases with its molecular weight due to the higher molecular weights suggest longer polymer chains, which entangle more easily and increase flow resistance [230]. The average value of viscosity for each IL calculated from the Newtonian shear rate for each temperature and the measurements were repeated three times to calculate an average value of

viscosity. The standard deviation in the measurements was calculated. The viscosity value for each IL at 50 °C is shown in Table 4.11.

[C2mim][OAc] (Pa.s)	**[C4mim][OAc] (Pa.s)**	**[C2mim][Oct] (Pa.s)**
0.034 ± 0.025	0.103 ± 0.032	0.125 ± 0.047

Table 4.11: The zero-shear rate viscosity for each IL at 50 °C.

The viscosities η for both ILs [C4mim][OAc] and [C2mim][Oct] as a function of temperatures ranging from 30 °C to 80 °C were measured. Figure 4.18 shows viscosity as a function of shear rate for each IL calculated from the Newtonian shear rate for each temperature, averaged over three measurements. Viscosity is expected to decrease as temperature increases; however, the viscosity generally increases as the molecular weight and the length of the anion chain increases. Each IL presents a decreasing viscosity as temperature increases, with [C2mim][Oct] having a higher viscosity than [C4mim][AOc] across the temperature range studied (30 °C to 80 °C). This is due to the longer chain of the octanoate anion and the higher molecular weight make the molecules moves slower and making fewer attempts to overcome the barriers, leading to increase the viscosity at all temperature. While, [C4mim][OAc] has a lower molecular weight, its molecular move faster, making more attempts to overcome barriers, which lower its viscosity at all temperature.

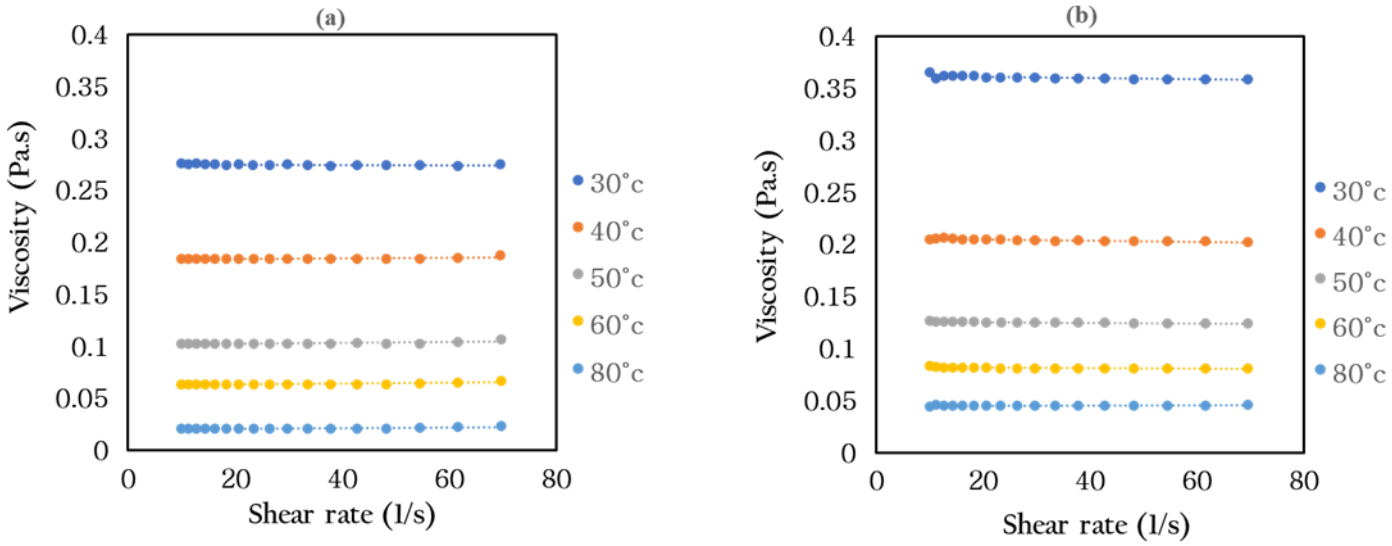

Figure 4.18: Viscosity as a function of shear rate at temperatures of 30, 40, 50, 60 and 80 ˚C for both pure ILs (a) [C4mim][OAc] and (b) [C2mim][Oct].

Figure 4.19 (a and b) shows the viscosity (how measured) for obtained at each temperature plotted against the inverse of the temperature for [C4mim][OAc] and [C2mim][Oct]. The activation energies were found by using the slope of this Arrhenius plots for the data of viscosity. For both ILs, the plots of ln (η) inverse temperature are linear in the range of temperatures studied. The corresponding $E_{a,\eta}$ values are showing in the Table 4.12. Table 4.12 highlights that the activation energy values are higher for [C4mim][OAc] than that of [C2mim][Oct]. The activation energy of viscosity is a measure of the energy required for molecular motion within a substance to overcome intermolecular force, flow, and interaction in a fluid. It describes the temperature dependence of viscosity, indicating how the viscosity of a fluid changes with temperature. A high activation energy of [C4mim][OAc] suggests that the substance has a strong intermolecular structure, resulting in higher resistance to flow and a larger change in viscosity with temperature, while a lower activation energy of [C2mim][Oct] indicates that the substance has a week intermolecular structure and is more easily able to flow with a smaller change in viscosity with temperature. Generally, longer alkyl chains enhance molecular packing and ordering, which can result a higher degree of aggregation and stronger intermolecular interactions and thus higher activation energies [280, 281].

The activation energy for viscos flow $E_{a,\eta}$ of ILs [C2mim][Oct] and [C4mim][OAc], measured over a temperature range of 30 ˚C to 80 ˚C, were found to be 40 $\pm$ 1 kJ/mol and 46 $\pm$ 2 kJ/mol, respectively. For IL[C2mim][OAc], the $E_{a,\eta}$ values were found to be 37 $\pm$ 1 kJ/mol, as shown in previous chapter. These findings indicate that [C4mim][OAc] needs a higher amount of energy to overcome the molecular interactions for flow in comparison to [C2mim][OAc], and [C2mim][Oct]. These differences can be related to the higher viscosity resulting from the longer cation chain [C4mim]. While the difference between the common cation, [C2mim], and the differences in anions (Oct) and (OAc), their interactions with the [C2mim] cation led to exhibits higher viscosity energy barriers for viscous flow of (Oct) due to the longer anion chain. It is also interesting to note that that the activation energies of the pure ILs, is significantly lower than that found in the dissolution experiments. This enhances our hypothesis that the diffusion coefficients determined from the growth of the coagulated regions refers to the diffusion of the ILs in an IL/cellulose solution, not just the diffusion of the pure ILs themselves.

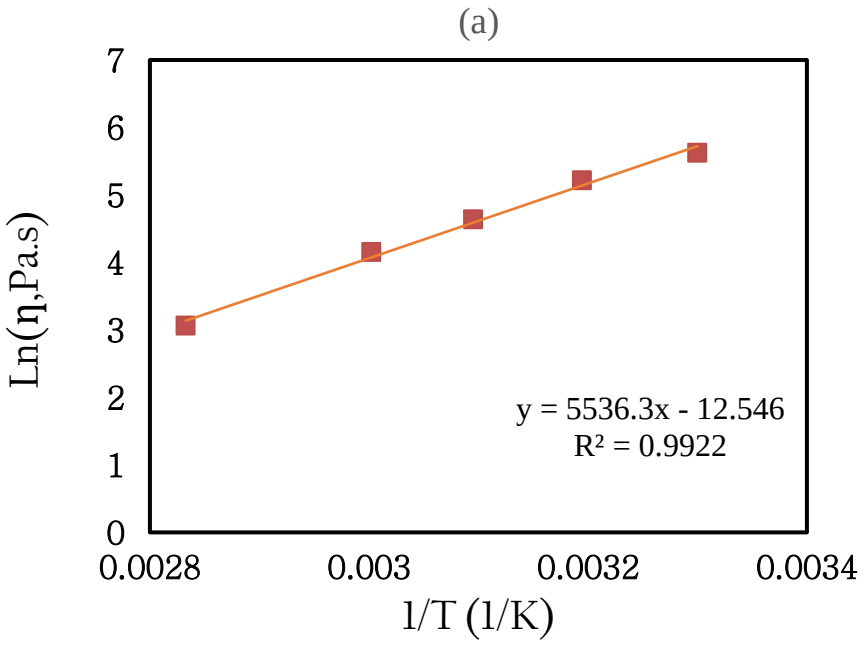

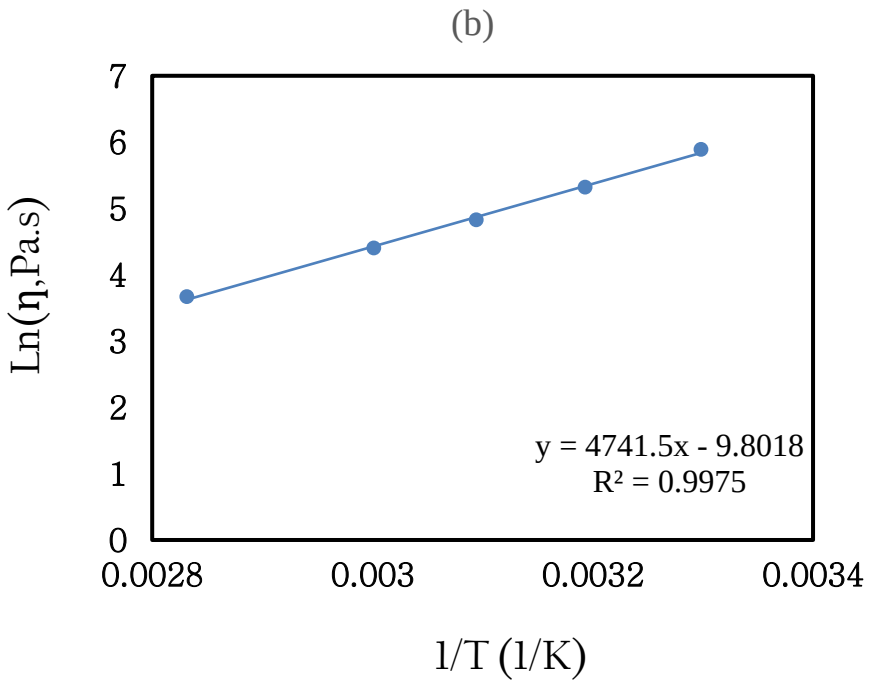

Figure 4.19: Shows ln (***η***) viscosity verses inverse temperature (a) [C4mim][OAc], and (b) [C2mim][Oct].

Activation Energy, kJ/mol	**[C4mim][OAc]**	**[C2mim][Oct]**	**[C2mim][OAc]**
$E_{a,\eta}$	46 ± 2	40 ± 1	37 ± 1

Table 4.12: Activation energies for viscous flow for both ILs.

4.3.8 Self- diffusion coefficient (NMR)- Pure ILs

The spectrum of pure ILs with full peak assignments, which correspond to the various proton environments, is seen above in Figure 4.3, (H1–H9) and (H1-H10) for [C4mim][OAc] and [C2mim][Oct], respectively. One can observe how the diffusion of the anion and cation of ILs changes, at temperatures (30 °C, 40 °C, 50 °C and 60 °C) using ^{1}H NMR spectroscopy. The assigned proton resonances (1−9) for the [C4mim][OAc], and (1-10) for the [C2mim][Oct] molecules were shown above in Figures (4.2) and (4.3). In our work, we used the proton resonance (peak 5) as a reference point to determine the chemical shift of all the other resonances by measuring their distances from this peak. Previous research on imidazolium based ionic liquids (ILs) has conducted many ^{1}H NMR investigations. These studies have demonstrated that the chemical shift position of the methyl group (peak 5) is least affected by external factors [110, 113, 243, 282]. Both the anion and cation show an increase in intensity as temperature increase suggesting that molecular mobility for both ions also increases with temperature. Higher temperatures lead to lower viscosity and higher diffusion rates [283]. The results of self-diffusion coefficients as a function of temperatures in Table 4.13 and Table 4.14 show that both ions are increased in diffusion coefficient with increasing temperature for [C4mim][OAc] and [C2mim][Oct], respectively.

T (°C**)**	**NMR diffusion coefficient (m^2/s)**	
	$[C4mim]^+$	**$[OAc]^-$**
30	4.69E-12	4.53E-12
40	8.73E-12	8.50E-12
50	1.43E-11	1.38E-11
60	2.28E-11	2.22E-11

Table 4.13: NMR self-Diffusion Coefficients of $[C4mim]^+$and $[OAc]^-$ as a Function of temperatures.

T (°C**)**	**NMR diffusion coefficient (m^2/s)**	
	$[C2mim]^+$	**$[Oct]^-$**
30	3.94E-12	3.17E-12
40	6.82E-12	5.28E-12
50	1.12E-11	8.93E-12
60	1.55E-11	1.26E-11

Table 4.14: NMR self-Diffusion Coefficients of $[C2mim]^+$ and $[Oct]^-$ as a Function of temperatures.

With increasing temperature, there may be changes in the structure of the ionic liquid, such as a transition from more ordered to less ordered structures, which can also contribute to easier ion movement. It was found that the larger cation diffuses faster than the anion in both ILs. Moreover, both the cation and anion in [C2mim][Oct] have lower self-diffusion coefficient values compared to [C4mim][OAc] across the same range of temperatures.

The study examined the self-diffusion coefficients, D, of both ILs throughout a temperature range of 30 °C to 60 °C of [C4mim][OAc] and [C2mim][Oct] are presented in Figure 4.20 (a) and (b). The diffusion data could be used to calculate the activation energy for diffusion of the cation and anion. Arrhenius plots Eq. 3.10, which graph the natural logarithm of diffusion coefficients versus the inverse of temperature (in kelvin), provides the activation energies, indicating the sensitivity of diffusion to temperature changes. Both ILs show a linear trend within the temperature range studied. The activation energies obtained from the Arrhenius plots are given in Table 4.15 for both ions. Table 4.15 represents the activation energy values of [C4mim][OAc] and [C2mim][OAc] were obtained from NMR diffusion measurement which is very close to the activation energy value of viscosity, so both ILs follow a Stokes-Einstein relationship [223], as will be described later.

It was observed that the diffusion coefficient of the anion and cation in the [C4mim][OAc] is larger than that of [C2mim][Oct] at each temperature studied.

However, both ILs are observed to have cation higher self-diffusion coefficient values than anion. Since the imidazolium anion is smaller than cation and therefore the diffusion of anion is expected to be faster than cation, but experimentally this is not the case. This unexpected slower diffusion of the anion is related to the rich aggregation in anion compered to cation, as suggested in [284]. Ion diffusivities are influenced by ions' size, shape, and intensity of interactions [282].

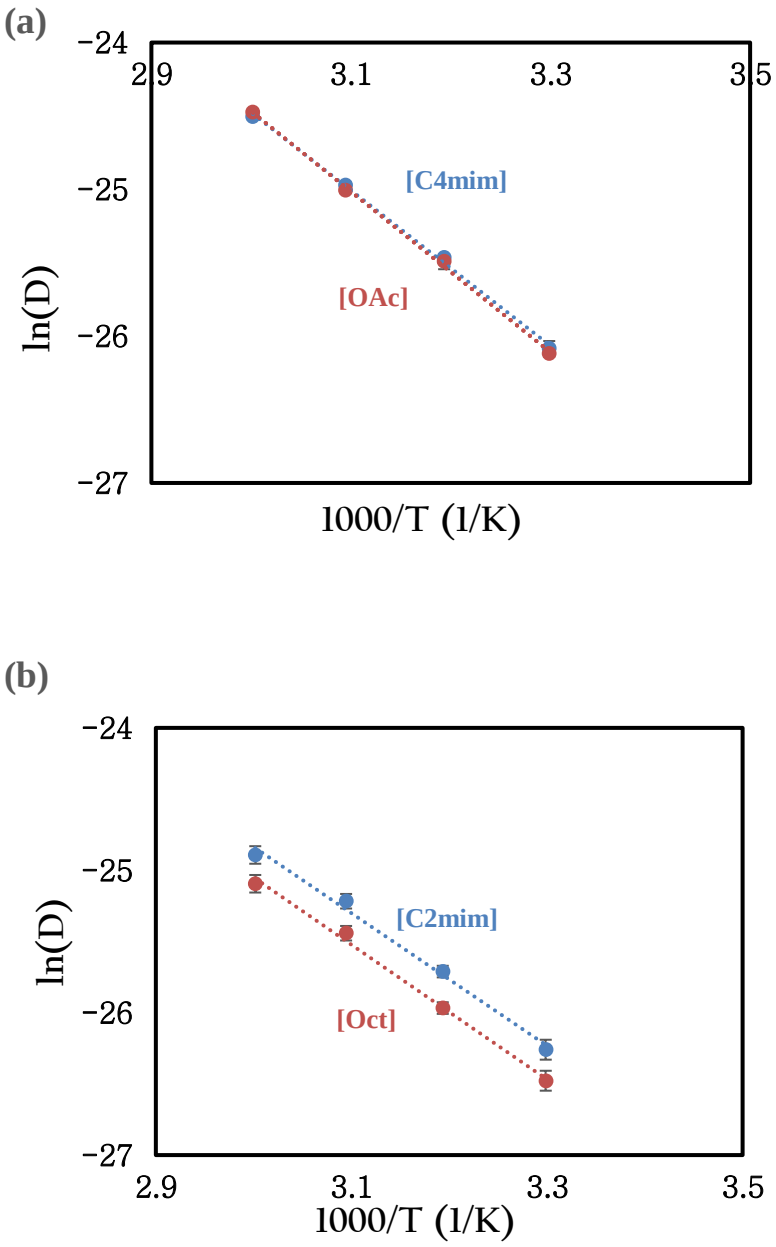

Figure 4.20: Arrhenius plots of the self-diffusion coefficient for the anion and cation of the ILs as a function of the inverse temperature. (a) [C4mim][OAc] and (b) [C2mim][Oct]. Uncertainty in ln(D) of 7% is approximately the size of data points.

ILS	[C2mim][OAc]	[C4mim][OAc]	[C2mim][Oct]
Viscosity E_a (kJ/mol)	37 ± 1	46 ± 2	40 ± 1
NMR D cation E_a (kJ/mol)	42 ± 2	44 ± 1	38 ± 2
NMR D anion E_a (kJ/mol)	43 ± 2	45 ± 1	39 ± 3

Table 4.15: The activation energies of the viscous flow and NMR diffusion of cation and anion for the three ILs.

4.3.9 Stokes-Einstein- Analysis

ILs can be analysed using Stokes-Einstein analysis in order to understand the relationship between microscopic (diffusion) and macroscopic (viscosity) properties. The Stokes-Einstein equation (Eq. 3.11) can be rearranged to calculate the hydrodynamic radius of an ion or a molecular with the knowledge of both data of the viscosity and diffusion coefficient. The hydrodynamic radius $R_{h,i}$ was also determined using the density data and Eq. 3.12.

From this formula the values of $R_{h,i}$ for the ILs [C4mim][OAc] and [C2mim][Oct] are 3.41 Å and 3.65 Å, respectively. The effective values of $R_{h,i}$ were found to be 3.03 Å and 2.28 Å for the [C4mim] and [OAc], respectively, which are close to previously published values of 3.01 Å and 2.26 Å [133].

For the radius of the [C2mim] and [Oct] are 2.77 Å and 3.01 Å, respectively, which are close to previously published values of 2.86 Å and 3.11 Å [113]. These values of $R_{h,i}$will be referred to as ‘density’ values or theoretical values.

Experimentally, the data of NMR diffusion coefficient against the ratio of temperature to the viscosity form a single master curve for each ion, as seen in Figure 4.21. These plots of D against T/η for all species in [C4mim][OAc] and [C2mim][Oct] are presented. It was found that, the plots of D against T/η showed linear relationships, and this linear correlation in the experimental data demonstrates that the Stokes-Einstein equation provides a suitable description of the relationship between D and T/η for Both systems of [C4mim][OAc]and [C2mim][Oct].

The gradients from the Stokes-Einstein fitting are used to calculate the values of $R_{h,i}$, refer to Eq. 3.11. The values of the $R_{h,i}$ are 2.47 Å and 2.54 Å, for the cation and anion of [C4mim][OAc], respectively. For the radius of the cation and anion at [C_2mim][Oct] are 2.75 and 3.40 Å, respectively. The average values of $R_{h,i}$ for the ILs [C4mim][OAc] and [C2mim][Oct] are 2.51 Å and 3.07 Å, respectively. These results acquired using the slopes of each ion from SE approach which referred as Stokes-Einstein values (SE) are determined from Figure 4.21. It should be noticed that the larger anion in IL [C2mim][Oct] diffuses slower experimentally and theoretically than the cation due to the large size of anion. So, the use of microscopic data (diffusional) compared to bulk attributes (density) distinguishes the two approaches. Both approaches produce consistent results, which give insight on the systems' microscopic behaviour (e.g., aggregation and ionic packing) and macroscopic features (e.g., viscosity) that follow to the SE system.

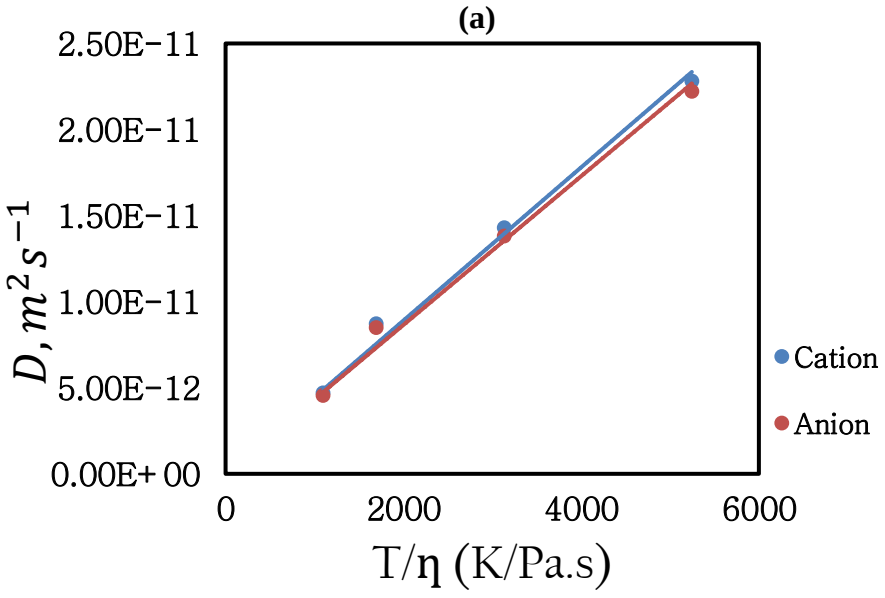

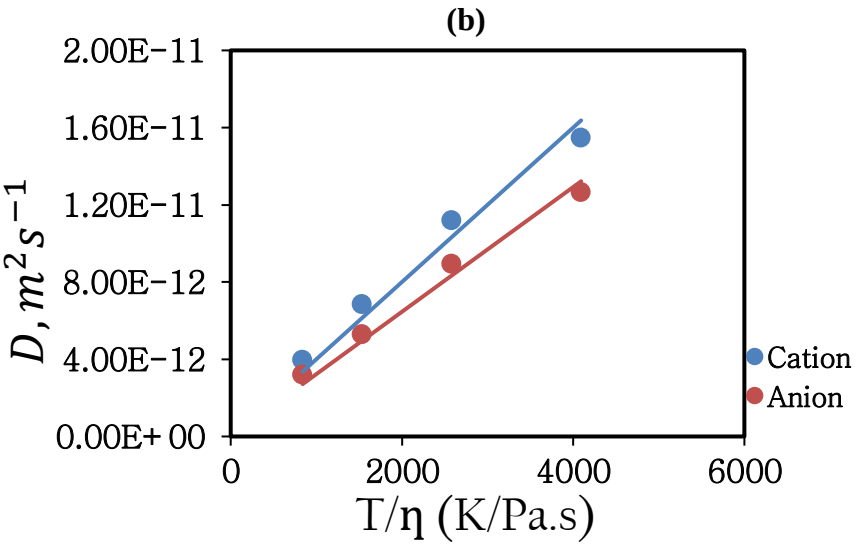

Figure 4.21: NMR diffusion coefficients as a function of the ratio of temperature to the viscosity for (a) [C4mim][OAc] and (b) [C2mim][Oct]. linear fits are used as a visual guide calculated from Eq. 3.11 and each ion $R_{h,i}$ from Eq. 3.12.

4.3.10 Investigating the dissolution speed and mechanisms of the three ILs: [C2mim][OAc] [C4mim][OAc] and [C2mim][Oct] at 60 °C.

To do a comparison between the three ILs investigated, it is necessary to compare them all at the same reference temperature. The chosen temperature was 60 °C, as the two acetate anion ILs ([C2mim][OAc] [C4mim][OAc]) dissolved at a significant rate at this temperature. However (as shown in Figure 4.9) the Octanoate anion in the IL [C2mim][Oct], did not dissolve significantly at this temperature in a few hours. Therefore we need first to do a shifting process for the data of Arrhenius plot at 80 °C for IL [C2mim][Oct] to generate a master curve at 60 °C, as describe above. Figure 4.22 shows a comparison of the growth of the coagulation fraction as function of dissulotion time for all three ILs at a reference temperature of 60 °C. The differences between the three ionic liquids based on the information provided in the plot indicate that the IL[C2mim][OAc] has the fastest dissolution rate among the three, followed by the other acetate anion IL [C4mim][OAc]. The slowest dissolving rate is exhibited by [C2mim][Oct], as demonstrated by its CF curve.

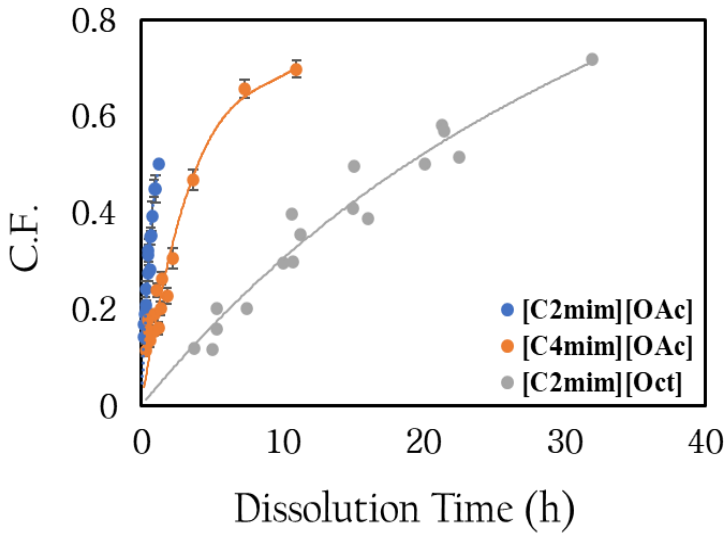

Figure 4.22: Master curves for the three ILs for the coagulation fraction as a function of dissolution time (h) at temperature of 60 °C.

These differences could be due to the length of the alkyl chain in the cation or the nature of the anion in the ionic liquids or the molecular weight of the ILs. Huddleston et al. carried out on investigation of ILs that contained $[C_nmim]^+$ cations and a variety of anions in order to determine the effects of altering the length of the cation chain [285]. They compared the alkyl side-chain lengths between octyl (n = 8) and methyl (n = 1). An increase in the chain length was observed to result in a uniform increase in viscosity, a decrease in melting point, and a reduction in density for the same anion. Moreover, longer chains typically resulted in lower solubility, which seems to be demonstrated by the difference between [C2mim] and [C4mim]. This is due to the hydrophobic interactions increased throughout longer chains, leading to a more ordered structure [286, 287]. Moreover, the anion difference between [OAc] (acetate) and [Oct] (octanoate) also seems to play a significant role in the dissolution characteristics.

One factor that could be important in affecting the dissolution speed is the pure IL viscosity. To study this effect, the results from Figure 4.22 were plotted with the x-axis now normalised by the measured viscosities from section 4.3.7. The datasets aim to eliminate the direct impact of viscosity on the dissolving rate by dividing the dissolution time by viscosity. This means that for substances with a higher viscosity, which would naturally take longer to dissolve, the dissolution time is adjusted to reflect what the dissolution time might be if the viscosity were the same as that of substances with lower viscosity. This means that the time scales are determined by

viscosity, so large time scales will give large viscosity, so we normalise the times by using viscosity, as seen in as seen in Figure 4.23. It is clearly seen that the two ILs acetate based, [C2mim][OAc] and [C4mim][OAc] when the viscosity is taken into account, they nearly overlap. In going from the [C2mim] to [C4mim] the cation is larger which slows diffusion and raises viscosity, but it has not significantly changed any other dissolution factor. When the anion is changed to octanoate then the data no longer overlaps with the acetate results, even when taking into account the change of viscosity. This hints at the more important role that the anion plays in the dissolution process.

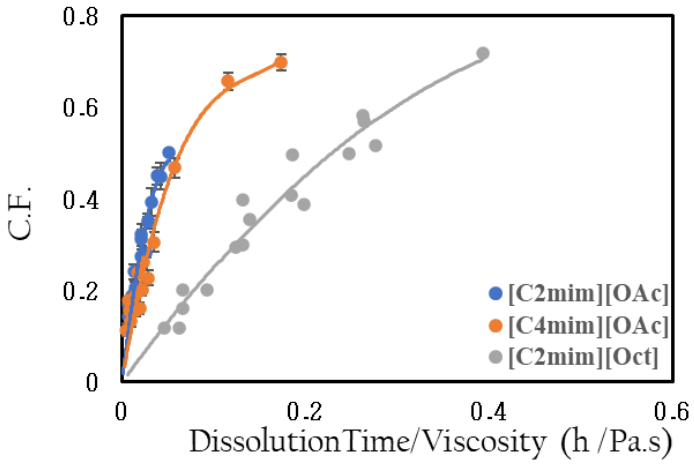

Figure 4.23: Master curves for the three ILs for the coagulation fraction (C.F.) as a function of dissolution time /Viscosity (h/Pa.s) at temperature of 60 °C.

In the next comparison (Figures 4.24 (a) and (b)) the dissolution time X-axis has been normalised by the self-diffusion coefficient D of the cations and anions measured from NMR. Here we multiply the time by the diffusion coefficient to take into account the greater mobility and its effects on dissolution timescales. A large D would suggest a short dissolution time. Figure 4.23 shows that with this normalisation the results are very similar to the viscosity normalisation of Figure 4.22. [C2mim][OAc] and [C4mim][OAc] have a similar relationship between the growth of the coagulation fraction and normalised time (using either the cation or anion diffusion coefficients) and as for Figure 4.23, [C2mim][Oct] results shows a slower overall dissolution process even when normalised.

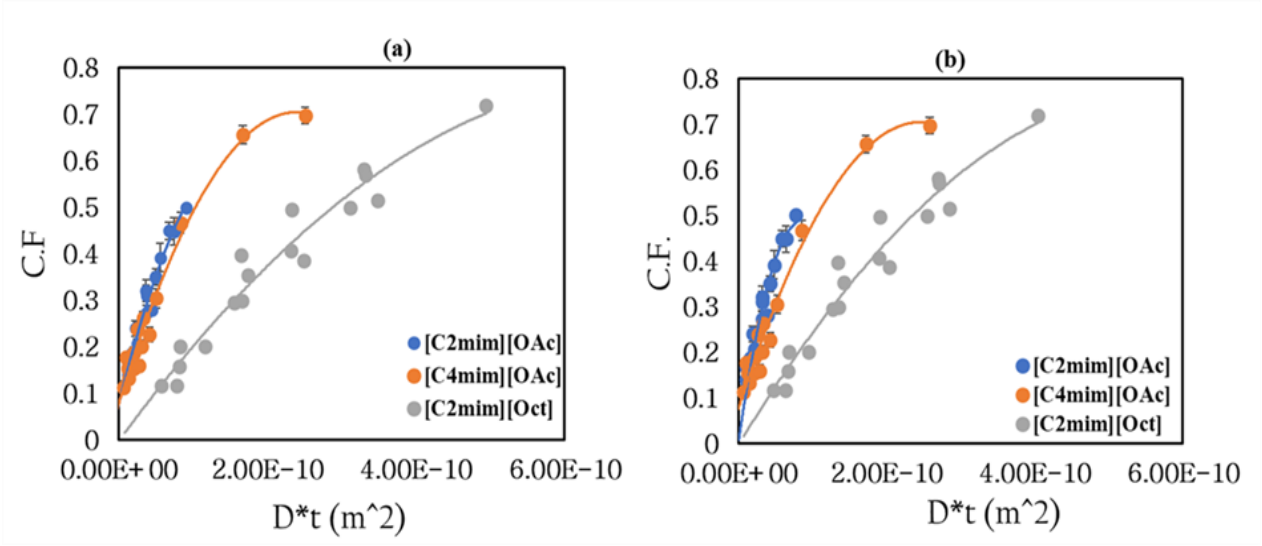

Figure 4.24: Master curves for the three ILs for the coagulation fraction (C.F.) as a function of normalisation the self-diffusion coefficient measured from NMR at temperature of 60 °C of the (a) cations and (b) anions.

Using either solution viscosity or NMR IL ion self-diffusion, the results with the same anion collapse to a similar dissolution curve, but the different anion is still slower. For the final normalisation, the dissolution time is normalised by the diffusion coefficients calculated directly from the growth of the thickness of the coagulated region and these results are shown in Figure 4.25. It is seen that normalising the dissolution time by this factor, that all data collapses onto a set of overlapping curves. Our hypothesis is therefore that the dissolution of the flax yarn is controlled by the diffusion of each IL through a saturated cellulose solution that surrounds each flax yarn as the dissolution progresses, such that when you take into account the additional slowing down of the ions due to the presence of cellulose, a master curve can be obtained.

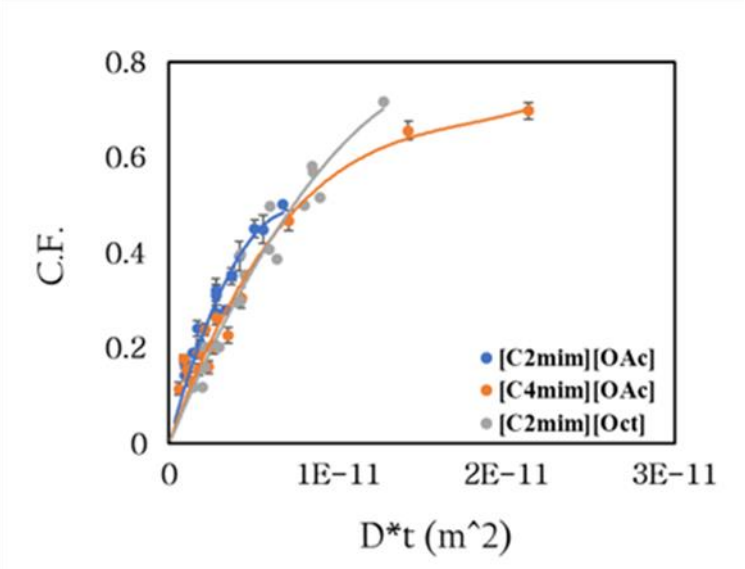

Figure 4.25: Master curve representing the results of the three ILs at temperature of 60 °C for the coagulation fraction as function (C.F.) of the D*t from thickness measurements.

A measure of the relative speed of dissolution in the three ILs can be obtained by shifting the generated master curves at 60 °C to make them overlap. Figure 4.26 below shows the datasets of the three ILs [C4mim][OAc], [C2mim][Oct] and [C2mim][OAc] in order to calculate the relative dissolution rate between systems. The procedure of forming these master curves was described in the TTS method shown in Figures (3.8) in previous chapter, and the TTS in Figures (4.6) and (4.10), so by choosing the data of [C2mim][OAc] as reference data, then shifting all the data again for these systems with now each master curve itself shifted separately in natural logarithmic time to overlap with the master curve of [C2mim][OAc] to create a master-master curve. So, for example, to overlap the data of [C4mim][OAc] with the master curve of the data of [C2mim][OAc], needed a scaling factor α of 0.25, determined from the shift factor ln(α). Hence, the dissolution rate is 4 times slower for this system. So, the shift factors of each IL that used to create the master-master curve can use to measure the relative dissolution speed of each IL directly. The obtained shift factor ln(α) and relative dissolution rates are summarised in Table 4.16.

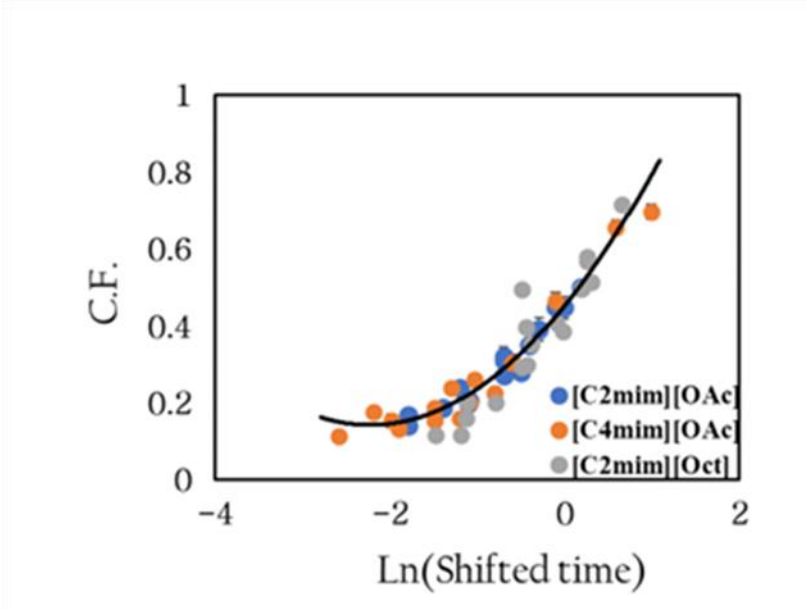

Figure 4.26: Master curve for the three ILs for the coagulation fraction (C.F.) as a function of Ln (shifted time) in order to calculate the relative dissolution rate between systems.

ILs	**ln(α)**	**Relative dissolution rate**
[C2mim][OAc]	0	1
[C4mim][OAc]	-1.40 ± 0.05	0.25
[C2mim][Oct]	-2.80 ± 0.03	0.06

Table 4.16: The obtained shift factor ln(α) and relative dissolution rate for the ILs.

Now, the hydrodynamic radius $R_{h,ILs}$ for each IL was determined to plot a relationship between the relative dissolution speed of each IL and their size to determine the relative dissolution speed between systems. The empirical equation (recall Eq. 3.12) was applied to the molar mass, utilising it as the input parameter to determine the effective size of the IL. For the ILs [C2mim][OAc], [C4mim][OAc] and [C2mim][Oct], the total size of cation/anion for each IL are 3.13 Å, 3.41 Å and 3.65 Å, respectively.

By plotting the relationship between the relative dissolution speed of each IL and their size, this plotted line suggests reveals that as the size of the ILs increases, the relative dissolution speed decreases rapidly, see Figure 4.27. This implies that the differences in hydrodynamic radii of ionic liquids (ILs) have an important impact on the ability to dissolve cellulose. The IL [C2mim][OAc] shows a smaller ion, which might be higher ability to penetrate the cellulose structure, therefore disrupting the hydrogen bonds between cellulose chains compared to other ILs. The IL [C2mim][Oct] might be less efficient in breaking down cellulose due to their larger size, which can prevent their ability to penetrate the tightly packed cellulose network. The dotted line of the graph shows a clear downward trend, indicating dissolution speed is inversely related to the size of the ILs. Broadly speaking, the [C2mim][OAc] is 5 times faster than [C4mim][OAc], and 10 times than [C2mim][Oct], as shown in Fig.4.27.

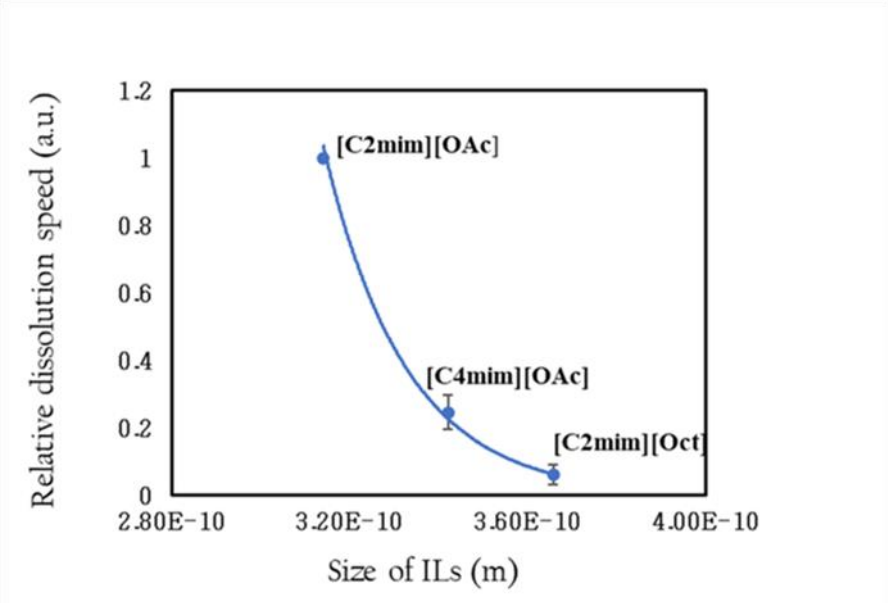

Figure 4.27: Master-master curve shows all the results of ILs in order to calculate the relative dissolution rate between systems. The exponential fit of the relationship is such that as the size of the ILs increases, the relative dissolution speed decreases rapidly.

4.4 Conclusion

In this chapter, we have investigated the imidazolium- based ILs [C4mim][OAc] and [C2mim][Oct] in both macroscopic and microscopic properties over a range of time and temperature. These results compared and combined with the previous chapter detailing a study of [C2mim][OAc] in the same flax yarns. This work reveals the role of cation and anion structure on the dynamics of cellulosic yarn dissolution. The dissolution process involved submerging the yarns in the ILs for a range of temperatures and times, followed by coagulation in water. The coagulated material formed as an outer ring that surrounded the central undissolved yarn. The growth of the coagulated cellulose was found to increase as the temperature and dissolution time increased. By shifting the data on to the natural logarithmic scale then shifting each temperature dependent data set using shift factors to overlap, a master curve could be formed. The formation of Arrhenius curve was dependent on the relationship between the shift factors against the inverse of the dissolution temperatures so, a linear fit revealed Arrhenius behaviour in the system using TTS analysis, allowing the activation energy to be calculated. The energy required for dissolution of flax yarns in ILs [C4mim][OAc] and [C2mim][Oct] were found to be 67 $\pm$ 1 kJ/mol and 79 $\pm$ 1, respectively. All of the above analysis is carried out again three times for each IL, by

using the other three temperatures as reference temperatures (T_{ref}), so for [C4mim][OAc], shifting all data to 30 °C and 40 °C and finally 60 °C, and for [C2mim][Oct], shifting all data to 80 °C and 90 °C and finally 100 °C in order to create a master curve for each set of data at each of these temperatures. The shift factors used to form the TTS shifting, can be plotted separately as a function of reference temperature as before for the 50 °C, and 85 °C TTS shifting results. Each set of shift factors for each of the reference temperatures is again found to display an Arrhenius behaviour, each giving a dissolution activation energy. The activation energies for the IL [C4mim][OAc] at 30 °C, 40 °C and 60 °C were found to be 67 ± 1 kJ/mol, which is similar with to the previous determined values at 50 °C. For [C2mim][Oct], the activation energies at 80 °C, 90 °C and 100 °C were found to be 79 ± 1 kJ/mol, which is consistent with our previous determined values at 85 °C. From these experimental results, we determine the intercepts lnα at each reference temperature themselves were follow an Arrhenius law, being linearly dependent on the inverse of the reference temperature, allowing to measure the activation energy for each IL. The intercepts activation energies for the IL [C4mim][OAc], and [C2mim][Oct] are found to be 69 ± 2 kJ/mol, and 79 ± 3 kJ/mol, which is identical with the previous determined values of the dissolution process.

The growth of the thickness of the outer coagulated layer was measured also for each processed yarn as one of important key to calculate the diffusion coefficients. The dataset of thickness as a function of the square root of time showed a linear relationship, this is indicative that diffusion controlled the dissolution process which can be described by Fick's law of diffusion. The calculated activation energies of ILs [C2mim][Oct] and [C4mom][OAc], the diffusion from the growth of thickness were found to be 77 $\pm$ 3 kJ/mol and 69 $\pm$ 5 kJ/mol for [C2mim][Oct] and [C4mim][OAc] respectively, very similar to those from the growth of the coagulation areas.

The pure IL solution viscosities were measured for both ILs [C4mim][OAc] and [C2mim][Oct], and as expected decreased when temperature is increased. [C2mim][Oct] has a higher viscosity than [C4mim][AOc] at all temperatures studied due to the longer chain of the octanoate anion and a higher molecular weight increasing the overall viscosity. However, the viscosity activation energy for [C4mim][OAc] is higher than [C2mim][Oct] this might became the acetate anion is less sensitive to flow and temperature changes. The viscosity activation energy for [C4mim][OAc] and [C2mim][Oct] were found to be 46 $\pm$ 2 kJ/mol and 40 $\pm$ 1 kJ/mol, respectively.

It has been demonstrated that NMR techniques are effective for examining the structure and dynamics of pure ILs. NMR self-diffusion coefficient for each component ($[C4mim]^+$,$[OAc]^-$,$[C2mim]^+$ and $[Oct]^-$ were measured using high field NMR (400 MHz). It was found that larger cations $[C4mim]^+$ and $[C2mim]^+$ diffuses faster than their anionic counterparts $[OAc]^-$ and $[Oct]^-$ in the pure ILs. The activation energy value of [C4mim][OAc] obtained from NMR diffusion measurement is same the activation energy value of viscosity, and the value of the activation energy for NMR diffusion and viscosity are also same for [C2mim][Oct], so both ILs follow a Stokes-Einstein relationship. These results could prove useful in the use and design of either type of IL in the future. Finally, normalising the results by the diffusion from the thickness measurements collapses all the data onto one curve. This suggest that it is the diffusion of each IL through a swollen solution of cellulose that is the controlling factor, rather than the self-diffusion/viscosity of the pure IL. The key conclusion is that the rate of dissolution of the flax yarns (in all three ILs) is controlled and limited by the diffusion of each IL through a region of swollen cellulose/IL around each yarn as it dissolves. This is an important result for controlling the fraction of coagulated material (and hence mechanical properties) in, for example, all-cellulose composites.

Chapter 5

Effect of water on the activation energy and dissolution speed of Ionic Liquids [C2mim][OAc] and [C4mim][OAc]

The significant work of this chapter has been published as follows; Albarakati, F.A., Hine, P.J. & Ries, M.E. Effect of water on the dissolution of flax fibre bundles in the ionic liquid 1-ethyl-3-methylimidazolium acetate. *Cellulose* 30, 7619–7632 (2023). https://doi.org/10.1007/s10570-023-05394-3

5.1 Introduction

In the previous chapters we have discussed the fundamental aspects of flax yarn dissolving in ionic liquids, providing insight into the complex mechanisms behind this process. Within these chapters, the dissolving of flax fibre in the three different ionic liquids [C2mim][OAc], [C4mim][OAc] and [C2mim][Oct] in their pure as received forms were the main topics. The dissolution in all three ionic liquids was found to follow TTS with Arrhenius behaviour allowing the activation energy of dissolution to be determined. These three ionic liquids allowed the effect of the cation and anion to be investigated, emphasizing how structural differences in ionic liquids affect their capacity to dissolve cellulose-based materials. Arrhenius analyses were used in these studies to clarify how the dissolving process is temperature dependent. This work provides valuable insights into the design and selection of ionic liquids for various dissolving applications. Building on these findings this chapter will investigate the effect of water on the activation energy and dissolution speed of two of these ionic liquids, namely [C2mim][OAc] and [C4mim][OAc]. The properties of ionic liquids are known to be significantly influenced by water, and the aim of this chapter is to quantify and understand these effects in order to optimise the usage of ionic liquids in various commercial and research applications. This will be studied by investigating how the addition of small amounts of distilled water to the IL solvent baths changes the activation energy required for dissolution as well as the overall dissolution rate. By investigating how water influences the activation energy and dissolution speed of [C2mim][OAc] and [C4mim][OAc], and understanding the role of water, we can gain deeper insights into the dissolution mechanisms of these ILs and potentially optimise

their use in various industrial and scientific applications. The findings from this study will contribute to the broader knowledge of IL behaviour and enhance the efficiency of processes where these ILs are utilized. For instance, in an industrial process using an ionic liquid, it might be important to remove water from the IL after a coagulation stage. This work will give valuable insight into what final level of water can be accepted for the recycled IL to still have appropriate dissolving power. In addition, studying the effect of water on the dissolution activation energy of flax fibres, which is an important parameter in quantifying the time scales/ temperatures needed to determine the dissolution of those fibres, would be useful for optimising the production of all cellulose composites.

The investigation will be structured as follows: firstly, a literature review exploring the role of water on the [C2mim][OAc] and [C4mim][OAc] will be provided. Subsequently, the experimental setup and methodology for measuring dissolution speed and activation energy with the addition of water will be detailed. Finally, the results will be analysed and discussed, highlighting the effects of water content on the dissolution characteristics of these ionic liquids, and builds on the insights from the results in this chapter. A final comparison presents the measured activation energies, and the relative and absolute dissolution speed for both ILs with percentage of added water.

5.1.1 Interaction between ionic liquids and water

The IL/water mixture exhibits a much higher vapor pressure and may thus evaporate under vacuum. Thus, the vacuum oven atmosphere was replaced with a nitrogen atmosphere to avoid evaporation during the dissolution experiments for both ILs. Several researchers have studied the interaction between [C2mim] [OAc] and water and found that its properties could be significantly changed in the presence of water; for example, the melting point, polarity, viscosity and surface tension of ILs are changed [172, 218, 288, 289]. The interaction between water and ionic liquids has been shown to exhibit unique behaviours such as water can alter the structure and properties of ionic liquids [172]. Studies have shown that water influences the layering, ordering, and aggregation behaviour of ionic liquids at interfaces [290-293]. This can lead to varied structuring effects, such as enhanced or diminished layering and ordering depending on the specific ionic liquid and its interactions with water [294]. The anion type in the ionic liquid plays a crucial role in these interactions. For instance, ionic liquids containing chloride anions exhibit less spreading at the water/IL interface compared to those containing bistriflimide anions. This occurs as both

positive ions and negative ions in the liquid are attracted to the surface, collaborating to form a stable layer on the water surface [295]. Moreover, Jonas et al. (2012) reported that the anion has a significant impact on the amount of water absorbed, with spectral changes in the Raman spectra providing insights into the intermolecular interactions between cations, anions, and water. For instance, the ionic liquids containing sulfate anions (SO_4) showed higher water absorption compared to fluorinated anions (BF_4^-) and (PF_6^-). This has been attributed to the increased hydrogen bond accepting capacity of sulfate anions, which enables stronger interactions with water. They also reported that the IL 1-ethyl-3-methylimidazolium ethyl sulfate [EMIM][EtSO4], exhibits higher water absorption due to the formation of H-bonds between the water molecules and sulfate anions, indicating that water molecules formed strong bonds with the sulfate anions, leading to modification of the structure of the ionic liquid, in contrast to the IL 1-butyl-3-methylimidazolium fluorinated anion [BMIM][BF_4] which has poor water absorption due to weak hydrogen bonding of fluorinated anions, resulting in decreased water uptake [296]. These examples demonstrate that the amount of water that an ionic liquid can absorb from the atmosphere is directly influenced by the type of anion present in the liquid. In addition, the presence of water tends to increase the ILs surface tension by changing the magnitude of their initial surface tensions in particular the ILs with the [C2mim] cation is more significantly affected by water than [C4mim][297].

The influence of hydrogen bonding, on how anions and cations interact in liquids is a topic of much discussion [298]. The main reason for the interaction between water and ions in an ionic liquid water mixture is the formation of hydrogen bonds between the water ion acting as the donors, and the ionic liquid anion acting as the acceptors [299]. The bonding strength between IL and water about 75 kJ/mol, which is almost three times higher than that between cellulose and water 21 kJ/mol [178, 300, 301]. The interactions between water and the ions of the ionic liquid lead to changes in how these two ions interact causing shifts in vibrational band locations between the pure ionic liquid and mixtures with water.

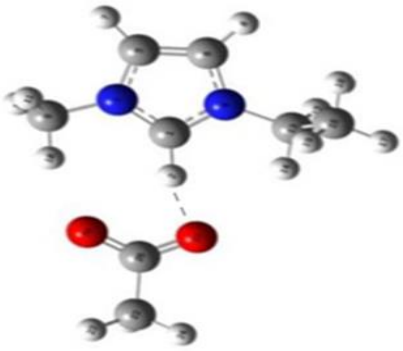

Figure 5.1: H-bonds (dashed lines) between the cation and anion [C2mim][OAc]**,** as illustrated in the molecular structures. Atoms are represented by different colors: red for oxygen, blue for nitrogen, gray for carbon, white for hydrogen. Taken from [302].

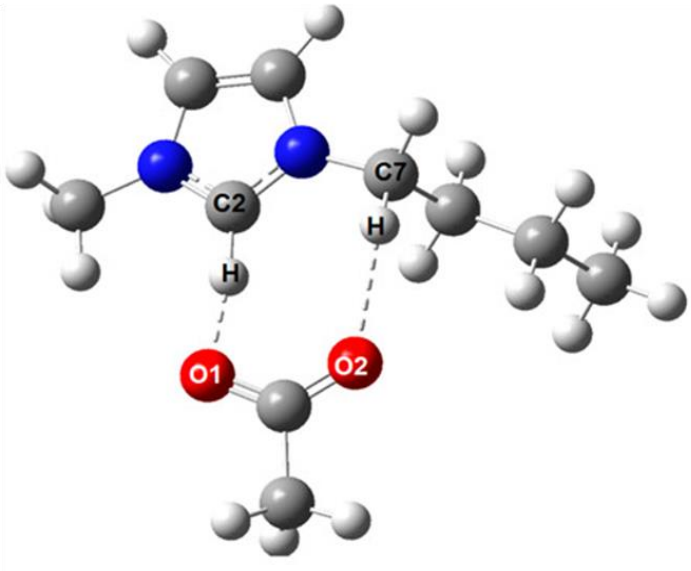

Figure 5.2: H-bonds (dashed lines) between the cation and anion within [C4mim][OAc], as illustrated in the molecular structures. Atoms are represented by different colors: red for oxygen, blue for nitrogen, gray for carbon, white for hydrogen. Taken from [178].

5.1.2 Interactions between cellulose and water

Cellulose is known to interact strongly with water considering the high amount of hydroxyl groups in its molecular chains; however, it is insoluble. The structural and functional properties of cellulose are significantly influenced by the hydrogen bond (H-bond) network that forms between multiple cellulose chains in the presence of water. The solubility, mechanical strength, and interaction with other molecules of cellulose are all significantly influenced by this network [303]. Cellulose forms microfibrils that have a lot of H-bonds within each molecule and between the molecules. The presence of water disrupts these H-bonds, impacting the cellulose structure and its interactions with surrounding molecules. Klemm et al. (2005) describe how water acts as a plasticizer, reducing intermolecular H-bonding through competitive bonding with hydroxyl groups on cellulose, leading to increased chain mobility and swelling of the cellulose structure [304]. The extensive H-bond network that forms between several cellulose chains when water is present, is shown in Figure 5.3.

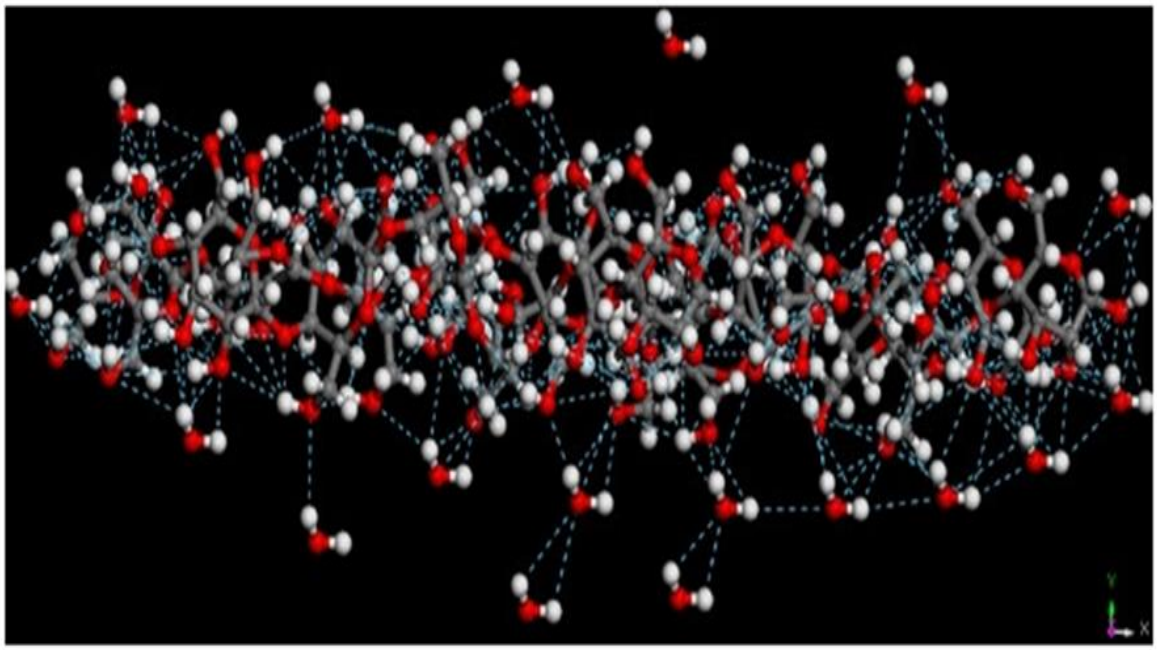

Figure 5.3: Hydrogen bonds form a network between water molecules and cellulose chains following interactions, indicated by blue dashed lines. Taken from [305].

5.1.3 Systems involving cellulose, ionic liquids [C2mim][OAc] and [C4mim][OAc], and water

When water is added to the IL- cellulose system, several interactions occur simultaneously to affect the dissolution mechanisms. Water molecules likely interact with both hydroxyl groups of cellulose and acetate anionic groups at the same time [306]. The addition of water is generally assumed to negatively impact cellulose dissolution in ionic liquids [307]. Nevertheless, recent publications describe a positive influence of low water concentration that can help in the breakdown of hydrogen bonds within cellulose solubilization in [C2mim][OAc] [308]. This may increase the ability of the acetate anions to dissolve cellulose thus encouraging dissolution. Hinner et al. (2019) have designed a system to improve the cellulose dissolution of [EMIM][OAc]-water system by adding 1-ethyl-2-hydroxylethyl3-methyl imidazolium (EHEMIM) to [EMIM][OAc]-water. Here they found that the conditions (50%-cation EHEMIM, 50%-cation EMIM, 8.5% w/w water) is able to solubilize 14% w/w cellulose at 80 °C in 3 h, while a [EMIM][OAc]/water (90,10 w/w) system only solubilize 2% w/w under the same conditions [309]. Moreover, when [EMIM][OAc] has a low concentration, a small amount of water can improve the dissolution mechanism of cellulose by weakening its hydrogen bonds, but when the water content goes higher, it results in the formation of another dense phase and this is the aqueous phase [310]. This phase separation weakens the concentration of acetate ions and subsequently those anions are available for interactions with cellulose in the solution [297]. As such, the dissolution capability of the [C2mim][OAc] is reduced here, indicating its dissolution capability is weaker than the pure [C2mim][OAc]. This solubility limit is critical in the regulation of the dissolution process and the achievement of high levels of cellulose solubility.

The presence of water also determines the viscosity of the [C2mim][OAc]-water mixture and its impact is seen in the cellulose dissolution mechanism. It can be observed that the addition of small amounts of water will slightly decrease the viscosity of the ionic liquid [311]. A lower value of the viscosity enhances the process of diffusion and consequently the interaction between cellulose and acetate anions. This may increase the general rate of dissolution. However, the positive impact of water on the dissolution becomes overshadowed after water gets to a certain point of optimum concentration of water. The water at high concentrations may cause the formation of water clusters that do not react well with cellulose to avail the acetate anions for dissolving cellulose [311]. In this case, any change in the dynamics of the solvent alters the stability and solubility of cellulose in the ionic liquid and therefore, the water content has to be controlled for desirable dissolution performance.

Water's influence on the dissolution of cellulose has immense practical implications in industries. It would therefore be proper to achieve the right water content that allows for the best cellulose dissolution while minimizing the viscosity of the solvent at this stage. The regeneration and utilization of ionic liquids can significantly benefit from the knowledge of the role of water in the process which in turn will enhance the dissolution of cellulose [312]. Moreover, the ability to control the dissolution and regeneration of cellulose will open up the means for designing and synthesizing new compositions of cellulose for different purposes. Textile, paper, and biodegradable fuel industries can benefit from the knowledge as well as other industries where cellulose makes up basic component [255]. Generally, the optimisation of water utilization is arguably the most promising approach for the improvement of the cellulose processing technologies based on the IL systems.

The experiments of the [C4mim][OAc]- water mixture has revealed new insight in the study of ionic liquids. Before this work, the interaction of [C4mim][OAc], with various water content had not been extensively investigated. Our findings illuminate the rate and dissolution process of this substance in different water concentrations. This implies that [C4mim][OAc] could be a good option for industrial applications, over other ionic liquids. This study opens the way for possibilities, in using [C4mim][OAc] in both research and industry suggesting that there is still much to be uncovered regarding its potential.

5.2 Method

The antisolvent (distilled water) was mixed into the pure ILs [C2mim][OAc] and [C4mim][OAc] with a magnetic stirrer for 10 minutes prior to use and left to preheat to the desired dissolution temperature. For the[C2mim][OAc], three water concentrations were used: 1%, 2% and 4% by weight. We have chosen 4 wt.% water as our upper limit, for when we exceed this, the dissolution process became too slow to be practically observed. This result is in line with a publication that demonstrated only swelling of single flax fibres occurred in this IL, when containing 5 wt.% water [18].

For the [C4mim][OAc], four water concentrations were used:1%, 2%, 4% and 8% by weight. Karl Fischer titration (KFT) was used before and after the dissolution process to determine the amount of water content of the IL. KFT on the IL [C2mim][OAc] as received from the manufactures Proionic, showed this to contain 0.2% water. By adding 0.8% water to the original 0.2% water to make 1%, 1.8% water added to make

2% water, and 3.8% water added to make 4% water. KFT on the IL [C4mim][OAc] as received from the manufactures Proionic, showed this to contain 0% water. By adding 1%, 2%, 4%, and 8% water to the IL [C4mim][OAc]. Then, applying Eq. 2.2 to determine the amount of water for both ILs in order to investigate the dissolving power and its effect of adding water.

All experiments methods applied in this chapter are identical to those outlined in sections (2.3), (3.3.2), and (3.3.3).

5.3 Results and Discussion

5.3.1 Investigation of the effect of water on the activation energy and dissolution speed of the ionic liquid [C2mim][OAc]

Optical micrograph cross sections of fibres after various dissolution times at a dissolution temperature of 50 °C are shown in Figures 5.4, 5.5 and 5.6. These cross sections correspond to dissolved fibres in the IL [C2mim][OAc] with water concentrations of 1%, 2% and 4% respectively. The mechanism of the dissolution observed in the IL [C2mim][OAc] with the water anti-solvent system was found to be similar as that of the pure IL systems that observed in the previous two chapters; with the inner fibre area surrounded by various outer layers, with the formation of the coagulation fraction around the core. The main difference seen when using water is the coagulation fraction decreases in size as a function of water content (at a fixed temperature and time). The rate at which fibres dissolve at various concentrations fell significantly, indicating that water is acting to decrease the dissolution rate. Optical microscopy cross sections documenting the decreasing coagulated fraction as function of water concentration after 2 hours at 50 °C can be seen in Figure 5.7.

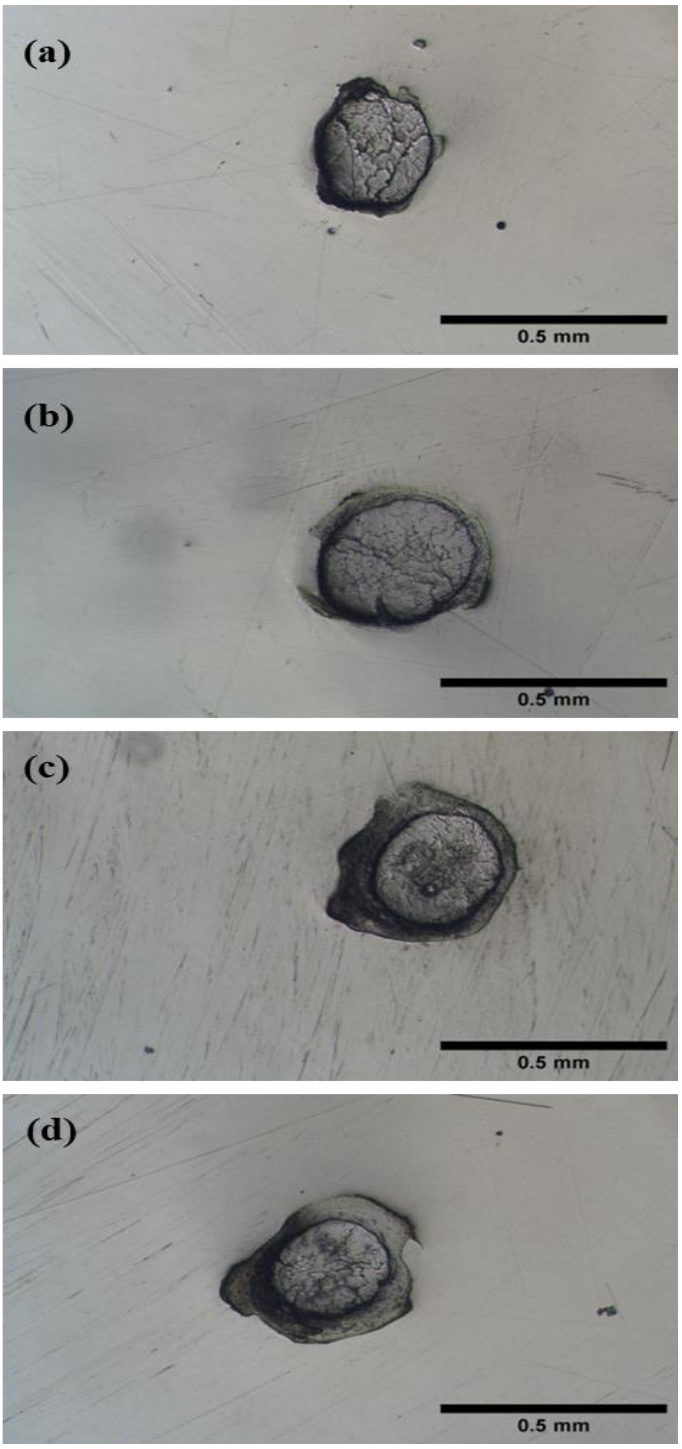

Figure 5.4: Cross sections of processed fibres at 50 °C for 0.5h (a), 1 h (b), 1.5h (c) and 2h (d) when using a water concentration of 1% in the IL [C2mim][OAc]. Scale bar 0.5mm

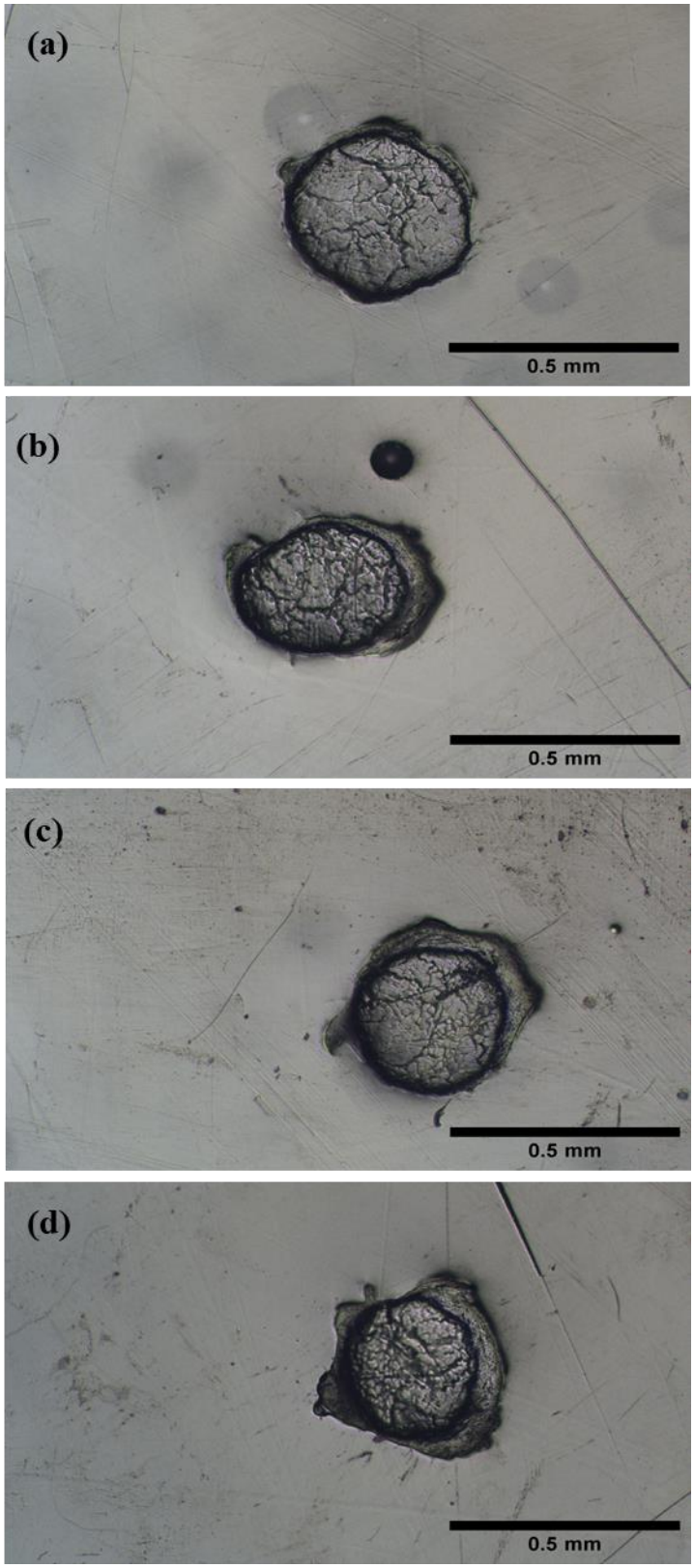

Figure 5.5: Cross sections of processed fibres at 50 °C for 0.5h (a), 1 h (b), 1.5h (c), and 2h (d) when using a water concentration of 2% in the IL [C2mim][OAc]. Scale bar 0.5 mm.

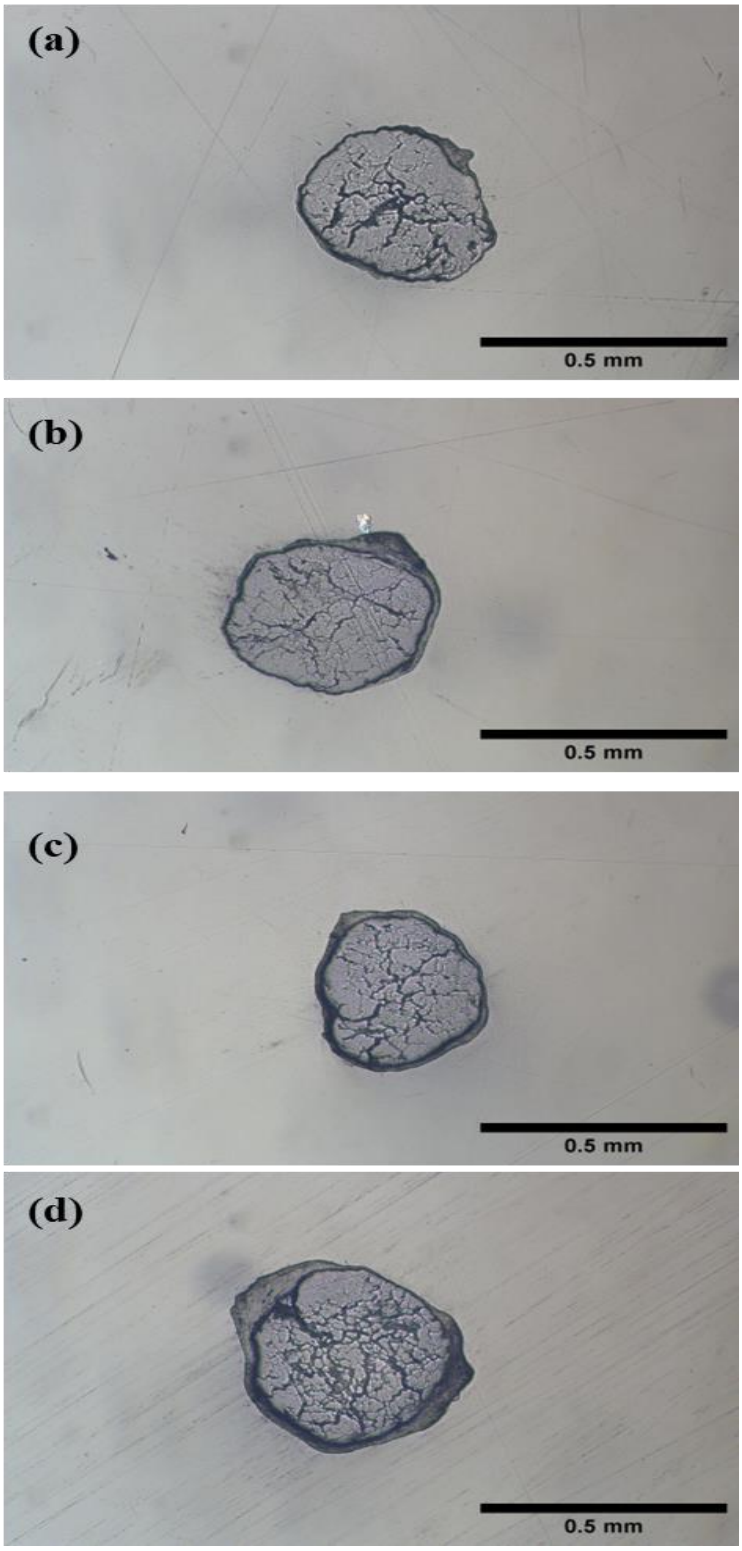

Figure 5.6: Cross sections of processed fibres at 50 °C for 0.5h (a), 1 h (b), 1.5h (c) and 2h (d) when using a water concentration of 4% in the IL [C2mim][OAc]. Scale bar 0.5 mm.

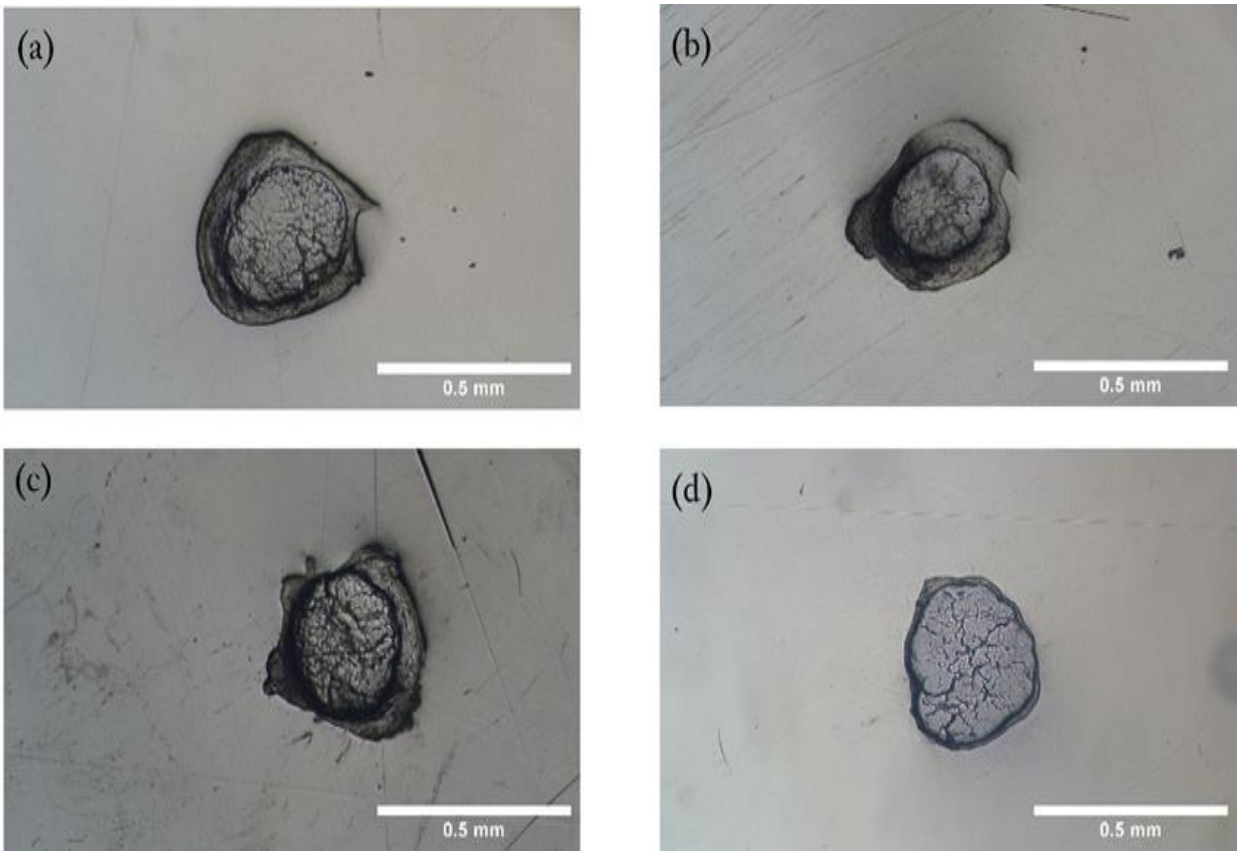

Figure 5.7: Microscopy images of partially dissolved flax fibres showing the inner and the outer distinct regions after 2 hours at 50 °C for various water contents a) 0.2%, b) 1%, c) 2%, and d) 4% in the IL [C2mim][OAc]. Coagulated fraction can be seen to decrease as a function of water concentration increases. Scale length 0.5 mm.

The master curves were generated for the 1%, 2% and 4% water/ IL [C2mim][OAc] systems separately following the same procedure as shown before in Chapter 3 sections (3.3.2) and (3.3.3). First, the data at 50 °C was chosen to be the reference set with a scaling factor α_{50}=1. Then, all of the previous analysis was applied to these data sets, the result of which can be seen in Figures 5.8, 5.10 and 5.12. In these figures, the coagulation fraction of dissolved cellulose (CF) data is initially plotted against linear time, and then transformed to natural logarithmic time to create a master curve. The shift factors used to create this master curve were plotted against the inverse dissolution temperatures, revealing a linear relationship. The data represents the average value of the coagulation fraction taken from the four cross-sectional fibres processed under the same condition of time and temperature, and the error bar is the standard error. These three systems all likewise obeyed Arrhenius behaviour when using water as an antisolvent.

By carrying out again the analysis three times for each concentration, now using the other three temperatures as reference temperatures (T_{ref}), in order to create a master curve for each set of data at each of these temperatures, as seen in Figures 5.9 (a-c), 5.11 (a-c), and 5. 13 (a-c). These plotted graphs give similar gradients, leading to similar E_a as calculated from 50 °C. More details of this process can be found in Chapter 3 section 3.3.2.

For 1%, 2% and 4% water systems, the activation energies were found to be 77 ± 5 kJ/mol, 97 ± 3 kJ/mol and 116 ± 6 kJ/mol respectively. Figure 5.9 (d), 5.11 (d), and 5.13 (d) show the intercepts $\ln \alpha_0$ determined at each reference temperature themselves followed an Arrhenius law, being linearly dependent on the inverse of the reference temperature. The gradient of the $\ln \alpha_0$ vs 1000/T_{ref} is predicted to give very similar gradient as the Arrhenius plots, as highlighted in Table 5.1. More details of this process can be found in Chapter 3 section 3.3.3.

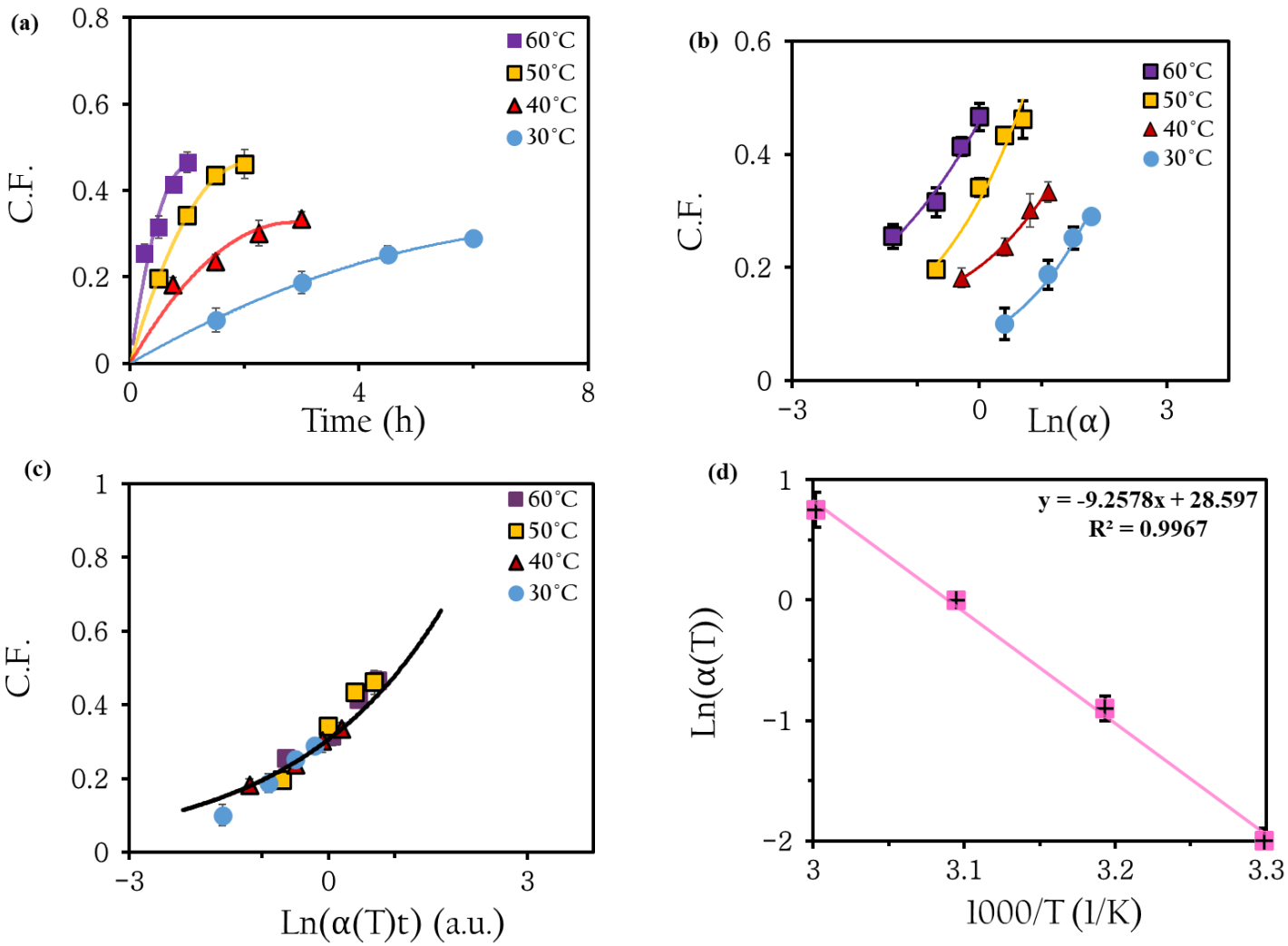

Figure 5.8: Data corresponding to the CF as function of temperature (a), the converted in ln time (b), the shifted data expressed in ln time as a master curve(c), and (d) Arrhenius plot when using 1% water by weight at 50 °C in [C2mim][OAc].

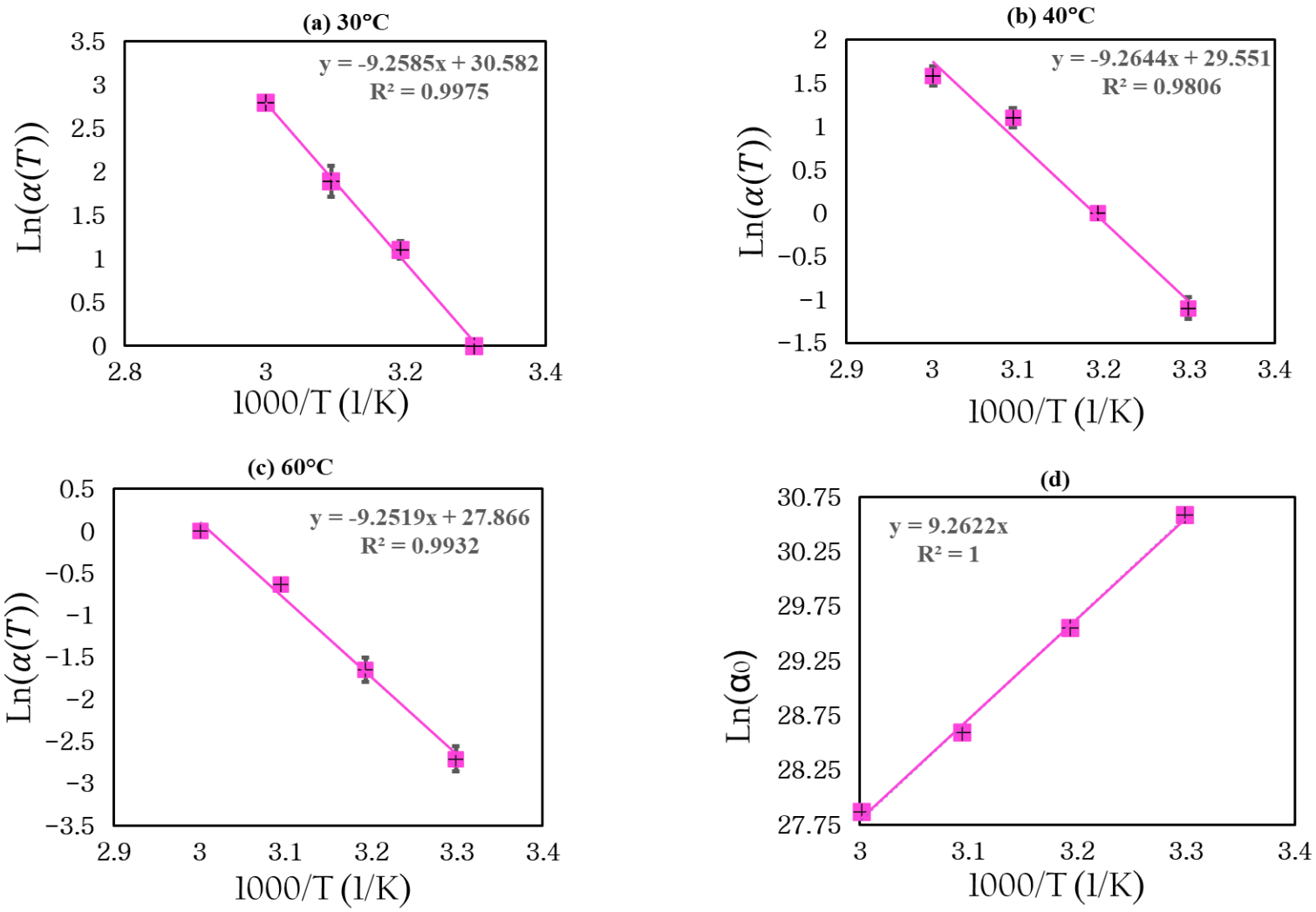

Figure 5.9: Data corresponding Arrhenius plots in [C2mim][OAc] when using 1% water by weight at each reference temperature as reference temperature for 30 °C (a), 40 °C (b), and 60 °C (c). Intercept process, showing shifting to all temperatures indicating Arrhenius dependence (d).

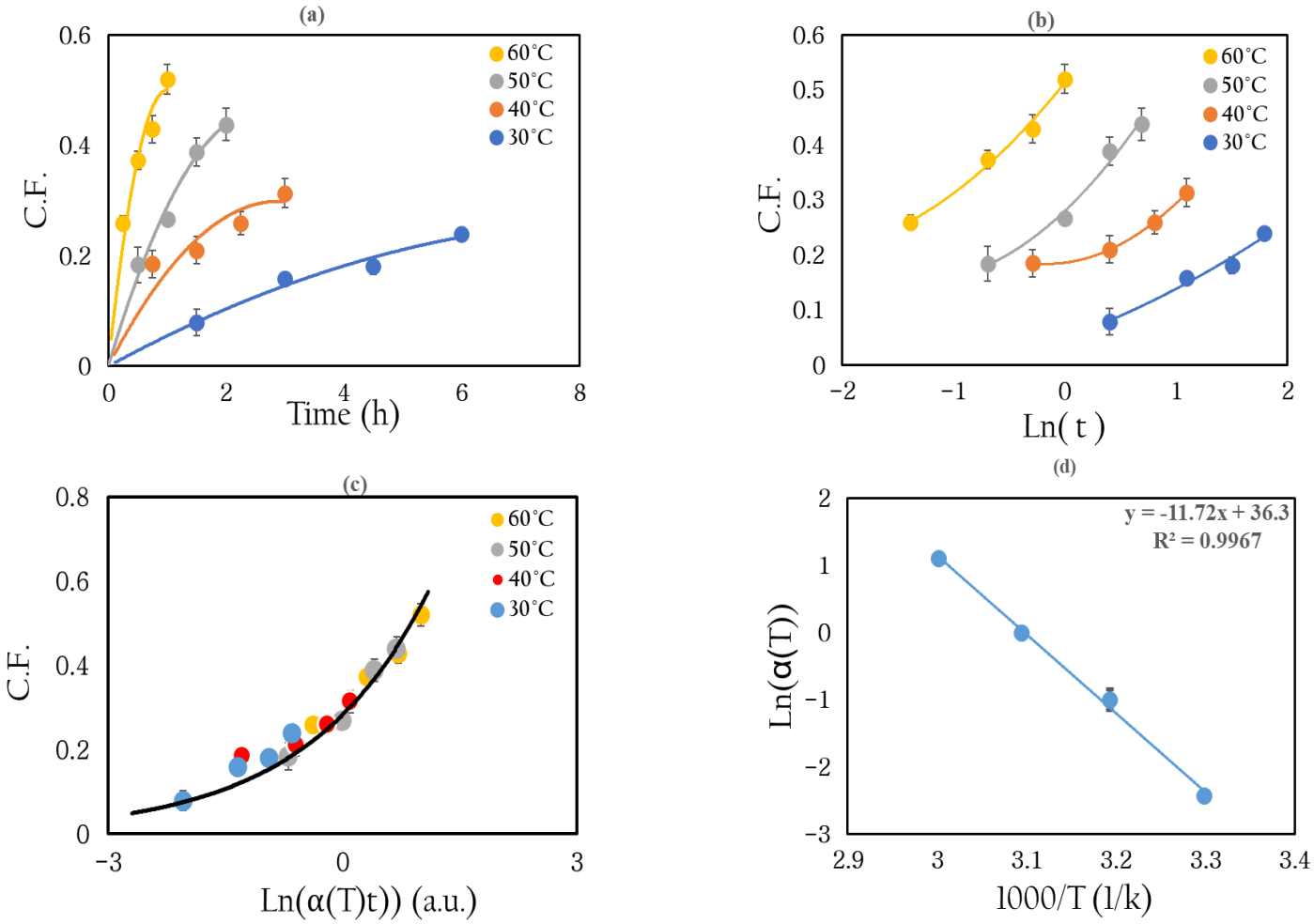

Figure 5.10: Data corresponding to the CF as function of temperature in [C2mim][OAc] (a), the converted in ln time (b), the shifted data expressed in ln time as a master curve(c), and Arrhenius plot when using 2% water by weight at 50 °C (d).

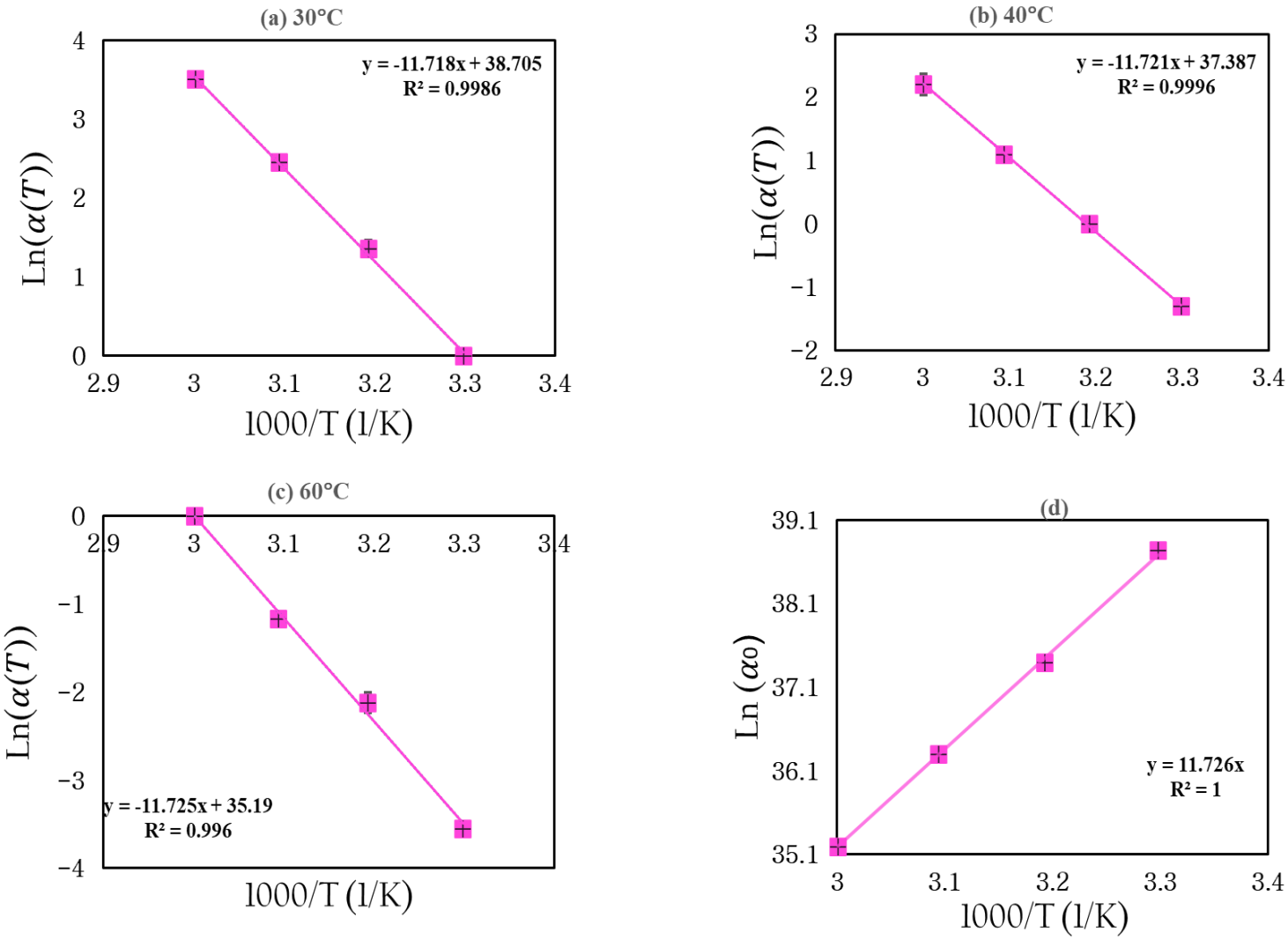

Figure 5.11: Data corresponding Arrhenius plots in [C2mim][OAc] when using 2% water by weight at each reference temperature as reference temperature for 30 °C (a), 40 °C (b), and 60 °C (c). Intercept process, showing shifting to all temperatures indicating Arrhenius dependence (d).

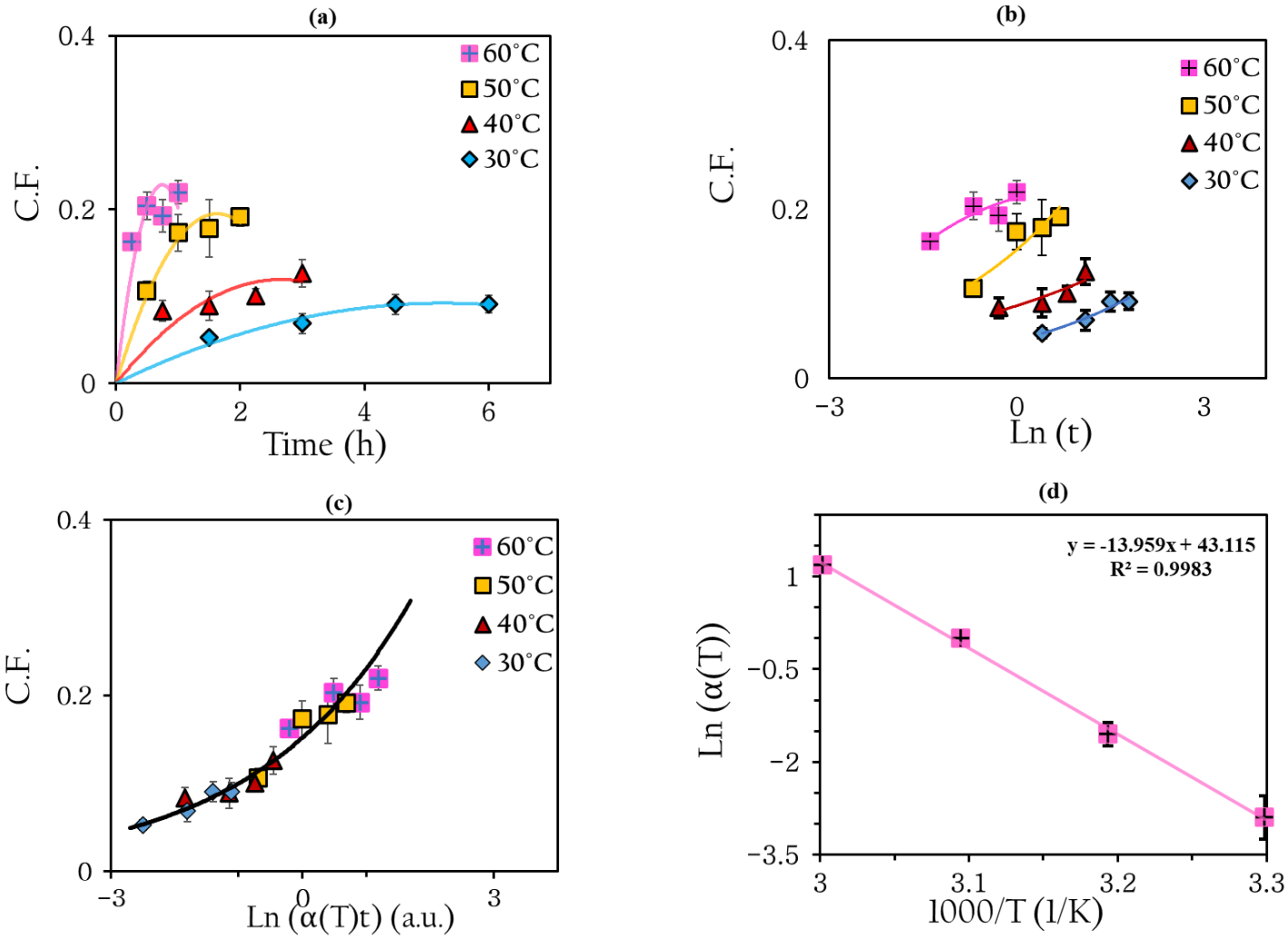

Figure 5.12: Data corresponding to the CF as function of temperature (a), the converted in ln time (b), the shifted data expressed in ln time as a master curve(c), and Arrhenius plot when using 4% water by weight at 50 °C in [C2mim][OAc].

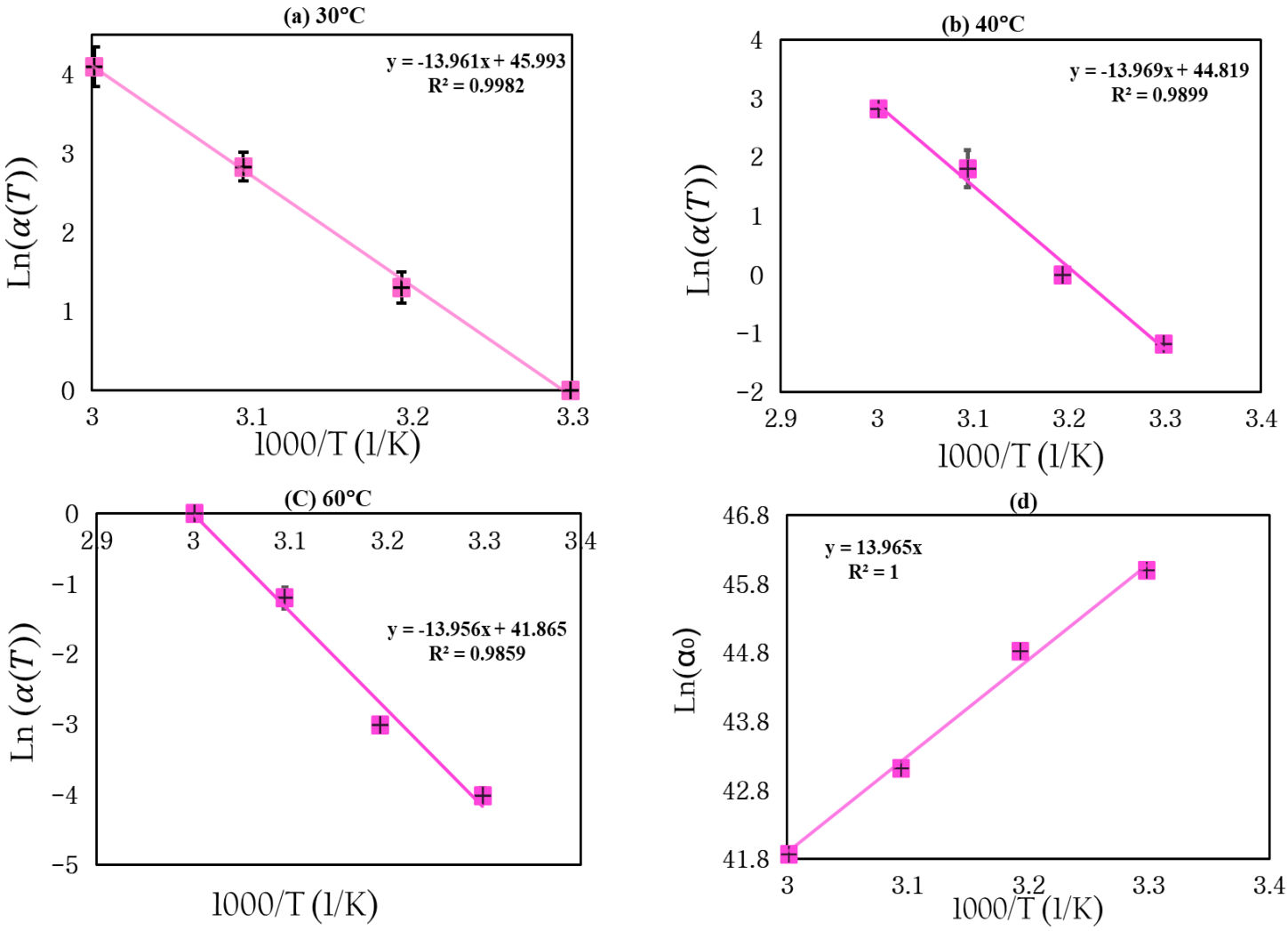

Figure 5.13: Data corresponding Arrhenius plots in [C2mim][OAc] when using 4% water by weight at each reference temperature as reference temperature for 30 °C (a), 40 °C (b), and 60 °C (c). Intercept process, showing shifting to all temperatures indicating Arrhenius dependence (d).

Water system (%)	Temperature (°C)	Average dissolution E_a kJ/mol	Intercept E_a kJ/mol
1%	30 40 50 60	77 ± 5	77 ± 3
2%	30 40 50 60	97 ± 3	97 ± 2
4%	30 40 50 60	116 ± 6	116 ± 7

Table 5.1: Summarising the values activation energy from two methods; dissolution method and intercept method in [C2mim][OAc].

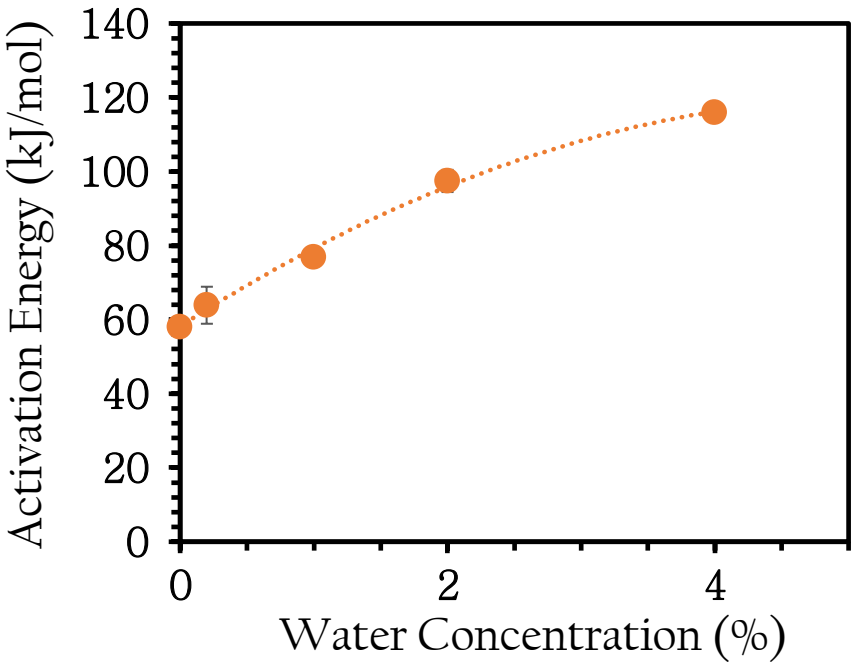

Figure 5.14: Required activation energy for dissolution as function of water concentrations in [C2mim][OAc].

Figure 5.14 displays that the activation energy for the dissolution of the flax fibres in [C2mim][OAc] increase as a function of water concentration. An extrapolation was used to calculate a theoretical value for dry IL 0% water to be 58 ± 4 kJ/mol. A polynomial function of order two was used to fit the data and extrapolate to zero water concentration, shown as the dotted line.

To calculate the change in the relative dissolution rate with the addition of water for a single chosen reference temperature (e.g. at 50 °C), the procedure above was repeated for the 1%, 2% and 4% water systems with now each master curve itself shifted separately in natural logarithmic time to overlap with the master curve of 0.2% water content of the IL as received from the manufacturer, shown before in Chapter 3 in Figure 3.10 (d). So, for example, to overlap the 2% water solvent with the master curve of 0.2% water solvent, this needed a scaling factor α of 0.33, determined from the shift factor ln(α). Hence, the dissolution rate is 3.3 times slower at this concentration $(\frac{1}{\alpha})$. The resulting master curve including all shifted water systems is seen in Figure 5.15 (a). Figure 5.15 (b) shows that the relative dissolution rate decreased exponentially as a function of water concentration at a temperature of 50 °C,

where we set the rate for the 'as received' IL equal to 1 (0.2% water). The decreasing rate of dissolution is thought to be related to the water molecules crowding the anion H-bond sites, which prevented the interactions between the IL and the cellulose [275]. Within their simulations, they discussed the interaction between cellulose, water and several ILs. They demonstrated that anions have the ability to form up to four hydrogen bonds with cellulose. By adding water, there was a strong disturbance in the frequency of hydrogen bonds between the anion and cellulose. This disturbance occurred because the water molecules occupied the hydrogen-bond accepting positions of the anion, preventing it from interacting with cellulose. It was demonstrated that as the amount of water increased, the crowding of these positions becomes more prominent. The authors suggest that the presence of water leads to a significant reduction in hydrogen bonding between anions and cellulose, and this may account for the rapid decline observed in the dissolution rate. This also agrees with experimental work done by Koide et al. which reported that the interaction between water molecules and [C2mim][Ac] is stronger than the [C2mim][Ac] with cellulose [313]**.**

From the exponential function in Figure 5.15 (b), the following equation obtained:

$$Y = 1.225e^{-0.668x} \tag{5.1}$$

where Y is the relative dissolution speed (relative to the IL as purchased) and x is the water concentration in weight percent.

This equation suggests that flax fibres would dissolve 23% faster at 0% water content, in a theoretically perfectly dry IL if this was achievable. For every 1% of additional water, the rate decreases by 49%, or in otherwards the dissolution takes twice as long.

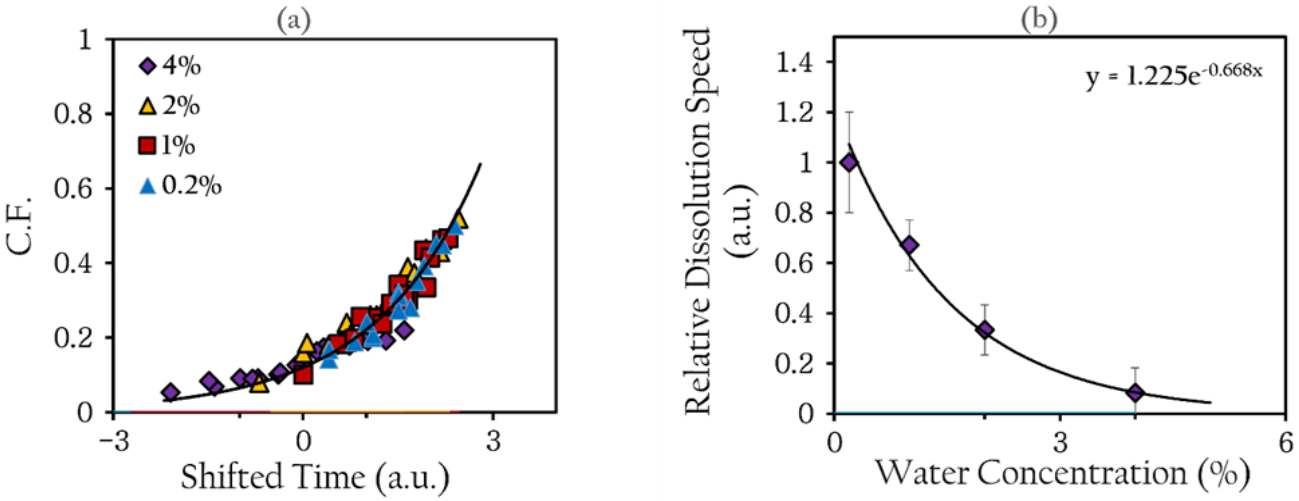

Figure 5.15: (a) Master curve representing all the results for the coagulation fraction as function of antisolvent concentration at 50 °C. (b) Relative dissolution rate of flax fibres as a function of antisolvent concentration. Exponential curve is a fit to the data.

5.3.2 Investigation of the effect of water on the activation energy and dissolution speed of the ionic liquid [C4mim][OAc]

Cross sections of processed fibres at various dissolution times at 60 °C for 1%, 2%, 4%, and 8% water systems, as shown in Figures 5.16, 5.17, 5.18, and 5.19. In these figures, the dissolution mechanisms are appeared to be similar to that observed in the IL [C2mim][OAc] with water systems within the coagulation fraction decreases in size as a function of water content as well as with the previous two chapters- with the growth of the CF as a function of dissolution time and temperature. However, no coagulation fraction was seen in the system containing 8% water, so no further images were analysed for this system. Optical microscopy cross sections documenting the decreasing coagulated fraction as function of water concentration after 2 hours at 60 °C can be seen Figure 5.20.

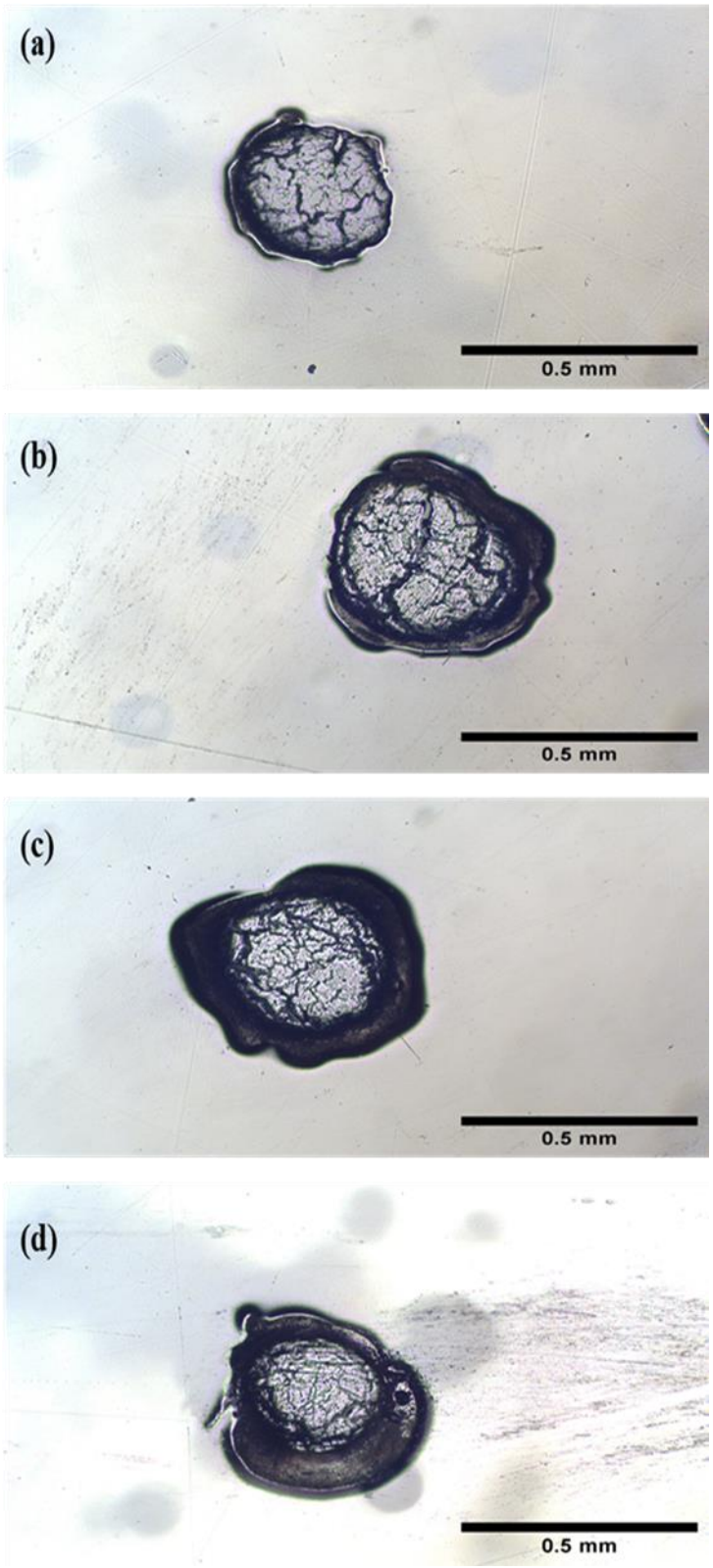

Figure 5.16: Cross sections of processed fibres at 60 °C for 0.5h (a), 1 h (b), 1.5h (c) and 2h (d) when using a water concentration of 1% in the IL [C4mim][OAc]. Scale bar 0.5mm.

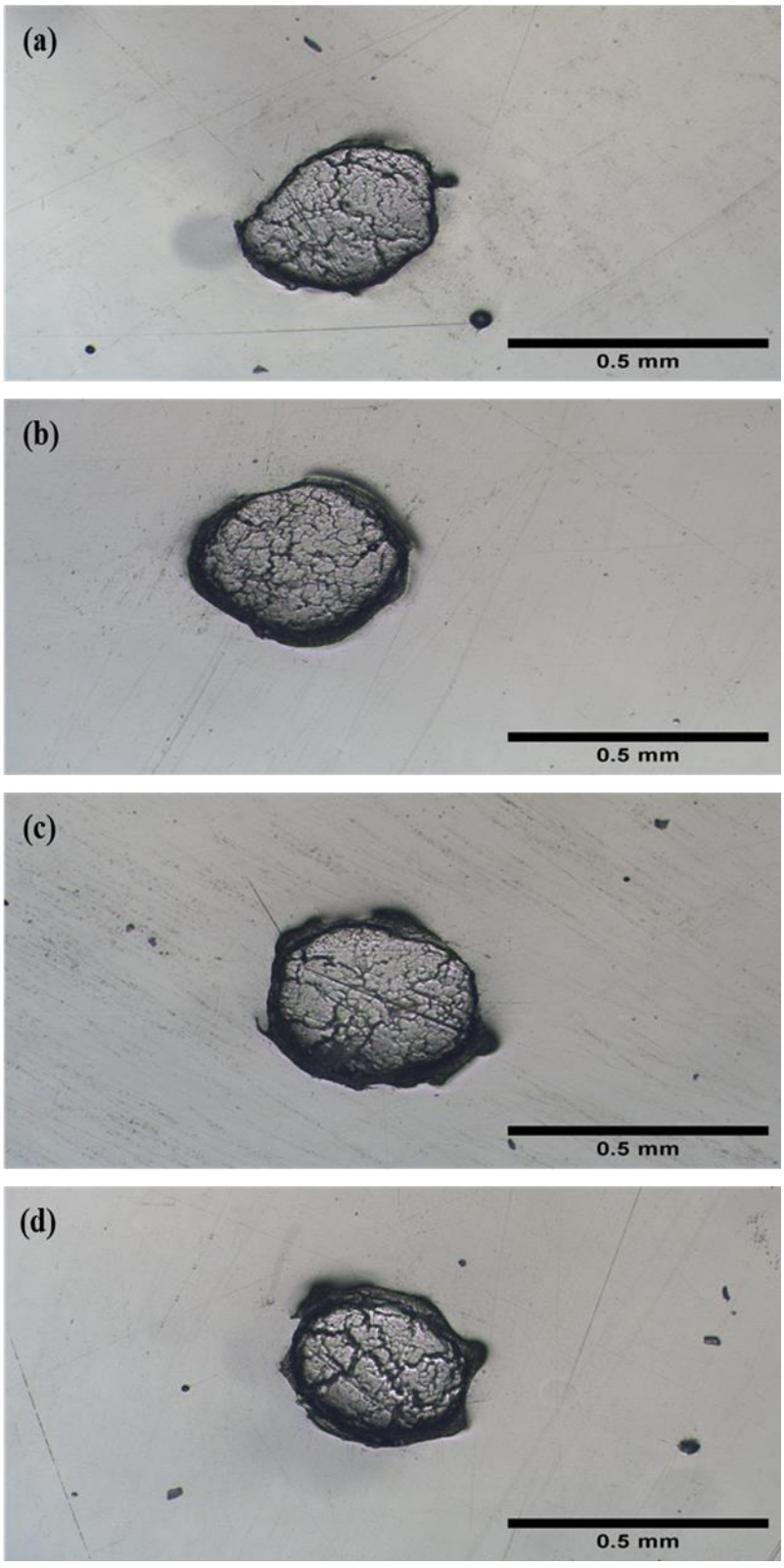

Figure 5.17: Cross sections of processed fibres at 60 °C for 0.5h (a), 1 h(b), 2 h (c) and 3h (d) when using a water concentration of 2% in the IL [C4mim][OAc]. Scale bar 0.5 mm.

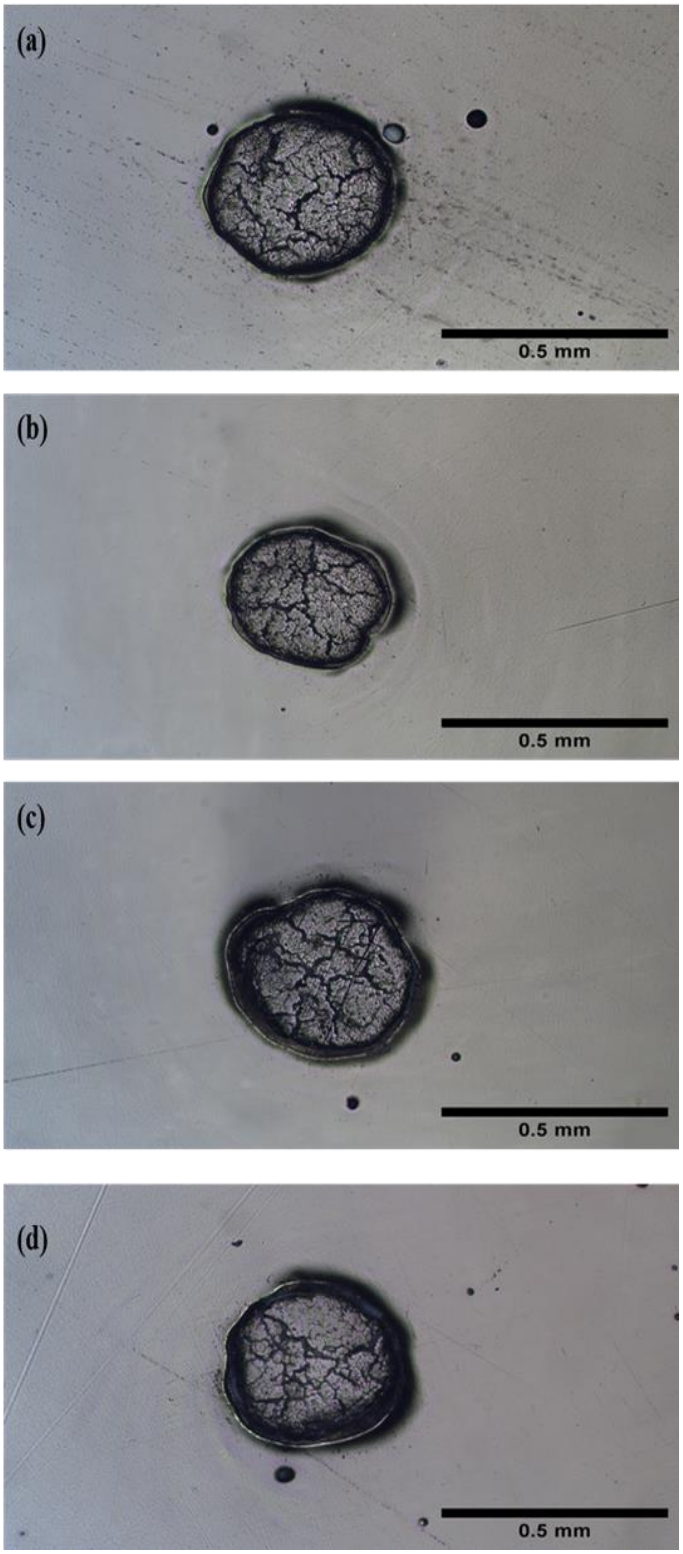

Figure 5.18: Cross sections of processed fibres at 60 °C for 0.5h (a), 1.5 h (b), 4.5 h (c) and 6 h (d) when using a water concentration of 4% in the IL [C4mim][OAc]. Scale bar 0.5 mm.

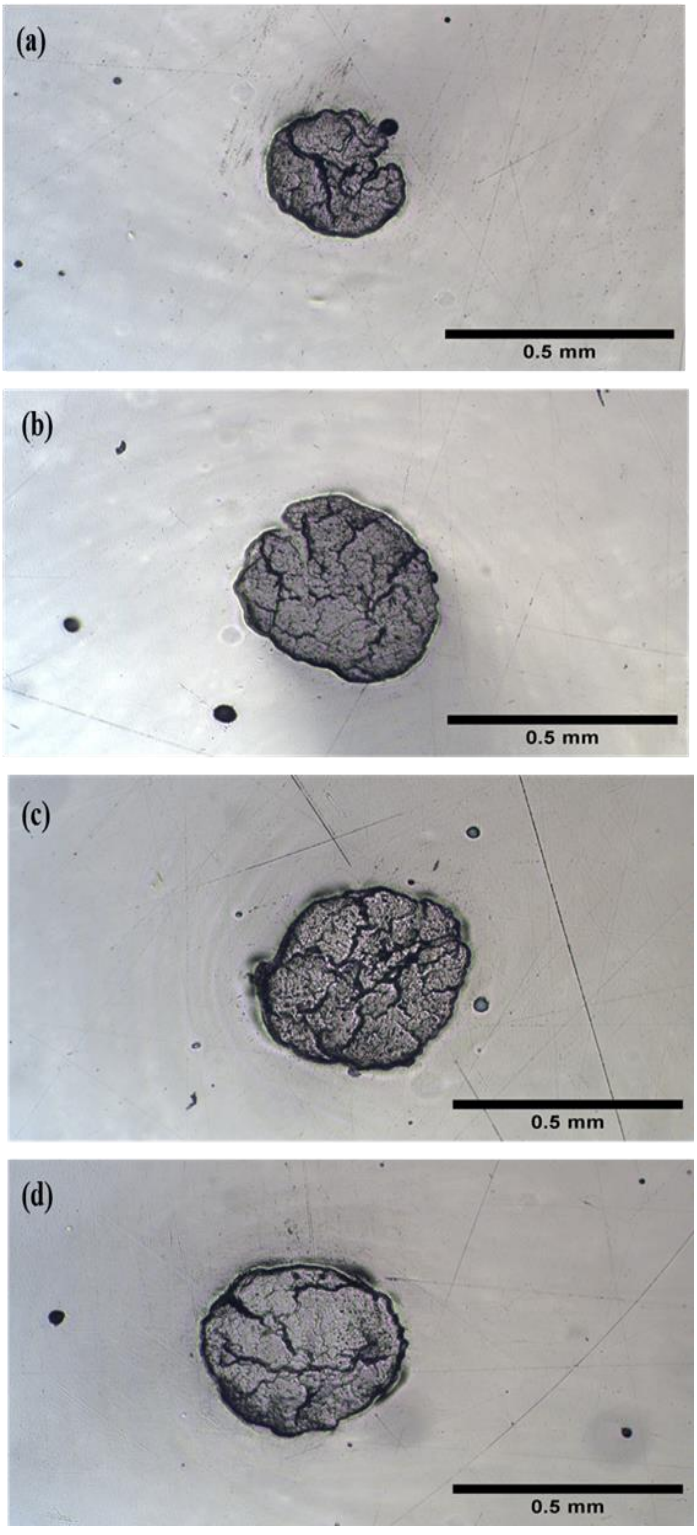

Figure 5.19: Cross sections of processed fibres at 70 °C for 1 h (a), 2 h (b), 3 h (c) and 4 h (d) when using a water concentration of 8% in the IL [C4mim][OAc]. Scale bar 0.5 mm.

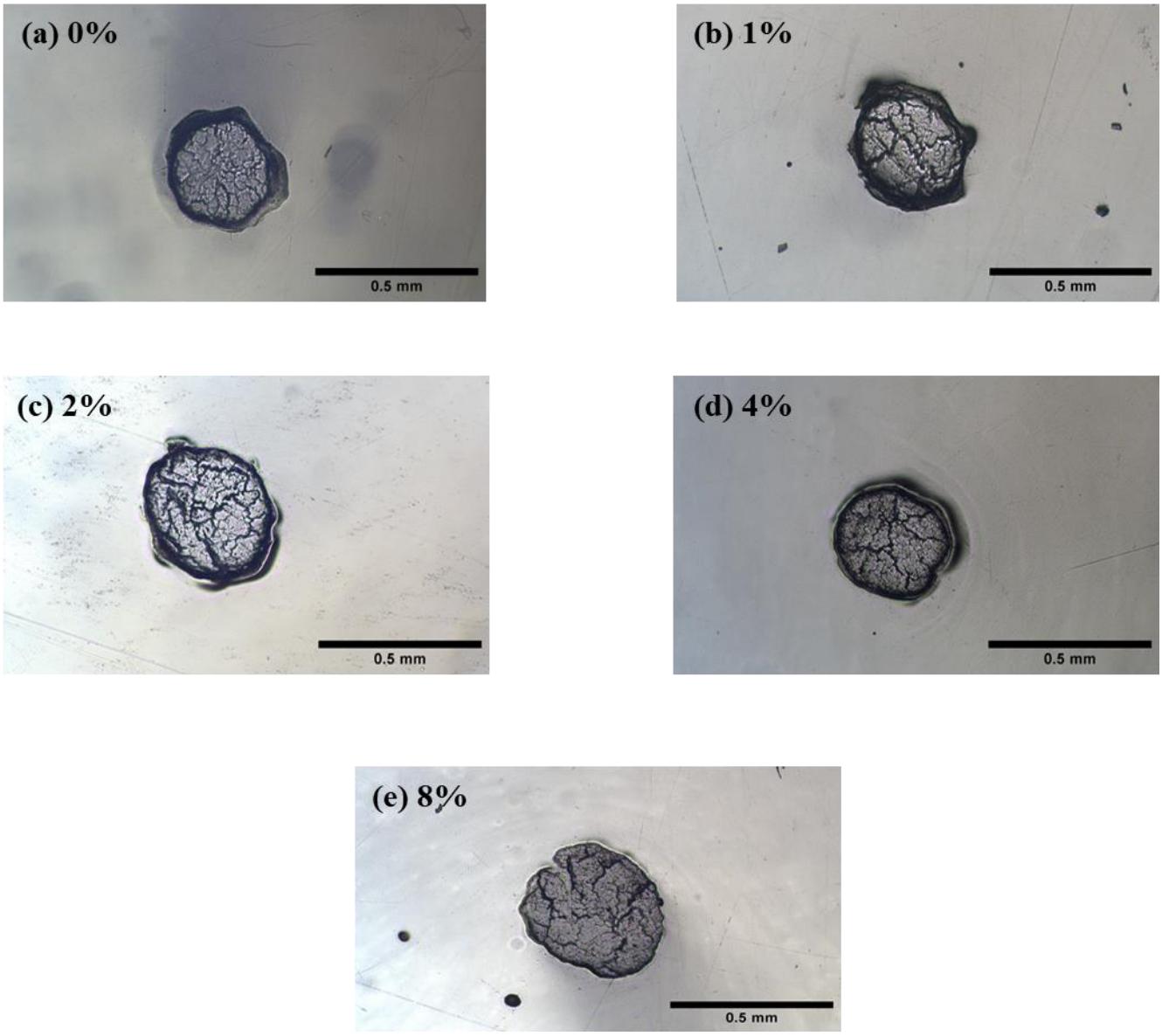

Figure 5.20: Microscopy images of raw single flax yarn and partially dissolved flax fibre showing the inner and the outer distinct regions after 2 hours at 60°C for various water contents a) 0%, b) 1%, c) 2%, d) 4%, and e) 8% after 2 hours at 70 °C. Coagulated fraction can be seen to decrease as a function of water concentration. Scale length 0.5 mm.

By using the similar experiments that used above for 1%, 2% and 4% water systems, the water systems master curves formed for the 1%, 2% and 4% water systems separately following the same procedure as shown before in Chapter 3 sections (3.3.2) and (3.3.3). First, the data at 60 °C was chosen to be the reference set with a scaling factor α_{60}=1. Then, all of the previous analysis was applied to these data sets, the result of which can be seen in Figures 5.21, 5.23 and 5.25. In these figures, the CF data is initially plotted against linear time, and then all the data transformed into the natural logarithmic time to create a master curve. The shaft factors used to create this master curve were plotted against the dissolution temperatures, revealing a linear relationship. The data represents the average value of the coagulation fraction taken from the four cross-sectional fibres processed under the same condition of time and temperature, and the error bar is the standard error. These three systems all likewise obeyed Arrhenius behaviour when using water as an antisolvent.

By carrying out again the analysis three times for each concentration, now using the other three temperatures as reference temperatures (T_{ref}), in order to create a master curve for each set of data at each of these temperatures, as seen in Figures 5.22 (a-c), 5.24 (a-c), and 5.26 (a-c). These plotted graphs give similar gradients, leading to similar E_a as calculated from 60 °C. More details of this process can be found in Chapter 3 section 3.3.2.

For 1%, 2% and 4% water systems, the activation energies were found to be 78 ± 7 kJ/mol, 83 ± 7 kJ/mol and 110 ± 6 kJ/mol respectively. Figure 5.22 (d), 5.24 (d), and 5.26 (d) show the intercepts $\ln \alpha_0$ determined at each reference temperature themselves followed an Arrhenius law, being linearly dependent on the inverse of the reference temperature. More details of this process can be found in Chapter 3 section 3.3.3. The gradient of the $\ln \alpha_0$ vs 1000/T_{ref} is predicted to give very similar gradient as the Arrhenius plots, as highlighted in Table 5.2.

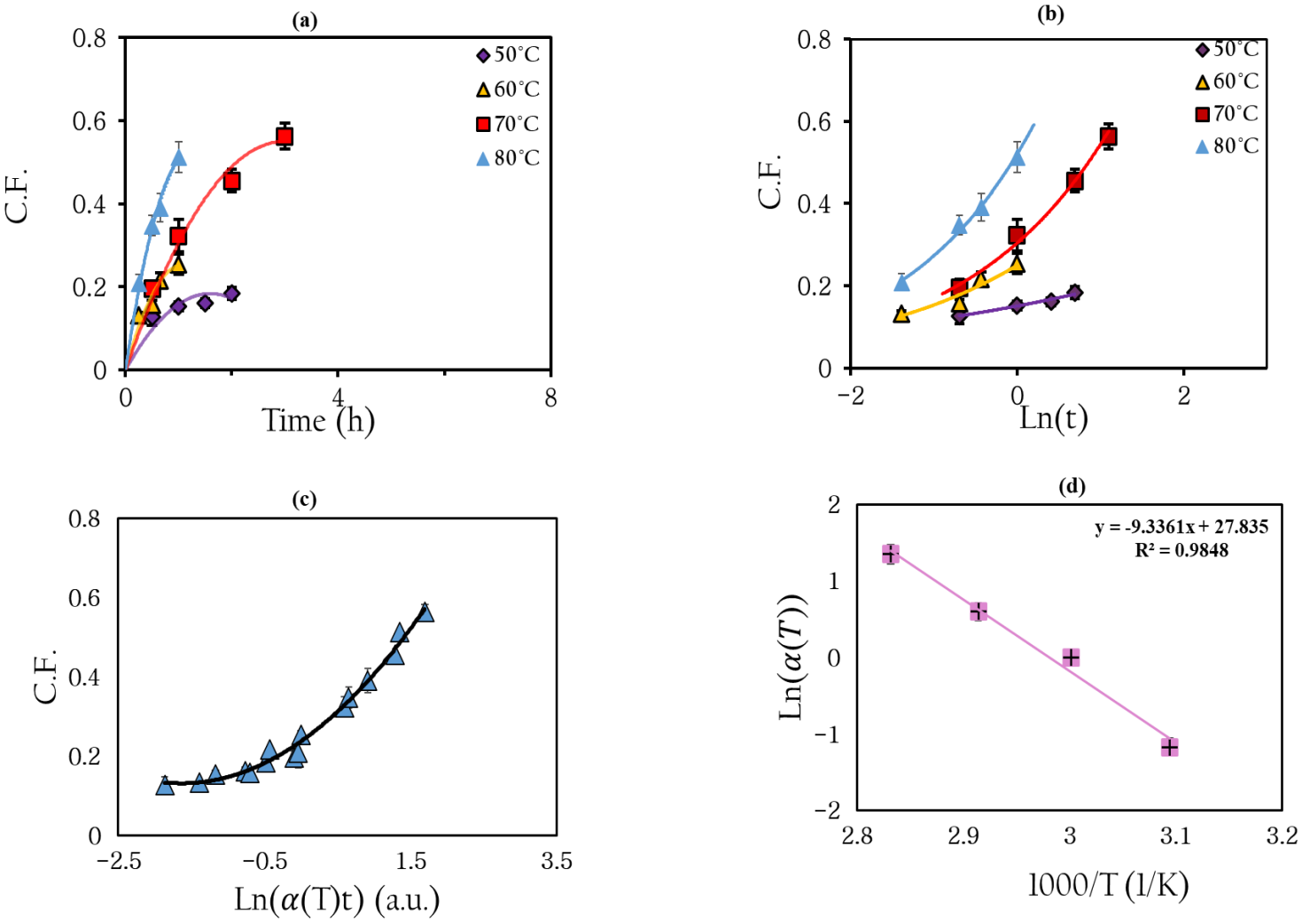

Figure 5.21: Data corresponding to the CF as function of temperature (a), the converted in ln time (b), the shifted data expressed in ln time as a master curve(c), and Arrhenius plot when using 1% water by weight at 60 °C in the IL [C4mim][OAc].

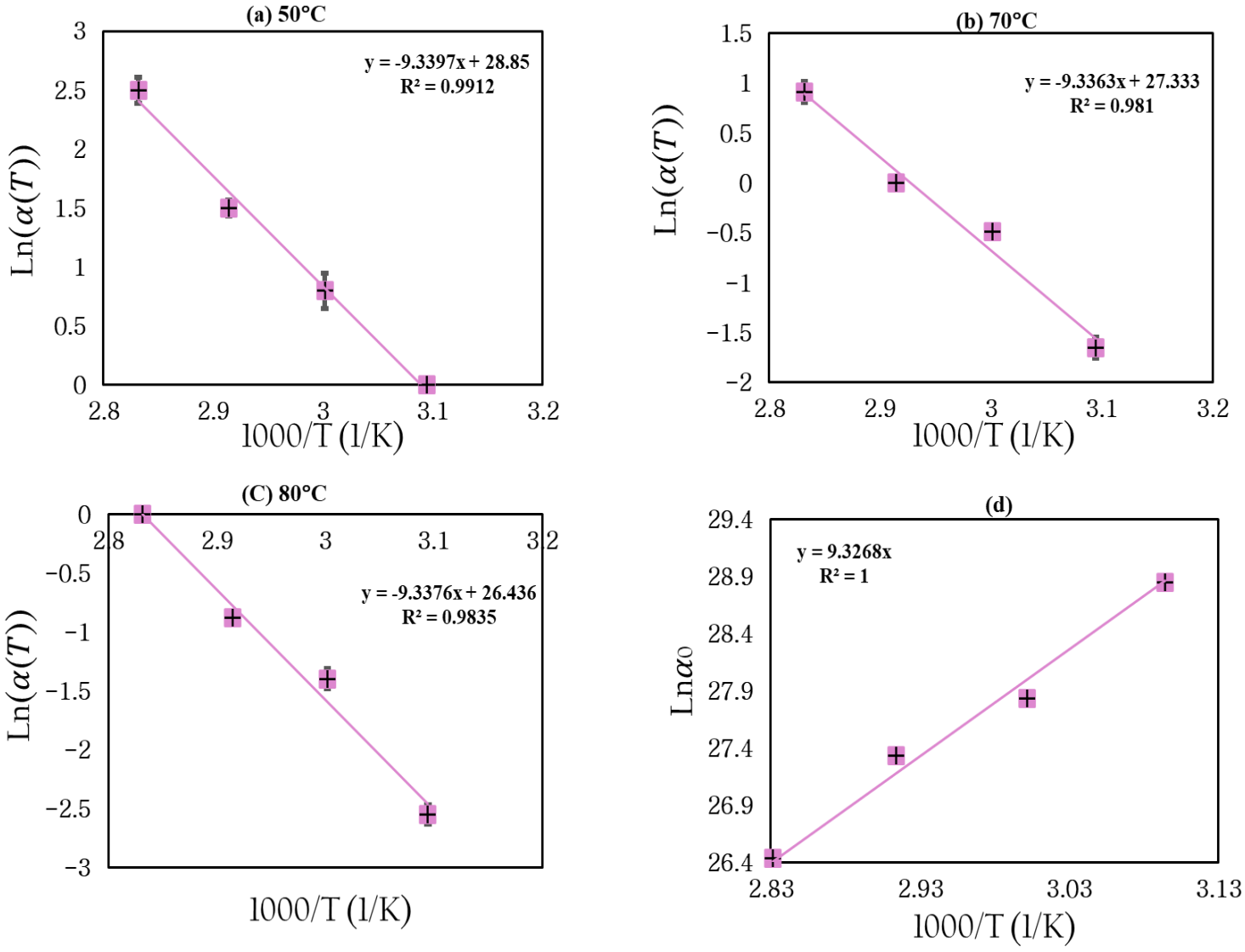

Figure 5.22: Data corresponding Arrhenius plots in the IL [C4mim][OAc] when using 1% water by weight at each reference temperature as reference temperature for 50 °C (a), 70 °C (b), and 80 °C (c). Intercept process, showing shifting to all temperatures indicating Arrhenius dependence (d).

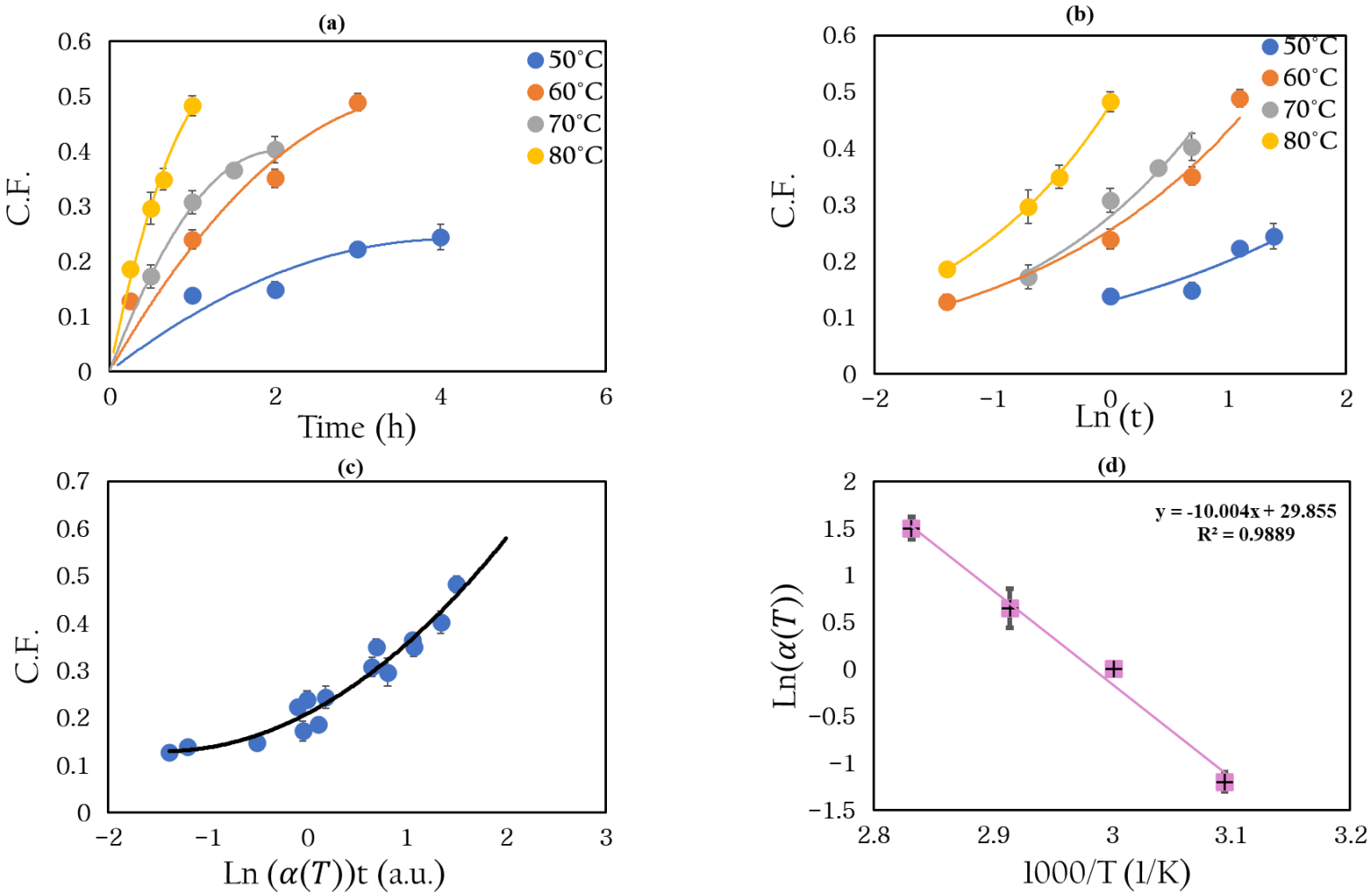

Figure 5.23: Data corresponding to the CF as function of temperature (a), the converted in ln time (b), the shifted data expressed in ln time as a master curve(c), and Arrhenius plot when using 2% water by weight at 60 °C in the IL [C4mim][OAc].

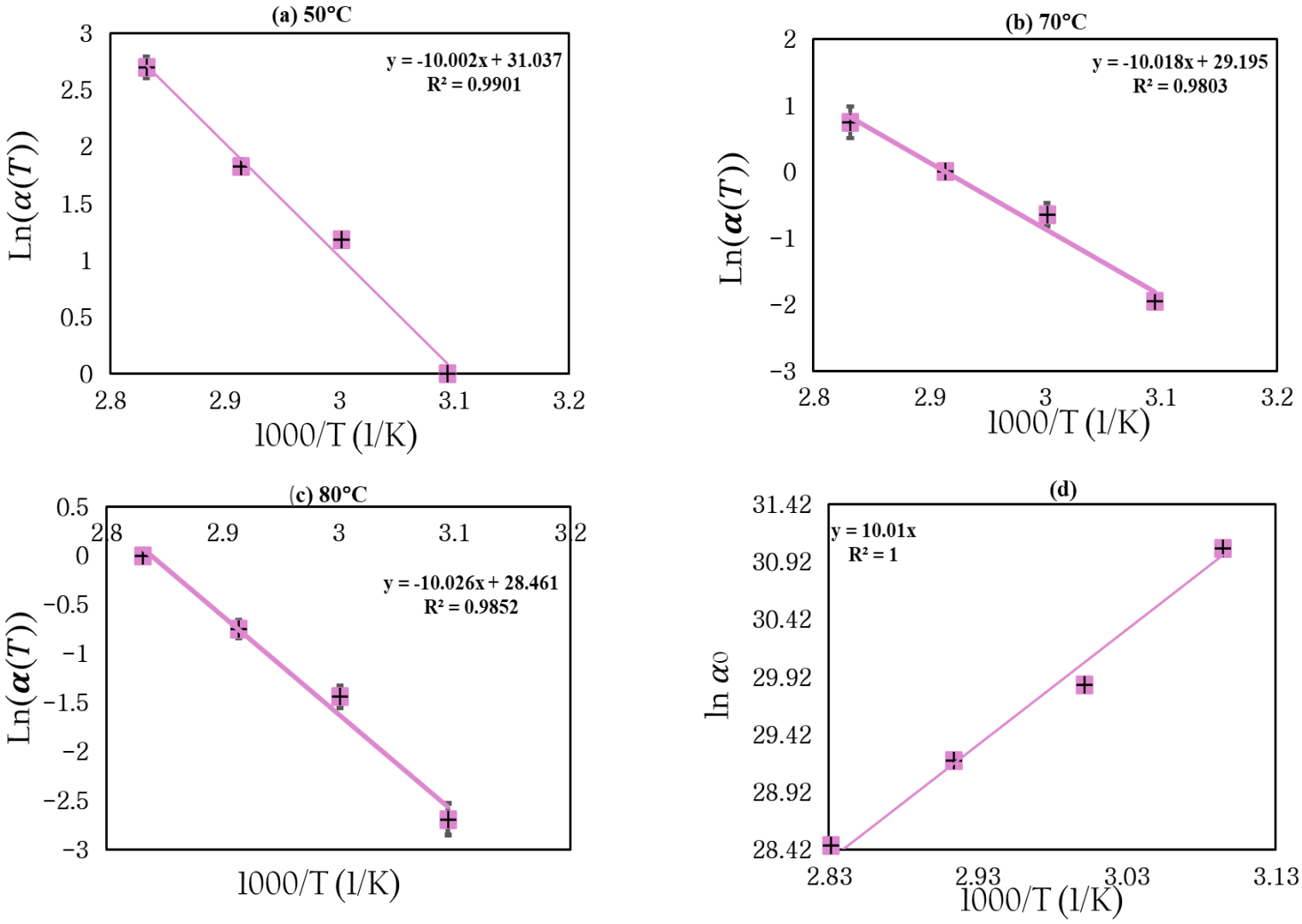

Figure 5.24: Data corresponding Arrhenius plots in the IL [C4mim][OAc] when using 2% water by weight at each reference temperature as reference temperature for 50 °C (a), 70 °C (b), and 80 °C (c). Intercept process, showing shifting to all temperatures indicating Arrhenius dependence (d).

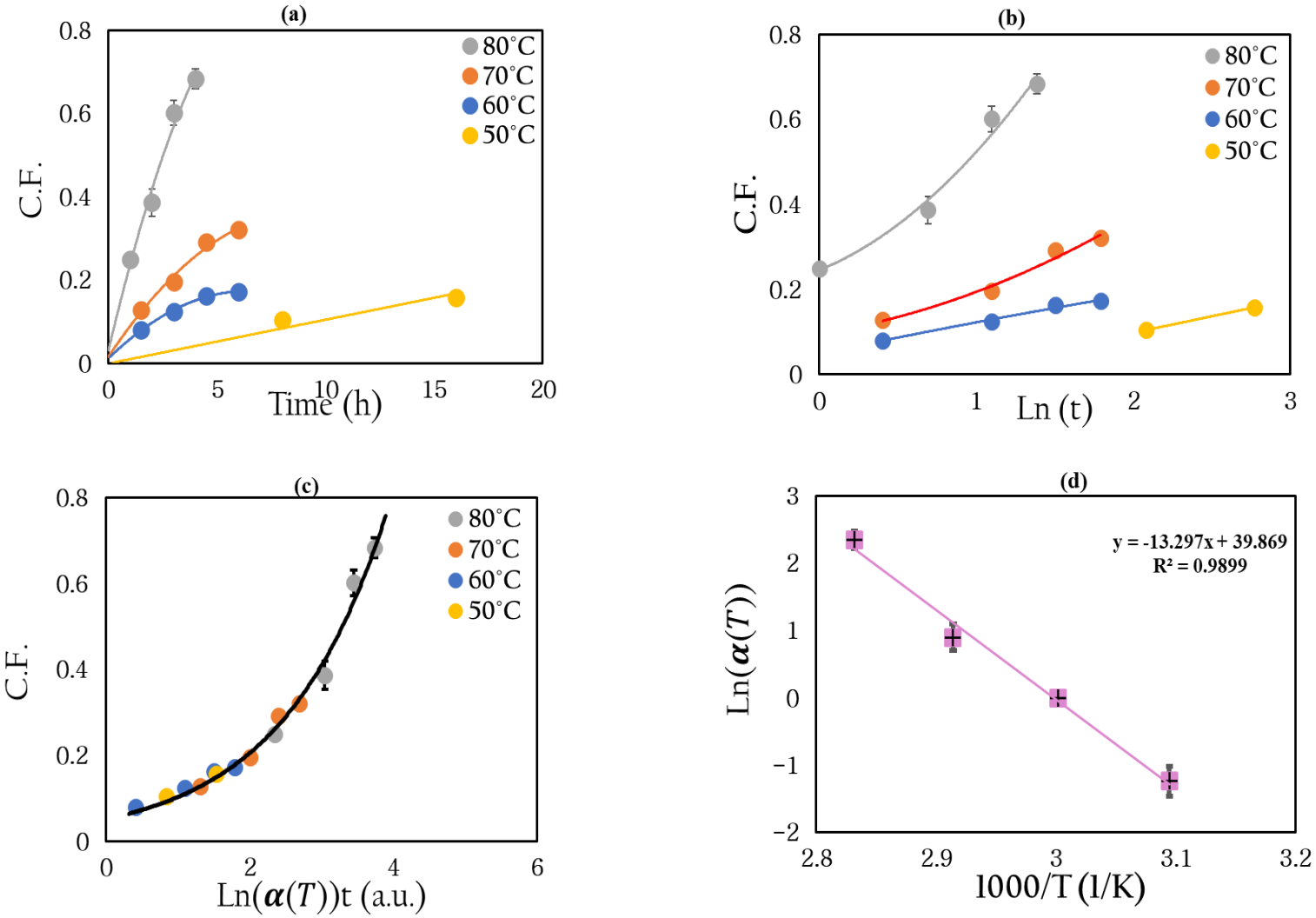

Figure 5.25: Data corresponding to the CF as function of temperature (a), the converted in ln time (b), the shifted data expressed in ln time as a master curve(c), and Arrhenius plot when using 4% water by weight at 60 °C in the IL [C4mim][OAc].

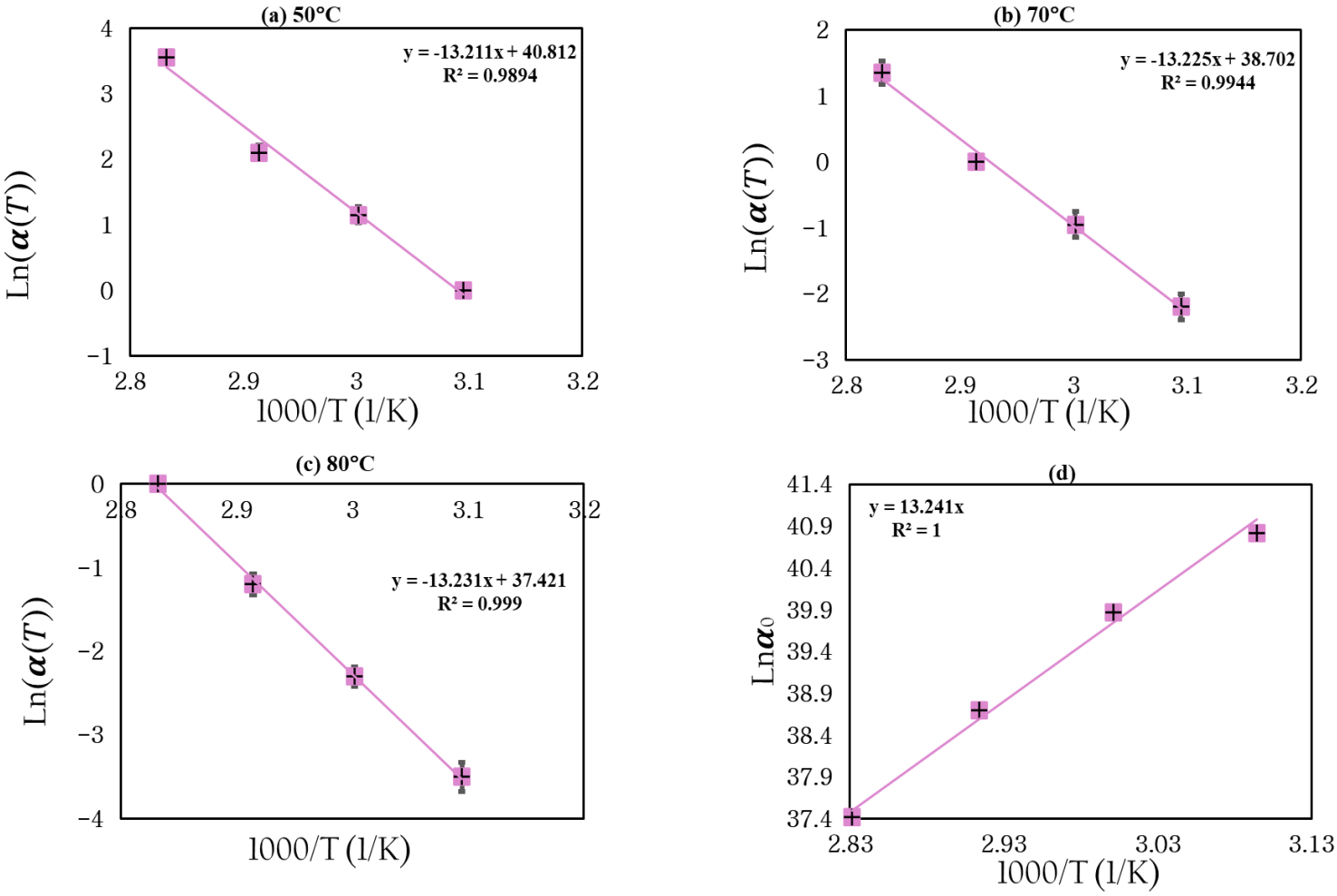

Figure 5.26: Data corresponding Arrhenius plots in the IL [C4mim][OAc] when using 4% water by weight at each reference temperature as reference temperature for 50 °C (a), 70 °C (b), and 80 °C (c). Intercept process, showing shifting to all temperatures indicating Arrhenius dependence (d).

Water system (%)	Temperature (°C)	Average dissolution E_a kJ/mol	Intercept E_a kJ/mol
1%	50 60 70 80	78 ± 7	78 ± 6
2%	50 60 70 80	83 ± 7	83 ± 7
4%	50 60 70 80	110 ± 6	110 ± 7

Table 5.2: Summarising the values activation energy from two methods; dissolution method and intercept method in the IL [C4mim][OAc].

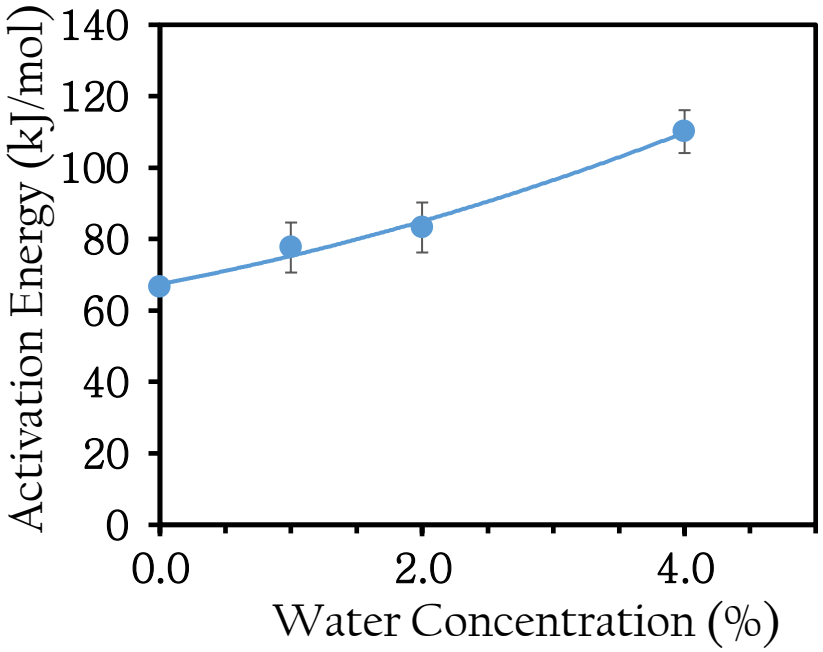

Figure 5.27: Activation energy for dissolution as function of water concentrations in [C4mim][OAc].

Figure 5.27 shows the activation energy increase as a function of water concentration. A polynomial function of order two was used to fit the data. In order to measure the relative dissolution rate between the 1%, 2% and 4% water systems to that of the 0% water content of the IL as received from the manufacturer. So, the procedure above repeated again for the 1%, 2% and 4% water systems at 50 °C with now each master curve itself shifted separately in natural logarithmic time to overlap with the master curve of 0% water results, shown before in Chapter 4 in Figure 4.6 (c). For example, to overlap the 2% water solvent with the master curve of 0% water solvent, needed a scaling factor α of 0.81, determined from the shift factor ln(α). Hence, the dissolution rate is 1.2 times slower at this concentration $(\frac{1}{\alpha})$. The resulting master curve including all water systems is seen in Figure 5.28 (a). Figure 5.28 (b) shows that the relative dissolution rate as a function of water concentration at 50 °C, where we set the rate for the 'as received' IL equal to 1 (0% water). It is clearly seen that the peak indicates that the dissolution rate in the system of 1% water is higher than that at 0% water. This could be related to decrease in the viscosity by adding 1% water. This is a very important result as it suggests an industrial IL recycling process for in the IL [C4mim][OAc] would benefit with 1%.

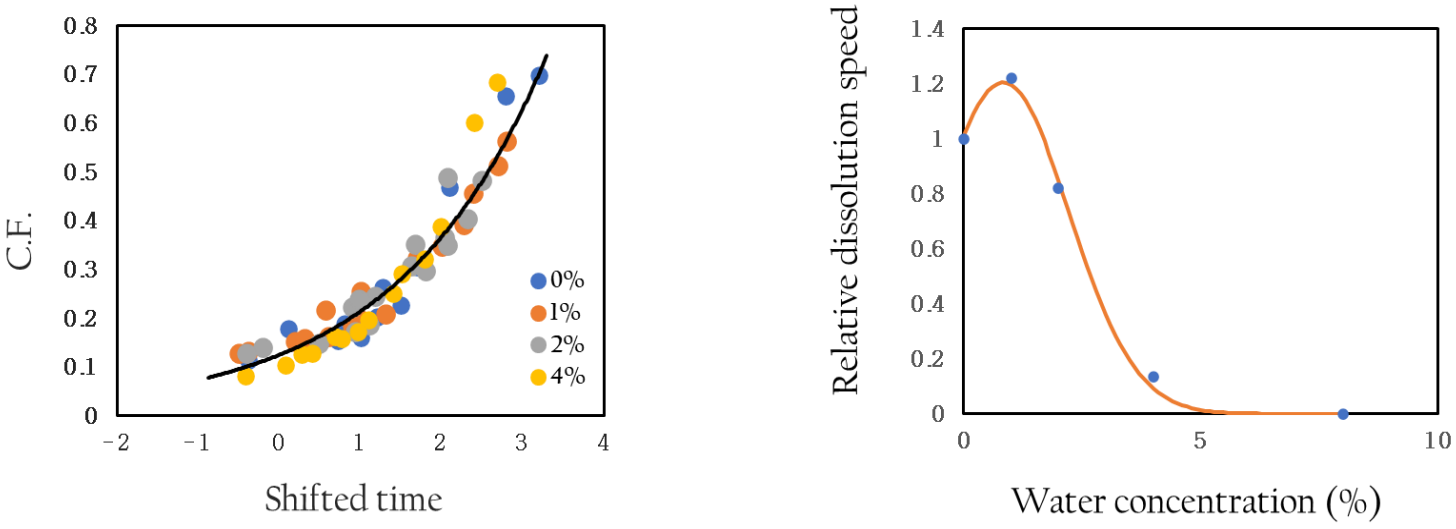

Figure 5.28: (a) Master curve representing all the results for the coagulation fraction as function of antisolvent concentration at 50 °C. (b) Relative dissolution rate of flax fibres as a function of antisolvent concentration.

5.4 Comparison of the water on the dissolution rate and activation energy of flax fibres in the ILs [C2mim][OAc] and [C4mim][OAc]

In the previous Figure 5.15 (b) the relative dissolution rate decreases as the water concentration increase so the rate of the dissolution at its highest at 0% water for [C2mim][OAc]. For [C4mim][OAc], the data fitted with a curve indicates an initial increase followed by a decrease suggests that the dissolution process has an optimal water concentration at which it is most efficient in the dissolution speed peak at 1% water, as shown previously in Figure 5.28 (b). This indicates that a small amount of water enhances the dissolution process, possibly by reducing the viscosity or breaking down some intermolecular forces in the ionic liquid [C4mim][OAc]. Therefore, minimize energy consumption in IL recycling can be reduced by controlling the initial water concentration for cellulose swelling, so a deep understanding of how IL-H_2O systems influence cellulose, as well as effective recycling of water/IL combinations, are required for reducing solvent consumption [314]. For both ILs, the dissolution speed drops significantly at around 4% water concentration, see Table 5.3.

water concentrations (%)	Relative dissolution speed [C2mim][OAc], at 50 °C	Relative dissolution speed [C4mim][OAc], at 50 °C
0	-	1
0.2	1	-
1	0.67 ± 0.06	1.22 ± 0.01
2	0.33 ± 0.10	0.81 ± 0.03
4	0.08 ± 0.06	0.13 ± 0.22
8	0	0

Table 5.3: Relative dissolution speed as a function of water content for both ILs; [C2mim][OAc] and [C4mim][OAc].

In Figure 5.29 shows the activation energy is increases as water concentration increase in both ILs. It is also interesting to compare the absolute dissolution speeds for the two ILs. We have done this for a reference temperature of 50 °C and for 1%, 2%, and 4% water. Figures (5.30 -5.32) show this comparison. It can be seen that the flax fibres dissolve faster in [C2mim][OAc] at all water concentrations. This might be related to the viscosity of [C2mim][OAc] is lower than that of [C4mim][OAc].

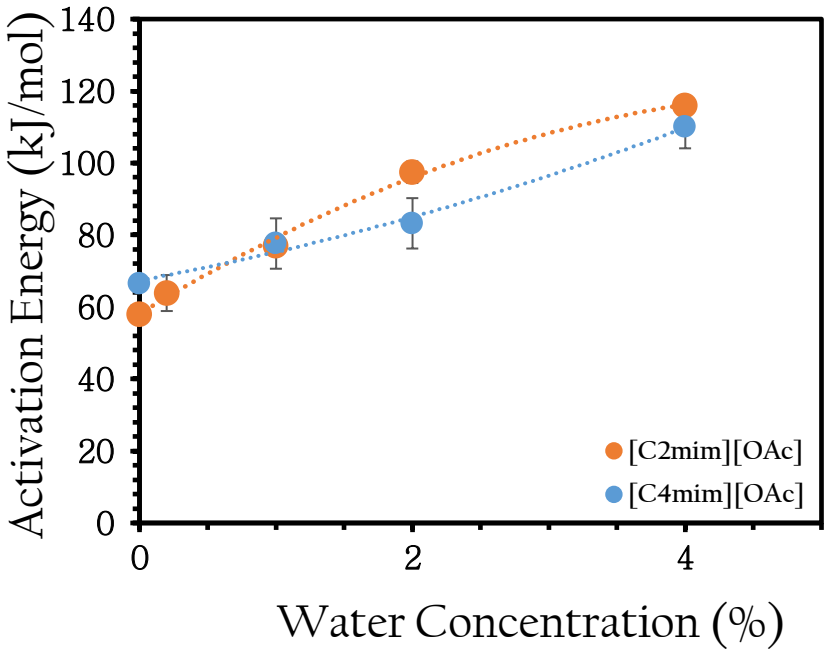

Figure 5.29: Activation energies for the dissolution of flax fibres as function of water concentrations for both ILs [C2mim][OAc] and [C4mim][OAc].

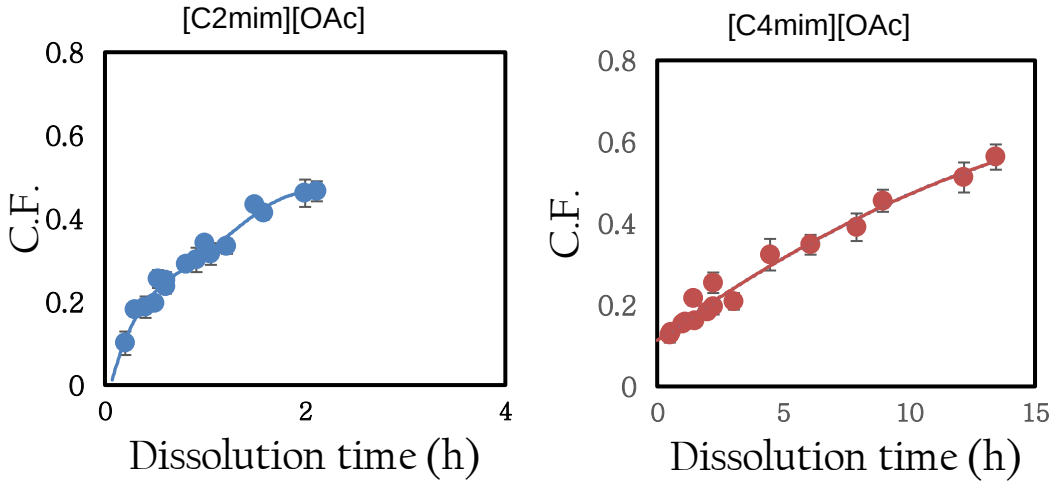

Figure 5.30: Absolute speed for the dissolution of flax fibres at 50 °C for both ILs [C2mim][OAc] and [C4mim][OAc] at 1% water.

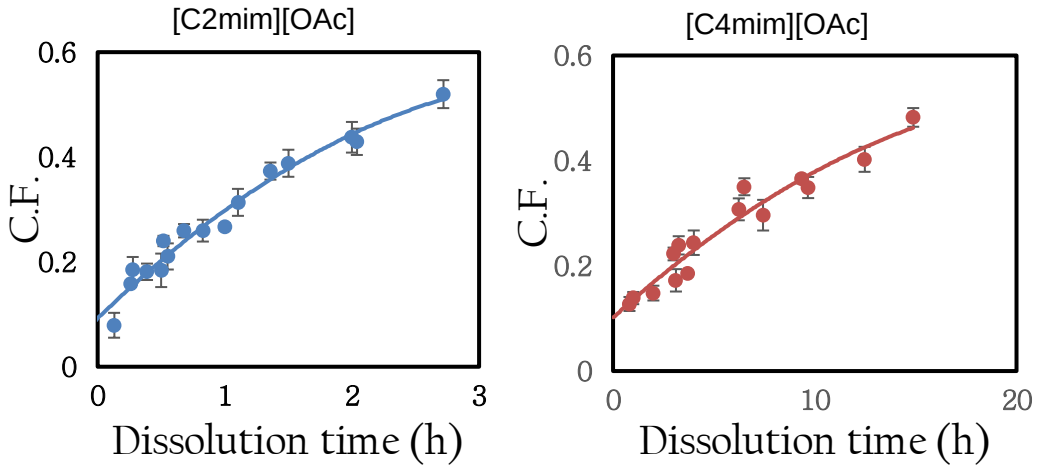

Figure 5.31: Absolute speed for the dissolution of flax fibres at 50 °C for both ILs [C2mim][OAc] and [C4mim][OAc] at 2% water.

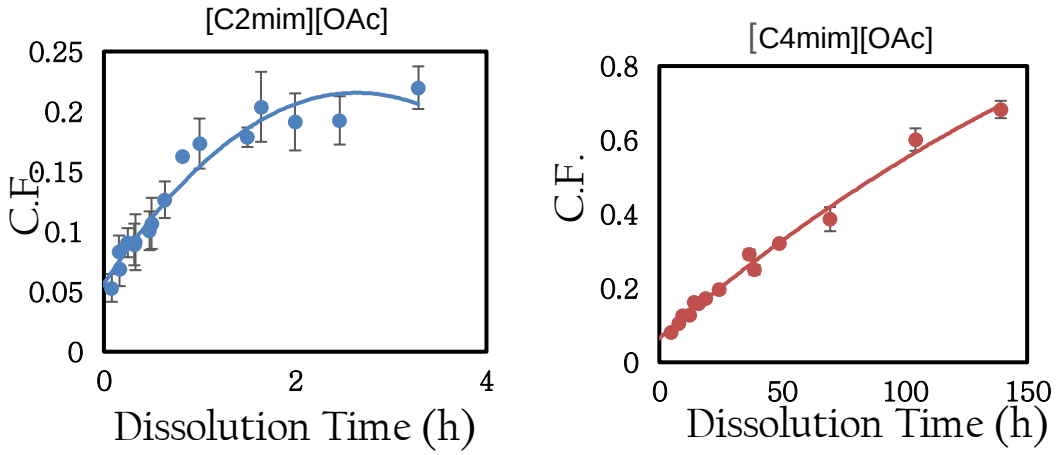

Figure 5.32: Absolute speed for the dissolution of flax fibres at 50 °C for both ILs [C2mim][OAc] and [C4mim][OAc] at 4% water.

5.5 Conclusion

The dissolution mechanism and rate of dissolution of the flax yarns in the ILs [C2mim][OAc] and [C4mim][OAc] has been investigated as a function of water concentrations, times, and temperatures. OM was employed to analyse the morphology of partially dissolved yarns and the results revealed that as the dissolving process progressed, a coagulated flax matrix phase formed around the core yarn as seen in all the reported studies in this thesis.

For the IL [C2mim][OAc], three different water content have been used 1%, 2% and 4% by weight and for the IL [C4mim][OAc], four different water concentration have been used 1%, 2%, 4%, and 8% by weight. The resultant data has also been compared to the results from chapters 3 (the pure IL [C2mim][OAc] was found to consist of 0.2% water), and chapter 4 (the pure IL [C4mim][OAc] was found to consist of 0% water). As expected, the coagulated outer layer was seen to form around the undissolved core fibre for the water systems of 1%, 2%, and 4%. However, no sign of dissolution was shown by the IL [C4mim][OAc]-water system of 8%.

For the IL[C2mim][OAc], the activation energies were found to be 77 ± 5 kJ/mol, 97 ± 3 kJ/mol and 116 ± 6 kJ/mol for the system containing 1%, 2% and 4% water respectively. For the IL [C4mim][OAc], the activation energies were found to be 78 ± 7 kJ/mol, 83 ± 7 kJ/mol and 110 ± 6 kJ/mol for the system containing 1%, 2% and 4% water respectively.

From these experimental results above, we determine the intercepts ($\ln\alpha$) for each water content at each reference temperature themselves were follow an Arrhenius law, being linearly dependent on the inverse of the reference temperature, allowing to measure the activation energy for each water concentration for each IL. The intercepts activation energies for the IL [C2mim][OAc], 77 ± 3 kJ/mol, 97 ± 2 kJ/mol, 116 ± 7 kJ/mol for the system containing 1%, 2% and 4% water respectively. For the IL [C4mim][OAc] the intercepts activation energy are found to be 78 ± 6 kJ/mol, 83 ± 7 kJ/mol, and 110 ± 7 kJ/mol for the system containing 1%, 2% and 4% water respectively. These results are identical with the previous determined values of the dissolution process for IL at each water system.

For each IL, master curves of the 1%, 2% and 4% water content were shifted in natural logarithmic time to overlap with that of the master curve of each pure IL (seen previously in Chapter 3 for [C2mim][OAc] and Chapter 4 for [C4mim][OAc]. Therefore, the shift factors used to create a master- master curve gave a direct measure of the relative dissolution rate between systems. The dissolution rate was found to exponentially decrease as a function of water content for [C2mim][OAc];

however, the dissolution rate at 1% water was found to be higher than that of 0% water for [C4mim][OAc]. This might be related to the reducing in the viscosity which make the dissolution faster at this concentration.

The IL [C2mim][OAc] is generally more efficient for industrial applications; however, it becomes less efficient with higher water content. While the IL [C4mim][OAc], with its higher initial activation energy with water content, shows a level of effectiveness at 1% water make it a viable option for both research and industrial use. This implies that [C4mim][OAc] can be used interchangeably with [C2mim][OAc] in processes where efficient dissolutions are crucial.

Chapter 6

Conclusion

6.1 Summary of Findings

The work presented in this thesis outlines a fundamental study of the dissolution mechanism of flax yarns in three different ILs [C2mim][OAc], [C4mim][OAc], and [C2mim][Oct]. The effects of the key factors such as time, temperature, the influence of altering the cation/anion chain length, and the addition of water as an anti-solvent on the dissolution behaviour of flax fibres were investigated. Results reveal that the growth of coagulated fraction in the partially dissolved flax fibres within the three ILs was shown to follow TTS, enabling the determination of the dissolution activation energy for all the different systems. In this study, measurements were carried out both of macroscopic and microscopic properties over a range of time and temperatures.

Dissolution of flax yarn in $[C2mim]^+[OAc]^-$

In chapter **3**, the dissolution of flax yarns in the pure ionic liquid [C2mim] [OAc] was studied as a function of dissolution times and temperatures, and water was used as the coagulant. Various techniques were used to analyse the dissolution dynamics and properties of the prepared single flax composites including optical microscopy, rheology, and nuclear magnetic resonance (NMR)

From optical microscopy, the cross-sections of processed flax yarns showed two regions: the raw (undissolved) region located in the core surrounded by a dissolved and coagulated region. The dissolution behaviour of the flax yarn sample in the IL [C2mim][OAc] is determined using two different measurement parameters, the coagulation fraction (CF) and the thickness of the outer coagulated cellulose ring, called the ring thickness (T_H). The CF was obtained from OM by measuring the total area and coagulated cellulose area. We used this approach to assess the applicability of our time-temperature superposition (TTS) analysis method. The results obtained from the TTS analysis allowed us to track the increase of the dissolved and coagulated fractions giving an activation energy of 64 ± 5 kJ/mol.

The second set of observations determined the difference in the diameters of the two regions and hence the growth of the coagulated fraction with time and temperature.

As there are 4 measurements per samples analysed for each time and temperature, this leads to a total of 4x4=16 measurements for each condition, giving an accurate calculation of the average thickness of the dissolved and coagulated layer. We plotted the average layer thickness against time (t) and then the square root of the dissolution time (√t). The thickness against (√t) was found to show a linear dependence, enabling the determination of the diffusion coefficient D from the slope of the line, which will be $(2D)^{1/2}$. The gradient of the $\ln D$ vs $1000/T_{ref}$ is used to give the diffusion activation energy, and this gradient of this method gave an activation energy similar gradient to that found from the previous analysis of 64 ± 6 kJ/mol. Our hypothesis is that because the coagulated thickness region grows as the square root of the dissolution time, then the controlling factor for dissolution is the diffusion of the IL through the outer region which comprises dissolved cellulose and IL.

An “intercept method” was introduced, which is highly sensitive to any curvature in an Arrhenius type plot and confirmed the Arrhenius behaviour of our data. This technique uses the intercept from each Arrhenius plot, formed at each reference temperature for the IL, $\ln \alpha_0$, and then these are plotted against the inverse temperature. This method confirmed an identical activation energy of 64 ± 5 kJ/mol.

The pure IL [C2mim][OAc] solution viscosity was measured for all our samples over a temperature range of 30 °C to 80 °C. As expected, the viscosity decreases when temperature is increased. The activation energy for viscous flow was measured from the obtained value of viscosity at each temperature, by plotting $ln\alpha$ vs the inverses temperature. The viscosity activation energy was found by using the slope of this Arrhenius plot for the data of viscosity. The corresponding $E_{a,\eta}$ value was found to be 37$\pm$ 1 kJ/mol, which is lower than that from the coagulated region studies.

Finally, the NMR self-diffusion coefficient for each component ([C2mim]+,[OAc]-) in the mixtures was measured using high field NMR (400 MHz). It was found that larger [C2mim]+ diffuses faster than its counterpart [OAc]- in the pure [C2mim][OAc]. The activation energy values of both ions [C2mim] and [OAc] obtained from NMR diffusion measurement are close to the activation energy value of viscosity, indicating that the IL follows a Stokes-Einstein relationship. Natural logarithm of self-diffusion coefficient vs the inverses their temperatures of $[C2mim]^+$, cation and $[OAc]^-$, anion was plotted. The diffusion activation energies were found 42 $\pm$ 2 kJ/mol and 43 $\pm$ 2 kJ/mol for $[C2mim]^+$ and $[OAc]^-$, respectively. These are in good agreement with the viscosity activation energy described above.

Influence of varying cation and anion chain lengths on the dissolution

In chapter **4**, the dissolution behaviour of the same flax yarns in two further imidazolium based ILs in their pure form was studied. For the first, the anion was kept the same as in the work described in the previous chapter (acetate $[OAc]^-$) but the cation was changed to (1-butyl-3-methylimidazolium) [C4mim]+. For the second part, the cation was kept the same (1-ethyl-3-methylimidazolium) [C2mim]+, but the anion is changed to an octanoate $[Oct]^-$. So, the investigation of the ILs [C4mim][OAc] and [C2mim][Oct] both macroscopic and microscopic properties. These results were then compared with the results in the previous chapter, detailing a study of [C2mim][OAc]. Similar approaches were used as described in the previous chapter to follow the dissolution behaviour. The same partial dissolution method was employed, also using the same flax yarns as in the previous chapter with dissolution carried out at a range of temperatures and times, using the ILs as the dissolving solvents, and water as the coagulant. For the two new ILs studied in this chapter, the dissolved and coagulated material produced an outer ring of a matrix phase as seen previously. Techniques used to study the dissolution included TTS (using Arrhenius plots and the intercept method), rheology, use of the growth of the matrix thickness with time to determine diffusion constants, together with using NMR data and Stokes-Einstein analysis. These two ILs were chosen to highlight how changing the cation/anion chain length might affect the dissolution behaviour compared to [C2mim][OAc].

Optical microscopy images were again collected for a range of dissolution times and temperatures in the IL [C4mim][OAc]. It can be clearly seen that, as in Chapter **3**, the growth of the coagulation fraction is dependent on the dissolution time and temperature, so the appearance of the dissolution process is similar to that in the previous chapter. The average activation energy required to dissolve flax yarn in the IL [C4mim] [OAc] was found to be 67 ± 1 kJ/mol. For the third IL studied, [C2mim][Oct], the dissolution process was started using a higher initial temperature of 50 °C within a specified time range, (as used for two acetate anion ILs), but no observable signs of dissolution were detected even for 3 hours processing time. Subsequently, the temperature was elevated to 60 °C at different dissolution times, but again no outer coagulation layer was observed. In response to these outcomes, the temperature was further increased to 80 °C, resulting in the formation of a coagulated fraction layer around the undissolved core. TTS master curve can be then formed, hence, an average activation energy required to dissolved flax yarn in the IL [C2mim][Oct] was found to be 79 ± 1 kJ/mol.

From the intercept method, the linear fit of $\ln \alpha_0$ vs 1000/T_{ref} were determined to be 69 $\pm$ 2 kJ/mol and 79 $\pm$ 3 kJ/mol for [C4mim][OAc] and [C2mim][Oct] respectively. The calculated activation energies from the intercept method are seen to be in excellent agreement to that obtained from the previous TTS analysis. In addition, the four master curves obtained from the TTS analysis gave similar gradients, leading to similar E_a for each IL. Although [C4mim][OAc] and [C2mim][OAc] have comparable activation energies, they differ slightly, which may be due to that the length size of the alkyl chain of [C4mim] being longer than [C2mim], which influences the dissolution process. Compared to the other ILs, [C2mim][Oct] was examined at lower temperature (30 °C-60 °C), but it was not providing enough energy to dissolve, while higher temperature ranges (80 °C -100 °C) provides sufficient energy for the dissolution process compared to [C2mim][OAc] and [C4mim][OAc].

The diffusion coefficient from the thickness measurements for both ILs over a range of temperatures were used to set the relation between the natural logarithm of diffusion against the inverse of temperature. These linear fits indicate that the system follows an Arrhenius behaviour. Interestingly, the values of the diffusion activation energies were again found to be very close to those of the dissolution activation energies that were found earlier, with values of 69 $\pm$ 5 kJ/mol, 77 $\pm$ 3 kJ/mol and for [C4mim][OAc] and [C2mim][Oct], respectively.

The viscosities for both pure ILs [C4mim][OAc] and [C2mim][Oct] as a function of temperatures ranging from 30 °C to 80 °C were measured. Viscosity is expected to decrease as temperature increases; however, the viscosity generally increases as the molecular weight and the length of the anion chain increases. Each IL presents a decreasing viscosity as temperature increases, with [C2mim][Oct] having a higher viscosity than [C4mim][AOc] across the temperature range studied. This is due to the longer chain of the octanoate anion and higher molecular weight increasing the overall viscosity. The activation energy for viscous flow $E_{a,\eta}$ of both ILs [C4mim][OAc] and [C2mim][Oct] were found to be 46 $\pm$ 2 kJ/mol, 40 $\pm$ 1 kJ/mol respectively.

The self-diffusion coefficients of both ILs throughout a temperature range of 30 °C to 60 °C of [C4mim][OAc] and [C2mim][Oct] found that the larger cation diffuses faster than the anion in both ILs. Moreover, both the ions in [C2mim][Oct] have lower self-diffusion coefficient values compared to [C4mim][OAc] across the same range of temperatures. The activation energies of the NMR diffusion of cation and anion for [C4mim][OAc] were found to be 44 $\pm$ 1 kJ/mol and 45 $\pm$ 1 kJ/mol, respectively. For [C2mim][Oct], the activation energies of NMR self-diffusion of cation and anion were found to be 38 $\pm$ 2 kJ/mol and 39 $\pm$ 3 kJ/mol. The activation energy values of

[C4mim][OAc] and [C2mim][Oct] were obtained from NMR diffusion measurement which are very close to the activation energy values from the viscosity measurements, indicating both ILs follow a Stokes-Einstein relationship.

Finally, a comparison was made between the diffusion behaviour (the growth of the coagulated fraction with time) of the three ILs. To do this it was necessary to compare them all at the same reference temperature. The chosen temperature was 60 °C, for the two acetate anion ILs ([C2mim][OAc] [C4mim][OAc]) as they dissolved at a significant rate at this temperature. However, the octanoate anion IL [C2mim][Oct], did not dissolve significantly at this temperature. Therefore, we need to generate data at 60 °C by a shifting process for the data of Arrhenius plot at 80 °C for IL [C2mim][Oct], to create a master curve at 60 °C. The differences between the three ionic liquids based on the information provided in the plot indicate that the IL [C2mim][OAc] has the fastest dissolution rate among the three, followed by the other acetate anion IL [C4mim][OAc]. The slowest dissolving rate is exhibited by [C2mim][Oct], as demonstrated by its CF curve. By normalising the dissolution time by the viscosity of each IL, it was found that this brought two ILs with the acetate anion much closer together. The [C2mim][Oct] dataset still showed a much slower dissolution rate even when normalising for its viscosity. Again, the dissolution time has been normalised by the NMR self-diffusion coefficient of the cations and anions separately. It showed that with this normalisation the results are very similar to the viscosity normalisation of [C2mim][OAc] and [C4mim][OAc] have a similar relationship between the growth of the coagulation fraction and normalised time (using either the cation or anion diffusion coefficients) and as for [C2mim][Oct] results shows a slower overall dissolution process even when normalised. For the final normalisation, the dissolution time was normalised by the diffusion coefficients calculated directly from the growth of the thickness of the coagulated region. It is seen that normalising the dissolution time by this factor, that this collapses the data of the three ILs onto a set of overlapping curves. Our hypothesis is that the dissolution of the flax is controlled by the diffusion of each IL through a saturated cellulose solution that surrounds each flax yarn as the dissolution progresses. A measure of the relative speed of dissolution in the three ILs can be obtained by shifting the generated master curves at 60 °C to make them overlap by choosing the data of [C2mim][OAc] as the reference data, then shifting all the data again for these systems with now each master curve itself shifted separately in natural logarithmic time to overlap with the master curve of [C2mim][OAc] to create a master-master curve. A master-master curve shows all the results of ILs in order to calculate the relative dissolution rate between systems. The exponential fit of the relationship is such that

as the size of the ILs increases, the relative dissolution speed decreases rapidly. It shows the [C2mim][OAc] is 5 times faster than [C4mim][OAc], and 10 times than [C2mim][Oct].

Effect of the anti-solvent water

In chapter **5**, the effect of water on the dissolution mechanism has been explored by adding small amounts of distilled water to the ILs [C2mim][OAc] and [C4mim][OAc]. The initial water content was found to be 0.2% for the [C2mim][OAc], and 0% water for the [C4mim][OAc], as determined by Karl Fischer titration. For the [C2mim][OAc], four water concentrations were studied: 1%, 2% and 4% by weight. For the [C4mim][OAc], five water concentrations were studied:1%, 2%, 4% and 8% by weight.

Optical microscopy was used to track the growth of the coagulation fraction as a function of time and temperature; however, no coagulation fraction was seen in the system containing 8% water in the [C4mim][OAc]. The mechanism of the dissolution observed in the [C2mim][OAc] with the water systems, and the [C4mim][OAc] with the water systems were found to be similar as that of their pure systems that was observed in the previous two chapters; with the inner fibre area surrounded by various outer layers, with the formation of the coagulation fraction around the core. The main difference seen when using water as an anti-solvent is the coagulation fraction decreases in size as a function of water content (at a fixed temperature and time). Also, the rate at which fibres dissolve at various concentrations fell significantly, indicating that water is acting to decrease the dissolution rate. Interestingly, adding 1% water to the [C4mim][OAc] makes the dissolution speed higher than that of 0% water for this system.

The TTS method was repeated again for each concentration studied: 1%, 2%, and 4% for both ILs separately. The master curves were generated with water systems separately at a chosen temperature as reference temperature, and the analysis repeating again using the other three temperatures as reference temperatures, each of which was used as a reference temperature to create a master curve for each set of data at these different temperatures for each concentration. All these eight systems again obeyed Arrhenius behaviour when using the addition of water. These plotted graphs give similar slopes for each concentration, leading to similar E_a as calculated. For the [C2mim][OAc], the activation energies were found to be 77 ± 5 kJ/mol, 97 ± 3 kJ/mol and 116 ± 6 kJ/mol for 1%, 2% and 4% water systems, respectively, so the activation energy increased as a function of water concentration. An extrapolation

was used to calculate a theoretical value for dry IL 0% water to be 58 ± 4 kJ/mol. A polynomial function of order two was used to fit the data and extrapolate to zero water concentration. From these experimental results above, the intercepts determined at each reference temperature themselves followed an Arrhenius law, being linearly dependent on the inverse of the reference temperature. The gradient of the $\ln \alpha_0$ vs $1000/T_{ref}$ is found to give very similar gradient as the Arrhenius plots 77 ± 3 kJ/mol, 97 ± 2 kJ/mol, and 116 ± 7 kJ/mol for 1%, 2% and 4% water systems, respectively. For the [C4mim][OAc], the activation energies were found to be 78 ± 7 kJ/mol, 83 ± 7 kJ/mol and 110 ± 6 kJ/mol for 1%, 2% and 4% water systems, respectively.

The intercepts determined at each reference temperature themselves followed an Arrhenius law, being linearly dependent on the inverse of the reference temperature. The gradient of the $\ln \alpha_0$ vs $1000/T_{ref}$ gave very similar gradient as the previous Arrhenius plots 78 ± 6 kJ/mol, 83 ± 7 kJ/mol, and 110 ± 7 kJ/mol for 1%, 2% and 4% water systems, respectively.

Finally, the comparison of water on the dissolution rate and activation energy of flax yarns in both ILs [C2mim][OAc] and [C4mim][OAc] showed that the relative dissolution rate decreases as the water concentration increases so the rate of the dissolution at its highest at 0% water for the [C2mim][OAc]. For the [C4mim][OAc], the data fitted with a curve indicates an initial small increase followed by a decrease suggesting that the dissolution process has an optimal water concentration at which it has a dissolution speed peak at 1% water. This indicates that a small amount of water enhances the dissolution process, possibly by reducing the viscosity or breaking down some intermolecular forces in the ionic liquid [C4mim][OAc]. For both ILs, the dissolution speed drops significantly at around 4% water concentration. The activation energies were increased as water concentration increases in both ILs. To conclude that it is also interesting to compare the absolute dissolution speeds for the two ILs. It can be seen that the flax yarns dissolve faster in the [C2mim][OAc] at all water concentrations. This might be related to the viscosity of [C2mim][OAc] being lower than that of [C4mim][OAc].

6.2 Suggestion for Future Directions and prospective

- The work presented in this study was concentrated on three complementary ILs to explore the dissolution behaviour on the flax yarns. It would also be interesting to study the dissolution using different ILs that are able to dissolve flax yarns to study the dependence of activation energy on the type of the IL, which can provide valuable insights into the kinetic aspects of the dissolution process.
- The work presented here also studied in two ILs [C2mim][OAc] and [C4mim][OAc] to investigate the influence of water on the solubility for dissolving flax fibres. It would also be worth to explore the effect of water on the dissolution of flax yarns in the third IL [C2mim][Oct] and other solvents in order to understand the changing of the solvent properties, and hence the solubility.

This study's focus is to understand and explore the underlying physics of preparing all-cellulose composites by investigating the dissolution of single flax yarns. The results obtained in this study will contribute to future research to consider preparing all-cellulose composites. The results of this study indicate that manufacturers are now able to predict the required temperature and dissolve time to obtain the right matrix fraction, increasing the reproducibility as w ell as effectiveness of ACC production.

References

1. Kamel, S., et al., *Pharmaceutical significance of cellulose: A review.* Express Polym Lett, 2008. **2**(11): p. 758-778.
2. Rahatekar, S.S., et al., *Solution spinning of cellulose carbon nanotube composites using room temperature ionic liquids.* Polymer, 2009. **50**(19): p. 4577-4583.
3. Kabir, S.F., et al., *Cellulose-based hydrogel materials: Chemistry, properties and their prospective applications.* Progress in biomaterials, 2018. **7**: p. 153-174.
4. Mu, R., et al., *Recent trends and applications of cellulose nanocrystals in food industry.* Trends in Food Science & Technology, 2019. **93**: p. 136-144.
5. Wang, Y., W. Xie, and D. Wu, *Rheological properties of magnetorheological suspensions stabilized with nanocelluloses.* Carbohydrate polymers, 2020. **231**: p. 115776.
6. Mishra, S., et al., *Biochemistry, synthesis, and applications of bacterial cellulose: a review.* Frontiers in bioengineering and biotechnology, 2022. **10**: p. 780409.
7. Olsson, C. and G. Westman, *Direct dissolution of cellulose: background, means and applications.* Cellulose-fundamental aspects, 2013. **10**: p. 52144.
8. Onwukamike, K., et al., *Critical review on sustainable homogeneous cellulose modification: why renewability is not enough. ACS Sustain Chem Eng 7: 1826–1840*. 2019.
9. Li, Y., et al., *Towards a molecular understanding of cellulose dissolution in ionic liquids: anion/cation effect, synergistic mechanism and physicochemical aspects.* Chemical science, 2018. **9**(17): p. 4027-4043.
10. Ahmadi, P., et al., *Development of ethyl cellulose-based formulations: A perspective on the novel technical methods.* Food Reviews International, 2022. **38**(4): p. 685-732.
11. Halder, P., et al., *Progress on the pre-treatment of lignocellulosic biomass employing ionic liquids.* Renewable and Sustainable Energy Reviews, 2019. **105**: p. 268-292.
12. Johnson, D.L., *Method of preparing polymers from a mixture of cyclic amine oxides and polymers*. 1970, Google Patents.
13. Rosenau, T., et al., *The chemistry of side reactions and byproduct formation in the system NMMO/cellulose (Lyocell process).* Progress in polymer science, 2001. **26**(9): p. 1763-1837.
14. Fink, H.-P., et al., *Structure formation of regenerated cellulose materials from NMMO-solutions.* Progress in Polymer Science, 2001. **26**(9): p. 1473-1524.
15. Luján-Ornelas, C., et al., *A life cycle thinking approach to analyse sustainability in the textile industry: A literature review.* Sustainability, 2020. **12**(23): p. 10193.
16. Eriksen, M., et al., *Plastic pollution in the world's oceans: more than 5 trillion plastic pieces weighing over 250,000 tons afloat at sea.* PloS one, 2014. **9**(12): p. e111913.
17. Wittmar, A.S.M., et al., *Formation of all-biopolymer-based composites with cellulose as main component.* RSC Applied Interfaces, 2025.
18. Chen, F., et al., *Swelling and dissolution kinetics of natural and man-made cellulose fibers in solvent power tuned ionic liquid.* Cellulose, 2020. **27**(13): p. 7399-7415.
19. Nishino, T., I. Matsuda, and K. Hirao, *All-cellulose composite.* Macromolecules, 2004. **37**(20): p. 7683-7687.
20. Moudood, A., et al., *Mechanical properties of flax fiber-reinforced composites at different relative humidities: Experimental, geometric, and displacement*

potential function approaches. Polymer Composites, 2020. **41**(12): p. 4963-4973.
21. Foulk, J.A., et al., *Flax fiber: potential for a new crop in the Southeast*. 2002, ASHS Press, Alexandria, VA.
22. Hawkins, J.E., et al., *Time temperature superposition of the dissolution of cellulose fibres by the ionic liquid 1-ethyl-3-methylimidazolium acetate with cosolvent dimethyl sulfoxide.* Carbohydrate Polymer Technologies and Applications, 2021. **2**: p. 100021.
23. Victoria, A., M.E. Ries, and P.J. Hine, *Use of interleaved films to enhance the properties of all-cellulose composites.* Composites Part A: Applied Science and Manufacturing, 2022: p. 107062.
24. Albarakati, F.A., P.J. Hine, and M.E. Ries, *Effect of water on the dissolution of flax fiber bundles in the ionic liquid 1-ethyl-3-methylimidazolium acetate.* Cellulose, 2023. **30**(12): p. 7619-7632.
25. Khalil, H.A., A. Bhat, and A.I. Yusra, *Green composites from sustainable cellulose nanofibrils: A review.* Carbohydrate polymers, 2012. **87**(2): p. 963-979.
26. French, A.D., *Glucose, not cellobiose, is the repeating unit of cellulose and why that is important.* Cellulose, 2017. **24**(11): p. 4605-4609.
27. Geyer, U., et al., *Formation, derivatization and applications of bacterial cellulose.* International Journal of Biological Macromolecules, 1994. **16**(6): p. 343-347.
28. Kalia, S., et al., *Cellulose-based bio-and nanocomposites: a review.* International journal of polymer science, 2011. **2011**.
29. Brehm, M., et al., *Dissolving Cellulose in 1,2,3-Triazolium- and Imidazolium-Based Ionic Liquids with Aromatic Anions.* Molecules, 2020. **25**(15).
30. Bluhm, T.L. and A. Sarko, *Packing analysis of carbohydrates and polysaccharides. V. Crystal structures of two polymorphs of pachyman triacetate.* Biopolymers: Original Research on Biomolecules, 1977. **16**(9): p. 2067-2089.
31. Wertz, J.-L., O. Bédué, and J.P. Mercier, *Cellulose science and technology*. 2010: EPFL press.
32. Kulichikhin, V.G., E.B. Kostikova, and D.P. Olenin, *The concentration and degree of polymerization of the cellulose as factors in the viscosity properties of the viscose.* Fibre Chemistry, 1973. **4**(2): p. 155-159.
33. Cousins, S.K. and R.M. Brown Jr, *Cellulose I microfibril assembly: computational molecular mechanics energy analysis favours bonding by van der Waals forces as the initial step in crystallization.* Polymer, 1995. **36**(20): p. 3885-3888.
34. Sweet, M.S. and J.E. Winandy, *Influence of degree of polymerization of cellulose and hemicellulose on strength loss in fire-retardant-treated southern pine.* 1999.
35. Neto, W.P.F., *Morphological investigation of cellulose nanocrystals and nanocomposite applications*. 2017, Université Grenoble Alpes; Universidade Federal de Uberlândia.
36. Yamane, C., et al., *Two different surface properties of regenerated cellulose due to structural anisotropy.* Polymer journal, 2006. **38**(8): p. 819-826.
37. Jarvis, M., *Cellulose stacks up.* Nature, 2003. **426**(6967): p. 611-612.
38. Li, Q. and S. Renneckar, *Supramolecular structure characterization of molecularly thin cellulose I nanoparticles.* Biomacromolecules, 2011. **12**(3): p. 650-659.
39. Medronho, B. and B. Lindman, *Competing forces during cellulose dissolution: From solvents to mechanisms.* Current Opinion in Colloid & Interface Science, 2014. **19**(1): p. 32-40.
40. Kroon-Batenburg, L. and J. Kroon, *The crystal and molecular structures of cellulose I and II.* Glycoconjugate journal, 1997. **14**(5): p. 677-690.

41. O'sullivan, A.C., *Cellulose: the structure slowly unravels.* Cellulose, 1997. **4**(3): p. 173-207.
42. Kovalenko, V.I., *Crystalline cellulose: structure and hydrogen bonds.* Russian Chemical Reviews, 2010. **79**(3): p. 231.
43. Gardiner, E.S. and A. Sarko, *Packing analysis of carbohydrates and polysaccharides. 16. The crystal structures of celluloses IVI and IVII.* Canadian journal of chemistry, 1985. **63**(1): p. 173-180.
44. Blackwell, J., et al., *X-ray Studies of the Structure of Cellulose Complexes*. 1987, ACS Publications.
45. Siró, I. and D. Plackett, *Microfibrillated cellulose and new nanocomposite materials: a review.* Cellulose, 2010. **17**: p. 459-494.
46. Huang, C., et al., *A comprehensive investigation on cellulose nanocrystals with different crystal structures from cotton via an efficient route.* Carbohydrate Polymers, 2022. **276**: p. 118766.
47. Gindl-Altmutter, W., et al., *All-cellulose composites prepared from flax and lyocell fibres compared to epoxy–matrix composites.* Composites Science and Technology, 2012. **72**(11): p. 1304-1309.
48. Shibata, M., et al., *All-cellulose and all-wood composites by partial dissolution of cotton fabric and wood in ionic liquid.* Carbohydrate polymers, 2013. **98**(2): p. 1532-1539.
49. Bapan, A. and M. Samrat, *Jute based all-cellulose composite laminates.* Indian Journal of Fibre & Textile Research (IJFTR), 2016. **41**(4): p. 380-384.
50. Shibata, M., et al., *All-wood biocomposites by partial dissolution of wood flour in 1-butyl-3-methylimidazolium chloride.* Journal of applied polymer science, 2013. **127**(6): p. 4802-4808.
51. Faruk, O., et al., *Progress report on natural fiber reinforced composites.* Macromolecular Materials and Engineering, 2014. **299**(1): p. 9-26.
52. TG, Y.G., S. MR, and S. Siengchin, *Natural fibers as sustainable and renewable resource for development of eco-friendly composites: a comprehensive review.* Frontiers in Materials, 2019. **6**: p. 226.
53. Yallew, T.B., et al., *Response of natural fiber reinforced polymer composites when subjected to various environments.* International Journal of Plastics Technology, 2018. **22**(1): p. 56-72.
54. Habibi, M., et al., *Combining short flax fiber mats and unidirectional flax yarns for composite applications: Effect of short flax fibers on biaxial mechanical properties and damage behaviour.* Composites Part B: Engineering, 2017. **123**: p. 165-178.
55. Ganesan, V., et al., *Optimisation of mechanical properties in saw-dust/woven-jute fibre/polyester structural composites under liquid nitrogen environment using response surface methodology.* Polymers, 2021. **13**(15): p. 2471.
56. Kalka, S., et al., *Biodegradability of all-cellulose composite laminates.* Composites Part A: Applied Science and Manufacturing, 2014. **59**: p. 37-44.
57. Moudood, A., et al., *Flax fiber and its composites: An overview of water and moisture absorption impact on their performance.* Journal of Reinforced Plastics and Composites, 2019. **38**(7): p. 323-339.
58. Yan, L., N. Chouw, and K. Jayaraman, *Flax fibre and its composites–A review.* Composites Part B: Engineering, 2014. **56**: p. 296-317.
59. Preisner, M., et al., *Flax fiber.* Kirk-Othmer Encyclopedia of Chemical Technology, 2000: p. 1-32.
60. Bledzki, A., et al., *The effects of acetylation on properties of flax fibre and its polypropylene composites.* Express polymer letters, 2008. **2**(6): p. 413-422.
61. Gassan, J. and A.K. Bledzki, *Thermal degradation of flax and jute fibers.* Journal of Applied Polymer Science, 2001. **82**(6): p. 1417-1422.
62. Ramesh, M., *Flax (Linum usitatissimum L.) fibre reinforced polymer composite materials: A review on preparation, properties and prospects.* Progress in Materials Science, 2019. **102**: p. 109-166.

63. Rong, M.Z., et al., *The effect of fiber treatment on the mechanical properties of unidirectional sisal-reinforced epoxy composites.* Composites Science and technology, 2001. **61**(10): p. 1437-1447.
64. Chen, F., et al., *Unidirectional All-Cellulose Composites from Flax via Controlled Impregnation with Ionic Liquid.* Polymers, 2020. **12**(5).
65. Amiri, A., C.A. Ulven, and S. Huo, *Effect of chemical treatment of flax fiber and resin manipulation on service life of their composites using time-temperature superposition.* Polymers, 2015. **7**(10): p. 1965-1978.
66. Stamboulis, A., C. Baillie, and T. Peijs, *Effects of environmental conditions on mechanical and physical properties of flax fibers.* Composites Part A: Applied Science and Manufacturing, 2001. **32**(8): p. 1105-1115.
67. Heinze, T. and A. Koschella, *Solvents applied in the field of cellulose chemistry: a mini review.* Polímeros, 2005. **15**: p. 84-90.
68. Zhang, S., et al., *Regenerated cellulose by the lyocell process, a brief review of the process and properties.* BioResources, 2018. **13**(2): p. 4577-4592.
69. Li, X., et al., *Room-temperature superbase-derived ionic liquids with facile synthesis and low viscosity: powerful solvents for cellulose dissolution by destroying the cellulose aggregate structure.* Macromolecules, 2020. **53**(9): p. 3284-3295.
70. Rosenau, T., et al., *Autocatalytic decomposition of N-methylmorpholine N-oxide induced by Mannich intermediates.* The Journal of Organic Chemistry, 1999. **64**(7): p. 2166-2167.
71. Rosenau, T., et al., *Cellulose solutions in N-methylmorpholine-N-oxide (NMMO)–degradation processes and stabilizers.* Cellulose, 2002. **9**(3): p. 283-291.
72. Zhang, Y., et al., *Formation and Characterization of Cellulose Membranes from N-Methylmorpholine-N-oxide Solution.* Macromolecular Bioscience, 2001. **1**(4): p. 141-148.
73. Andersson, C., *New ways to enhance the functionality of paperboard by surface treatment–a review.* Packaging Technology and Science: An International Journal, 2008. **21**(6): p. 339-373.
74. Yang, J., et al., *Inhibiting degradation of cellulose dissolved in ionic liquids via amino acids.* Green Chemistry, 2019. **21**(10): p. 2777-2787.
75. Sirviö, J.A. and J.P. Heiskanen, *Room-temperature dissolution and chemical modification of cellulose in aqueous tetraethylammonium hydroxide–carbamide solutions.* Cellulose, 2019. **27**(4): p. 1933-1950.
76. Cai, J., L. Wang, and L. Zhang, *Influence of coagulation temperature on pore size and properties of cellulose membranes prepared from NaOH–urea aqueous solution.* Cellulose, 2007. **14**(3): p. 205-215.
77. Cai, J. and L. Zhang, *Unique gelation behavior of cellulose in NaOH/urea aqueous solution.* Biomacromolecules, 2006. **7**(1): p. 183-189.
78. Huber, T., et al., *A critical review of all-cellulose composites.* Journal of Materials Science, 2012. **47**(3): p. 1171-1186.
79. Fink, H.-P., J. Ganster, and A. Lehmann, *Progress in cellulose shaping: 20 years industrial case studies at Fraunhofer IAP.* Cellulose, 2013. **21**(1): p. 31-51.
80. Cao, Y., et al., *Imidazolium-based ionic liquids for cellulose pretreatment: recent progresses and future perspectives.* Applied microbiology and biotechnology, 2017. **101**(2): p. 521-532.
81. Bochek, A., *Effect of hydrogen bonding on cellulose solubility in aqueous and nonaqueous solvents.* Russian journal of applied chemistry, 2003. **76**(11): p. 1711-1719.
82. Tanpichai, S., et al., *Review of the recent developments in all-cellulose nanocomposites: Properties and applications.* Carbohydrate polymers, 2022. **286**: p. 119192.

83. Soykeabkaew, N., T. Nishino, and T. Peijs, *All-cellulose composites of regenerated cellulose fibres by surface selective dissolution.* Composites Part A: Applied Science and Manufacturing, 2009. **40**(4): p. 321-328.
84. Swatloski, R.P., et al., *Dissolution of Cellose with Ionic Liquids.* Journal of the American Chemical Society, 2002. **124**(18): p. 4974-4975.
85. Vilaro, P., et al., *Use of Ionic Liquids for Hemp Fiber Degumming.* ACS Sustainable Chemistry & Engineering, 2024.
86. Miao, C. and W.Y. Hamad, *Cellulose reinforced polymer composites and nanocomposites: a critical review.* Cellulose, 2013. **20**(5): p. 2221-2262.
87. Walden, P., *Molecular magnitude and electrical conductivity of some fused salts.* Bull Acad Imp Sci St Petersb, 1914. **6**: p. 405-422.
88. Yang, G., et al., *Review of ionic liquids containing, polymer/inorganic hybrid electrolytes for lithium metal batteries.* Materials & Design, 2020. **190**: p. 108563.
89. Earle, M.J., et al., *The distillation and volatility of ionic liquids.* Nature, 2006. **439**(7078): p. 831-834.
90. Plechkova, N.V. and K.R. Seddon, *Applications of ionic liquids in the chemical industry.* Chemical Society Reviews, 2008. **37**(1): p. 123-150.
91. Swatloski, R.P., et al., *Ionic liquids for the dissolution and regeneration of cellulose*, in *Molten Salts Xiii*, P.C. Trulove, et al., Editors. 2002. p. 155-164.
92. Khan, A.S., et al., *Dicationic ionic liquids as sustainable approach for direct conversion of cellulose to levulinic acid.* Journal of Cleaner Production, 2018. **170**: p. 591-600.
93. Huber, T., et al., *A critical review of all-cellulose composites.* Journal of Materials Science, 2012. **47**(3): p. 1171-1186.
94. Bylin, S., et al., *Solvation behavior of cellulose and xylan in the MIM/EMIMAc ionic liquid solvent system: Parameters for small-scale solvation.* BioResources, 2014. **9**(1): p. 1038-1054.
95. Brehm, M., et al., *Triazolium-Based Ionic Liquids: A Novel Class of Cellulose Solvents.* Journal of Physical Chemistry B, 2019. **123**(18): p. 3994-4003.
96. Remsing, R.C., et al., *Solvation of carbohydrates in N, N'-dialkylimidazolium ionic liquids: a multinuclear NMR spectroscopy study.* The Journal of Physical Chemistry B, 2008. **112**(35): p. 11071-11078.
97. Youngs, T.G., et al., *A molecular dynamics study of glucose solvation in the ionic liquid 1, 3-dimethylimidazolium chloride.* ChemPhysChem, 2006. **7**(11): p. 2279-2281.
98. Roselli, A., et al., *Understanding the role of water in the interaction of ionic liquids with wood polymers.* Carbohydrate Polymers, 2017. **168**: p. 121-128.
99. Fukaya, Y., et al., *Cellulose dissolution with polar ionic liquids under mild conditions: required factors for anions.* Green Chemistry, 2008. **10**(1): p. 44-46.
100. Liebner, F., et al., *Thermal aging of 1-alkyl-3-methylimidazolium ionic liquids and its effect on dissolved cellulose.* 2010.
101. Zweckmair, T., et al., *On the mechanism of the unwanted acetylation of polysaccharides by 1, 3-dialkylimidazolium acetate ionic liquids: Part 1—Analysis, acetylating agent, influence of water, and mechanistic considerations.* Cellulose, 2015. **22**: p. 3583-3596.
102. Zhang, H., et al., *1-Allyl-3-methylimidazolium chloride room temperature ionic liquid: a new and powerful nonderivatizing solvent for cellulose.* Macromolecules, 2005. **38**(20): p. 8272-8277.
103. Meine, N., F. Benedito, and R. Rinaldi, *Thermal stability of ionic liquids assessed by potentiometric titration.* Green Chemistry, 2010. **12**(10): p. 1711-1714.
104. Welton, T., *Ionic liquids: a brief history.* Biophysical reviews, 2018. **10**(3): p. 691-706.

105. Shukla, M. and S. Saha, *A comparative study of piperidinium and imidazolium based ionic liquids: thermal, spectroscopic and theoretical studies.* Ionic liquids-new aspects for the future, 2013. **23**.
106. Xiao, M., et al., *CO2 capture with hybrid absorbents of low viscosity imidazolium-based ionic liquids and amine.* Applied Energy, 2019. **235**: p. 311-319.
107. Varfolomeev, M.A., et al., *Thermodynamics of hydrogen bonding and van der Waals interactions of organic solutes in solutions of imidazolium based ionic liquids:"Structure-property" relationships.* Thermochimica Acta, 2016. **633**: p. 12-23.
108. Gericke, M., P. Fardim, and T. Heinze, *Ionic liquids—promising but challenging solvents for homogeneous derivatization of cellulose.* Molecules, 2012. **17**(6): p. 7458-7502.
109. Ries, M.E., et al., *Microscopic and Macroscopic Properties of Carbohydrate Solutions in the Ionic Liquid 1-Ethyl-3-methyl-imidazolium Acetate.* The Journal of Physical Chemistry B, 2018. **122**(37): p. 8763-8771.
110. Ries, M.E., et al., *Diffusion of 1-ethyl-3-methyl-imidazolium acetate in glucose, cellobiose, and cellulose solutions.* Biomacromolecules, 2014. **15**(2): p. 609-617.
111. Yuan, C., et al., *Dissolution and transesterification of cellulose in γ-valerolactone promoted by ionic liquids.* New Journal of Chemistry, 2019. **43**(1): p. 330-337.
112. Zheng, B., et al., *Dissolution capacity and rheology of cellulose in ionic liquids composed of imidazolium cation and phosphate anions.* Polymers for Advanced Technologies, 2019. **30**(7): p. 1751-1758.
113. Green, S.M., et al., *NMR and rheological study of anion size influence on the properties of two imidazolium-based ionic liquids.* Scientific reports, 2017. **7**(1): p. 1-12.
114. Mahmood, H., M. Sulaiman, and M. Moniruzzaman, *Ionic Liquids as Green Solvents for Lignocellulosic Biomass Utilization.* Industrial Applications of Green Solvents: Volume II, 2019. **54**: p. 60-86.
115. Mahmood, H., et al., *Pretreatment of oil palm biomass with ionic liquids: a new approach for fabrication of green composite board.* Journal of Cleaner Production, 2016. **126**: p. 677-685.
116. Wu, L., S.-H. Lee, and T. Endo, *Effect of dimethyl sulfoxide on ionic liquid 1-ethyl-3-methylimidazolium acetate pretreatment of eucalyptus wood for enzymatic hydrolysis.* Bioresource technology, 2013. **140**: p. 90-96.
117. Cheng, G., et al., *Impact of ionic liquid pretreatment conditions on cellulose crystalline structure using 1-ethyl-3-methylimidazolium acetate.* The Journal of Physical Chemistry B, 2012. **116**(33): p. 10049-10054.
118. Zhang, J., et al., *A comparative study of enzymatic hydrolysis and thermal degradation of corn stover: understanding biomass pretreatment.* RSC Advances, 2015. **5**(46): p. 36999-37005.
119. Verma, C., et al., *Dissolution of cellulose in ionic liquids and their mixed cosolvents: A review.* Sustainable Chemistry and Pharmacy, 2019. **13**: p. 100162.
120. Doherty, T.V., et al., *Ionic liquid solvent properties as predictors of lignocellulose pretreatment efficacy.* Green chemistry, 2010. **12**(11): p. 1967-1975.
121. Fukaya, Y., A. Sugimoto, and H. Ohno, *Superior solubility of polysaccharides in low viscosity, polar, and halogen-free 1, 3-dialkylimidazolium formates.* Biomacromolecules, 2006. **7**(12): p. 3295-3297.
122. Zavrel, M., et al., *High-throughput screening for ionic liquids dissolving (ligno-) cellulose.* Bioresource technology, 2009. **100**(9): p. 2580-2587.

123. Hamidah, U., et al., *Recycled ionic liquid 1-ethyl-3-methylimidazolium acetate pretreatment for enhancing enzymatic saccharification of softwood without cellulose regeneration.* Journal of wood science, 2017. **64**(2): p. 149-156.
124. Wendler, F., L.-N. Todi, and F. Meister, *Thermostability of imidazolium ionic liquids as direct solvents for cellulose.* Thermochimica acta, 2012. **528**: p. 76-84.
125. Pinkert, A., et al., *Ionic Liquids and Their Interaction with Cellulose.* Chemical Reviews, 2009. **109**(12): p. 6712-6728.
126. Köhler, S., et al., *Interactions of Ionic Liquids with Polysaccharides 1. Unexpected Acetylation of Cellulose with 1-Ethyl-3-methylimidazolium Acetate.* Macromolecular Rapid Communications, 2007. **28**(24): p. 2311-2317.
127. Singh, S., B.A. Simmons, and K.P. Vogel, *Visualization of biomass solubilization and cellulose regeneration during ionic liquid pretreatment of switchgrass.* Biotechnology and bioengineering, 2009. **104**(1): p. 68-75.
128. Schuermann, J., et al., *Surface tension of concentrated cellulose solutions in 1-ethyl-3-methylimidazolium acetate.* Cellulose, 2016. **23**(2): p. 1043-1050.
129. Cosby, T., et al., *Kinetics of ionic liquid-facilitated cellulose decrystallization by Raman spectral mapping.* Cellulose, 2021: p. 1-10.
130. Radhi, A., et al., *Macroscopic and microscopic study of 1-ethyl-3-methyl-imidazolium acetate–DMSO mixtures.* The Journal of Physical Chemistry B, 2015. **119**(4): p. 1633-1640.
131. Bogolitsyn, K., T. Skrebets, and T. Makhova, *Physicochemical properties of 1-butyl-3-methylimidazolium acetate.* Russian Journal of General Chemistry, 2009. **79**: p. 125-128.
132. Belesov, A.V., et al., *New insights into the thermal stability of 1-butyl-3-methylimidazolium-based ionic liquids.* International Journal of Molecular Sciences, 2022. **23**(18): p. 10966.
133. Lefroy, K.S., B.S. Murray, and M.E. Ries, *Rheological and NMR studies of cellulose dissolution in the ionic liquid BmimAc.* The Journal of Physical Chemistry B, 2021. **125**(29): p. 8205-8218.
134. Castro, M.C., et al., *Thermophysical characterization of the mixtures of the ionic liquid 1-ethyl-3-methylimidazolium acetate with 1-propanol or 2-propanol.* Journal of Chemical & Engineering Data, 2016. **61**(7): p. 2299-2310.
135. Safarov, J., et al., *Thermophysical properties of 1-butyl-3-methylimidazolium acetate over a wide range of temperatures and pressures.* Fluid Phase Equilibria, 2014. **383**: p. 144-155.
136. Ju, Z., et al., *Theoretical Mechanism on the Cellulose Regeneration from a Cellulose/EmimOAc Mixture in Anti-Solvents.* Materials, 2022. **15**(3): p. 1158.
137. Lindman, B., G. Karlström, and L. Stigsson, *On the mechanism of dissolution of cellulose.* Journal of molecular liquids, 2010. **156**(1): p. 76-81.
138. Glasser, W.G., et al., *About the structure of cellulose: debating the Lindman hypothesis.* Cellulose, 2012. **19**(3): p. 589-598.
139. Lindman, B., et al., *The relevance of structural features of cellulose and its interactions to dissolution, regeneration, gelation and plasticization phenomena.* Physical Chemistry Chemical Physics, 2017. **19**(35): p. 23704-23718.
140. Novoselov, N., et al., *Study of dissolution of cellulose in ionic liquids by computer modeling.* Fibre Chemistry, 2007. **39**(2): p. 153-158.
141. Feng, L. and Z.-l. Chen, *Research progress on dissolution and functional modification of cellulose in ionic liquids.* Journal of Molecular Liquids, 2008. **142**(1-3): p. 1-5.
142. Zhang, J., et al., *Application of ionic liquids for dissolving cellulose and fabricating cellulose-based materials: state of the art and future trends.* Materials Chemistry Frontiers, 2017. **1**(7): p. 1273-1290.

143. Miller-Chou, B.A. and J.L. Koenig, *A review of polymer dissolution.* Progress in polymer science, 2003. **28**(8): p. 1223-1270.
144. Le Moigne, N., *Swelling and dissolution mechanisms of cellulose fibres*. 2008, Ecole Nationale Supérieure des Mines de Paris.
145. Le Moigne, N. and P. Navard, *On the specific behaviour of native cellulose fibers upon dissolution*, in *Cellulose Solvents: For Analysis, Shaping and Chemical Modification*. 2010, ACS Publications. p. 137-148.
146. Vrentas, J. and C.M. Vrentas, *Dissolution of rubbery and glassy polymers.* Journal of Polymer Science Part B: Polymer Physics, 1998. **36**(14): p. 2607-2614.
147. Zhang, L., D. Ruan, and S. Gao, *Dissolution and regeneration of cellulose in NaOH/thiourea aqueous solution.* Journal of Polymer Science Part B: Polymer Physics, 2002. **40**(14): p. 1521-1529.
148. Norgren, M., et al., *Perspectives on the Lindman hypothesis and cellulose interactions.* Molecules, 2023. **28**(10): p. 4216.
149. Alves, L., et al., *On the role of hydrophobic interactions in cellulose dissolution and regeneration: Colloidal aggregates and molecular solutions.* Colloids and Surfaces A: Physicochemical and Engineering Aspects, 2015. **483**: p. 257-263.
150. Glasser, W.G., et al., *About the structure of cellulose: debating the Lindman hypothesis.* Cellulose, 2012. **19**: p. 589-598.
151. Swatloski, R.P., et al., *Ionic Liquids for the Dissolution and Regneration of Cellulose.* ECS Proceedings Volumes, 2002. **2002**(1): p. 155.
152. Tan, X., et al., *Effect of anti-solvents on the characteristics of regenerated cellulose from 1-ethyl-3-methylimidazolium acetate ionic liquid.* International journal of biological macromolecules, 2019. **124**: p. 314-320.
153. Hauru, L.K.J., et al., *Role of Solvent Parameters in the Regeneration of Cellulose from Ionic Liquid Solutions.* Biomacromolecules, 2012. **13**(9): p. 2896-2905.
154. Perez, S. and D. Samain, *Structure and engineering of celluloses.* Advances in carbohydrate chemistry and biochemistry, 2010. **64**: p. 25-116.
155. Meenatchi, B., V. Renuga, and A. Manikandan, *Cellulose dissolution and regeneration using various imidazolium based protic ionic liquids.* Journal of Molecular Liquids, 2017. **238**: p. 582-588.
156. Gupta, K.M., Z. Hu, and J. Jiang, *Molecular insight into cellulose regeneration from a cellulose/ionic liquid mixture: effects of water concentration and temperature.* Rsc Advances, 2013. **3**(13): p. 4425-4433.
157. Mazlan, N.S.N., et al., *Comparison of regenerated cellulose membrane coagulated in sulphate based coagulant.* Cerne, 2019. **25**: p. 18-24.
158. Hedlund, A., et al., *Microstructures of cellulose coagulated in water and alcohols from 1-ethyl-3-methylimidazolium acetate: contrasting coagulation mechanisms.* Cellulose, 2019. **26**: p. 1545-1563.
159. Hedlund, A., T. Köhnke, and H. Theliander, *Coagulation of EmimAc-cellulose solutions: dissolutionprecipitation disparity and effects of non-solvents and cosolvent.* Nordic Pulp & Paper Research Journal, 2015. **30**(1): p. 32-42.
160. Hauru, L.K., et al., *Role of solvent parameters in the regeneration of cellulose from ionic liquid solutions.* Biomacromolecules, 2012. **13**(9): p. 2896-2905.
161. Wawro, D., et al., *Strong cellulosic film cast from ionic liquid solutions.* Fibres & Textiles in Eastern Europe, 2014(3 (105): p. 35-42.
162. Bang, Y.H., et al., *Effect of coagulation conditions on fine structure of regenerated cellulosic films made from cellulose/N-methylmorpholine-N-oxide/H2O systems.* Journal of Applied Polymer Science, 1999. **73**(13): p. 2681-2690.
163. Hedlund, A., H. Theliander, and T. Köhnke, *Mass transport during coagulation of cellulose-ionic liquid solutions in different non-solvents.* Cellulose, 2019. **26**: p. 8525-8541.

164. Hedlund, A., T. Köhnke, and H. Theliander, *Diffusion in ionic liquid–cellulose solutions during coagulation in water: mass transport and coagulation rate measurements.* Macromolecules, 2017. **50**(21): p. 8707-8719.
165. Zeng, B., X. Wang, and N. Byrne, *Cellulose beads derived from waste textiles for drug delivery.* Polymers, 2020. **12**(7): p. 1621.
166. Taokaew, S. and W. Kriangkrai, *Recent Progress in Processing Cellulose Using Ionic Liquids as Solvents.* Polysaccharides, 2022. **3**(4): p. 671-691.
167. Wurmitzer, M., *Computational analysis of chemical vapor deposition for nitride-based hard coatings.* 2023.
168. Germgård, U., *The Arrhenius equation is still a useful tool in chemical engineering.* Nordic Pulp & Paper Research Journal, 2017. **32**(1): p. 21-24.
169. Olowoyo, S.O., *Kinetics and Activation Energy Parameters for Hydrolysis of Acetic Anhydride in a Water-Acetone Cosolvent System*. 2018, East Tennessee State University.
170. Le, K.A., R. Sescousse, and T. Budtova, *Influence of water on cellulose-EMIMAc solution properties: a viscometric study.* Cellulose, 2012. **19**(1): p. 45-54.
171. Gericke, M., et al., *Rheological properties of cellulose/ionic liquid solutions: from dilute to concentrated states.* Biomacromolecules, 2009. **10**(5): p. 1188-1194.
172. Reid, J.E., et al., *Interactions in water–ionic liquid mixtures: comparing protic and aprotic systems.* The Journal of Physical Chemistry B, 2017. **121**(3): p. 599-609.
173. Saha, D. and A. Mukherjee, *Effect of water and ionic liquids on biomolecules.* Biophysical reviews, 2018. **10**(3): p. 795-808.
174. Jiang, W., Y. Wang, and G.A. Voth, *Molecular dynamics simulation of nanostructural organization in ionic liquid/water mixtures.* The Journal of Physical Chemistry B, 2007. **111**(18): p. 4812-4818.
175. Ficke, L.E. and J.F. Brennecke, *Interactions of ionic liquids and water.* The Journal of Physical Chemistry B, 2010. **114**(32): p. 10496-10501.
176. Ju, Z., et al., *Theoretical studies on glycolysis of poly (ethylene terephthalate) in ionic liquids.* RSC advances, 2018. **8**(15): p. 8209-8219.
177. Miyamoto, H., U. Schnupf, and J.W. Brady, *Water structuring over the hydrophobic surface of cellulose.* Journal of agricultural and food chemistry, 2014. **62**(46): p. 11017-11023.
178. Zhao, Y., et al., *Is there any preferential interaction of ions of ionic liquids with DMSO and H2O? A comparative study from MD simulation.* The Journal of Physical Chemistry B, 2015. **119**(22): p. 6686-6695.
179. Mazza, M., et al., *Influence of water on the dissolution of cellulose in selected ionic liquids.* Cellulose, 2009. **16**(2): p. 207-215.
180. Manna, B. and A. Ghosh, *Dissolution of cellulose in ionic liquid and water mixtures as revealed by molecular dynamics simulations.* Journal of Biomolecular Structure and Dynamics, 2019. **37**(15): p. 3987-4005.
181. Hall, C.A., et al., *Macroscopic and microscopic study of 1-ethyl-3-methyl-imidazolium acetate–water mixtures.* The Journal of Physical Chemistry B, 2012. **116**(42): p. 12810-12818.
182. Liu, X., et al., *Rodlike micelle structure and formation of ionic liquid in aqueous solution by molecular simulation.* Industrial & Engineering Chemistry Research, 2015. **54**(5): p. 1681-1688.
183. Yao, J., Z. Zhou, and H. Zhou, *Highway engineering composite material and its application.* 2019.
184. Clyne, T.W. and D. Hull, *An introduction to composite materials*. 2019: Cambridge university press.
185. Maiti, S., et al., *Sustainable fiber-reinforced composites: a Review.* Advanced Sustainable Systems, 2022. **6**(11): p. 2200258.
186. Barbero, E.J., *Introduction to composite materials design*. 2010: CRC press.

187. Zweben, C., *Composite Materials, chapter 10*, in *Mechanical Engineers' Handbook*. 2015. p. 1-37.
188. Joshi, S.V., et al., *Are natural fiber composites environmentally superior to glass fiber reinforced composites?* Composites Part A: Applied science and manufacturing, 2004. **35**(3): p. 371-376.
189. Ratna Prasad, A.V. and K. Mohana Rao, *Mechanical properties of natural fibre reinforced polyester composites: Jowar, sisal and bamboo.* Materials & Design, 2011. **32**(8): p. 4658-4663.
190. Kerni, L., et al., *A review on natural fiber reinforced composites.* Materials Today: Proceedings, 2020. **28**: p. 1616-1621.
191. Koronis, G., A. Silva, and M. Fontul, *Green composites: A review of adequate materials for automotive applications.* Composites Part B: Engineering, 2013. **44**(1): p. 120-127.
192. Nurazzi, N., et al., *Treatments of natural fiber as reinforcement in polymer composites—a short review.* Functional Composites and Structures, 2021. **3**(2): p. 024002.
193. Pickering, K.L., M.A. Efendy, and T.M. Le, *A review of recent developments in natural fibre composites and their mechanical performance.* Composites Part A: Applied Science and Manufacturing, 2016. **83**: p. 98-112.
194. Zini, E. and M. Scandola, *Green composites: an overview.* Polymer composites, 2011. **32**(12): p. 1905-1915.
195. Mulenga, T.K., A.U. Ude, and C. Vivekanandhan, *Techniques for modelling and optimizing the mechanical properties of natural fiber composites: A review.* Fibers, 2021. **9**(1): p. 6.
196. Karthi, N., et al., *An overview: Natural fiber reinforced hybrid composites, chemical treatments and application areas.* Materials today: proceedings, 2020. **27**: p. 2828-2834.
197. Charlet, K., et al., *Tensile deformation of a flax fiber.* Procedia Engineering, 2009. **1**(1): p. 233-236.
198. Huber, T., S. Pang, and M.P. Staiger, *All-cellulose composite laminates.* Composites Part A: Applied Science and Manufacturing, 2012. **43**(10): p. 1738-1745.
199. Chen, F., et al., *Unidirectional all-cellulose composites from flax via controlled impregnation with ionic liquid.* Polymers, 2020. **12**(5): p. 1010.
200. Haverhals, L.M., et al., *Process variables that control natural fiber welding: time, temperature, and amount of ionic liquid.* Cellulose, 2012. **19**: p. 13-22.
201. Shakeri, A., A.P. Mathew, and K. Oksman, *Self-reinforced nanocomposite by partial dissolution of cellulose microfibrils in ionic liquid.* Journal of composite materials, 2012. **46**(11): p. 1305-1311.
202. Marion, R., *Flax Fiber Offers Cotton Cool Comfort.* Agricultural Research, 2005. **53**(11).
203. Mohanty, A.K., M. Misra, and L.T. Drzal, *Surface modifications of natural fibers and performance of the resulting biocomposites: An overview.* Composite Interfaces, 2001. **8**(5): p. 313-343.
204. Spörl, J.M., et al., *Ionic liquid approach toward manufacture and full recycling of all-cellulose composites.* Macromolecular Materials and Engineering, 2018. **303**(1): p. 1700335.
205. Le Moigne, N., J. Bikard, and P. Navard, *Rotation and contraction of native and regenerated cellulose fibers upon swelling and dissolution: the role of morphological and stress unbalances.* Cellulose, 2010. **17**(3): p. 507-519.
206. Hermanutz, F., et al., *Processing of cellulose using ionic liquids.* Macromolecular Materials and Engineering, 2019. **304**(2): p. 1800450.
207. Jonoobi, M., et al., *Mechanical properties of cellulose nanofiber (CNF) reinforced polylactic acid (PLA) prepared by twin screw extrusion.* Composites science and technology, 2010. **70**(12): p. 1742-1747.

208. Han, D. and L. Yan, *Preparation of all-cellulose composite by selective dissolving of cellulose surface in PEG/NaOH aqueous solution.* Carbohydrate Polymers, 2010. **79**(3): p. 614-619.
209. Li, J., et al., *All-cellulose composites based on the self-reinforced effect.* Composites Communications, 2018. **9**: p. 42-53.
210. Wang, Y. and Y. Deng, *The kinetics of cellulose dissolution in sodium hydroxide solution at low temperatures.* Biotechnology and bioengineering, 2009. **102**(5): p. 1398-1405.
211. Lingwood, M.D., et al., *Unraveling the local energetics of transport in a polymer ion conductor.* Chemical communications, 2013. **49**(39): p. 4283-4285.
212. Chen, K., et al., *Hemp-based all-cellulose composites through ionic liquid promoted controllable dissolution and structural control.* Carbohydrate polymers, 2020. **235**: p. 116027.
213. Zhang, J., et al., *Dissolution of microcrystalline cellulose in phosphoric acid—molecular changes and kinetics.* Molecules, 2009. **14**(12): p. 5027-5041.
214. Uusi-Tarkka, E.-K., M. Skrifvars, and A. Haapala, *Fabricating sustainable all-cellulose composites.* Applied Sciences, 2021. **11**(21): p. 10069.
215. Ewoldt, R.H., M.T. Johnston, and L.M. Caretta, *Experimental challenges of shear rheology: how to avoid bad data.* Complex Fluids in Biological Systems: Experiment, Theory, and Computation, 2015: p. 207-241.
216. Annat, G., D.R. MacFarlane, and M. Forsyth, *Transport properties in ionic liquids and ionic liquid mixtures: the challenges of NMR pulsed field gradient diffusion measurements.* The Journal of Physical Chemistry B, 2007. **111**(30): p. 9018-9024.
217. Stejskal, E.O. and J.E. Tanner, *Spin diffusion measurements: spin echoes in the presence of a time-dependent field gradient.* The journal of chemical physics, 1965. **42**(1): p. 288-292.
218. Zhou, G., et al., *Insight into the behavior at the hygroscopicity and interface of the hydrophobic imidazolium-based ionic liquids.* Chinese Journal of Chemical Engineering, 2020.
219. Horne, M., et al., *The production and extraction of flax-fibre for textile fibres.* Journal of Biobased Materials and Bioenergy, 2010. **4**(2): p. 98-105.
220. Renouard, S., et al., *Protection of flax fiber-based yarns against natural soil degradation by chitosan.* Materials Letters, 2014. **137**: p. 269-273.
221. Heller, K., et al., *A comparative study between Europe and China in crop management of two types of flax: linseed and fibre flax.* Industrial Crops and Products, 2015. **68**: p. 24-31.
222. Sescousse, R., et al., *Viscosity of cellulose− imidazolium-based ionic liquid solutions.* The Journal of Physical Chemistry B, 2010. **114**(21): p. 7222-7228.
223. Lovell, C.S., et al., *Influence of cellulose on ion diffusivity in 1-ethyl-3-methyl-imidazolium acetate cellulose solutions.* Biomacromolecules, 2010. **11**(11): p. 2927-2935.
224. Kosan, B., C. Michels, and F. Meister, *Dissolution and forming of cellulose with ionic liquids.* Cellulose, 2008. **15**: p. 59-66.
225. Bazbouz, M.B., et al., *Dry-jet wet electrospinning of native cellulose microfibers with macroporous structures from ionic liquids.* Journal of Applied Polymer Science, 2019. **136**(10): p. 47153.
226. Sun, N., et al., *Complete dissolution and partial delignification of wood in the ionic liquid 1-ethyl-3-methylimidazolium acetate.* Green Chemistry, 2009. **11**(5): p. 646-655.
227. Cendra, C., et al., *Role of the anion on the transport and structure of organic mixed conductors.* Advanced Functional Materials, 2019. **29**(5): p. 1807034.
228. Liang, Y., et al., *Dissolution of cotton by 1-ethyl-3-methylimidazolium acetate studied with time–temperature superposition for three different fibre arrangements.* Cellulose, 2021. **28**(2): p. 715-727.

229. Zhang, X., M.E. Ries, and P.J. Hine, *Time–Temperature Superposition of the Dissolution of Silk Fibers in the Ionic Liquid 1-Ethyl-3-methylimidazolium Acetate.* Biomacromolecules, 2021. **22**(3): p. 1091-1101.
230. Budtova, T. and P. Navard, *Viscosity-temperature dependence and activation energy of cellulose solutions.* Nordic Pulp and Paper Research Journal, 2015. **30**(01): p. 99-104.
231. Druel, L., et al., *Rheology of cellulose-[DBNH][CO 2 Et] solutions and shaping into aerogel beads.* Green Chemistry, 2018. **20**(17): p. 3993-4002.
232. Villar, L., et al., *Dissolution kinetics of cellulose in ionic solvents by polarized light microscopy.* Cellulose, 2023: p. 1-13.
233. Alrefaei, N.S., P.J. Hine, and M.E. Ries, *Dissolution of hemp yarns by 1-ethyl-3-methylimidazolium acetate studied with time-temperature superposition.* Cellulose, 2023. **30**(16): p. 10039-10055.
234. Sescousse, R., R. Gavillon, and T. Budtova, *Aerocellulose from cellulose–ionic liquid solutions: Preparation, properties and comparison with cellulose–NaOH and cellulose–NMMO routes.* Carbohydrate Polymers, 2011. **83**(4): p. 1766-1774.
235. Alghamdi, A.S., P.J. Hine, and M.E. Ries, *Time–Temperature Superposition of the Dissolution of Wool Yarns in the Ionic Liquid 1-Ethyl-3-methylimidazolium Acetate.* Materials, 2024. **17**(1): p. 244.
236. Biganska, O. and P. Navard, *Kinetics of precipitation of cellulose from cellulose− NMMO− water solutions.* Biomacromolecules, 2005. **6**(4): p. 1948-1953.
237. Gavillon, R. and T. Budtova, *Kinetics of cellulose regeneration from cellulose− NaOH− water gels and comparison with cellulose− N-methylmorpholine-N-oxide− water solutions.* Biomacromolecules, 2007. **8**(2): p. 424-432.
238. Sescousse, R. and T. Budtova, *Influence of processing parameters on regeneration kinetics and morphology of porous cellulose from cellulose–NaOH–water solutions.* Cellulose, 2009. **16**: p. 417-426.
239. Ghatee, M.H., et al., *Temperature dependence of viscosity and relation with the surface tension of ionic liquids.* Fluid Phase Equilibria, 2010. **291**(2): p. 188-194.
240. Okoturo, O. and T. VanderNoot, *Temperature dependence of viscosity for room temperature ionic liquids.* Journal of Electroanalytical Chemistry, 2004. **568**: p. 167-181.
241. Freire, M.G., et al., *Thermophysical characterization of ionic liquids able to dissolve biomass.* Journal of Chemical & Engineering Data, 2011. **56**(12): p. 4813-4822.
242. Quijada-Maldonado, E., et al., *Experimental densities, dynamic viscosities and surface tensions of the ionic liquids series 1-ethyl-3-methylimidazolium acetate and dicyanamide and their binary and ternary mixtures with water and ethanol at T=(298.15 to 343.15 K).* The Journal of Chemical Thermodynamics, 2012. **51**: p. 51-58.
243. Zhang, J., et al., *NMR spectroscopic studies of cellobiose solvation in EmimAc aimed to understand the dissolution mechanism of cellulose in ionic liquids.* Physical Chemistry Chemical Physics, 2010. **12**(8): p. 1941-1947.
244. Antony, J.H., et al., *13C NMR relaxation rates in the ionic liquid 1-methyl-3-nonylimidazolium hexafluorophosphate.* The Journal of Physical Chemistry A, 2005. **109**(30): p. 6676-6682.
245. Tokuda, H., et al., *Physicochemical properties and structures of room temperature ionic liquids. 1. Variation of anionic species.* The Journal of Physical Chemistry B, 2004. **108**(42): p. 16593-16600.
246. McLaughlin, E., *Viscosity and self-diffusion in liquids.* Transactions of the Faraday Society, 1959. **55**: p. 28-38.

247. Zaccaria, F., et al., *Extraction of reliable molecular information from diffusion NMR spectroscopy: hydrodynamic volume or molecular mass?* Chemistry–A European Journal, 2019. **25**(42): p. 9930-9937.
248. Li, J.C. and P. Chang, *Self-diffusion coefficient and viscosity in liquids.* The Journal of Chemical Physics, 1955. **23**(3): p. 518-520.
249. Vitz, J., et al., *Extended dissolution studies of cellulose in imidazolium based ionic liquids.* Green chemistry, 2009. **11**(3): p. 417-424.
250. Cho, H.M., A.S. Gross, and J.-W. Chu, *Dissecting force interactions in cellulose deconstruction reveals the required solvent versatility for overcoming biomass recalcitrance.* Journal of the American Chemical Society, 2011. **133**(35): p. 14033-14041.
251. Lu, B., A. Xu, and J. Wang, *Cation does matter: how cationic structure affects the dissolution of cellulose in ionic liquids.* Green Chemistry, 2014. **16**(3): p. 1326-1335.
252. Zhang, J., et al., *Understanding cellulose dissolution: effect of the cation and anion structure of ionic liquids on the solubility of cellulose.* Science China Chemistry, 2016. **59**: p. 1421-1429.
253. Zhao, Y., et al., *Effects of anionic structure on the dissolution of cellulose in ionic liquids revealed by molecular simulation.* Carbohydrate polymers, 2013. **94**(2): p. 723-730.
254. Bonifacio, A., et al., *Plasticizer design strategies enabling advanced applications of cellulose acetate.* European Polymer Journal, 2023: p. 112360.
255. El Seoud, O.A., T.A. Bioni, and M.T. Dignani, *Understanding cellulose dissolution in ionic liquid-dimethyl sulfoxide binary mixtures: Quantification of the relative importance of hydrogen bonding and hydrophobic interactions.* Journal of Molecular Liquids, 2021. **322**: p. 114848.
256. Xu, A., J. Wang, and H. Wang, *Effects of anionic structure and lithium salts addition on the dissolution of cellulose in 1-butyl-3-methylimidazolium-based ionic liquid solvent systems.* Green chemistry, 2010. **12**(2): p. 268-275.
257. Xu, A., et al., *Effect of alkyl chain length in anions on thermodynamic and surface properties of 1-butyl-3-methylimidazolium carboxylate ionic liquids.* Industrial & engineering chemistry research, 2012. **51**(8): p. 3458-3465.
258. Xu, A., et al., *Effect of alkyl chain length in anion on dissolution of cellulose in 1-butyl-3-methylimidazolium carboxylate ionic liquids.* Journal of Molecular Liquids, 2014. **197**: p. 211-214.
259. Hua, L., et al., *Molecular dynamics study on effects of the synergistic effect of anions and cations on the dissolution of cellulose in ionic liquids.* Journal of Molecular Liquids, 2024. **415**: p. 126348.
260. Xu, A., et al., *Dissolution behavior of cellulose in IL+ DMSO solvent: effect of alkyl length in imidazolium cation on cellulose dissolution.* Advances in Materials Science and Engineering, 2015. **2015**.
261. Zhao, Y., et al., *Effects of cationic structure on cellulose dissolution in ionic liquids: a molecular dynamics study.* ChemPhysChem, 2012. **13**(13): p. 3126-3133.
262. Ocreto, J.B., et al., *Ionic liquid dissolution utilized for biomass conversion into biofuels, value-added chemicals and advanced materials: A comprehensive review.* Chemical Engineering Journal, 2022. **445**: p. 136733.
263. Klähn, M., et al., *On the different roles of anions and cations in the solvation of enzymes in ionic liquids.* Physical Chemistry Chemical Physics, 2011. **13**(4): p. 1649-1662.
264. Gupta, K.M. and J. Jiang, *Cellulose dissolution and regeneration in ionic liquids: A computational perspective.* Chemical Engineering Science, 2015. **121**: p. 180-189.

265. Fernandes, A.M., et al., *Evaluation of cation− anion interaction strength in ionic liquids.* The Journal of Physical Chemistry B, 2011. **115**(14): p. 4033-4041.
266. Mezzetta, A., et al., *Insights into the levulinate-based ionic liquid class: Synthesis, cellulose dissolution evaluation and ecotoxicity assessment.* New Journal of Chemistry, 2019. **43**(33): p. 13010-13019.
267. Yao, Y., et al., *Mechanistic study on the cellulose dissolution in ionic liquids by density functional theory.* Chinese Journal of Chemical Engineering, 2015. **23**(11): p. 1894-1906.
268. Moyer, P., et al., *Relationship between lignocellulosic biomass dissolution and physicochemical properties of ionic liquids composed of 3-methylimidazolium cations and carboxylate anions.* Physical Chemistry Chemical Physics, 2018. **20**(4): p. 2508-2516.
269. Remsing, R.C., et al., *Mechanism of cellulose dissolution in the ionic liquid 1-n-butyl-3-methylimidazolium chloride: a 13 C and 35/37 Cl NMR relaxation study on model systems.* Chemical Communications, 2006(12): p. 1271-1273.
270. Parviainen, A., et al., *Predicting cellulose solvating capabilities of acid–base conjugate ionic liquids.* ChemSusChem, 2013. **6**(11): p. 2161-2169.
271. Moulthrop, J.S., et al., *High-resolution 13C NMR studies of cellulose and cellulose oligomers in ionic liquid solutions.* Chemical communications, 2005(12): p. 1557-1559.
272. Roy, H.A. and M. Rodgers, *1-Alkyl-3-methylimidazolium cation binding preferences in hexafluorophosphate ionic liquid clusters determined using competitive TCID measurements and theoretical calculations.* Physical Chemistry Chemical Physics, 2021. **23**(33): p. 18145-18162.
273. Erdmenger, T., et al., *Homogeneous tritylation of cellulose in 1-butyl-3-methylimidazolium chloride.* Macromolecular bioscience, 2007. **7**(4): p. 440-445.
274. Roy, H. and M. Rodgers, *Absolute trends and accurate and precise gas-phase binding energies of 1-alkyl-3-methylimidazolium tetrafluoroborate ionic liquid clusters from combined independent and competitive TCID measurements.* The Journal of Physical Chemistry A, 2020. **124**(49): p. 10199-10215.
275. Rabideau, B.D. and A.E. Ismail, *Mechanisms of hydrogen bond formation between ionic liquids and cellulose and the influence of water content.* Physical Chemistry Chemical Physics, 2015. **17**(8): p. 5767-5775.
276. Haghtalab, A. and A. Shojaeian, *Volumetric and viscometric behaviour of the binary systems of N-methyldiethanolamine and diethanolamine with 1-butyl-3-methylimidazolium acetate at various temperatures.* The Journal of Chemical Thermodynamics, 2014. **68**: p. 128-137.
277. Fendt, S., et al., *Viscosities of acetate or chloride-based ionic liquids and some of their mixtures with water or other common solvents.* Journal of Chemical & Engineering Data, 2011. **56**(1): p. 31-34.
278. Seki, S., et al., *Effects of cation and anion on physical properties of room-temperature ionic liquids.* Journal of Molecular Liquids, 2010. **152**(1-3): p. 9-13.
279. Yadav, A., et al., *Densities and dynamic viscosities of ionic liquids having 1-butyl-3-methylimidazolium cation with different anions and bis (trifluoromethylsulfonyl) imide anion with different cations in the temperature range (283.15 to 363.15) K.* The Journal of Chemical Thermodynamics, 2018. **116**: p. 67-75.
280. Ahosseini, A. and A.M. Scurto, *Viscosity of imidazolium-based ionic liquids at elevated pressures: cation and anion effects.* International Journal of Thermophysics, 2008. **29**: p. 1222-1243.

281. Tokuda, H., et al., *Physicochemical properties and structures of room temperature ionic liquids. 2. Variation of alkyl chain length in imidazolium cation.* The Journal of Physical Chemistry B, 2005. **109**(13): p. 6103-6110.
282. Zhao, Y., et al., *Aggregation of Ionic Liquids [C n mim] Br (n= 4, 6, 8, 10, 12) in D2O: A NMR Study.* The Journal of Physical Chemistry B, 2008. **112**(7): p. 2031-2039.
283. Zhang, Y., et al., *Dissolution of cellulose in 1-allyl-3-methylimizodalium carboxylates at room temperature: A structure–property relationship study.* Carbohydrate polymers, 2015. **117**: p. 666-672.
284. Hou, J., Z. Zhang, and L.A. Madsen, *Cation/anion associations in ionic liquids modulated by hydration and ionic medium.* The Journal of Physical Chemistry B, 2011. **115**(16): p. 4576-4582.
285. Huddleston, J.G., et al., *Characterization and comparison of hydrophilic and hydrophobic room temperature ionic liquids incorporating the imidazolium cation.* Green chemistry, 2001. **3**(4): p. 156-164.
286. Wang, Y. and G.A. Voth, *Tail aggregation and domain diffusion in ionic liquids.* The Journal of Physical Chemistry B, 2006. **110**(37): p. 18601-18608.
287. Freire, M.G., et al., *Impact of self-aggregation on the formation of ionic-liquid-based aqueous biphasic systems.* The Journal of Physical Chemistry B, 2012. **116**(26): p. 7660-7668.
288. Jacquemin, J., et al., *Density and viscosity of several pure and water-saturated ionic liquids.* Green Chemistry, 2006. **8**(2): p. 172-180.
289. Duchemin, B.J., M.P. Staiger, and R.H. Newman. *High-Temperature Viscoelastic Relaxation in All-Cellulose Composites*. in *Macromolecular Symposia*. 2014. Wiley Online Library.
290. Shimizu, K., J.N. Canongia Lopes, and A.M. Goncalves da Silva, *Ionic liquid films at the water–air interface: Langmuir isotherms of tetra-alkylphosphonium-based ionic liquids.* Langmuir, 2015. **31**(30): p. 8371-8378.
291. Jitvisate, M. and J.R. Seddon, *Near-wall molecular ordering of dilute ionic liquids.* The Journal of Physical Chemistry C, 2017. **121**(34): p. 18593-18597.
292. Henderson, Z., et al., *Water-induced reordering in ultrathin ionic liquid films.* Journal of Physics: Condensed Matter, 2018. **30**(33): p. 334003.
293. Sastry, N.V., et al., *Aggregation behavior of pyridinium based ionic liquids in water–surface tension, 1H NMR chemical shifts, SANS and SAXS measurements.* Journal of colloid and interface science, 2012. **371**(1): p. 52-61.
294. Zhang, F., C. Fang, and R. Qiao, *Effects of water on mica–ionic liquid interfaces.* The Journal of Physical Chemistry C, 2018. **122**(16): p. 9035-9045.
295. Walz, M.M., et al., *The Surface of Ionic Liquids in Water: From an Ionic Tug of War to a Quasi-Ordered Two-Dimensional Layer.* ChemPhysChem, 2024. **25**(1): p. e202300551.
296. Jonas, S., P. Ulrich, and A. Merwe, *Interaction of Levitated Ionic Liquid Droplets with Water.* 2012.
297. Kraemer, R., et al., *Ionic liquid interactions with cellulose and the effect of water.* 2023.
298. Kempter, V. and B. Kirchner, *The role of hydrogen atoms in interactions involving imidazolium-based ionic liquids.* Journal of Molecular Structure, 2010. **972**(1-3): p. 22-34.
299. Cammarata, L., et al., *Molecular states of water in room temperature ionic liquids.* Physical Chemistry Chemical Physics, 2001. **3**(23): p. 5192-5200.
300. Medronho, B., et al., *Rationalizing cellulose (in) solubility: reviewing basic physicochemical aspects and role of hydrophobic interactions.* Cellulose, 2012. **19**: p. 581-587.

301. Dong, K., S. Zhang, and J. Wang, *Understanding the hydrogen bonds in ionic liquids and their roles in properties and reactions.* Chemical communications, 2016. **52**(41): p. 6744-6764.
302. Xing, D.Y., S.Y. Chan, and T.-S. Chung, *Molecular interactions between polybenzimidazole and [EMIM] OAc, and derived ultrafiltration membranes for protein separation.* Green Chemistry, 2012. **14**(5): p. 1405-1412.
303. Sahputra, I.H., A. Alexiadis, and M.J. Adams, *Effects of moisture on the mechanical properties of microcrystalline cellulose and the mobility of the water molecules as studied by the hybrid molecular mechanics–molecular dynamics simulation method.* Journal of Polymer Science Part B: Polymer Physics, 2019. **57**(8): p. 454-464.
304. Klemm, D., et al., *Cellulose: fascinating biopolymer and sustainable raw material.* Angewandte chemie international edition, 2005. **44**(22): p. 3358-3393.
305. Chami Khazraji, A. and S. Robert, *Interaction effects between cellulose and water in nanocrystalline and amorphous regions: A novel approach using molecular modeling.* Journal of Nanomaterials, 2013. **2013**(1): p. 409676.
306. Shi, J., et al., *Understanding the role of water during ionic liquid pretreatment of lignocellulose: co-solvent or anti-solvent?* Green Chemistry, 2014. **16**(8): p. 3830-3840.
307. Minnick, D.L., et al., *Cellulose solubility in ionic liquid mixtures: temperature, cosolvent, and antisolvent effects.* The Journal of Physical Chemistry B, 2016. **120**(32): p. 7906-7919.
308. Olsson, C., et al., *Influence of water on swelling and dissolution of cellulose in 1-ethyl-3-methylimidazolium acetate.* Carbohydrate Polymers, 2014. **99**: p. 438-446.
309. Hinner, L.P., et al., *Efficient cellulose dissolution in a tertiary [EHEMIM]-[EMIM] OAc-water system.* Journal of Molecular Liquids, 2019. **281**: p. 236-242.
310. Medronho, B. and B. Lindman, *Brief overview on cellulose dissolution/regeneration interactions and mechanisms.* Advances in colloid and interface science, 2015. **222**: p. 502-508.
311. Etale, A., et al., *Cellulose: a review of water interactions, applications in composites, and water treatment.* Chemical reviews, 2023. **123**(5): p. 2016-2048.
312. Baghaei, B. and M. Skrifvars, *All-Cellulose Composites: A Review of Recent Studies on Structure, Properties and Applications.* Molecules, 2020. **25**(12): p. 2836.
313. Koide, M., et al., *Influence of water on the intrinsic characteristics of cellulose dissolved in an ionic liquid.* Cellulose, 2020. **27**: p. 7389-7398.
314. Cao, R., et al., *Swelling and dissolution behaviors of cellulose in phosphate-based ionic liquids-H2O binary systems: In-situ observation and molecular dynamics simulation.* Journal of Molecular Liquids, 2024. **415**: p. 126315.